

Electronic Thesis and Dissertation Repository

4-4-2024 10:00 AM

Chest Computed Tomography and Magnetic Resonance Imaging Texture Measurements of Chronic Obstructive Pulmonary Disease

Maksym Sharma, *The University of Western Ontario*

Supervisor: Parraga, Grace, *The University of Western Ontario*

A thesis submitted in partial fulfillment of the requirements for the Doctor of Philosophy degree in Medical Biophysics

© Maksym Sharma 2024

Follow this and additional works at: <https://ir.lib.uwo.ca/etd>



Part of the [Medical Biophysics Commons](#)

Recommended Citation

Sharma, Maksym, "Chest Computed Tomography and Magnetic Resonance Imaging Texture Measurements of Chronic Obstructive Pulmonary Disease" (2024). *Electronic Thesis and Dissertation Repository*. 9998.

<https://ir.lib.uwo.ca/etd/9998>

This Dissertation/Thesis is brought to you for free and open access by Scholarship@Western. It has been accepted for inclusion in Electronic Thesis and Dissertation Repository by an authorized administrator of Scholarship@Western. For more information, please contact wlsadmin@uwo.ca.

Abstract

Pulmonary imaging using computed tomography (CT) and magnetic resonance imaging (MRI) provide a method to measure airway and parenchymal pathologic information that cannot be provided using spirometry. Currently, it remains difficult to predict which chronic obstructive pulmonary disease (COPD) patients will worsen using spirometry, which although safe and inexpensive, does not provide small airway information where COPD is believed to initiate. Quantitative CT and MRI measurements provide regional structure and function information but are not included in mortality risk assessments, prognosis, or COPD staging. Therefore, my overarching hypothesis is that CT and MRI ventilation texture measurements combined with machine learning will classify at-risk ex-smokers, as well as predict accelerated lung function decline and mortality in ex-smokers with and without COPD. I first accurately detected the presence of abnormal diffusing capacity in ex-smokers without COPD or CT evidence of emphysema, by quantifying visually unapparent CT textures and applying machine-learning models. Next, using baseline MR imaging textures, I evaluated longitudinal data to predict accelerated lung function decline in ex-smokers across 3-years. I identified a subset of MRI texture features that independently predicted rapid worsening, where the longitudinal changes of these texture features correlated with changes in lung function. Finally, I used baseline CT and MRI texture measurements and accurately predicted 10-year mortality, which is the ultimate patient outcome. The series of studies presented here are among the first to demonstrate the feasibility of predicting clinically-relevant outcomes exclusively using CT and MR imaging textures. In addition, machine-learning models trained on established clinical and demographic measurements were outperformed by models trained only using texture features. Taken together, these results

suggest that quantitative imaging measurements provide additional prognostic value and perhaps should be considered as potential biomarkers for early detection of COPD and evaluating disease progression and longitudinal patient outcomes.

Keywords

Machine-learning, Texture Analysis, Magnetic Resonance Imaging, Computed Tomography, Hyperpolarized Gas, Ex-smokers, COPD, Gas-exchange, Disease Progression, Mortality.

Summary for Lay Audience

It is hard to predict how chronic obstructive pulmonary disease (COPD) will progress and ultimately affect patients in the long run. The limitation arises from the fact that conventional clinical metrics, such as spirometry, offer a global perspective on lung function and may not adequately capture nuances in disease progression. Similarly, established clinical risk factors in such assessments may often capture extra-pulmonary manifestations of the lung disease. The small airways are considered the major site of airflow limitation in COPD, which spirometry measured at the mouth is not sensitive to. In contrast, quantitative computed tomography (CT) measurements allow for the evaluation of airway structural changes, while magnetic resonance imaging (MRI) can provide complementary information on regional ventilation within the lungs. Unfortunately, measurements obtained from chest imaging modalities are currently not included in widely accepted clinical assessments, diagnosis, prognosis, or staging of COPD. Consequently, to address this gap, I developed texture analysis and machine learning algorithms to predict longitudinal clinical outcomes and quantify structural and functional changes occurring in the lungs of ex-smokers with and without COPD. First, I demonstrated the sensitivity of CT texture measurements by detecting abnormal diffusing capacity in patients with clinically-normal CT images. Next, I evaluated MRI texture features at baseline and 3-year follow-up to predict an accelerated lung function decline in ex-smokers with and without COPD. Notably, changes in select texture features over time also correlated with changes in lung function, emphasizing the sensitivity of texture features. Lastly, I predicted 10-year mortality using CT and MRI textures, outperforming all other clinical measurements available to physicians. Together, these results tell us that quantitative imaging textures provide additional prognostic value and perhaps should be considered for evaluating disease progression and clinical outcomes in COPD.

Co-Authorship Statement

The following thesis contains three manuscripts: two of these manuscripts have been published in scientific journals and one manuscript has been submitted for publication. As first author of these manuscripts, I was a significant contributor to all aspects of the studies as well as manuscript preparation and submission. Specifically, I was responsible for conceiving study design, performing study visits, data collection and analysis, image processing, statistical analysis, and drafting, final approval and submission of the manuscripts. I was also responsible for the conceptualization and development of a CT and an MRI texture analysis and machine-learning pipelines, which can quantify the signal intensities as well as their spatial distribution and generate pulmonary imaging measurements. As the Principal Investigator and thesis Supervisor, Dr. Grace Parraga provided continued guidance and was responsible for the conception of the study, experimental design, data interpretation, drafting and approval of the manuscript. She was also the guarantor of data integrity and responsible for Good Clinical Practice. The management of all study visits and acquisition of pulmonary function data were performed under the supervision of Danielle Knipping and Angela Wilson. MRI acquisition for participants was performed by David Reese. Polarization of hyperpolarized gas was performed by myself, Andrew Westcott, Jonathan MacNeil, Alexander M Matheson, Tamas Lindenmaier and Ivailo Petrov. For each manuscript included in the thesis, all co-authors approved the final manuscript draft and the specific contributions are as follows:

Chapter 2 is an original research article entitled “*Machine Learning and CT Texture Features in Ex-smokers with no CT Evidence of Emphysema and Mildly Abnormal Diffusing Capacity*” and was published in Academic Radiology Journal in 2023. This manuscript was co-authored by Maksym Sharma, Miranda Kirby, David G. McCormack and Grace Parraga. Miranda Kirby and

Grace Parraga assisted with drafting and approval of the manuscript. Miranda Kirby and David G. McCormack assisted with data acquisition. Miranda Kirby, David G. McCormack and Grace Parraga assisted with clinical interpretation of the data. Miranda Kirby, David G. McCormack and Grace Parraga assisted with manuscript editing.

Chapter 3 is an original research article entitled “*Machine Learning and MR Image Texture Analysis Predicts Accelerated Lung Function Decline in Ex-Smokers with and without COPD*” and was submitted to the Journal of Medical Imaging in 2024. This manuscript was co-authored by Miranda Kirby, Aaron Fenster, David G. McCormack and Grace Parraga. Miranda Kirby and David G. McCormack assisted with data acquisition. Miranda Kirby, David G. McCormack and Grace Parraga assisted with clinical interpretation of the data. Aaron Fenster assisted with data interpretation and study design. Miranda Kirby, Aaron Fenster, David G. McCormack and Grace Parraga assisted with manuscript editing and drafting the final manuscript.

Chapter 4 is an original research article entitled “*Chest MRI and CT Predictors of 10-year All-cause Mortality in COPD*” and was published in the Journal of Chronic Obstructive Pulmonary Disease in 2023. This manuscript was co-authored by Paulina V. Wyszkievicz, Alexander M. Matheson, David G. McCormack and Grace Parraga. Paulina V. Wyszkievicz and Alexander M. Matheson assisted with data acquisition and analysis. David G. McCormack was responsible for recruiting study participants and providing clinical input and interpretation of the data. Grace Parraga was responsible for study design, data analysis and interpretation. All authors were responsible for manuscript editing.

Acknowledgments

I would first like to thank my supervisor, Dr. Grace Parraga, for providing exceptional opportunities and ongoing guidance throughout my graduate journey. I am extremely appreciative of the endless support and unique research environment you created over the years, which I was fortunate to be a part of. I appreciate the countless opportunities to conduct innovative research, work directly with our study participants, and collaborate with the brightest minds. I cannot thank you enough for sharing your wisdom, knowledge and experience, which have shaped me in many aspects of my graduate career. My skills and accomplishments are a direct result of your work and dedication, and for this I am deeply grateful. I am glad I had a supervisor like you, thank you.

I would also like to thank all the members of my advisory committee: Dr. Aaron Fenster, Dr. Hanif Ladak, and Dr. David Palma. To Dr. Fenster, thank you for always probing my knowledge with the unique big-picture questions, which further stimulated my interest in the field and helped prepare for my final thesis defense. To Dr. Ladak, thank you for always providing valuable insights about the technical aspects of my projects and thoroughly walking through and critiquing my image processing workflow, which was invaluable for my thesis. To Dr. Palma, thank your for always validating my work and providing your valuable clinical insights during my graduate journey, and thank you so much for your flexibility throughout and collaboration opportunities.

A special thank you to everyone within the Parraga lab, both past and present. To Marrison, thank you for being my first friend here and your companionship throughout my entire graduate journey. Thank you for your great sense of humor and all the great discussions we had at lunch or our coffee runs, all the while helping me achieve my research goals. To Rachel and Alex, thank you for being such excellent role models and senior students, setting a great example for the lab. Thank you for your genuine interest in all life and science related conversations and discussions we had, your

profound insights were truly impactful. To Kiran and Paulina, thank you for being positive, kind and amazing friends and lab members. You always managed to lighten up my mood and made my graduate journey immensely more fun. Thank you for all the laughs we shared and interesting conversations about life and research topics, which I will miss dearly.

To Angela, thank you for always being helpful and caring. The mornings were always brightened with your presence, thank you for all the snacks and wealth of motivation that you provided to keep me going throughout the day, the week, and the end of my degree. To Andrea, Jonathan, Andrew, Dante, Tamas, Danielle, Ivailo and Lauren, thank you for all your contributions to my growth as a person and researcher. You were all instrumental in the collection of the data that this thesis is based on, which I greatly appreciate, thank you. To Sam and Ali, thank you for allowing me to mentor you and I hope that you will keep in touch in your future endeavours and journey to triumph.

Thank you to all the students and researchers at Robarts and beyond, who have created a work-life balance that allowed me to thrive while working hard towards my goals. Thank you to everyone in the first year communication course for introducing me to so many great people that have now become lifelong cherished friendships. I feel incredibly lucky and have a deep sense of honour to be introduced to such a wonderful group of people in my life and have such great relationships.

Finally, my deepest gratitude is reserved for my parents and my better half, Phoenix. Without you, none of this would be possible. Thank you for all the sacrifices that you have personally made to get me here, and no matter where I end up, I will never forget all the love and support you relentlessly offered to me.

Table of Contents

Abstract.....	ii
Summary for Lay Audience.....	iv
Co-Authorship Statement	v
Acknowledgments	vii
Table of Contents	ix
List of Tables	xiv
List of Figures.....	xvi
List of Appendices.....	xviii
List of Abbreviations	xix
CHAPTER 1	1
1 INTRODUCTION.....	1
1.1 Motivation and Rationale.....	1
1.2 Structure and Function of the Lung	6
1.2.1 Airways	8
1.2.2 Alveoli.....	9
1.2.3 Ventilation and Perfusion	10
1.3 Pathophysiology of Chronic Obstructive Pulmonary Disease	11
1.3.1 Airflow Obstruction and Small Airways Disease	12
1.3.2 Emphysema.....	13
1.3.3 Pulmonary Vascular Changes	14
1.4 Clinical Measures of Global Lung Function	15
1.4.1 Spirometry.....	15
1.4.2 Plethysmography.....	17
1.4.3 Diffusing Capacity of the Lung	19
1.4.4 Six Minute Walk Test	20
1.4.5 St. George’s Respiratory Questionnaire	21

1.4.6	Lung Function Decline	21
1.4.6.1	Normal Lung Aging.....	21
1.4.6.2	COPD: Accelerated Lung Aging	22
1.5	Imaging Pulmonary Structure and Function	25
1.5.1	Planar Chest X-ray.....	25
1.5.2	X-ray Computed Tomography	26
1.5.3	Magnetic Resonance Imaging.....	29
1.5.3.1	Proton MRI	30
1.5.3.2	Hyperpolarized Noble Gas MRI.....	31
1.5.4	Nuclear Medicine Imaging	33
1.6	Texture Analysis in Pulmonary Imaging.....	35
1.6.1	Typical Workflow	37
1.7	Thesis Hypotheses and Objectives.....	44
1.8	References	48
CHAPTER 2	67
2	MACHINE LEARNING AND CT TEXTURE FEATURES IN EX-SMOKERS WITH NO CT EVIDENCE OF EMPHYSEMA AND MILDLY ABNORMAL DIFFUSING CAPACITY	67
2.1	Introduction.....	67
2.2	Methods.....	69
2.2.1	Participants.....	69
2.2.2	Pulmonary function tests and questionnaires.....	70
2.2.3	CT acquisition and analysis	70
2.2.4	MRI acquisition and analysis.....	71
2.2.5	CT feature extraction, selection and machine-learning	72
2.2.6	Statistical analysis.....	73
2.3	Results	74
2.3.1	Demographics, pulmonary function and imaging measurements	75
2.3.2	Texture feature extraction and selection	76

2.3.3	Machine-learning classification	80
2.3.4	Relationships.....	83
2.4	Discussion.....	85
2.5	References	90
2.6	Supplemental Material	93
2.6.1	Supplementary Tables.....	93
CHAPTER 3.....	101	
3	MACHINE LEARNING AND MR IMAGE TEXTURE ANALYSIS PREDICTS ACCELERATED LUNG FUNCTION DECLINE IN EX- SMOKERS WITH AND WITHOUT COPD	101
3.1	Introduction.....	101
3.2	Materials and Methods.....	103
3.2.1	Study Design and Participants	103
3.2.2	Pulmonary Function Tests and Image Acquisition.....	104
3.2.4	Feature Extraction and Selection Pipeline	109
3.2.5	Machine learning and Statistical Analysis	110
3.3	Results	111
3.3.1	Participant Demographics.....	112
3.3.2	Imaging Measurements and Texture Features	113
3.3.3	Machine learning Modeling.....	115
3.3.4	Relationships with Clinical Measurements.....	119
3.4	Discussion.....	121
3.5	Conclusions.....	123
3.6	References	124
CHAPTER 4.....	127	
4	CHEST MRI AND CT PREDICTORS OF 10-YEAR ALL-CAUSE MORTALITY IN COPD.....	127
4.1	Introduction.....	127
4.2	Materials and Methods.....	129

4.2.1	Study Participants	129
4.2.2	Pulmonary Function Tests and Questionnaires.....	130
4.2.3	CT Acquisition and Analysis	130
4.2.4	MRI Acquisition and Analysis.....	131
4.2.5	Texture Feature Extraction, Selection and Machine-learning	132
4.2.6	Statistical Analysis.....	134
4.3	Results	134
4.3.1	Participant Demographics and Mortality	134
4.3.2	Texture Extraction and Selection.....	138
4.3.3	Predicting 10-year All-cause Mortality	142
4.4	Discussion.....	147
4.5	Conclusion	151
4.6	References	152
4.7	Supplemental Material	158
4.7.1	Supplementary Tables.....	158
CHAPTER 5	161
5	CONCLUSIONS AND FUTURE DIRECTIONS.....	161
5.1	Overview and Research Questions.....	161
5.2	Summary and Conclusions	163
5.3	Limitations.....	167
5.3.1	Study Specific Limitations.....	167
5.3.2	General Limitations	170
5.4	Future Directions	172
5.4.1	Generating synthetic MRI ventilation maps using CT and Deep-learning	172
5.4.2	Texture Analysis and Machine Learning for Predicting Quality-of-life Worsening and Exercise Limitation.....	175
5.5	Significance and Impact	179
5.6	References	181

APPENDICES 188

List of Tables

Table 1-1. COPD severity stages based on GOLD criteria	17
Table 1-2. Summary of pulmonary imaging techniques and their quantitative measurements, strengths and challenges	35
Table 2-1. Baseline participant demographics and pulmonary function measurements	75
Table 2-2. Imaging measurements of ex-smokers with normal and mildly abnormal DL _{CO}	76
Table 2-3. Machine-learning model classification accuracies.....	81
Table 2-4. Texture analysis matrices and CT features extracted from each participant	93
Table 2-5. CT texture feature descriptors for machine-learning modelling	95
Table 2-6. Extracted texture feature differences between DL _{CO} subgroups	96
Table 2-7. Distribution of significant texture features based on extraction method and matrices	97
Table 2-8. Top PCA components from orthogonally rotated correlation matrix.....	98
Table 2-9. Machine-learning model accuracies using only PCA and emergent components for classification	99
Table 2-10. Correlations of texture features with clinically-relevant measurements.....	100
Table 3-1. Baseline participant demographics and pulmonary function measurements	112
Table 3-2. Participant demographics and pulmonary function measurements at follow-up visit	113
Table 3-3. Imaging measurements of participants with stable and accelerated lung function decline	114
Table 3-4. Imaging measurements of participants with stable and accelerated lung function decline at follow-up visit.....	114
Table 3-5. MRI texture feature descriptors for machine-learning modelling.....	115
Table 3-6. Machine-learning performance at predicting accelerated lung function decline	116

Table 3-7. DeLong’s test for comparing the models for predicting accelerated disease progression in ex-smokers.....	117
Table 4-1. Participant demographics, pulmonary function and imaging measurements in survivors and deceased ex-smokers.....	137
Table 4-2. MRI and CT texture features in survivors and deceased ex-smokers.....	138
Table 4-3. Machine-learning performance at predicting all-cause mortality after 10-years	142
Table 4-4. Summary of top performing measurements for the key statistical analyses	147
Table 4-5. Participant demographics, pulmonary function and imaging by COPD status	158
Table 4-6. MRI and CT texture feature descriptors.....	159
Table 4-7. Correlations of selected CT and MRI predictor variables in machine-learning models	160

List of Figures

Figure 1-1. Leading causes of death worldwide in 2019.....	2
Figure 1-2. Hospitalizations by chronic illness condition at first admission in Canada	3
Figure 1-3. Structural and functional lung components	8
Figure 1-4. Airways and parenchyma histology for Healthy vs COPD patient	12
Figure 1-5. Axial CT images for absence of emphysema and different emphysema subtypes.....	14
Figure 1-6. Pulmonary function test using spirometry.....	16
Figure 1-7. Pulmonary function test using plethysmography.....	18
Figure 1-8. Lung Function Decline.....	23
Figure 1-9. Coronal high resolution CT quantitative measurements	28
Figure 1-10. Inhaled hyperpolarized gas MR imaging.....	32
Figure 1-11. Standard image processing and texture analysis pipeline.....	38
Figure 2-1. CONSORT Flow Diagram	74
Figure 2-2. Image Processing and Model Generation Pipeline	77
Figure 2-3. Diffusion weighted MRI ADC and CT imaging for representative ex- smokers in normal and abnormal DL _{CO} subgroups	79
Figure 2-4. Receiver-operator characteristic curves of texture features and clinical variables.....	82
Figure 2-5. Relationships between selected texture features and clinical measurements.....	84
Figure 3-1. CONSORT Flow Diagram	104
Figure 3-2. Ventilation Defect Cluster Volume Output from Custom-developed Algorithm.....	108
Figure 3-3. Image Processing and Model Generation Pipeline	109
Figure 3-4. Receiver-operator Characteristic Curves of Clinical and Texture Measurements	118
Figure 3-5. Relationships between Selected Texture Features and Change in FEV ₁	120
Figure 4-1. CONSORT flow diagram	135

Figure 4-2. Participant enrollment and follow-up timeframe	136
Figure 4-3. Chest CT for representative surviving and deceased ex-smokers with and without COPD	139
Figure 4-4. Hyperpolarized gas MRI for representative surviving and deceased ex-smokers with and without COPD	141
Figure 4-5. Receiver-operator characteristic curves of texture features and clinical variables	144
Figure 4-6. Logistic regression models for associations between all-cause mortality and clinical, imaging and textural measurements	145
Figure 4-7. Kaplan-Meier survival curves of 10-year all-cause mortality in ex-smokers	146
Figure 5-1. Baseline and follow-up visit ³He MRI ventilation images with associated texture and imaging measurements	177
Figure 5-2. Logistic regression analysis of individual ³He MRI ventilation features	178

List of Appendices

Appendix A – Quantification of Pulmonary Functional MRI: State-of-the-Art and Emerging Image Processing Methods and Measurements	188
Appendix B – Hyperpolarized Gas Magnetic Resonance Imaging Texture Analysis and Machine Learning to explain Accelerated Lung Function Decline in Ex-smokers with and without COPD.....	253
Appendix C – Don’t Forget the Kids!: Novel Pulmonary MRI and AI of Neonatal Lung Disease	263
Appendix D – Permission for Reproduction of Scientific Articles	266
Appendix E – Health Science Research Ethics Board Approval Notices	298
Appendix F – Curriculum Vitae	305

List of Abbreviations

6MWD	Six Minute Walk Distance
A	Surface Area of Tissue Barrier
ADC	Apparent Diffusion Coefficients
ATS	American Thoracic Society
AUC	Area Under Receiver-operator Characteristic Curve
BD	Bronchodilator
BMI	Body Mass Index
BV ₅	Blood volume in vessels with cross-sectional-area < 5 mm ²
BV ₅₋₁₀	Blood volume in vessels with cross-sectional-area 5-10 mm ²
BV ₁₀	Blood volume in vessels with cross-sectional-area > 10 mm ²
CBIR	Content-based Image Retrieval
CNN	Convolutional Neural Networks
COPD	Chronic Obstructive Pulmonary Disease
CT	Computed Tomography
CV	Coefficient of Variation
D	Diffusivity of Test Gas
DL _{CO}	Diffusing Capacity of the Lung for Carbon Monoxide
ERS	European Respiratory Society
ERV	Expiratory Reserve Volume
FD	Fourier Decomposition
FeNO	Fraction of Exhaled Nitric Oxide
FEV ₁	Forced Expiratory Volume in One Second
FOV	Field of View
FRC	Functional Residual Capacity
FVC	Forced Vital Capacity
GAN	Generative Adversarial Networks
GLCM	Gray-level Co-occurrence Matrix
GOLD	Global Initiative for Chronic Obstructive Lung Disease
HU	Hounsfield Unit
IBSI	Image Biomarker Standardization Initiative
IC	Inspiratory Capacity
IRV	Inspiratory Reserve Volume
LA	Lumen Area
MCID	Minimal Clinically Important Difference
MRI	Magnetic Resonance Imaging
ΔP	Partial Pressure Difference
PET	Positron Emission Tomography
PRM	Parametric Response Map
RA ₉₅₀	Relative Area of the Lung <-950 HU
RA ₈₅₆	Relative Area of the Lung <-856 HU
RBC	Red Blood Cell
RLM	Run Length Matrix
ROI	Region of Interest

RV	Residual Volume
SGRQ	St. George's Respiratory Questionnaire
SPECT	Single Photon Emission Computed Tomography
T ₁	Longitudinal Magnetization Relaxation Time
T ₂	Transverse Magnetization Relaxation Time
T	Tissue Barrier Thickness
TAC	Total Airway Count
TBV	Total Blood Volume
TE	Echo Time
TLC	Total Lung Capacity
TR	Repetition Time
TV	Tidal Volume
UTE	Ultra-short Echo Time
VC	Vital Capacity
VDP	Ventilation Defect Percent
VDV	Ventilation Defect Volume
VV	Ventilated Volume
WA%	Wall Area Percent
WHO	World Health Organization
WT	Wall thickness
ZTE	Zero-Echo Time

CHAPTER 1

1 INTRODUCTION

*Chronic obstructive pulmonary disease (COPD) is characterized by non-reversible airflow limitation resulting from airway obstruction and/or parenchymal destruction, which causes the lung to be heterogeneously ventilated. In this thesis, machine-learning and texture analysis tools are applied to hyperpolarized gas magnetic resonance imaging (MRI) to study the ventilation heterogeneity and patchiness, and to thoracic computed tomography (CT) imaging to study the parenchyma and structural changes within the lung. Parts of this chapter were adapted from a published review article in **Appendix A – Quantification of Pulmonary Functional MRI: State-of-the-Art and Emerging Image Processing Methods and Measurements** (Sharma et al. 2022). The extracted texture measurements were investigated and used to predict clinically-relevant outcomes in COPD.*

1.1 Motivation and Rationale

Chronic obstructive pulmonary disease (COPD) is one of the most common pulmonary diseases, which affects hundreds of millions of lives worldwide and accounts for millions of deaths every year. Furthermore, the statistics presented by the World Health Organization (WHO) indicate that COPD is the third leading cause of death globally, as shown in **Figure 1-1**. COPD is also the leading cause of death among all other chronic respiratory diseases and caused over 3.2 million deaths in 2019 alone.^{1,2} Tobacco smoking accounts for over 70% of COPD cases in high-income countries, and about 40% in low and middle-income, where household air pollution is a major risk factor.¹

Global causes of death

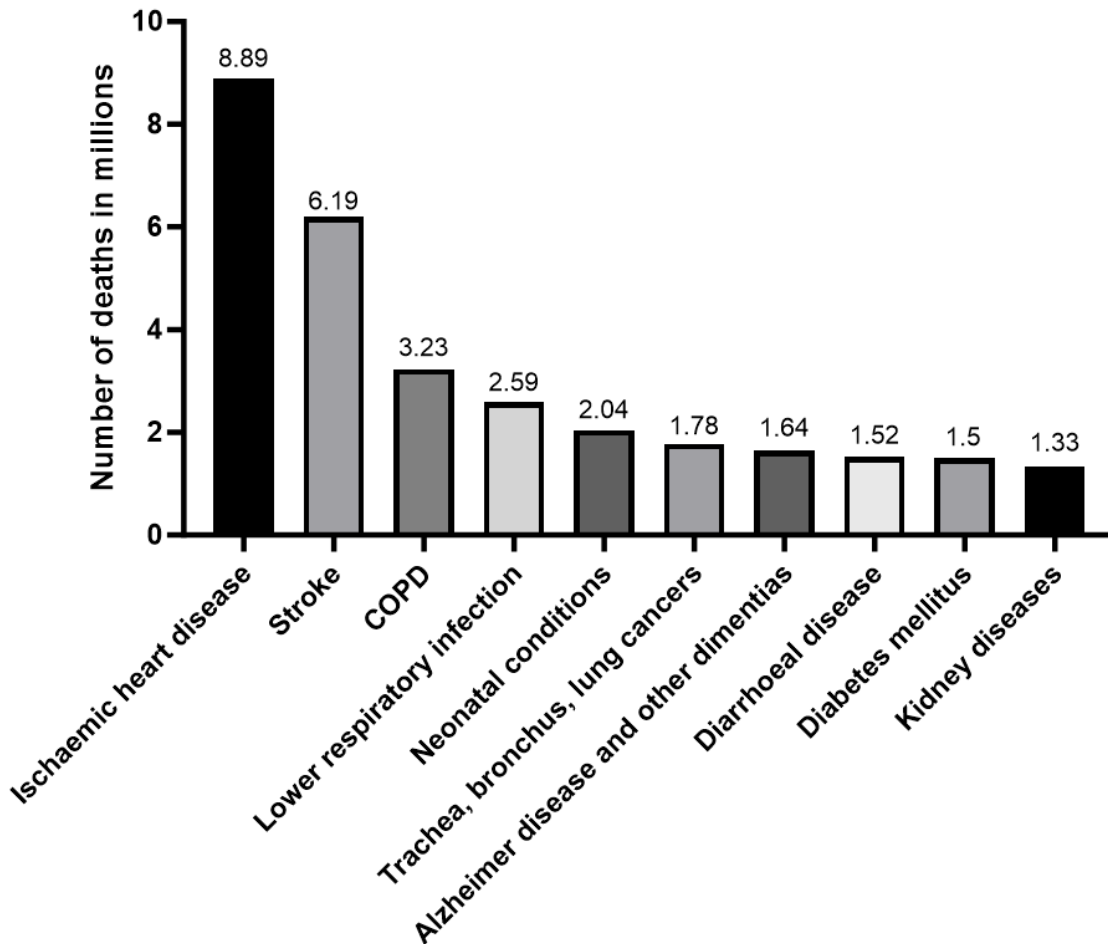


Figure 1-1. Leading causes of death worldwide in 2019

Statista² and World Health Organization¹ statistics on the leading causes of death worldwide in 2019 (in millions).

In Canada, COPD caused 4.4% of all deaths in 2011.³ Among those aged 35 to 79 years, only about 3% of individuals reported a COPD diagnosis by a health care professional in 2013, while 11% of Canadians in this age range had a measured airflow obstruction consistent with COPD.⁴ Furthermore, of the 11% with measured airflow obstruction, 90% reported not being diagnosed by a health care professional previously. This disparity between reported and measured COPD highlights the underdiagnosis of COPD in Canada. In 2006, the Canadian Institute for Health Information determined that COPD accounted for the highest rate of hospital admissions among

other major chronic illnesses.⁵ There was also an increase in hospitalization rates due to COPD from 83 per 100,000 Canadians from 2006 to 2010 to 86 per 100,000 Canadians in the period from 2011 to 2015.⁶ These rates also include repeat hospitalizations, where COPD has much higher rate of readmissions among other chronic diseases especially due to exacerbations, as summarized in **Figure 1-2**. These hospitalizations impose a significant economic burden on the healthcare system in Canada, where, on average, the hospital stay is about \$10,000 for a COPD patient, and the total cost is approximately \$1.5 billion per year.^{7,8}

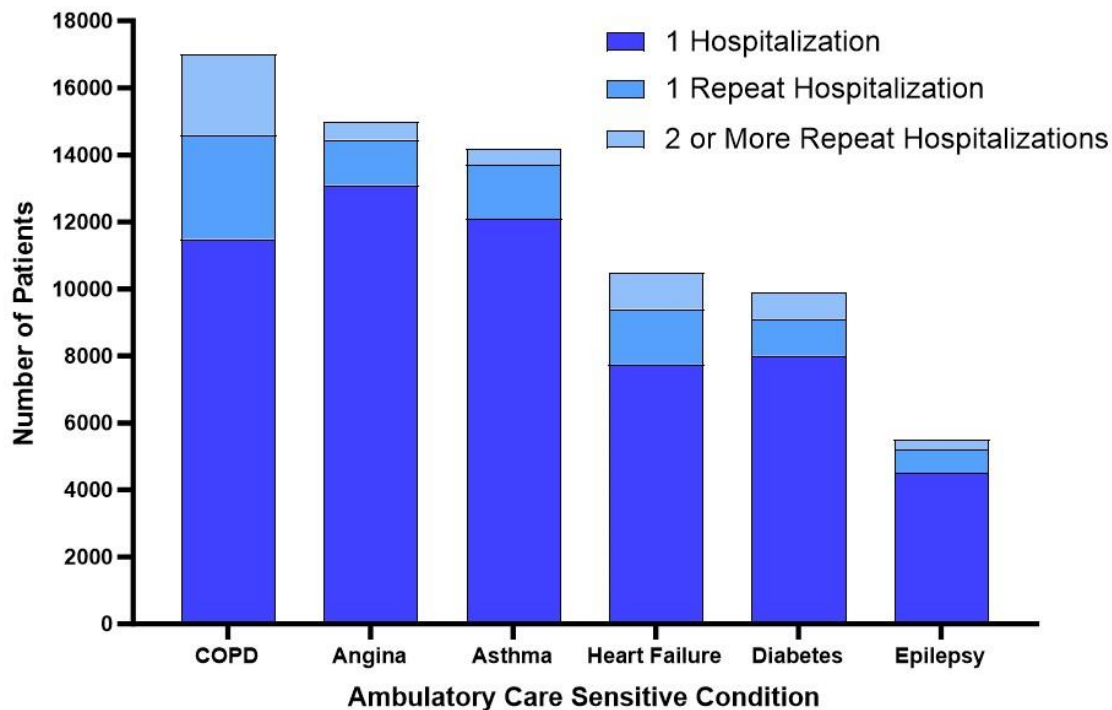


Figure 1-2. Hospitalizations by chronic illness condition at first admission in Canada

The graph shows number of patients by condition with single, one repeat, and two or more repeat hospitalizations. Adapted from Canadian Institute of Health Information publication entitled Health Indicators 2008.⁵

These alarming COPD statistics and the overwhelming economic and health care burden indicates that a clinical gap still remains in the treatment and management of patients. COPD is an umbrella term encompassing progressive lung disorders that are characterized by irreversible airflow

limitation and difficulty in breathing.⁹ The disease process includes remodelling of the small airway compartment and emphysematous destruction of the lung parenchyma,¹⁰ or combination of both.¹¹ The ‘gold-standard’ measurements used to diagnose, stage, and determine treatment effect in COPD are the lung volumes derived from pulmonary function tests measured at the mouth. Airflow obstruction is primarily measured using forced expiratory volume in one second (FEV₁), which represents the maximum amount of air forcefully exhaled within a single second. Recently, symptom severity and exacerbation risk have been considered for COPD management since individuals with the earliest symptoms of COPD often ignore them, making COPD a ‘silent killer’ disease.^{12,13} Although these measurements are straightforward, inexpensive and easy to obtain, they cannot directly provide any regional information about the small airway compartment that is believed to drive COPD pathogenesis.¹³⁻¹⁵ This is one of the major limitations of such clinical measurements of lung function that has motivated the development of pulmonary magnetic resonance imaging (MRI) and computed tomography (CT) imaging approaches to generate regional measurements of pulmonary structure and function for a better understanding of the underlying disease pathophysiology.

Although COPD is diagnosed and staged using pulmonary function testing,¹⁶ CT provides a way to quantify abnormal changes in lung parenchyma that overlap with COPD severity.¹⁷ Furthermore, changes visible on CT predate those detected with spirometry and pathological studies demonstrate that up to one-third of the lung tissue may be destroyed by emphysema before spirometry becomes abnormal.¹⁸ CT is used as the cornerstone modality in the evaluation of emphysema. CT measurements of emphysema have been shown to correlate with histologic findings,¹⁹ are associated with symptoms among smokers and the general population,²⁰ and used to independently predict mortality in subjects with and without COPD.²¹ However, radiologist-

based and the established quantitative CT measurements are limited by the associated time requirements, training, reproducibility, and are often categorical in nature, not capturing the full spectrum of the signal and spatial information available on CT. Emergent imaging methods based on pulmonary hyperpolarized gas MRI have also been developed to visualize and quantify the ventilation within the lungs. Ventilation defects can be quantified as ventilation defect percent (VDP),²² which has been shown to predict future COPD exacerbations,²³ longitudinal changes in quality-of-life and exercise capacity.²⁴ Importantly, MRI measurements are sensitive to COPD disease-related changes in patients in whom CT and pulmonary function test results have not changed.^{25,26} However, VDP is also a categorical measurement and does not provide any information regarding ventilation ‘quality’ (i.e., heterogeneity or size and arrangement of defects within the lung).

CT and MR images can also undergo computerized extraction of quantitative ‘radiomic’ features, which machine-learning systems use to learn how to differentiate and/or predict clinically-relevant outcomes in COPD patients. Texture analysis provides a way to quantify patterns within an image, which may be related to various determinants of the underlying pathophysiology. Image texture analysis provides the advantage of rapidly generating automated quantitative measures, which are continuous and simultaneously capture the signal intensities, as well as their spatial arrangement within the image at voxel level. The utility of this approach in pulmonary imaging has been demonstrated in the detection and classification of tumours,²⁷⁻³¹ and recently in COPD, has been shown to be associated with lung function and disease severity,³² predictive of COPD exacerbations,³³ and provides complementary information to quantitative CT measurements.^{34,35} However, despite the plentiful studies that have demonstrated the conclusive opportunities for clinically-relevant imaging biomarkers, the translation of such pulmonary CT and MR imaging

approaches into the clinical setting has been extremely limited. This is driven by the fact that very few analytic tools exist capable of generating validated imaging features that capture the underlying structural complexity of the lung and the relationships between these complex structures. Therefore, there is an urgent need to develop sensitive CT and MRI measurements that can inform on early-stage COPD pathophysiology and the pulmonary structural and functional changes occurring in the lungs of patients.

In this chapter, the relevant background knowledge for this thesis is provided in order to motivate the original research presented in **Chapters 2 to 4**. First, an overview of the structure and function of the lung organ will be presented (**1.2**), followed by the underlying pathophysiology of COPD (**1.3**). The established clinical tools and measurements for the management of COPD (**1.4**), followed by a summary of the currently available imaging approaches and measurements developed to provide a better understating of lung diseases (**1.5**), are provided. Texture analysis of medical images as well as the recent developments and applications in pulmonary imaging will be introduced next (**1.6**). Finally, I will introduce and summarize the hypothesis and objectives of this thesis (**1.7**).

1.2 Structure and Function of the Lung

The lung is an essential organ in the sustainment of human life, where the complex structure-function relationships allow for an efficient transfer of oxygen into the bloodstream. The airways, parenchyma, and vasculature compose the structural base that works cohesively to provide optimal functioning of gas exchange within the lung and bloodstream. The automatic and rhythmic act of breathing is driven by networks of neurons in the hindbrain (pons and medulla) that together direct the thoracic and abdominal muscles to actively produce pressure gradients that help move ambient air into and out of the lungs. As depicted in **Figure 1-3**, this activity drives the exchange of oxygen

from outside the body with carbon dioxide waste produced inside the body at the alveolar-capillary membrane (~0.2-0.5 μm thickness).³⁶ The lungs are also necessarily elastic, allowing for the respiratory system to undergo complex biomechanical changes that enable breathing and highly efficient gas exchange.

In a healthy human adult, the end of the bronchioles in the lung is where gas exchange occurs and it involves approximately 300-500 million alveoli, which are themselves wrapped in approximately 500-1000 pulmonary capillaries per alveolus.^{37,38} In humans, the heart and lung systems work together at two different frequencies (~1 Hz for heart and 0.25 Hz for lungs) to move approximately 6L of blood and 6L of air through the body every minute.

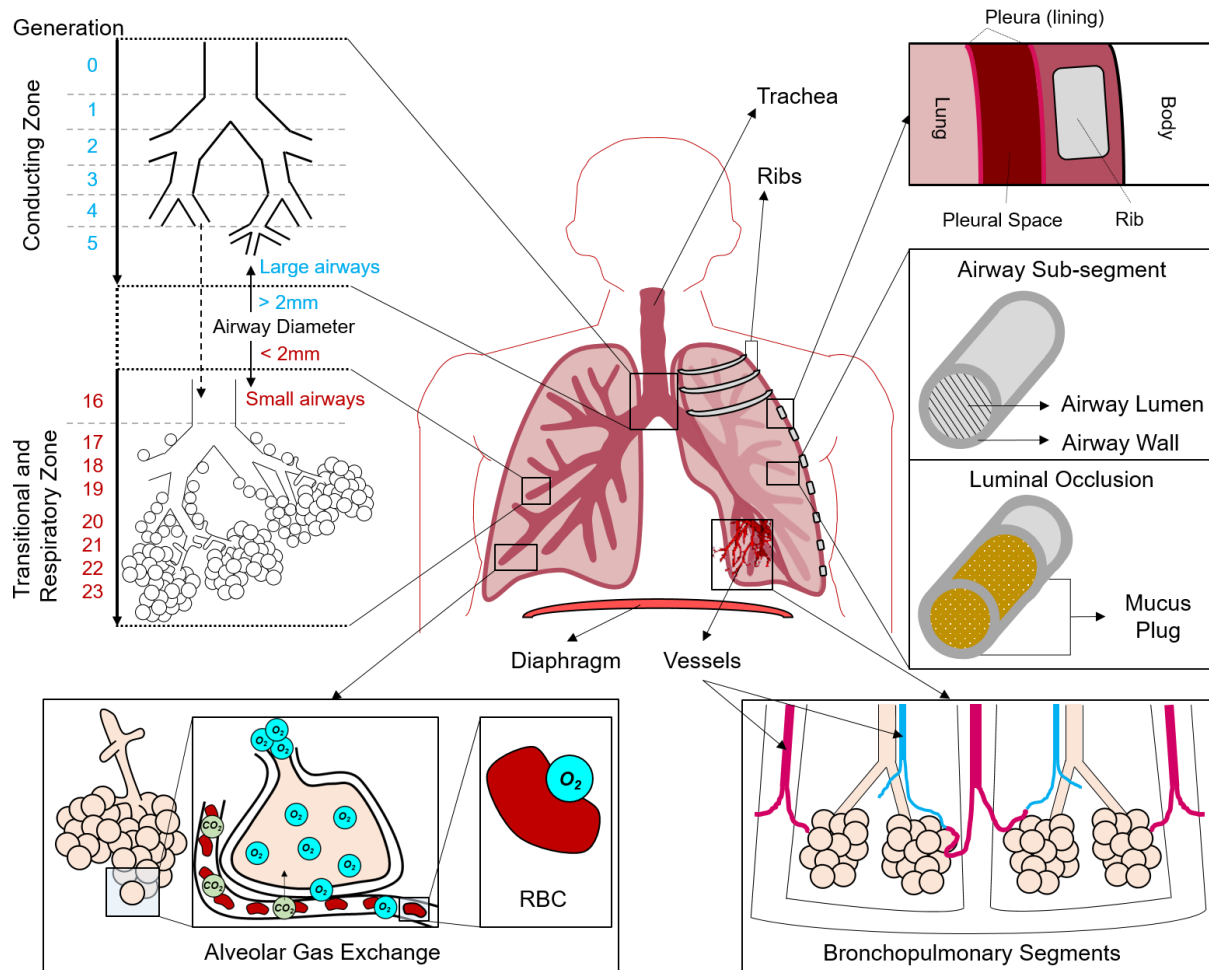


Figure 1-3. Structural and functional lung components

Respiratory system structure showing the airway tree generations that provide passage for air to travel from the nose through the large and small airways to the alveoli. Subsegmental airways branch from larger airway segments and are composed of the airway wall and lumen, which may be occluded with a mucus plug. Bronchopulmonary segments are richly supplied with red blood cells by the segmental bronchi and its vessels to participate in pulmonary gas exchange and perfusion. Oxygen travels through the airways into the alveoli, where gas exchange occurs, and carbon dioxide is removed from the body. Reproduced from Sharma *et al.* 2022.³⁹

1.2.1 Airways

As shown in **Figure 1-3** in the top left panels, air is transported through bulk flow and then diffuses through the airway tree through as many as 23 branch-point generations. Bronchi decrease in diameter, but increase dramatically in number, as the asymmetrical branching of the airway tree continues. The first 16 generations of the airway tree is referred to as the conducting zone, which

contains no alveoli and thus does not participate in the gas exchange with the pulmonary capillary red blood cells (RBC). Since the mixed venous blood does not come in contact with air, the conducting airways therefore constitute the anatomic dead space, which is approximately 150mL in a healthy individual.⁴⁰ Overall, the total length of the airways running through the lungs is approximately 2400 kilometers.⁴¹

In contrast, alveoli start to populate the terminal airways from the 17th through 19th airway generations in the so-called respiratory bronchioles, which constitute the transitional zone. The air now moves through the branches via diffusion and not bulk flow. These alveolar ducts are followed by the airway sacs, which are the last airway structures that have the alveoli budding off or enveloping to maximize the surface area available for gas exchange. Therefore, once air arrives at the 20th to 23rd airway generations, the terminal airways are completely populated with alveoli that are available for gas exchange.⁴²

1.2.2 Alveoli

The alveolus is the fundamental unit of the lung and the site where gas exchange occurs, as shown in **Figure 1-3**. The lungs contain approximately 300-500 million alveoli, with a combined surface area of about 130m² to facilitate gas exchange.⁴³ Alveoli contain two types of cells to maximize diffusion (Type I and Type II cells). Type I cells (pneumocytes) are thin, flat cells that form the majority of the alveolar surface area and allow for gas exchange to occur. The alveoli are also lined by a thin fluid film called surfactant. The type II cells are cuboidal-shaped cells interspersed among the Type I cells and can produce surfactant. Additionally, type II cells can serve as progenitor cells, capable of proliferating and differentiating into Type I cells. The surfactant is composed of phospholipids and proteins and reduces surface tension to prevent collapse of the alveolus.⁴⁴ The

walls of the alveolar sacs are often called the alveolar septa (or barrier or membrane). The alveoli are covered in a thin mesh of capillaries, where one layer of cells from the alveolar epithelium and another from the capillary endothelium, separate the alveolar cavity from the blood stream.⁴⁵

1.2.3 Ventilation and Perfusion

To move air into or out of the alveoli, a pressure difference between the atmosphere and the alveoli must be established first. During inspiration, the contraction of the diaphragm causes it to descend and contractions of the intercostal muscles causes the ribs to rise, which increases the thoracic cavity volume and decreases the alveolar pressure. In contrast, during expiration the respiratory muscles passively relax and alveolar pressure increases. Approximately 500 mL of air is taken into the lungs during normal breathing, but 150 mL of this resides in the conducting zone and does not participate in gas exchange (anatomic dead space). Total ventilation is the total volume of air that leaves the lung per minute, which is known to be about 7.5L/min for an individual with an average breathing rate (~15 breaths/min).^{46,47} Adjusting for dead space, the volume of air that participates in gas exchange is about 5.25L/min, which is referred to as alveolar ventilation.⁴⁶

As shown in the right panels of **Figure 1-3**, the pulmonary vascular tree runs parallel to the airways, and many of the structural properties that affect flow are common to both tree structures. Similar to airways, the muscular arteries consist of a smooth muscle layer that can contract and relax in order to regulate blood pressure within the pulmonary circuit. The bronchopulmonary segments and capillary network are richly supplied with blood containing red blood cells, each packed with hemoglobin tetramers. Gas exchange occurs at the alveolar-capillary tissue membrane, which itself is one cell thick (~0.2-0.5 μm),³⁶ where oxygen binds to the hemoglobin. This diffusion is governed by Fick's law, where the rate of gas transfer through a surface is

proportional to the area of the surface, the partial pressure difference of the gas across the surface, and inversely proportional to the thickness.⁴⁸ Reaction of O₂ with hemoglobin is fast, but because of the little time available in the capillary, the rate of reaction may become a limiting factor and depends on the resistances offered by the blood-gas membrane and that attributable to the time taken for O₂ to react with hemoglobin.

1.3 Pathophysiology of Chronic Obstructive Pulmonary Disease

Any abnormality or dysfunction in the components discussed above can lead to lung disease by preventing the optimal delivery of oxygen to the bloodstream. The persistent airflow limitation that characterizes COPD is caused by a combination of parenchymal destruction (emphysema) and airways disease (chronic bronchitis and/or small airways disease),⁴⁹ as shown in **Figure 1-4**. COPD is a result of exposure to exogenous irritants such as cigarette smoke, environmental factors and pollution, occupational irritants, or genetic conditions such as alpha-1 antitrypsin deficiency, and is progressive over time.⁴⁹

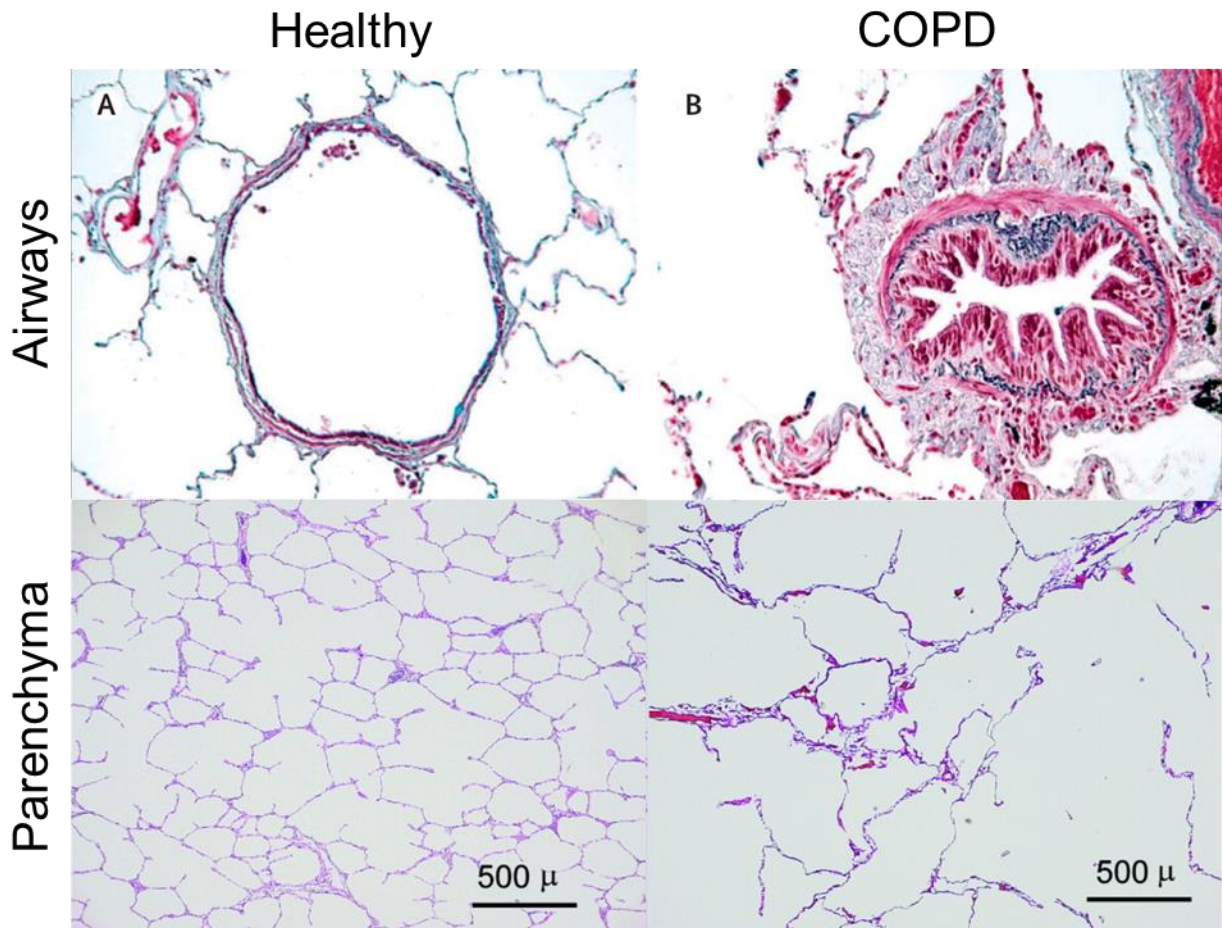


Figure 1-4. Airways and parenchyma histology for Healthy vs COPD patient

Top panels depict small airway in healthy and COPD participants, adapted from Hogg 2004.¹⁰ Bottom panels depict healthy and emphysematous destruction of parenchyma, adapted from Woods *et al.* 2006.⁵⁰

1.3.1 Airflow Obstruction and Small Airways Disease

At the pathological level, exposure to smoke leads to infiltration of the mucosa, submucosa, and glandular tissue by inflammatory cells. As a result, increased mucus content and disturbed tissue repair with wall thickening in the small conducting airways are hallmark features of COPD. In COPD, chronic bronchitis is defined as a productive cough lasting more than 3-months and occurring within a span of 2-years. It is thought to be caused by overproduction and hypersecretion of mucus by goblet cells and there is a strong causal association with smoking. There is excessive production of mucus in the large airways, specifically the epithelium of the central airways and

extending to the mucous gland ducts.⁵¹ Excess mucous can cause airway obstruction, cough, and can prevent regions of the lung to be ventilated, causing reduced lung function.⁵² The small airways (<2mm in diameter) contain the bronchioles, as shown in **Figure 1-3**, which are the major site of airflow obstruction in COPD.⁵³ However, small airway disease may go unnoticed at first and accumulate due to their large number and cross-sectional area, which consequently contributes very little to the overall measured airflow resistance.⁵⁴

1.3.2 Emphysema

Emphysema is characterized by the destruction of parenchymal tissue and irreversible enlargement of airspaces, which leads to loss of alveolar walls, reduced number of small airways, and reduced surface area for gas exchange.⁵⁵ This destruction of alveolar walls causes a loss of elastic recoil of the lungs. As shown in **Figure 1-5**, there are three main types of emphysema: centrilobular, panlobular, and paraseptal. Centrilobular emphysema begins in the respiratory bronchioles and mainly spreads in the upper regions of the lungs, since the upper lobes of the lungs receive a greater proportion of the inspired air. This is the most common type of emphysema and is usually linked to cigarette smoking. It can be recognized on CT by the presence of round lucencies of varying size, sometimes associated with a visible central artery.⁵⁶ Importantly, progression of emphysema on quantitative CT scan imaging is greater in those with higher degrees of centrilobular emphysema at baseline.⁵⁷ Panlobular emphysema, unlike centrilobular, involves the entire pulmonary lobule and ‘Pan’ means ‘all’ or ‘entire’. It commonly resides in the lower half of the lungs and destroys the tissue of the air sacs, causing a uniform enlargement of air spaces. This is because the lower lobes receive a greater blood flow and are therefore more exposed to circulating irritants, which contribute to the development of emphysema. It is mainly associated with homozygous alpha-1 antitrypsin deficiency, a genetic mutation that results in the development of

emphysema in patients irrespective of smoking history.⁵⁸ Paraseptal emphysema tends to localize around the septa or pleura and comprises of focal lucencies that can be relatively large. It is characterized by cyst-like lucencies along the pleural margin, usually within the upper lobes. It is often associated with inflammatory processes, such as prior lung infections, smoking, pneumothorax and fibrosis. Bullae (an air-filled space of > 1 cm in diameter within the lung because of emphysematous destruction) are most common with paraseptal emphysema.⁵⁶

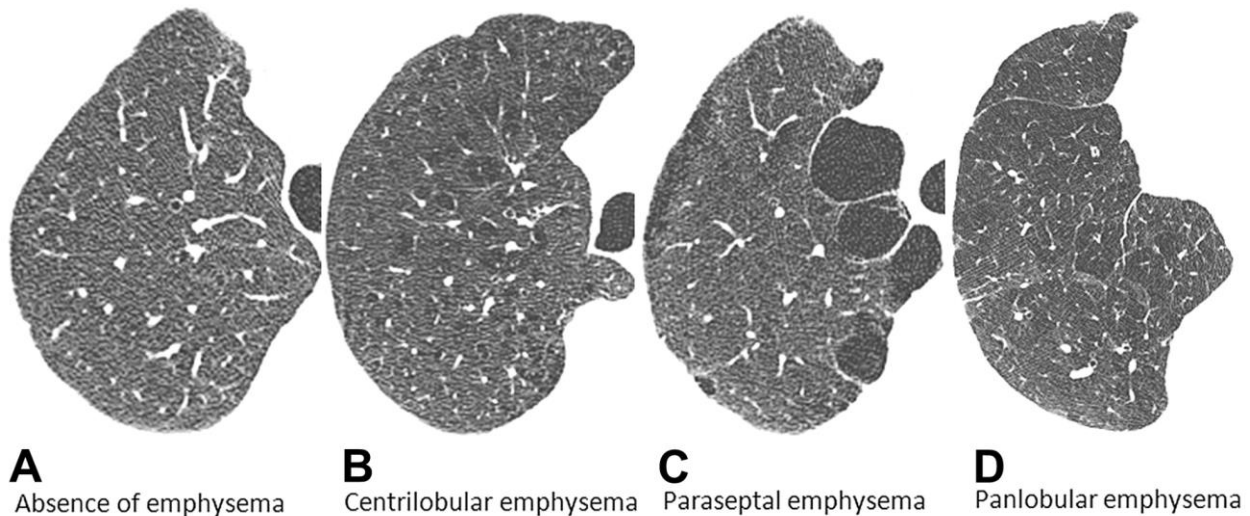


Figure 1-5. Axial CT images for absence of emphysema and different emphysema subtypes
 A) Absence of emphysema; B) Centrilobular emphysema; C) Paraseptal emphysema; D) Panlobular emphysema. Adapted from Smith *et al.* 2014.⁵⁹

1.3.3 Pulmonary Vascular Changes

In the later stages of COPD, cardiovascular function may be impaired and the gas exchange becomes less efficient.⁶⁰⁻⁶³ Thus, pulmonary hypertension is an important comorbidity of COPD as it is linked to worse mortality and morbidity and typically develops late in COPD. In response to low blood oxygen, the intrapulmonary arteries constrict to optimize ventilation and perfusion efficiency (hypoxic pulmonary vasoconstriction).⁶⁴ There is an inner wall thickening of the arteries adjacent to the bronchioles due to smooth muscle proliferation and deposition of elastin and collagen. These arteries are unable to dilate fully in response to exercise, acetylcholine, or

increases in airflow.⁶⁵ Increases in pulmonary arterial pressure become pathological in instances of chronic hypoxic vasoconstriction. Oxygen therapy is used in the treatment of COPD to overcome this chronic hypoxemia and assist in decreasing pulmonary arterial pressure. pulmonary arterial pressure.^{66,67} Recent studies in COPD showed that vascular remodelling results in a loss of small vessels and decreased vessel density, which was validated by histology.⁶⁸ This vascular remodeling has been shown to be a direct result of exposure to cigarette smoke.^{69,70}

1.4 Clinical Measures of Global Lung Function

Clinicians primarily rely on pulmonary function tests to diagnose and monitor COPD. Pulmonary function tests include spirometry, plethysmography, and the diffusing capacity of the lung for carbon monoxide (DL_{CO}). These tests are measured at the mouth and rely on simple breathing maneuvers in order to assess flow rates, calculate lung volumes, and evaluate gas exchange efficiency, providing information about lung function. The measured values are typically expressed as a percent of the predicted value, which compare values to an average for a person of the same ethnicity, sex, height, weight and age.⁷¹ Quality-of-life questionnaires and exercise capacity tests can also be useful in measuring the impact of obstructive lung disease on patients.

1.4.1 Spirometry

Spirometry is the simplest and most widely used of the currently available breathing tests.^{72,73} Spirometry can be performed using a handheld device, where the patient is asked to breathe normally through the device, making a tight seal around the mouthpiece. After taking a couple of tidal breaths, the patient takes a deep inspiration up to total lung capacity (TLC) and then forcefully exhales by blasting the air out until no more can be expelled. A sample lung volume-time curve from a spirometer is shown in **Figure 1-6**. The volume of air the patient can expel from TLC in 1

second is known as the FEV₁ measurement, and the volume expelled from TLC to full exhalation is known as the forced vital capacity (FVC).

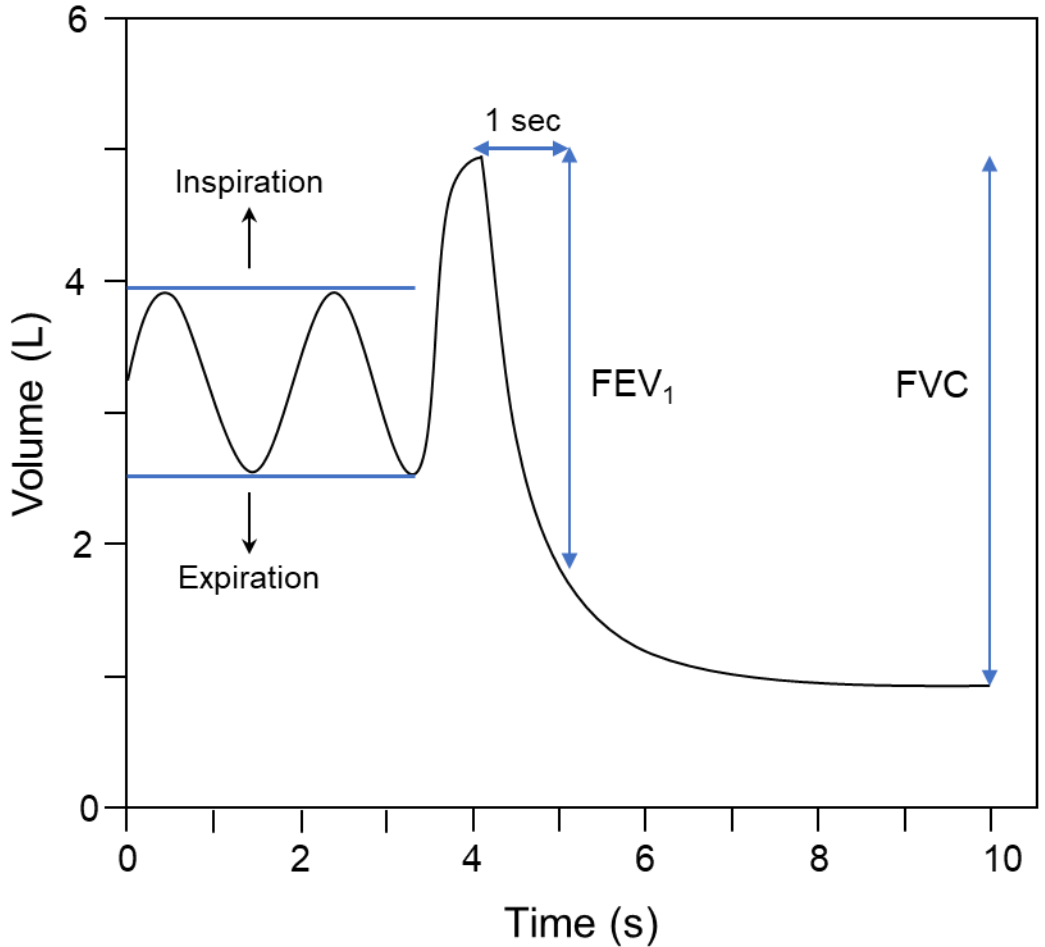


Figure 1-6. Pulmonary function test using spirometry

Volume-time curve measured via a spirometer to determine the forced expiratory volume in one second (FEV₁) and the forced vital capacity (FVC) volumes.

The normal ranges for FEV₁ and FVC is $>80\%$ _{predicted}, for a healthy adult with a TLC of about 6 Litres. The clinical diagnosis of COPD is based on these two lung volume measurements of FEV₁ and FVC obtained via spirometry, as shown in **Table 1-1**. A post-bronchodilator ratio of FEV₁ to FVC of less than 70 percent is the diagnostic cut-off for COPD according to the Global Initiative for Chronic Lung Disease (GOLD) criteria.^{74,75} COPD severity can then be graded based on four

FEV₁ thresholds, where a lower percent of predicted value is indicative of increased airflow obstruction and disease severity.

Table 1-1. COPD severity stages based on GOLD criteria

FEV ₁ /FVC < 0.70:		
GOLD I	Mild	FEV ₁ % _{pred} ≥ 80%
GOLD II	Moderate	50% ≤ FEV ₁ % _{pred} < 80%
GOLD III	Severe	30% ≤ FEV ₁ % _{pred} < 50%
GOLD IV	Very Severe	FEV ₁ % _{pred} < 30%

Adapted from GOLD Global Strategy for the Diagnosis, Management, and Prevention of Chronic Obstructive Pulmonary Disease 2020 report.⁷⁶

1.4.2 Plethysmography

Plethysmography can be used to measure additional lung volumes and it operates based on the principles from Boyle's Law.⁷⁷ The lung volume measurements are performed in a body plethysmograph, which is a controlled and sealed chamber. The patient sits upright inside the sealed chamber and performs a set of breathing maneuvers, including tidal breathing, full inspiration, and full expiration. A sample volume-time curve, including lung volumes and capacities, is displayed in **Figure 1-7**. The primary volume measured is the functional residual capacity (FRC), from which the TLC and residual volume (RV) can be quantified.⁷⁸ FRC is the amount of air remaining in the lungs at the end of a normal expiration, RV is the volume of air remaining in the lungs after a maximal expiration, while TLC represents the maximum volume of air contained in the lungs at the end of a maximal inspiration. Inspiratory capacity (IC) is the sum of tidal volume and inspiratory reserve volume, representing the amount of air a person can breathe in after a normal breath. Tidal volume (VT) represents the amount of air moved in and out of the lungs with each breath during regular, non-forced breathing. Vital capacity (VC) is the maximum amount of air a person can expel from the lungs after a maximum inhalation. It represents the sum of TV, inspiratory reserve volume, and expiratory reserve volume.

In the context of COPD, the RV and FRC are often increased due to gas trapping from the collapse of airways and/or loss of elastic recoil. The IC and VT may be decreased, especially during exacerbations or advanced stages of COPD. The reduction in VC is a result of factors such as airway obstruction, loss of lung elasticity and increased airway resistance. These alterations in lung volumes contribute to the characteristic symptoms of COPD, including shortness of breath, difficulty breathing, and reduced exercise tolerance. The hyperinflation is measured as an increase in RV as well as a decrease in VC, therefore monitoring lung volumes such as VC, is essential in the management of COPD.

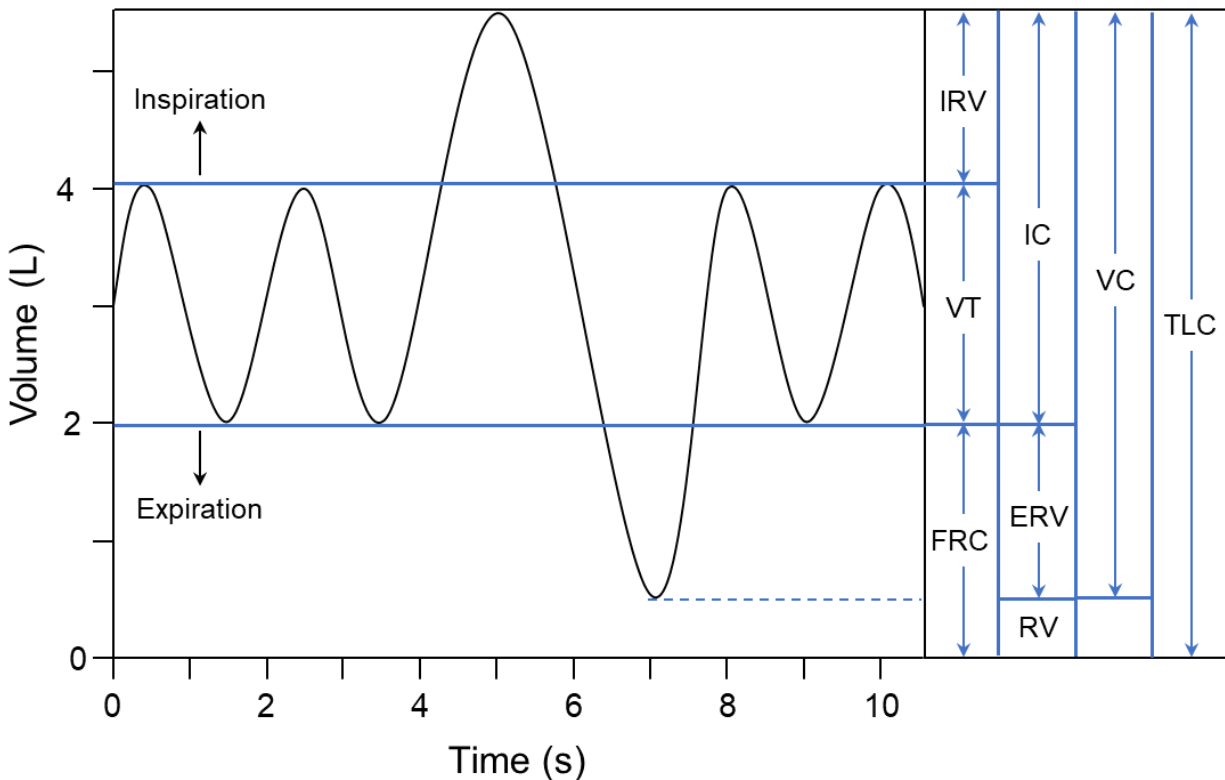


Figure 1-7. Pulmonary function test using plethysmography

Volume-time curve measured via the plethysmograph and used to determine airflows at the mouth, lung volumes and capacities.

1.4.3 Diffusing Capacity of the Lung

The DL_{CO} is an indirect measure of gas exchange efficiency across the alveolar-capillary barrier and can be used to probe alveolar tissue integrity in patients with emphysema. This test is performed in the plethysmograph chamber, where the patient is instructed to exhale to RV, then inhale a specific gas mixture to TLC, which contains room air, a tracer gas (neon or helium), and a small amount of carbon monoxide (typically 0.3% CO). Then for about 10 seconds the patient holds their breath, allowing for CO to diffuse into the bloodstream, and then exhales. The exhaled gas mixture is analyzed, accounting for anatomic dead space, and the difference in the concentration of CO between the inhaled and exhaled gas mixtures is used to calculate the diffusing capacity of the lung for carbon monoxide.⁷⁹ The uptake of CO is not only determined by the diffusion properties of the alveolar-capillary barrier, but also the volume of blood and the rate of combination of CO with blood.

Carbon monoxide is used for this test as it has about 200 times high affinity for hemoglobin than oxygen, and it follows the same pathway as that of oxygen to finally bind with hemoglobin. In summary, DL_{CO} measures the uptake of CO per unit time per mm of driving pressure of CO (cc of CO/sec/mm of Hg), according to Fick's law for gas diffusion.⁴⁸ Based on **Equation 1-1**,⁴⁸ the factors influencing the gas uptake are: surface area of the barrier (A), barrier thickness (T), diffusivity of the gas in the barrier (D), and partial pressure difference of the gas across the alveolar-capillary barrier (ΔP).

Equation 1-1. Fick's law equation.

$$V_g = \frac{D * A * \Delta P}{T}$$

In conjunction with spirometry, DL_{CO} can be indicated in the evaluation of parenchymal and non-parenchymal lung diseases. Preoperative risk and the severity of obstructive lung diseases and pulmonary vascular disease can be evaluated using DL_{CO}.⁸⁰ In terms of severity and classification, a normal DL_{CO} is considered to be >75% of the predicted value (about 25 ml/min/mmHg) and up to 140%_{pred}.⁸¹ Studies indicate that asymptomatic ex-smokers with abnormal DL_{CO} are at a significantly increased risk of developing COPD within just four years.⁸² Furthermore, DL_{CO} strongly predicted all-cause mortality in COPD, independent of BODE index and CT measurements.⁸³ Nevertheless, it is important to acknowledge that such pulmonary function test measurements require significant cooperation from patients, which may pose challenges, particularly for children and patients with severe lung disease. Additionally, they lack reproducibility and only provide global rather than regional measurements of pulmonary complications, which are believed to be notably heterogeneous.^{84,85} Despite these limitations, pulmonary function tests are routinely performed in clinical settings and continue to serve as the primary method for clinical lung disease management largely due to the low cost, wide availability, and relative ease of use.

1.4.4 Six Minute Walk Test

The six-minute walk test is an exercise test that measures the distance a person can walk, self-paced based on their comfort and ability, on a flat surface in six minutes. In individuals with respiratory disease, this test is thought to reflect their functional exercise level for daily physical activities. Unlike pulmonary function testing, there is a strong correlation between six-minute walk distance (6MWD) and clinical outcomes in COPD,⁸⁶ it is recognized as a strong predictor of mortality,⁸⁷⁻⁸⁹ and it is believed that 6MWD captures both the pulmonary and extra-pulmonary manifestations of the disease.⁸⁷ Studies observing changes in 6MWD over a 2-year period found

improved survival per 100-meter increment increases in 6MWD,^{90,91} and they reported that the rate of decline in 6MWD between survivors and non-survivors was significantly different; however, they did not detect a parallel change in FEV₁ measurement.⁹¹

1.4.5 St. George's Respiratory Questionnaire

The St. George's Respiratory Questionnaire (SGRQ) is a questionnaire that consists of three component scores: the symptom frequency and severity records, activities that cause or are limited by breathlessness, and impact components like social functioning and psychological disturbances. The total score is also calculated out of 100, where a higher score indicates worse health. The SGRQ score is standardized,^{92,93} and captures information that typical physiologic or radiologic measures do not, partly due to its comprehensiveness and focus on the impact of illness and treatment. In COPD, SGRQ score at baseline is a significant predictor of exacerbations, hospital admissions, and death.⁹⁴

1.4.6 Lung Function Decline

1.4.6.1 Normal Lung Aging

As we age, the physiological changes occurring in the lung result in changes of clinical measurements of lung function such as airflow, gas exchange, lung volumes, and capacities. The reduction in lung elasticity observed with aging is believed to stem from alterations in the lung connective tissue.⁹⁵ Likewise, the decrease in chest wall compliance is attributed to structural modifications occurring within the rib cage, which results in stiffening of the chest.⁹⁶ In addition, respiratory muscle strength is known to decline with age, which is also related to a decrease in muscle mass and number of muscle fibers.⁹⁷⁻⁹⁹

Structural changes that occur within the lung parenchyma during aging are also known as ‘senile emphysema’. It is associated with risk factors such as cigarette smoking, air pollution, and genetic predisposition and the pathogenesis involves chronic inflammation, oxidative stress, and imbalance in proteolytic enzyme activity, leading to tissue destruction. While senile emphysema primarily affects older individuals, it can also occur in younger individuals with significant exposure to risk factors such as smoking. Recent studies in healthy individuals over the age of 60 showed that there is a uniform increase in the size of airspaces within the lungs, which occurs without a loss of alveolar attachments or the presence of chronic inflammation.¹⁰⁰ Additionally, studies indicate that there is a thickening of alveolar walls and a decrease in the number of small airways located in the periphery of the lungs.¹⁰⁰ This may lead to a tendency for collapse of the small airways at high lung volumes.

Studies have shown that during normal lung aging, the RV increases with a constant TLC.^{101,102} This can be attributed to the decreased expiratory muscle strength and a tendency for the small airways to collapse, which is a consequence of the reduction in supporting tissues around the airways. There is also an increase in anatomic dead space with age due to the calcification of bronchial cartilage or cartilage in the walls of large airways.¹⁰³ Studies¹⁰⁴ on gas exchange efficiency have also demonstrated a decline in DL_{CO} with age, which is likely due to the reduction of alveolar surface area and a decline in pulmonary capillary blood volume.⁹⁶

1.4.6.2 COPD: Accelerated Lung Aging

The hallmark study by Fletcher and Peto in 1977¹⁰⁵ provided the foundation for our current understanding of lung function decline with aging. As shown in **Figure 1-8**, the study shows that FEV₁ measurement continuously declines with age, both in healthy individuals and those who

smoked regularly. In this study, FEV₁ was measured every 6 months for a period of 8 years in a cohort of 792 men, where FEV₁ was expressed as a percentage of the value calculated by backward extrapolation to the age of 25. Among many inferences, this study demonstrated the unavoidable progression of lung function decline once COPD is established, the possibility of reducing the decline in FEV₁ after smoking cessation, and that the rate of FEV₁ decline increased progressively with time.¹⁰⁵ The rate of decline in FEV₁ in healthy never smokers was 42 ± 6 mL/year, while this rate was accelerated in light smokers and heavy smokers to 47 ± 3 mL/year and 66 ± 4 mL/year, respectively.¹⁰⁵ These findings were also extended to include the evaluation of a female population, where studies have shown an FEV₁ decline of 22 mL/year in females who quit smoking at the beginning of the study, while those females who continued to smoke had an FEV₁ decline of 54 mL/year.¹⁰⁶ However, when it was expressed as a percentage of the predicted value, there were no significant differences in FEV₁ decline between males and females.¹⁰⁶

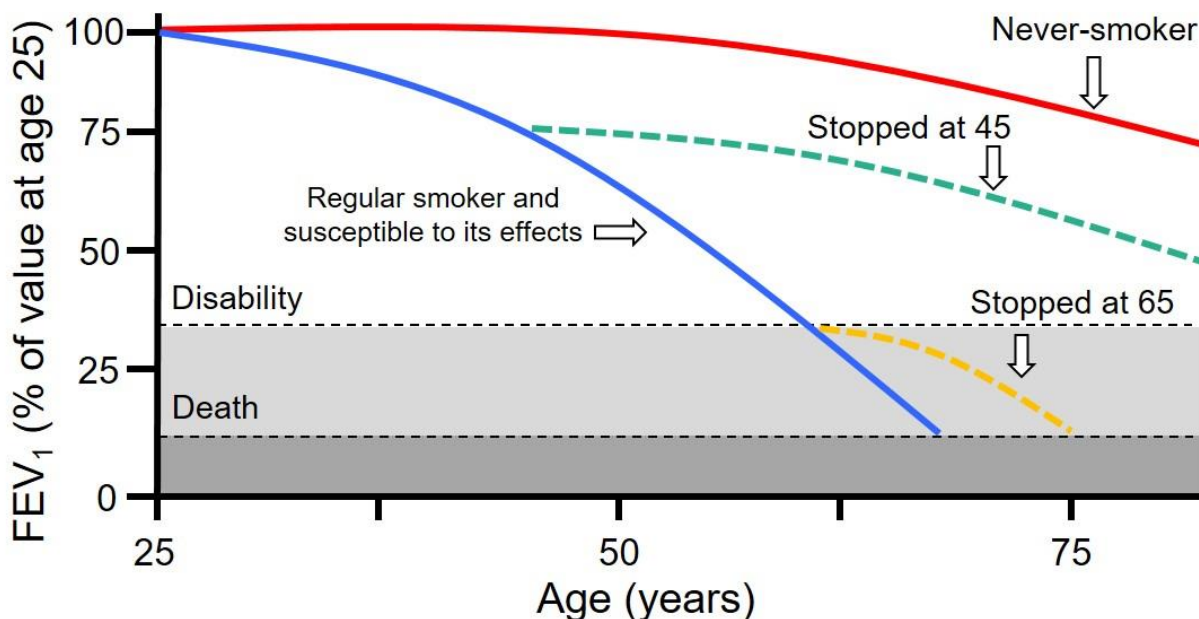


Figure 1-8. Lung Function Decline

In individuals who smoke regularly and are susceptible to its effects, smoking-related lung function decline (blue) has an accelerated trajectory towards disability, and ultimately death.

Smokers who quit at age 45, the decline is slowed and may return to a more normal trajectory (green). In smokers that quit after age 65, the decline can also be slowed (yellow) but to a lesser extent. Never-smoker lung function decline trajectory is shown in red. Adapted from Fletcher and Peto 1977.¹⁰⁵

According to the GOLD recommendations, a post-bronchodilator $FEV_1/FVC < 0.70$ confirms the presence of COPD, and the percent predicted of FEV_1 defines disease severity.^{74,107} The rationale for using the fixed threshold is its simplicity. However, there is an ongoing discussion about the fixed threshold value since it is being criticized for leading to misdiagnosis.¹⁰⁸ In middle-aged and elderly individuals, using the decades-old fixed ratio leads to over-diagnosis, and in younger individuals, it leads to under-diagnosis.¹⁰⁹ Other causes for misdiagnosis include: errors linked to primary care and spirometry tests, differential diagnoses, and patient-related factors such as ethnicity, obesity, consumption of drugs, absence of obvious symptoms, etc.¹¹⁰ More recent studies also confirm that misdiagnosis is common in primary care,^{111,112} with a lack of precision in COPD diagnosis leading to over-diagnosis rates ranging from 16% in Canada¹¹³ to 43% in the USA,¹¹⁴ and under-diagnosis rates ranging from 14-70% in Canada^{115,116} and 12-72% in USA.^{117,118} The significant underdiagnosis of COPD shown in these studies indicates that there is a much higher prevalence of the disease than previously thought and, thus, exposing a clinical gap where those not diagnosed are not being treated.

Although the reasons behind why certain smokers develop COPD while others do not remain uncertain, it is now recognized that the inflammatory response in COPD is amplified and it persists long after smoking cessation.¹⁰¹ Notably, the pathological processes affecting the airways and lung parenchyma can manifest in tandem or in isolation. While the pulmonary function tests described above are simple and cost-effective, they do not have the ability to provide highly sensitive, quantitative, or regional measurements of lung disease. In healthy individuals, the small airways

contribute only a minor portion of the total lung resistance. However, in COPD, the small airways are believed to be the primary site of disease onset,¹¹⁹ and therefore may not be detected by measuring lung volumes, exercise tolerances and health-related questionnaires.

1.5 Imaging Pulmonary Structure and Function

As previously discussed, the structure and function of the lungs are closely interconnected with each other. Unlike conventional clinical assessments, pulmonary imaging techniques offer an opportunity to measure regional abnormalities in the lung. Imaging modalities focusing on pulmonary anatomy present provide a unique opportunity to visualize and quantify the structural abnormalities that occur within the lung. These findings may play a crucial role in determining the functional abnormalities, which can be measured using functional imaging methods.

1.5.1 Planar Chest X-ray

Chest X-rays are among the most common methods used to evaluate lung abnormalities, particularly due to universal availability, rapid image acquisition at low cost, and low radiation dose. However, planar chest X-rays are limited to a two-dimensional projection of lung structure. Chest X-rays in posterior-anterior direction are performed in the upright position, where the patient places the hands on the back of the hips, and the scapulae are removed from the field of view by rolling elbows slightly forward. X-rays are absorbed to varying extents by different tissues, a phenomenon known as X-ray attenuation.¹²⁰ Highly attenuating tissues appear as bright areas, while low attenuating tissues appear darker on the X-ray images.

In COPD, hyperinflation can be detected in patients with moderate-to-severe emphysema that presents with a flattened diaphragm, elongated lung volumes, and a change in the cardiac silhouette.¹²¹ Limiting factors such as poor depth information and contrast have motivated the

development of X-ray CT imaging, which is a three-dimensional imaging method, discussed in the next section.

1.5.2 X-ray Computed Tomography

First introduced in the late 1970s, X-ray CT allows for visualization of the structure within the lung.¹²² Through continuous improvements with new generations, multi-detector technology allows imaging of the entire lung volume at a millimeter-scale and within a single breath-hold, with three-dimensional reconstruction capabilities. CT images are generated via an opposing X-ray source and detector array that rotate around the patient and acquire multi-angle X-ray projection images. Typical image reconstruction techniques include iterative reconstruction and filtered back projection, which generate three-dimensional image volumes.¹²³

The Hounsfield scale is based on the linear attenuation coefficients of X-rays, represented by μ , as they pass through tissues. The scale is determined using **Equation 1-2** and anchored by assigning water a value of 0 Hounsfield Units, while air is assigned a value of approximately -1000 Hounsfield Units.¹²⁴ Thoracic CT can be acquired at full inspiration, full expiration, and under breath-hold conditions, where a patient is instructed to inhale a pre-determined gas volume. CT can map the attenuation within the lung, where -1000 Hounsfield units (HU) indicate the presence of air, while HU density thresholds on inspiratory and expiratory CT may indicate regions of tissue destruction and gas trapping, respectively. Clinical chest CT protocols impart about 7-8 mSv of radiation dose,¹²⁵ while research protocols are low-dose and can achieve doses on the order of ~1mSv.¹²⁶⁻¹²⁸

Equation 1-2. Hounsfield Units (HU)

$$\text{Hounsfield Unit (HU)} = 1000 \times \left(\frac{\mu_{\text{tissue}} - \mu_{\text{water}}}{\mu_{\text{water}}} \right)$$

Anatomical measurements of the lung airways, blood vessels, and parenchyma may be generated using chest CT on a regional (apex, base, central, peripheral), lobar, and slice-by-slice basis. The coronal central slice for a representative ex-smoker is shown in **Figure 1-9**, which enables the generation of quantitative measurements through computational analysis. Deriving CT measurements of tissue density, volumes, perfusion, ventilation, and structural mechanics is referred to as quantitative CT. Several commercial CT analysis software platforms are available, such as VIDAvision from VIDA Diagnostics Inc. (Coralville, Iowa, USA), which was used for analysis in this thesis.

Quantitative CT measurements are related to the airways, including airway lumen area (LA),¹²⁹ airway wall thickness (WT),¹²⁹ total airway count (TAC),^{15,130} and wall area percent (WA%).¹²⁹ Typical breath-hold CT measurements include the relative area of the lung with attenuation below -950 Hounsfield Units (RA₉₅₀),¹³¹ generated from inspiratory CT acquisition, and similarly, the relative area of the lung with attenuation below -856 Hounsfield Units (RA₈₅₆) from expiratory CT.¹³² Emphysema on CT is quantified using the RA₉₅₀ HU threshold, where a threshold of >6.8% indicates a presence of emphysema,^{131,133} while air-trapping is quantified on an expiratory CT using the RA₈₅₆ threshold. Furthermore, parametric response maps (PRM)¹³⁴ can be generated on a voxel-by-voxel basis by co-registering inspiratory and expiratory CT scans, providing novel emphysema and gas-trapping phenotypes of small airways disease beyond simple thresholds.

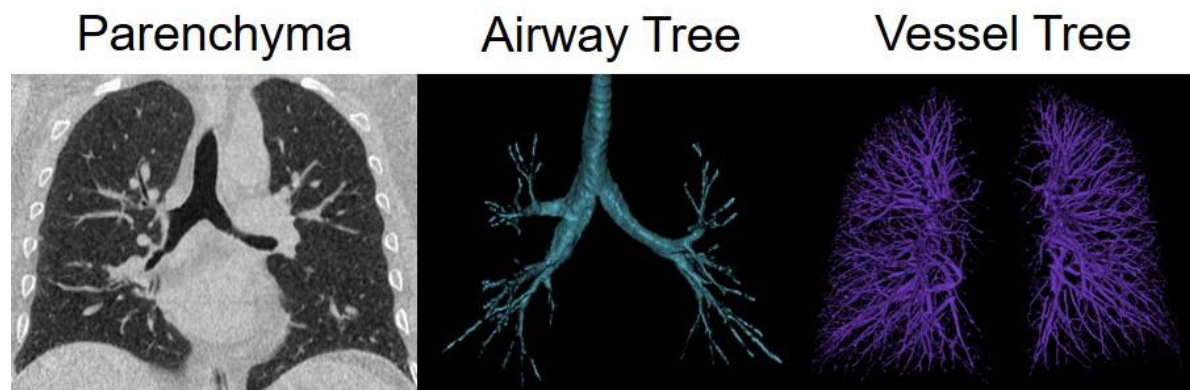


Figure 1-9. Coronal high resolution CT quantitative measurements

From left to right: quantitative CT measures of parenchyma for emphysema and/or air-trapping; quantitative CT airway measurements (pink); and quantitative CT vessel measurements (purple).

In COPD, such evaluations of the airways have provided novel insights into understanding structural abnormalities and the small airways. Recent work involving airway measurements suggested loss of airways in severe emphysema,¹³⁵ which was shown to be an independent predictor of quality-of-life.¹³⁶ Studies have shown that a percentage of emphysema and airway wall thickening are risk factors for exacerbations and are both associated with exacerbation frequency in COPD.¹³⁷ Furthermore, a recent study in ex-smokers with and without COPD has shown that TAC worsens over time, with potential airway narrowing and obliteration.¹³⁸

Pulmonary vasculature can also be quantified on CT using automated methods, such as Chest Imaging Platform, to generate measures of total blood volume (TBV), the volume of blood in vessels with a cross-sectional area less than 5 mm² (BV₅), between 5 and 10 mm² (BV₅₋₁₀), and greater than 10 mm² (BV₁₀).^{139,140} In COPD, studies have shown evidence of pulmonary CT vascular remodelling or vessel pruning and a decrease in small vessel blood volume in patients across COPD severity.¹⁴⁰⁻¹⁴⁶ In addition, these vascular abnormalities were associated with exacerbations and worse patient outcomes.¹⁴¹⁻¹⁴⁶

Four-dimensional CT (4DCT) can measure changes in volume by reconstructing images at many points throughout the breathing cycle and has shown that deformation throughout the respiratory cycle is nonlinear and demonstrates hysteresis.¹⁴⁷ Pulmonary vascular measurements from dynamic perfusion CT can be generated by analyzing the temporal change in injected iodine concentration within the lung parenchyma and vascular spaces as a function of time.^{148,149} The temporal data of iodine concentration is combined with kinetic models to derive physiological measurements such as blood flow, total blood volume, and mean transit time.^{150,151}

Chest X-ray CT has demonstrated its capability to offer detailed insights into the anatomical structures within the lungs. However, it is crucial to acknowledge that the application of X-ray-based methods is limited, particularly in treatment response studies and longitudinal investigations, especially in the context of children and younger adults with chronic lung diseases. This is partly due to the potential risks related to radiation doses from ionizing X-ray radiation.¹⁵²⁻¹⁵⁴

1.5.3 Magnetic Resonance Imaging

Unlike CT, MRI is attractive for longitudinal studies due to its use of non-ionizing radiation and flexibility for acquiring rapid, dynamic, multidimensional signals in response to changes in lung function by involving complex image processing techniques. Using conventional proton (¹H) MRI, without special echo time adjustments, the thoracic cavity appears dark because the typical density of lung tissue (or ¹H density) is relatively low in comparison to air density.¹⁵⁵ Additionally, the tissue signal in ¹H MRI may be degraded due to the presence of air-tissue interfaces, which introduce local magnetic field inhomogeneities, as well as due to respiratory and cardiac motion. In pulmonary imaging, there are multiple approaches and advanced techniques for MRI acquisition to obtain structural and functional measurements, some of which are discussed below.

1.5.3.1 Proton MRI

The lung parenchyma has a short transverse magnetization relaxation time (T_2), which is the time taken by excited protons to lose phase coherence. This results in a reduction in this transverse magnetization and a much faster MRI signal decay for the lung parenchyma in comparison to other tissues.¹⁵⁶ The difference in magnetic susceptibilities between air and alveolar wall tissue leads to local magnetic field inhomogeneity and results in faster spin dephasing (shorter T_2^*). High spatial resolution images of the lung parenchyma can be obtained by maximizing signal strength and minimizing degradation due to susceptibility dephasing, which can be achieved by minimizing the time between excitation and acquisition of the signal called echo time (TE).¹⁵⁷ Short,¹⁵⁸ ultra-short (UTE)^{159,160} and zero (ZTE)¹⁶¹ echo time ^1H lung MRI as well as advanced MR hardware (such as multi-element RF coil arrays) have since significantly improved the visualization of lung parenchyma.

The enhancements in spatial resolution due to shorter TE sequences and advancements in MR hardware have also been coincident with new ways to perform free-breathing ^1H MRI to capture dynamic information as well as with multi-volume static breath-hold approaches. One such multi-volume approach utilizes 3D cones UTE sequence to acquire MR images at four lung volumes in order to evaluate the signal changes and generate voxel-wise dynamic proton-density maps that reflect the change of lung signal intensities.¹⁶² Analyzing MRI signal variations in the lung resulting from respiration also lies at the heart of Fourier decomposition (FD) MRI, first proposed in 2009.¹⁶³ In FD-MRI, the dynamically acquired images of the lung are elastically registered, preserving the signal variations in the individual voxels from respiration. The time series is then analyzed in the temporal domain, separating the high-frequency signals of pulsating blood from the low-frequency signals of respiratory motion on a voxel-by-voxel level. Finally, the magnitudes

of the appropriate respiratory and cardiac peaks of the Fourier spectrum are calculated in order to generate corresponding ventilation and perfusion maps.¹⁶⁴

1.5.3.2 Hyperpolarized Noble Gas MRI

Hyperpolarized gas MRI uses an exogenous noble gas, which is polarized to have an additional atomic spin. Spin exchange optical pumping,¹⁶⁵ first reported in the 1950s and recently reviewed,¹⁶⁶⁻¹⁶⁸ is the method of choice for polarization of noble gases for MRI studies. An intermediary rubidium vapor is exploited where the valence electrons of the rubidium vapor are polarized by absorption of circularly polarized light from the laser source, and it was shown that angular momentum from electron spins could be transferred to nuclear spins of high-pressure noble gases.^{169,170} This technique generates polarizations of about 40–70% for ^3He and 10–40% for ^{129}Xe in a typical dose of 1 L or less for breath-holds.¹⁷¹⁻¹⁷³ This enhances the MRI signal by a factor of up to 100,000 above thermal equilibrium levels.¹⁷⁴ In 1994,¹⁷⁵ the first *ex-vivo* hyperpolarized ^{129}Xe MRI study in animals was completed, which initiated a cascade of critical developments in the field,^{176,177} including the first ^3He MRI studies in patients with lung disease in 1996.^{178,179} Most of the initial human studies were performed using ^3He ,¹⁸⁰ which has a greater gyromagnetic ratio than ^{129}Xe (-32.43 MHz/T for ^3He vs -11.77 MHz/T for ^{129}Xe) and offered greater polarization and SNR.

In breath-hold ventilation MRI, sensitive biomarkers such as ventilation defect percent (VDP),¹⁸¹ ventilated volume (VV),¹⁸² and ventilation coefficient of variation (CV) can be quantified. VDP quantifies the ventilation abnormalities within the lung, which is calculated by normalizing the total volume of ventilation defects to the thoracic cavity volume.²² To probe the microstructure of the lung, the Brownian motion under diffusion gradients of hyperpolarized gas can be utilized to calculate the apparent diffusion coefficient (ADC) or airway morphometry.¹⁸³⁻¹⁸⁶ The ventilation

patterns and microstructure measured using hyperpolarized ^3He MRI in an ex-smoker and a mild COPD participant are shown in **Figure 1-10**. The cyan regions reflect the ventilated volume in the lungs, within a single breath-hold, whereas the corresponding dark regions indicate no ventilation.

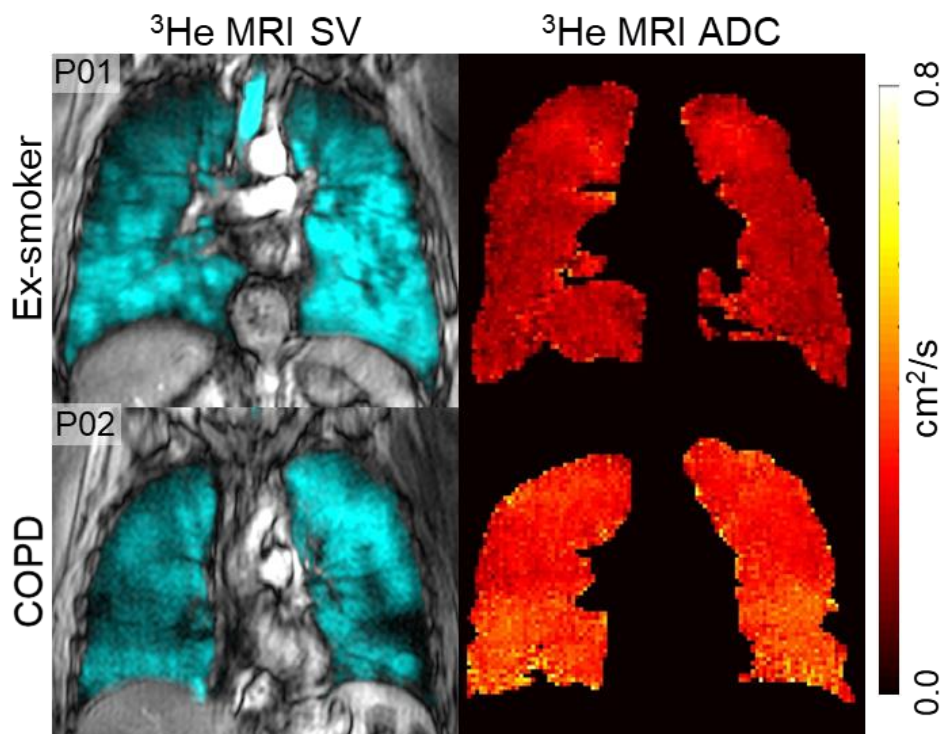


Figure 1-10. Inhaled hyperpolarized gas MR imaging

Hyperpolarized ^3He MRI Static Ventilation and ADC Map in a representative ex-smoker without and with COPD.

In COPD, several pivotal studies have identified the hallmark finding of regional ventilation defects, even in those with normal clinical measurements on spirometry and CT.¹⁸⁷⁻¹⁹⁰ Hyperpolarized ^3He and ^{129}Xe MRI VDP reflects airway abnormalities such as narrowing and remodeling,^{130,191} and is associated with disease exacerbations,^{23,192} symptoms and severity,^{187,193,194} CT-derived emphysema measurements.¹⁹⁵ MRI VDP is also strongly correlated with clearance index,¹⁹⁶ which is thought to be reflective of ventilation heterogeneity caused by small airway abnormalities, even in those with normal spirometry.^{197,198} Ventilation defects are also sensitive to bronchodilation for both asthma and COPD patients,¹⁹⁹ and to bronchoconstriction

in asthma patients.^{200,201} The minimal-clinically-important-difference (MCID) in VDP has been established to be 2-4%²⁰² using the gold-standard FEV₁ measurement as an anchor, which equates to about 110-200 mL of ventilation defect volume.²⁰²

The recent scarcity and corresponding increased price of ³He gas has driven the development of improved ¹²⁹Xe gas polarization methods,²⁰³ which have become the mainstay method in the field. In 1980,²⁰⁴ investigations showed that xenon displayed increased solubility in body tissues and blood with increased hematocrit, compared to helium gas, due to its modest Ostwald solubility.^{205,206} Thus, ¹²⁹Xe is also capable of transmembrane diffusion, and in the timeframe of an MRI acquisition, it may be independently detected in three pulmonary compartments: the gas, alveoli-capillary membrane, and the blood RBC in the capillary network, where it exhibits distinct resonance frequencies. This was initially shown in animal studies,²⁰⁷ and later demonstrated in human studies.^{176,208,209} In more recent years, the developments in this technique have been focused on visualizing and quantifying lung airspaces, and measuring gas exchange and uptake.^{208,210-212} Dissolved-phase MR images are typically quantified in terms of the normalized ratio of the membrane to gas and RBC to gas signal ratio maps. This provides an opportunity to evaluate pulmonary microvasculature and perfusion beyond the larger vessels.^{211,213}

1.5.4 Nuclear Medicine Imaging

In the realm of nuclear medicine, the utilization of radioisotopes or radiolabelled tracers is instrumental for capturing detailed images of lung function parameters such as ventilation, perfusion, and the intricate interplay observed in ventilation-perfusion mismatches. These images are commonly integrated with anatomical representations, such as planar X-ray or CT, facilitating the correlation of pulmonary functional data with corresponding structural information. Advanced

hybrid nuclear medicine imaging systems, incorporating CT or MRI, have emerged more recently to enable concurrent assessment of lung function and structure.²¹⁴⁻²¹⁶ The most common nuclear medicine imaging techniques that were developed and used to generate ventilation images are positron emission tomography (PET) and single photon emission computed tomography (SPECT). SPECT imaging involves patients inhaling radioisotopes, which emit a single gamma ray upon decay. Patients lie on a bed, while a ring of gamma cameras or the rotation of single/multiple gamma cameras around them captures various projections from diverse angles. This process enables the reconstruction of projections to generate volumetric data on the distribution of radioisotopes in the lungs. In PET imaging, three-dimensional information is also obtained. In contrast to SPECT, PET utilizes positron-emitting isotopes to visualize metabolic activity. Following injection or inhalation, the radionuclide undergoes decay, emitting a positron. The ensuing annihilation process generates two gamma photons of equal energy, emitted 180° apart, detected coincidentally by circumferentially arranged gamma cameras. The spatial location of the source particle is determined along the straight line between the two detectors, and all detected sources are reconstructed into a volumetric image.^{217,218} While both SPECT and PET provide three-dimensional imaging and functional insights, they share inherent limitations related to low spatial resolution and potential risks associated with radiation exposure, distinguishing them from scintigraphy. Consequently, SPECT and PET have unique applications in physiological studies involving ventilation, perfusion, and ventilation-perfusion mismatch. Nevertheless, they continue to serve as research tools rather than routine evaluation methods for COPD. A summary **Table 1-2** is provided below that summarizes the advantages and disadvantages of various pulmonary modalities and the associated quantitative imaging measurements.

Table 1-2. Summary of pulmonary imaging techniques and their quantitative measurements, strengths and challenges

Method	Measurements	Strengths	Challenges
X-ray CT	-Total airway count (TAC) -Wall area percent (WA%) -Lumen area percent (LA%) -Wall thickness percent (WT%) -Mucus score	• Morphologic information • Widely available • Inexpensive	• Radiation exposure • Extensive manual analysis
Inspiratory-Expiratory CT	-Relative area of the lung with attenuation < -950 Hounsfield Units (RA ₉₅₀) -Relative area of the lung with attenuation < -856 Hounsfield Units (RA ₈₅₆) -Parametric response map (PRM) -Jacobian determinant (J _{det})	• Morphologic information • Widely available • Inexpensive	• Radiation exposure • Relies on thresholds • Complex registration and post-processing
4D CT	-Deformation anisotropy -Ventilation measure	• Morphologic and functional information	• Radiation exposure • Indirect interpretation
¹ H MRI UTE, free breathing Fourier decomposition and other related methods	-Proton density measures -Ventilation defect percent (VDP) -Ventilated Volume (VV) -Perfusion defect percent (QDP)	• Radiation free • Morphologic and functional information • Non-contrast enhanced	• Complex post-processing • Longer scan times • Cardiac artefacts
³ He/ ¹²⁹ Xe MRI	-Ventilation defect percent (VDP) -Ventilated Volume (VV) -Ventilation Coefficient of Variation (CV) -Apparent Diffusion Coefficient (ADC)	• Radiation free • Functional information • High SNR	• Expensive • Requires specialized equipment and personnel
¹²⁹ Xe MRI	-RBC to Gas ratio -Membrane to RBC ratio -Membrane to Gas ratio	• Radiation free • Functional information • Cheaper than ³ He • Gas exchange parameters	• Requires specialized equipment and personnel • Lower SNR than ³ He
PET/SPECT	-Pulmonary blood flow -Perfusion -3D perfusion changes	• Functional information • Ventilation and perfusion evaluation	• Radiation exposure • Low spatial resolution

CT=computed tomography; MRI=magnetic resonance imaging; UTE=ultra-short echo time; SNR=signal-to-noise ratio; RBC=red blood cells; PET=positron emission tomography; SPECT=single photon emission computed tomography.

1.6 Texture Analysis in Pulmonary Imaging

In the realm of medical imaging, texture analysis provides a quantitative approach that systematically characterizes inherent patterns within an image, potentially indicative of various underlying pathophysiological determinants. This analytical method has been significantly

instrumental in the domain of computer-aided diagnosis, wherein biomedical images undergo thorough scrutiny to extract information reflective of the underlying pathophysiological processes. The insights derived from texture analysis are subsequently harnessed for the purpose of disease detection and diagnosis.²¹⁹ The Conventional image interpretation process is time-consuming and error-prone since the clinicians or researchers have to exhaustively browse image series having upwards of a thousand slices. As a consequence, computerized analysis has become one of the major research subjects in medical imaging, particularly in radiology, known as computer-aided diagnosis. In pulmonary imaging, there has been rapid growth in texture analysis and machine learning applications, particularly using the CT modality.^{33-35,220-225} Applications using the MRI modality have been limited, partly due to its availability, with much fewer applications using the hyperpolarized gas MR imaging approach.^{28,226-229}

The image analysis involves image segmentation, image transformation, pattern classification, and feature extraction. Texture is a perceptual quality that, while easily recognizable, presents a considerable challenge in terms of precise definition. Primarily associated with spatially repetitive structures on surfaces, texture emerges from the recurrence of specific elements or multiple elements arranged in diverse spatial positions. The conceptualization of texture revolves around three fundamental components: (i) the repetition of local order across a region significantly larger than the size of the order itself; (ii) the nonrandom disposition of elementary components comprising the order; and (iii) the roughly uniform nature of these components, exhibiting approximately consistent dimensions throughout the textured region.^{31,230} Thus, texture cannot be defined for a point, but can be defined as a repeating pattern of local variations in image intensity. Texture consists of texture primitives or texture elements, sometimes called texels. If texels are small and tonal differences between texels are large, it results in a fine texture, whereas a coarse

texture results when the texels are large and consist of several pixels. Such features are found in the tone and structure of a texture. Image tone is based on pixel intensity properties in the texel, whilst structure represents the spatial relationship between texels.

Texture features are useful in many applications in medical imaging,²³¹ remote sensing^{232,233} and content-based image retrieval (CBIR) systems. There are many approaches to quantifying texture differences and similarities, where typical methods rely on comparing values of features known as second-order statistics that are calculated from images. Briefly, they calculate the relative brightness or signal intensity of selected pairs of pixels across the image. The data is typically stored in a matrix form that accounts for the spatial distribution of intensities. From these, it is possible to determine underlying textures such as the contrasts within the image, coarseness, directionality and regularity,²³⁴ or periodicity and randomness.²³⁵ Features can be extracted either directly from the raw input images or after applying different filters or transforms (such as Gaussian and Gabor filters, wavelet transforms, Laplacian transforms, fractal analysis, etc.).^{29,31,230,232,236,237} The research presented here endeavors to contribute to the expanding body of knowledge at the intersection of medical imaging and computational analysis.

1.6.1 Typical Workflow

A typical texture analysis workflow is outlined in **Figure 1-11**. It begins with image acquisition, followed by segmenting the region of interest, extracting features from this region, and conducting feature analysis and post-processing. Feature analysis may encompass determining unique features specific to certain regions through feature selection methods or incorporating features into a machine learning algorithm. The subsequent section elaborates on the methodologies employed for each of these steps. Segmentation and registration serve to delineate the regions of interest,

while feature selection and machine learning techniques are employed to analyze the extracted features.

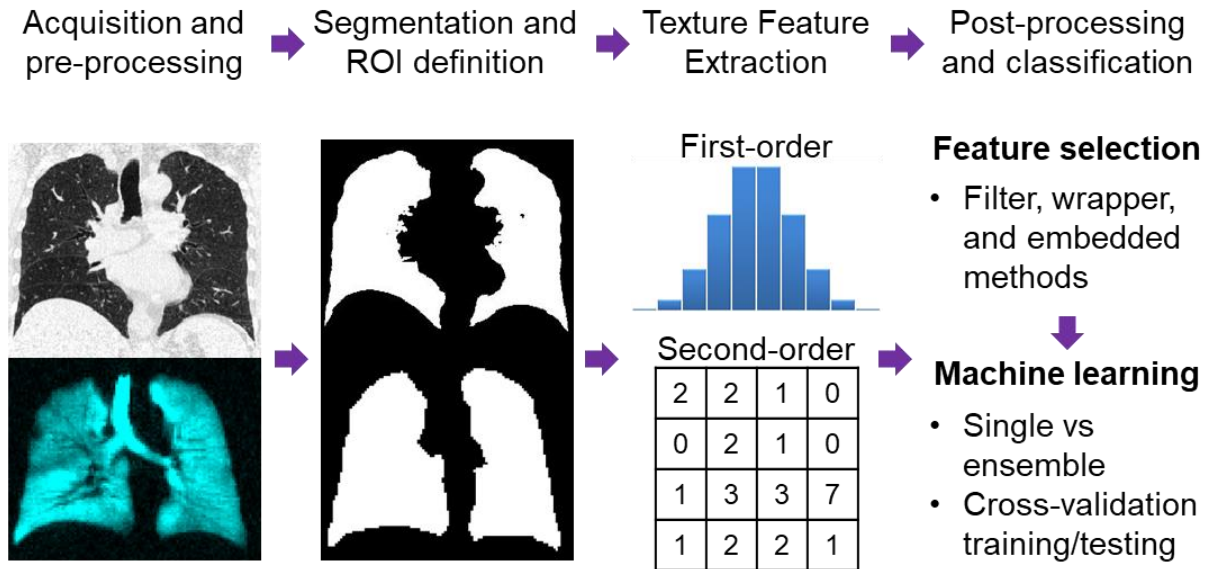


Figure 1-11. Standard image processing and texture analysis pipeline

The typical workflow for texture analysis include image acquisition, pre-processing, region of interest definition, feature extraction, feature selection followed by classification or regression.

Segmentation

Medical image segmentation involves the division of an image into distinct regions guided by a specified similarity characteristic. The conventional manual segmentation method relies on an observer outlining the desired structure. However, this approach is time-consuming and subject to significant variability based on the observer. To mitigate these limitations, medical imaging has transitioned towards semi-automated or fully automated segmentation techniques. Segmentation of the lung cavity is relatively straightforward owing to the discernible density contrast between lung tissue and surrounding structures. Nonetheless, challenges arise from the presence of vasculature, diseased tissue, and the need to differentiate the trachea from lung tissue.

A fundamental computer-aided segmentation strategy involves thresholding the image. This approach partitions the image into distinct regions based on a predetermined set or algorithmically

determined signal intensity. This shift towards automated methods enhances efficiency and reduces variability, particularly in complex segmentation tasks like delineating the lung cavity amid anatomical intricacies.^{238,239} Another segmentation method involves the utilization of region-growing techniques, where regions connected by intensity similarities are segmented. This process can be performed by manually or automatically selecting a seed location and iteratively expanding the region by including neighboring pixels that meet specific similarity criteria.^{240,241} These techniques have been previously used to segment proton MRI thoracic cavity.²² More advanced methods including watershed,²⁴² clustering,^{243,244} and model based techniques²⁴⁵ have also been utilized. Numerous iterations of these techniques have been employed to develop automated lung segmentation algorithms, serving as a pivotal component in the workflow of computer-aided diagnosis pipelines.²⁴⁶⁻²⁴⁸

Registration

Image registration is primarily used to determine the transform function to map one image onto the domain of the other. Rigid registration methods are limited to rotation, translation, scaling, and other linear or affine transformations. In contrast, elastic or deformable registration with reduced restrictions on the transform function allows local adjustments to register the input images. However, other restrictions in deformable registration tasks may be applied in order to preserve the original structural characteristics and anatomy in the input image. This method deforms acquired images by applying transformations and allows discontinuous sliding window motion, designed to specifically accommodate motion present during respiration. These methods are typically used in free-breathing acquisitions or for inter-modality co-registrations, such as between CT and MRI.²⁴⁹⁻²⁵¹ Image registration enhances the utility of texture analysis in medical images

by providing a means to integrate information from various sources, compare images over time, and facilitate more comprehensive and accurate analysis in clinical and research settings.²⁵²⁻²⁵⁵

Feature Extraction

The process of feature extraction is employed to characterize inherent patterns within an image. The most straightforward features can be derived from the histogram of values within the region of interest. These primary or first-order features encompass statistics such as mean, median, mode, standard deviation, skewness, etc. In the context of CT imaging, these features pertain to tissue density and encompass quantitative CT measures discussed earlier, such as the relative area of the lung below a set threshold value.

While first-order features provide information on voxel values within a region of interest, they lack insights into the spatial distribution of voxels. To address this limitation, commonly employed approaches are rooted in second-order statistics that quantify voxel relationships. Two extensively used second-order statistical features include gray level co-occurrence matrix (GLCM)²⁵⁶ and run length matrix (RLM)²⁵⁷ derived texture features.²⁵⁸ The GLCM records the frequency of gray-level values appearing in proximity to each other, with each element indicating the number of times pixel values appear sequentially. Consequently, a GLCM with prominent values near the diagonal suggests an image with fewer sharp edges. The RLM records the number of runs within an image, with row indices representing pixel values, column indices representing the length of a run, and each element indicating the number of runs. A predominant presence of values in the first columns of the RLM indicates an image with substantial heterogeneity in appearance.

Numerous additional texture features can be computed, encompassing filter-based methods, local binary patterns, spherical harmonics, Markov models, and wavelets.²⁵⁸ To mitigate noise and optimize computational efficiency, it is essential to bin values when creating both RLM and

GLCM. Failure to perform binning could lead to an absence of runs within the RLM, as the likelihood of exact same values appearing is exceedingly low. A parallel issue may arise with the GLCM. The bin width serves as a critical determinant influencing how effectively features describe the region of interest. If the bin width is too narrow, features may become noisy, while an excessively large bin width may result in insensitivity to physiologically relevant differences. Careful consideration, typically through experimental determination, is necessary when selecting the bin width as a parameter. This ensures optimal adaptation to the specific task at hand. Additionally, to address these challenges, image filtering and smoothing techniques can be employed. Recent advances in texture analysis methods continue to refine these processes, offering more sophisticated approaches for noise reduction and feature extraction while optimizing hyperparameters for standardized feature extraction.^{233,259,260}

Feature Selection

Many of the extracted features would typically be redundant. Therefore, initial efforts should focus on identifying appropriate endpoints with a potential clinical application to select information useful for a specific task via feature selection and dimensionality reduction methods.³⁹ Feature selection is a process that either includes or excludes some features without modifying them, while dimensionality reduction transforms original features into a lower dimension that creates an entirely new feature space representation of the original input. There are three main types of feature selection methods – filter, wrapper, and embedded approaches.

Filter methods select features from a dataset independently, and such methods rely only on the characteristics of the input variables and a subset of features are filtered out in this relatively quick step to continue the analysis. Filter methods include analyses like the Pearson/Spearman coefficient correlations and statistical/ranking methods based on measures like mutual

information, chi-square or uni- and multi-variate ANOVA tests. Wrapper methods function by evaluating a subset of input features using a machine learning algorithm. This approach employs a search strategy to navigate through the space of possible feature subsets, evaluating each subset based on the performance of a given computational algorithm. Typically such methods are known as greedy algorithms, since they assume that input features are independent and aim to find the best possible combination of features that would result in the best-performing model. Unlike filter methods, this method is able to detect the interaction between variables or features and then find the optimal feature subset for the desired classifier and task.²⁶¹ The embedded methods perform the selection of features within the construction of the machine learning algorithm itself.²⁶² A machine learning algorithm has the advantage of using its own variable selection processes and perform feature selection and classification/regression tasks simultaneously. These are faster than wrapper methods and are as accurate, but they are also able to find the feature subset for the specific algorithm being trained and are also significantly less prone to overfitting. There is a myriad of methods available, but the most common seem to be either using regularization methods (like lasso/ridge regression or elastic nets) in which a penalty is added to different parameters of the model to reduce its freedom.^{262,263}

Machine-learning Modelling

After selecting features that effectively represent an image or a region within an image, the application of machine learning becomes instrumental in determining optimal combinations of information to minimize a specified cost function. This process is pivotal for enhancing the interpretability and predictive capabilities of the analysis. Traditional linear regression serves as a fundamental example, aiming to minimize the sum of the squares of the distance from the line that

best fits each data point. However, as the number of features increases, the complexity of this task escalates.

Advancements in machine learning and texture analysis methods have significantly expanded the repertoire of approaches for feature integration. These contemporary methodologies leverage the power of supervised and unsupervised learning paradigms. In unsupervised learning, the focus is on identifying patterns within a feature set, leading to the creation of feature clusters without prior knowledge of associated labels for each cluster. On the other hand, supervised learning aims to partition the feature space based on known labels associated with each data point.

A multitude of supervised machine learning algorithms have gained prominence in medical imaging applications. These include but are not limited to support vector machines, logistic regressions, linear discriminants, decision trees, and neural networks.²⁶⁴ These algorithms facilitate the extraction of meaningful information from complex datasets, enabling the development of predictive models and enhancing the diagnostic and prognostic capabilities of medical image analysis. Ongoing advancements in machine learning continue to refine these techniques, paving the way for more sophisticated and accurate analyses in the realm of medical imaging and texture analysis.²⁶⁴⁻²⁶⁹

Applications and Challenges

The applications of such techniques in hyperpolarized gas MRI have been scarce. In 2012, texture analysis was shown to quantify changes in hyperpolarized ^3He MRI ventilation after therapeutic intervention in rat asthma-model²²⁶ and this has more recently been implemented in humans.^{34,227,263,270,271} Due to advancements in computational hardware, it is now possible to combine texture analysis and machine-learning classifiers in order to generate predictive models. The realm of computer-aided diagnosis predates the digitization of medical images, incorporating

a pattern recognition approach for image preprocessing, feature extraction, and classification.²⁷² This methodology has been employed extensively in lung imaging, with numerous studies leveraging feature analysis on chest X-ray images. Within lung imaging, a series of studies have been conducted titled "Image Feature Analysis and Computer-Aided Diagnosis in Digital Radiography," contributing significantly to the advancement of this approach.²⁷³⁻²⁸⁰ This approach shows a lot of promise with applications in tumor segmentation,²⁸¹ image registration²⁸² and outcome predictions.^{30,34,283-285}

In recent years, texture analysis tools in CT imaging have been applied to detect and classify pulmonary nodules,²⁸⁶⁻²⁸⁹ typically referred to as radiomics. These investigations concluded that, apart from examining the tumor volume alone, it is also beneficial to analyze the parenchymal tissue as well.^{290,291} Texture analysis has also been utilized to develop automated classification models for various lung diseases, including fibrosis,²⁹² pneumonia²⁹³ and obstructive lung diseases such as emphysema.^{222,294-297} Several efforts have been made to standardize the texture analysis process and the resultant extracted textural features. Recently, twenty-five research teams have come together to address this limitation as part of their Image Biomarker Standardization Initiative (IBSI). They have found an agreement for the calculation of 167 standardized radiomics features derived from an MR image of a patient and validated across other modalities, achieving good to excellent reproducibility.²⁶⁰

1.7 Thesis Hypotheses and Objectives

In patients with COPD, progressive worsening of expiratory airflow occurs over time and it is believed to stem from deterioration of airway wall and lumen microstructure, as well as irreversible destruction of the lung parenchyma.¹⁰ COPD is a complex and heterogeneous disease and it remains difficult to predict patients with obstruction measured using FEV₁ that will experience

accelerated disease progression over short time-periods. While spirometry is the cornerstone of COPD diagnosis,⁷⁴ they cannot directly provide spatial nor functional information about the small airway compartment, that is believed to drive COPD pathogenesis.²⁹⁸ CT enables quantification of abnormal changes in lung parenchyma that overlap with COPD severity.¹⁷ Hyperpolarized gas MRI provides highly sensitive and unique microstructural and functional information in COPD,¹⁸⁰ and can quantify ventilation defects that stem from abnormalities in large and small airways as well as emphysema.²⁹⁹ MRI biomarkers are highly reproducible,³⁰⁰ associated with clinically relevant outcomes in COPD³⁰¹ and have shown to detect disease related changes before CT or FEV₁ measurements.^{25,302} Currently, COPD is the third leading cause of death worldwide¹ and there are approximately 20% of patients misdiagnosed or undetected for COPD.³⁰³ It remains difficult to predict disease progression and longitudinal outcomes, such as mortality, in these patients using currently established clinical and demographic measurements, which emphasizes the need to develop novel imaging tools and thereby promote a better understanding of structure-function relationships in COPD.

The overarching objective of this thesis work was to develop original tools for the extraction of additional measurements from CT and hyperpolarized ³He MR image textures to better understand the underlying pathophysiology and predict longitudinal outcomes in ex-smokers with and without COPD. Therefore, the overarching hypothesis is that CT and MRI ventilation texture measurements combined with machine learning will classify at-risk ex-smokers, as well as predict accelerated lung function decline and mortality in ex-smokers with and without COPD.

In **Chapter 2**, the objective was to develop a CT texture analysis pipeline using machine learning and detect unexplainably reduced lung diffusion from a structural CT, in order to differentiate ex-smokers with mild emphysematous or gas trapping abnormalities from regular ex-smokers. We

also wanted to evaluate the association of selected CT texture features with clinical outcomes and examine correlations of CT measurements with DL_{CO}, not previously observed in these at risk ex-smokers.²⁵ Given the known variability and insensitivity of DL_{CO} measurements,³⁰⁴ their reliance on technique and calibration,³⁰⁵ and the absence of other abnormal cardiovascular or pulmonary measurements,³⁰⁶ it remains difficult to explain mildly abnormal DL_{CO} measurements in these ex-smokers. We hypothesized that texture features extracted from CT images of regular ex-smokers will be significantly different from ex-smokers with lowered DL_{CO} and will accurately (>80%) differentiate these ex-smokers with subclinical disease, who otherwise have conventional CT and spirometry measures.

Next, we wanted to investigate clinically-relevant outcomes across two time points and investigate whether changes in imaging texture correspond with changes in disease state. Thus, in **Chapter 3**, the objective was to develop a different pipeline for extracting unique texture features residing within hyperpolarized ³He MR ventilation images in order to identify COPD participants at risk of accelerated lung function decline, defined by annual FEV₁ worsening. We hypothesized that texture features extracted from baseline hyperpolarized MR images of COPD participants with stable FEV₁ worsening will be significantly different from those with rapid FEV₁ decline (≥ 60 ml/year)³⁰⁷ observed over a 2-3 year period, and will accurately (>80%) differentiate these at-risk participants from otherwise regular COPD participants.

To further understand the prognostic value and importance of imaging textural features, we endeavored to predict the ultimate patient outcome of mortality. In **Chapter 4**, the objective was to evaluate conventional MRI and CT measurements and employ imaging texture analysis to predict all-cause mortality in ex-smokers with and without COPD after 10-years. We hypothesized that incorporating chest MRI and CT measurements and image texture analysis in combination

with machine-learning would provide unique prognostic information and improve mortality risk assessments in ex-smokers.

In **Chapter 5**, I provide an overview and summary of the important findings and conclusions from **Chapters 2 to 4**. Next, the general limitations of this work as well as specific limitations of each chapter are discussed. This thesis concludes with an outline of future investigations that can build on the work presented in this thesis.

1.8 References

- 1 WHO. *World Health Organization: The top 10 causes of death in 2019*, <<https://www.who.int/news-room/fact-sheets/detail/the-top-10-causes-of-death>> (2020).
- 2 Elflein, J. *Statista - Leading causes of death worldwide in 2019 (in millions)*, <<https://www.statista.com/statistics/288839/leading-causes-of-death-worldwide/>> (2023).
- 3 Shirley, B. N., T. Deaths from Chronic Obstructive Pulmonary Disease in Canada, 1950 to 2011. *Health at a Glance. Statistics Canada catalogue no. 82-624-X*. (2015).
- 4 Statistics-Canada. Chronic obstructive pulmonary disease in adults, 2012 to 2013. *Health Fact Sheets 82-625-X* (2015).
- 5 Statistics-Canada. Canadian Institute for Health Information (CIHI): Health Indicators 2008. . *Canadian Institute for Health Information* (2008).
- 6 CIHI. *Canadian Institute for Health Information: Hospitalization rates for COPD across Canadian cities.*, <<https://www.cihi.ca/en/hospitalization-rates-for-copd-across-canadian-cities>> (2019).
- 7 Mittmann, N. *et al.* The cost of moderate and severe COPD exacerbations to the Canadian healthcare system. *Respir Med* **102**, 413-421, doi:10.1016/j.rmed.2007.10.010 (2008).
- 8 WHO. The top 10 causes of death. *The Top 10 Causes of Death* (2018). <<https://www.who.int/news-room/fact-sheets/detail/the-top-10-causes-of-death>>.
- 9 Vestbo, J. COPD: definition and phenotypes. *Clin Chest Med* **35**, 1-6, doi:10.1016/j.ccm.2013.10.010 (2014).
- 10 Hogg, J. C. *et al.* The Nature of Small-Airway Obstruction in Chronic Obstructive Pulmonary Disease. *N Engl J Med* **350**, 2645-2653, doi:10.1056/NEJMoa032158 (2004).
- 11 Hogg, J. C. Pathophysiology of airflow limitation in chronic obstructive pulmonary disease. *Lancet* **364**, 709-721, doi:10.1016/s0140-6736(04)16900-6 (2004).
- 12 Sarkar, M., Bhardwaz, R., Madabhavi, I. & Modi, M. Physical signs in patients with chronic obstructive pulmonary disease. *Lung India* **36**, 38-47, doi:10.4103/lungindia.lungindia_145_18 (2019).
- 13 Leap, J., Arshad, O., Cheema, T. & Balaan, M. Pathophysiology of COPD. *Critical Care Nursing Quarterly* **44**, 2-8, doi:10.1097/cnq.0000000000000334 (2021).
- 14 Elbehairy, A. F. *et al.* Mild chronic obstructive pulmonary disease: why spirometry is not sufficient! *Expert review of respiratory medicine* **11**, 549-563, doi:10.1080/17476348.2017.1334553 (2017).
- 15 Kirby, M. *et al.* Total Airway Count on Computed Tomography and the Risk of Chronic Obstructive Pulmonary Disease Progression. Findings from a Population-based Study. *Am J Respir Crit Care Med* **197**, 56-65, doi:10.1164/rccm.201704-0692OC (2018).
- 16 Singh, D. *et al.* Global Strategy for the Diagnosis, Management, and Prevention of Chronic Obstructive Lung Disease: the GOLD science committee report 2019. *Eur Respir J* **53**, doi:10.1183/13993003.00164-2019 (2019).
- 17 Pompe, E. *et al.* Five-year Progression of Emphysema and Air Trapping at CT in Smokers with and Those without Chronic Obstructive Pulmonary Disease: Results from the COPDGene Study. *Radiology* **295**, 218-226, doi:10.1148/radiol.2020191429 (2020).
- 18 Crossley, D., Renton, M., Khan, M., Low, E. V. & Turner, A. M. CT densitometry in emphysema: a systematic review of its clinical utility. *Int J Chron Obstruct Pulmon Dis* **13**, 547-563, doi:10.2147/copd.S143066 (2018).

- 19 Madani, A., Van Muylem, A., de Maertelaer, V., Zanen, J. & Gevenois, P. A. Pulmonary emphysema: size distribution of emphysematous spaces on multidetector CT images--comparison with macroscopic and microscopic morphometry. *Radiology* **248**, 1036-1041, doi:10.1148/radiol.2483071434 (2008).
- 20 Regan, E. A. *et al.* Clinical and Radiologic Disease in Smokers With Normal Spirometry. *JAMA Intern Med* **175**, 1539-1549, doi:10.1001/jamainternmed.2015.2735 (2015).
- 21 Oelsner, E. C. *et al.* Association between emphysema-like lung on cardiac computed tomography and mortality in persons without airflow obstruction: a cohort study. *Ann Intern Med* **161**, 863-873, doi:10.7326/m13-2570 (2014).
- 22 Kirby, M. *et al.* Hyperpolarized ³He magnetic resonance functional imaging semiautomated segmentation. *Acad Radiol* **19**, 141-152, doi:10.1016/j.acra.2011.10.007 (2012).
- 23 Kirby, M., Pike, D., Coxson, H. O., McCormack, D. G. & Parraga, G. Hyperpolarized (³He) ventilation defects used to predict pulmonary exacerbations in mild to moderate chronic obstructive pulmonary disease. *Radiology* **273**, 887-896, doi:10.1148/radiol.14140161 (2014).
- 24 Kirby, M. *et al.* Chronic obstructive pulmonary disease: longitudinal hyperpolarized (³He) MR imaging. *Radiology* **256**, 280-289, doi:10.1148/radiol.10091937 (2010).
- 25 Fain, S. B. *et al.* Early emphysematous changes in asymptomatic smokers: detection with ³He MR imaging. *Radiology* **239**, 875-883, doi:10.1148/radiol.2393050111 (2006).
- 26 Fain, S., Schiebler, M. L., McCormack, D. G. & Parraga, G. Imaging of lung function using hyperpolarized helium-3 magnetic resonance imaging: Review of current and emerging translational methods and applications. *J Magn Reson Imaging* **32**, 1398-1408, doi:10.1002/jmri.22375 (2010).
- 27 Han, F. *et al.* Texture Feature Analysis for Computer-Aided Diagnosis on Pulmonary Nodules. *Journal of Digital Imaging* **28**, 99-115, doi:10.1007/s10278-014-9718-8 (2015).
- 28 Ahmed, S., Iftekharuddin, K. M. & Vossough, A. Efficacy of texture, shape, and intensity feature fusion for posterior-fossa tumor segmentation in MRI. *IEEE Trans Inf Technol Biomed* **15**, 206-213, doi:10.1109/TITB.2011.2104376 (2011).
- 29 Alobaidli, S. *et al.* The role of texture analysis in imaging as an outcome predictor and potential tool in radiotherapy treatment planning. *Br J Radiol* **87**, 20140369, doi:10.1259/bjr.20140369 (2014).
- 30 Chaddad, A., Sabri, S., Niazi, T. & Abdulkarim, B. Prediction of survival with multi-scale radiomic analysis in glioblastoma patients. *Medical & biological engineering & computing* **56**, 2287-2300, doi:10.1007/s11517-018-1858-4 (2018).
- 31 Depeursinge, A., Al-Kadi, O. S. & Mitchell, J. R. *Biomedical texture analysis: fundamentals, tools and challenges*. (Academic Press, 2017).
- 32 Li, Z. *et al.* A Novel CT-Based Radiomics Features Analysis for Identification and Severity Staging of COPD. *Acad Radiol* **29**, 663-673, doi:10.1016/j.acra.2022.01.004 (2022).
- 33 Hoffman, E. A. *et al.* in *C5. C005 DIAGNOSIS AND PROGNOSIS IN COPD* A1122-A1122.
- 34 Makimoto, K., Hogg, J. C., Bourbeau, J., Tan, W. C. & Kirby, M. CT Imaging With Machine Learning for Predicting Progression to COPD in Individuals at Risk. *Chest*, doi:https://doi.org/10.1016/j.chest.2023.06.008 (2023).

- 35 Sørensen, L. *et al.* Chronic Obstructive Pulmonary Disease Quantification Using CT Texture Analysis and Densitometry: Results From the Danish Lung Cancer Screening Trial. *AJR Am J Roentgenol* **214**, 1269-1279, doi:10.2214/ajr.19.22300 (2020).
- 36 D'Agnillo, F., Zhang, X. & Williams, M. C. Structural Integrity of the Alveolar–Capillary Barrier in Cynomolgus Monkeys Challenged with Fully Virulent and Toxin-Deficient Strains of *Bacillus anthracis*. *Am J Pathol* **190**, 2095-2110, doi:https://doi.org/10.1016/j.ajpath.2020.06.007 (2020).
- 37 Willführ, A. *et al.* Estimation of the number of alveolar capillaries by the Euler number (Euler-Poincaré characteristic). *Am J Physiol Lung Cell Mol Physiol* **309**, L1286-1293, doi:10.1152/ajplung.00410.2014 (2015).
- 38 Federle, M. P. *et al.* in *Imaging Anatomy: Chest, Abdomen, Pelvis (Second Edition)* (eds Michael P. Federle *et al.*) 86-105 (Elsevier, 2017).
- 39 Sharma, M. *et al.* Quantification of pulmonary functional MRI: state-of-the-art and emerging image processing methods and measurements. *Phys. Med. & Biol.* (2022).
- 40 MacIntyre, N. *et al.* Standardisation of the single-breath determination of carbon monoxide uptake in the lung. *Eur.Respir.J.* **26**, 720-735 (2005).
- 41 American-Lung-Association. *How your lungs get the job done*, <<https://www.lung.org/blog/how-your-lungs-work>> (2017).
- 42 Tschirren, J., McLennan, G., Palágyi, K., Hoffman, E. A. & Sonka, M. Matching and anatomical labeling of human airway tree. *IEEE transactions on medical imaging* **24**, 1540-1547, doi:10.1109/TMI.2005.857653 (2005).
- 43 Lumb, A. B. *Nunn's applied respiratory physiology*. Eighth edition. edn, (Elsevier, 2017).
- 44 Han, S. & Mallampalli, R. K. The Role of Surfactant in Lung Disease and Host Defense against Pulmonary Infections. *Ann Am Thorac Soc* **12**, 765-774, doi:10.1513/AnnalsATS.201411-507FR (2015).
- 45 Thurlbeck, W. M. The pathology of small airways in chronic airflow limitation. *Eur.J.Respir.Dis.Suppl* **121**, 9-18 (1982).
- 46 West, J. B. *Respiratory Physiology: The Essentials*. 9 edn, (Lippincott Williams & Wilkins, 2012).
- 47 West, J. B. *Pulmonary Pathophysiology: The Essentials*. 7 edn, (Lippincott Williams & Wilkins, 2008).
- 48 Roetman, E. L. & Barr, R. E. The mechanical basis for Fick's law and its generalizations. *Adv Exp Med Biol* **75**, 261-265, doi:10.1007/978-1-4684-3273-2_32 (1976).
- 49 Vogelmeier, C. F. *et al.* Global Strategy for the Diagnosis, Management, and Prevention of Chronic Obstructive Lung Disease 2017 Report. GOLD Executive Summary. *Am J Respir Crit Care Med* **195**, 557-582, doi:10.1164/rccm.201701-0218PP (2017).
- 50 Woods, J. C. *et al.* Hyperpolarized ³He diffusion MRI and histology in pulmonary emphysema. *Magn Reson Med*. **56**, 1293-1300 (2006).
- 51 Decramer, M., Janssens, W. & Miravittles, M. Chronic obstructive pulmonary disease. *The Lancet* **379**, 1341-1351, doi:https://doi.org/10.1016/S0140-6736(11)60968-9 (2012).
- 52 West, J. B. *Respiratory Pathophysiology: The Essentials*. 3rd edn, (Williams & Wilkins, 1987).
- 53 Hogg, J. C., McDonough, J. E. & Suzuki, M. Small airway obstruction in COPD: new insights based on micro-CT imaging and MRI imaging. *Chest* **143**, 1436-1443, doi:10.1378/chest.12-1766 (2013).

- 54 Hogg, J. C., Macklem, P. T. & Thurlbeck, W. M. Site and nature of airway obstruction in chronic obstructive lung disease. *N Engl J Med.* **278**, 1355-1360 (1968).
- 55 Thurlbeck, W. M. & Muller, N. L. Emphysema: definition, imaging, and quantification. *AJR Am J Roentgenol* **163**, 1017-1025 (1994).
- 56 Raouf, S. *et al.* Lung Imaging in COPD Part 1: Clinical Usefulness. *Chest* **164**, 69-84, doi:10.1016/j.chest.2023.03.007 (2023).
- 57 El Kaddouri, B. *et al.* Fleischner Society Visual Emphysema CT Patterns Help Predict Progression of Emphysema in Current and Former Smokers: Results from the COPDGene Study. *Radiology* **298**, 441-449, doi:10.1148/radiol.2020200563 (2021).
- 58 Anzueto, A. Alpha-1 Antitrypsin Deficiency-Associated Chronic Obstructive Pulmonary Disease: A Family Perspective. *COPD: J Chron Obstruct Pulmon Dis* **12**, 462-467, doi:10.3109/15412555.2014.974746 (2014).
- 59 Smith, B. M. *et al.* Pulmonary emphysema subtypes on computed tomography: the MESA COPD study. *Am J Med* **127**, 94.e97-23, doi:10.1016/j.amjmed.2013.09.020 (2014).
- 60 Almagro, P. *et al.* Mortality after hospitalization for COPD. *Chest.* **121**, 1441-1448 (2002).
- 61 Austin, P. C., Stanbrook, M. B., Anderson, G. M., Newman, A. & Gershon, A. S. Comparative ability of comorbidity classification methods for administrative data to predict outcomes in patients with chronic obstructive pulmonary disease. *Ann Epidemiol* **22**, 881-887, doi:10.1016/j.annepidem.2012.09.011 (2012).
- 62 Barnes, P. J. & Celli, B. R. Systemic manifestations and comorbidities of COPD. *Eur Respir J* **33**, 1165-1185 (2009).
- 63 Barr, R. G. *et al.* Comorbidities, patient knowledge, and disease management in a national sample of patients with COPD. *Am J Med* **122**, 348-355 (2009).
- 64 Dunham-Snary, K. J. *et al.* Hypoxic Pulmonary Vasoconstriction: From Molecular Mechanisms to Medicine. *Chest* **151**, 181-192, doi:10.1016/j.chest.2016.09.001 (2017).
- 65 William, M. Pathology, pathogenesis, and pathophysiology. *Br Med J* **332**, 1202, doi:10.1136/bmj.332.7551.1202 (2006).
- 66 Shujaat, A., Minkin, R. & Eden, E. Pulmonary hypertension and chronic cor pulmonale in COPD. *Int J Chron Obstruct Pulmon Dis* **2**, 273-282 (2007).
- 67 Lai, Y. C., Potoka, K. C., Champion, H. C., Mora, A. L. & Gladwin, M. T. Pulmonary arterial hypertension: the clinical syndrome. *Circ Res* **115**, 115-130, doi:10.1161/circresaha.115.301146 (2014).
- 68 Rahaghi, F. N. *et al.* Pulmonary vascular density: comparison of findings on computed tomography imaging with histology. *Eur Respir J* **54**, doi:10.1183/13993003.00370-2019 (2019).
- 69 Estépar, R. S. *et al.* Computed tomographic measures of pulmonary vascular morphology in smokers and their clinical implications. *Am J Respir Crit Care Med* **188**, 231-239, doi:10.1164/rccm.201301-0162OC (2013).
- 70 Diaz, A. A. *et al.* Quantitative CT Measures of Bronchiectasis in Smokers. *Chest* **151**, 1255-1262, doi:10.1016/j.chest.2016.11.024 (2017).
- 71 Quanjer, P. H. *et al.* Multi-ethnic reference values for spirometry for the 3-95-yr age range: the global lung function 2012 equations. *Eur Respir J* **40**, 1324-1343, doi:10.1183/09031936.00080312 (2012).
- 72 Miller, M. R. *et al.* Standardisation of spirometry. *Eur Respir J* **26**, 319-338, doi:10.1183/09031936.05.00034805 (2005).

- 73 Graham, B. L. *et al.* Standardization of Spirometry 2019 Update. An Official American Thoracic Society and European Respiratory Society Technical Statement. *Am J Respir Crit Care Med* **200**, e70-e88, doi:10.1164/rccm.201908-1590ST (2019).
- 74 Vestbo, J. *et al.* Global strategy for the diagnosis, management, and prevention of chronic obstructive pulmonary disease: GOLD executive summary. *Am J Respir Crit Care Med* **187**, 347-365, doi:10.1164/rccm.201204-0596PP (2013).
- 75 Vestbo, J. & Wedzicha, J. NICE and GOLD response. *Lancet Respir Med* **1**, 442, doi:10.1016/S2213-2600(13)70172-3 (2013).
- 76 Agusti, A. *Global Strategy for the Diagnosis, Management and Prevention of Chronic Obstructive Pulmonary Disease 2020 Report*, (2020).
- 77 Wanger, J. *et al.* Standardisation of the measurement of lung volumes. *Eur Respir J* **26**, 511-522, doi:10.1183/09031936.05.00035005 (2005).
- 78 Wanger, J. *et al.* Standardisation of the measurement of lung volumes. *Eur. Respir. J.* **26**, 511-522 (2005).
- 79 Graham, B. L. *et al.* 2017 ERS/ATS standards for single-breath carbon monoxide uptake in the lung. *Eur Respir J* **49**, doi:10.1183/13993003.00016-2016 (2017).
- 80 Heckman, E. J. & O'Connor, G. T. Pulmonary function tests for diagnosing lung disease. *Jama* **313**, 2278-2279, doi:10.1001/jama.2015.4466 (2015).
- 81 Ponce, M. C., Sankari, A. & Sharma, S. in *StatPearls* (StatPearls Publishing Copyright © 2024, StatPearls Publishing LLC., 2024).
- 82 Harvey, B. G. *et al.* Risk of COPD with obstruction in active smokers with normal spirometry and reduced diffusion capacity. *Eur Respir J* **46**, 1589-1597, doi:10.1183/13993003.02377-2014 (2015).
- 83 Balasubramanian, A. *et al.* Diffusing Capacity and Mortality in Chronic Obstructive Pulmonary Disease. *Annals of the American Thoracic Society* **20**, 38-46, doi:10.1513/AnnalsATS.202203-226OC (2023).
- 84 Ahumada, S. *et al.* Prevalence of abnormal lung volumes, DLCO and chest HRCT in smokers with normal spirometry. *Eur Respir J* **42**, P418 (2013).
- 85 Balasubramanian, A. *et al.* Diffusing Capacity of Carbon Monoxide in Assessment of COPD. *Chest* **156**, 1111-1119, doi:10.1016/j.chest.2019.06.035 (2019).
- 86 Ramon, M. A. *et al.* Hospital admissions and exercise capacity decline in patients with COPD. *Eur Respir J* **43**, 1018-1027, doi:10.1183/09031936.00088313 (2014).
- 87 Agarwala, P. & Salzman, S. H. Six-Minute Walk Test: Clinical Role, Technique, Coding, and Reimbursement. *Chest* **157**, 603-611, doi:10.1016/j.chest.2019.10.014 (2020).
- 88 Casanova, C. *et al.* The 6-min walking distance: long-term follow up in patients with COPD. *Eur Respir J* **29**, 535-540 (2007).
- 89 Cote, C. G., Pinto-Plata, V., Kasprzyk, K., Dordelly, L. J. & Celli, B. R. The 6-min walk distance, peak oxygen uptake, and mortality in COPD. *Chest* **132**, 1778-1785 (2007).
- 90 Fermont, J. M. *et al.* Biomarkers and clinical outcomes in COPD: a systematic review and meta-analysis. *Thorax* **74**, 439-446, doi:10.1136/thoraxjnl-2018-211855 (2019).
- 91 Pinto-Plata, V. M., Cote, C., Cabral, H., Taylor, J. & Celli, B. R. The 6-min walk distance: change over time and value as a predictor of survival in severe COPD. *Eur Respir J* **23**, 28-33, doi:10.1183/09031936.03.00034603 (2004).
- 92 Jones, P. W. St. George's Respiratory Questionnaire: MCID. *COPD*. **2**, 75-79 (2005).

- 93 Jones, P. W., Quirk, F. H., Baveystock, C. M. & Littlejohns, P. A self-complete measure of health status for chronic airflow limitation. The St. George's Respiratory Questionnaire. *Am Rev.Respir.Dis.* **145**, 1321-1327 (1992).
- 94 Müllerova, H. *et al.* St George's Respiratory Questionnaire Score Predicts Outcomes in Patients with COPD: Analysis of Individual Patient Data in the COPD Biomarkers Qualification Consortium Database. *Chronic Obstr Pulm Dis* **4**, 141-149, doi:10.15326/jcopdf.4.2.2017.0131 (2017).
- 95 Mahler, D. (1993).
- 96 Janssens, J. P., Pache, J. C. & Nicod, L. P. Physiological changes in respiratory function associated with ageing. *Eur Respir J* **13**, 197-205, doi:10.1034/j.1399-3003.1999.13a36.x (1999).
- 97 Barker, B. L. *et al.* Systemic and pulmonary inflammation is independent of skeletal muscle changes in patients with chronic obstructive pulmonary disease. *Int J Chron Obstruct Pulmon Dis* **9**, 975-981, doi:10.2147/COPD.S63568 (2014).
- 98 Celli, B. R. Pulmonary rehabilitation in patients with COPD. *Am J Respir Crit Care Med* **152**, 861-864 (1995).
- 99 Diaz, A. A. *et al.* Chest CT measures of muscle and adipose tissue in COPD: gender-based differences in content and in relationships with blood biomarkers. *Acad Radiol* **21**, 1255-1261, doi:10.1016/j.acra.2014.05.013 (2014).
- 100 Verbeke, E. K. *et al.* The senile lung. Comparison with normal and emphysematous lungs. 1. Structural aspects. *Chest* **101**, 793-799, doi:10.1378/chest.101.3.793 (1992).
- 101 Mullen, J. B., Wright, J. L., Wiggs, B. R., Pare, P. D. & Hogg, J. C. Structure of central airways in current smokers and ex-smokers with and without mucus hypersecretion: relationship to lung function. *Thorax* **42**, 843-848 (1987).
- 102 Mullen, J. B., Wright, J. L., Wiggs, B. R., Pare, P. D. & Hogg, J. C. Reassessment of inflammation of airways in chronic bronchitis. *Br Med J (Clin.Res.Ed)* **291**, 1235-1239 (1985).
- 103 Rosenthal, R. A., Zenilman, M. E. & Katlic, M. R. *Principles and practice of geriatric surgery.* (Springer, 2011).
- 104 Sharma, G. & Goodwin, J. Effect of aging on respiratory system physiology and immunology. *Clinical interventions in aging* **1**, 253-260 (2006).
- 105 Fletcher, C. & Peto, R. The natural history of chronic airflow obstruction. *Br Med J* **1**, 1645-1648 (1977).
- 106 Anthonisen, N. R., Connett, J. E. & Murray, R. P. Smoking and lung function of Lung Health Study participants after 11 years. *Am J Respir Crit Care Med* **166**, 675-679 (2002).
- 107 Vogelmeier, C. F. *et al.* Global Strategy for the Diagnosis, Management, and Prevention of Chronic Obstructive Lung Disease 2017 Report: GOLD Executive Summary. *Arch Bronconeumol* **53**, 128-149, doi:10.1016/j.arbres.2017.02.001 (2017).
- 108 BRAZZALE, D. J., UPWARD, A. L. & PRETTO, J. J. Effects of changing reference values and definition of the normal range on interpretation of spirometry. *Respirology* **15**, 1098-1103, doi:https://doi.org/10.1111/j.1440-1843.2010.01830.x (2010).
- 109 Ashutosh, N. A., Dheeraj, G., Ritesh, A. & Surinder, K. J. Comparison of the Lower Confidence Limit to the Fixed-Percentage Method for Assessing Airway Obstruction in Routine Clinical Practice. *Respiratory Care* **56**, 1778, doi:10.4187/respcare.01160 (2011).

- 110 Hangaard, S., Helle, T., Nielsen, C. & Hejlesen, O. K. Causes of misdiagnosis of chronic obstructive pulmonary disease: A systematic scoping review. *Respiratory Med* **129**, 63-84, doi:https://doi.org/10.1016/j.rmed.2017.05.015 (2017).
- 111 Terence, H., Ruth, P. C., Nagendra, C., Imran, S. & Om, P. K. Under- and over-diagnosis of COPD: a global perspective. *Breathe* **15**, 24, doi:10.1183/20734735.0346-2018 (2019).
- 112 Nardini, S. *et al.* Accuracy of diagnosis of COPD and factors associated with misdiagnosis in primary care setting. E-DIAL (Early DIAgnosis of obstructive lung disease) study group. *Respiratory Medicine* **143**, 61-66, doi:https://doi.org/10.1016/j.rmed.2018.08.006 (2018).
- 113 Hill, K. *et al.* Prevalence and underdiagnosis of chronic obstructive pulmonary disease among patients at risk in primary care. *Cmaj* **182**, 673-678, doi:10.1503/cmaj.091784 (2010).
- 114 Ghattas, C., Dai, A., Gemmel, D. J. & Awad, M. H. Over diagnosis of chronic obstructive pulmonary disease in an underserved patient population. *Int J Chron Obstruct Pulmon Dis* **8**, 545-549, doi:10.2147/copd.S45693 (2013).
- 115 Gershon, A. S. *et al.* Health Services Burden of Undiagnosed and Overdiagnosed COPD. *Chest* **153**, 1336-1346, doi:10.1016/j.chest.2018.01.038 (2018).
- 116 Labonté, L. E. *et al.* Undiagnosed Chronic Obstructive Pulmonary Disease Contributes to the Burden of Health Care Use. Data from the CanCOLD Study. *Am J Respir Crit Care Med* **194**, 285-298, doi:10.1164/rccm.201509-1795OC (2016).
- 117 Coultas, D. B., Mapel, D., Gagnon, R. & Lydick, E. The health impact of undiagnosed airflow obstruction in a national sample of United States adults. *Am J Respir Crit Care Med* **164**, 372-377, doi:10.1164/ajrccm.164.3.2004029 (2001).
- 118 Martinez, C. H. *et al.* Undiagnosed Obstructive Lung Disease in the United States. Associated Factors and Long-term Mortality. *Ann Am Thorac Soc* **12**, 1788-1795, doi:10.1513/AnnalsATS.201506-388OC (2015).
- 119 Hogg, J. C., Macklem, P. T. & Thurlbeck, W. M. Site and nature of airway obstruction in chronic obstructive lung disease. *N Engl J Med* **278**, 1355-1360, doi:10.1056/NEJM196806202782501 (1968).
- 120 Thurlbeck, W. M. & Simon, G. Radiographic appearance of the chest in emphysema. *AJR Am J Roentgenol* **130**, 429-440 (1978).
- 121 Cerveri, I. *et al.* Assessment of emphysema in COPD: a functional and radiologic study. *Chest* **125**, 1714-1718 (2004).
- 122 Goodman, L. R. The Beatles, the Nobel Prize, and CT scanning of the chest. *Radiol Clin North Am* **48**, 1-7, doi:10.1016/j.rcl.2009.09.008 (2010).
- 123 Goldman, L. W. Principles of CT and CT technology. *J Nucl Med Technol* **35**, 115-128; quiz 129-130, doi:10.2967/jnmt.107.042978 (2007).
- 124 Hounsfield, G. N. Computerized transverse axial scanning (tomography). 1. Description of system. *Br J Radiol* **46**, 1016-1022, doi:10.1259/0007-1285-46-552-1016 (1973).
- 125 Mettler, F. A., Jr., Huda, W., Yoshizumi, T. T. & Mahesh, M. Effective doses in radiology and diagnostic nuclear medicine: a catalog. *Radiology* **248**, 254-263, doi:10.1148/radiol.2481071451 (2008).
- 126 Regan, E. A. *et al.* Genetic epidemiology of COPD (COPDGene) study design. *COPD* **7**, 32-43, doi:10.3109/15412550903499522 (2010).
- 127 Couper, D. *et al.* Design of the Subpopulations and Intermediate Outcomes in COPD Study (SPIROMICS). *Thorax* **69**, 491-494, doi:10.1136/thoraxjnl-2013-203897 (2014).

- 128 Bourbeau, J. *et al.* Canadian Cohort Obstructive Lung Disease (CanCOLD): Fulfilling the need for longitudinal observational studies in COPD. *COPD* **11**, 125-132, doi:10.3109/15412555.2012.665520 (2014).
- 129 de Jong, P. A., Muller, N. L., Pare, P. D. & Coxson, H. O. Computed tomographic imaging of the airways: relationship to structure and function. *Eur Respir J* **26**, 140-152, doi:10.1183/09031936.05.00007105 (2005).
- 130 Eddy, R. L. *et al.* Is Computed Tomography Airway Count Related to Asthma Severity and Airway Structure and Function? *Am J Respir Crit Care Med* **201**, 923-933, doi:10.1164/rccm.201908-1552OC (2020).
- 131 Gevenois, P. A. *et al.* Comparison of computed density and microscopic morphometry in pulmonary emphysema. *Am J Respir Crit Care Med* **154**, 187-192, doi:10.1164/ajrccm.154.1.8680679 (1996).
- 132 Schroeder, J. D. *et al.* Relationships between airflow obstruction and quantitative CT measurements of emphysema, air trapping, and airways in subjects with and without chronic obstructive pulmonary disease. *AJR Am J Roentgenol* **201**, W460-470, doi:10.2214/AJR.12.10102 (2013).
- 133 Lynch, D. A. *et al.* CT-Definable Subtypes of Chronic Obstructive Pulmonary Disease: A Statement of the Fleischner Society. *Radiology* **277**, 192-205, doi:10.1148/radiol.2015141579 (2015).
- 134 Galban, C. J. *et al.* Computed tomography-based biomarker provides unique signature for diagnosis of COPD phenotypes and disease progression. *Nat Med* **18**, 1711-1715, doi:10.1038/nm.2971 (2012).
- 135 McDonough, J. E. *et al.* Small-airway obstruction and emphysema in chronic obstructive pulmonary disease. *N Engl J Med* **365**, 1567-1575, doi:10.1056/NEJMoa1106955 (2011).
- 136 Diaz, A. A. *et al.* Airway count and emphysema assessed by chest CT imaging predicts clinical outcome in smokers. *Chest* **138**, 880-887, doi:10.1378/chest.10-0542 (2010).
- 137 Han, M. K. *et al.* Chronic obstructive pulmonary disease exacerbations in the COPD Gene study: associated radiologic phenotypes. *Radiology* **261**, 274-282, doi:10.1148/radiol.11110173 (2011).
- 138 Wyszkievicz, P. V. *et al.* Reduced Total Airway Count and Airway Wall Tapering after Three-Years in Ex-Smokers. *Copd* **20**, 186-196, doi:10.1080/15412555.2023.2222831 (2023).
- 139 Ross, J. C., Harmouche, R., Onieva, J., Diaz, A. A. & Washko, G. R. in *C66. LUNG IMAGING II: NEW PROBES AND EMERGING TECHNOLOGIES* A4975-A4975 (2015).
- 140 Estepar, R. S. *et al.* Computational Vascular Morphometry for the Assessment of Pulmonary Vascular Disease Based on Scale-Space Particles. *Proc IEEE Int Symp Biomed Imaging*, 1479-1482, doi:10.1109/ISBI.2012.6235851 (2012).
- 141 Ash, S. Y. *et al.* Pruning of the Pulmonary Vasculature in Asthma. The Severe Asthma Research Program (SARP) Cohort. *Am J Respir Crit Care Med* **198**, 39-50, doi:10.1164/rccm.201712-2426OC (2018).
- 142 Barker, A. L. *et al.* CT Pulmonary Vessels and MRI Ventilation in Chronic Obstructive Pulmonary Disease: Relationship with worsening FEV1 in the TINCan cohort study. *Acad Radiol*, doi:10.1016/j.acra.2020.03.006 (2020).
- 143 Diaz, A. A. *et al.* Pulmonary vascular pruning in smokers with bronchiectasis. *ERJ Open Res* **4**, doi:10.1183/23120541.00044-2018 (2018).

- 144 Pistenmaa, C. L. *et al.* Pulmonary Arterial Pruning and Longitudinal Change in Percent Emphysema and Lung Function: The Genetic Epidemiology of COPD Study. *Chest*, doi:10.1016/j.chest.2021.01.084 (2021).
- 145 Synn, A. J. *et al.* Vascular remodeling of the small pulmonary arteries and measures of vascular pruning on computed tomography. *Pulm Circ* **11**, 20458940211061284, doi:10.1177/20458940211061284 (2021).
- 146 Washko, G. R. *et al.* Arterial Vascular Pruning, Right Ventricular Size, and Clinical Outcomes in Chronic Obstructive Pulmonary Disease. A Longitudinal Observational Study. *Am J Respir Crit Care Med* **200**, 454-461, doi:10.1164/rccm.201811-2063OC (2019).
- 147 Jahani, N. *et al.* A four-dimensional computed tomography comparison of healthy and asthmatic human lungs. *J Biomech* **56**, 102-110, doi:10.1016/j.jbiomech.2017.03.012 (2017).
- 148 Wildberger, J. E. *et al.* Multislice computed tomography perfusion imaging for visualization of acute pulmonary embolism: animal experience. *Eur Radiol* **15**, 1378-1386, doi:10.1007/s00330-005-2718-9 (2005).
- 149 Grob, D. *et al.* Imaging of pulmonary perfusion using subtraction CT angiography is feasible in clinical practice. *Eur Radiol* **29**, 1408-1414, doi:10.1007/s00330-018-5740-4 (2019).
- 150 Schoepf, U. J. *et al.* Pulmonary embolism: comprehensive diagnosis by using electron-beam CT for detection of emboli and assessment of pulmonary blood flow. *Radiology* **217**, 693-700, doi:10.1148/radiology.217.3.r00dc08693 (2000).
- 151 Ohno, Y. *et al.* Contrast-enhanced CT- and MRI-based perfusion assessment for pulmonary diseases: basics and clinical applications. *Diagn Interv Radiol* **22**, 407-421, doi:10.5152/dir.2016.16123 (2016).
- 152 Mayo, J. R., Jackson, S. A. & Muller, N. L. High-resolution CT of the chest: radiation dose. *AJR Am J Roentgenol* **160**, 479-481 (1993).
- 153 Diederich, S. & Lenzen, H. Radiation exposure associated with imaging of the chest: comparison of different radiographic and computed tomography techniques. *Cancer*. **89**, 2457-2460 (2000).
- 154 Ravenel, J. G., Scalzetti, E. M., Huda, W. & Garrisi, W. Radiation exposure and image quality in chest CT examinations. *AJR Am J Roentgenol* **177**, 279-284 (2001).
- 155 Kauczor, H. U. & Kreitner, K. F. MRI of the pulmonary parenchyma. *Eur Radiol* **9**, 1755-1764 (1999).
- 156 Bergin, C. J., Pauly, J. M. & Macovski, A. Lung parenchyma: projection reconstruction MR imaging. *Radiology* **179**, 777-781, doi:10.1148/radiology.179.3.2027991 (1991).
- 157 Bergin, C. J., Glover, G. M. & Pauly, J. Magnetic resonance imaging of lung parenchyma. *J Thorac Imaging* **8**, 12-17 (1993).
- 158 Gold, G. E. *et al.* Short echo time MR spectroscopic imaging of the lung parenchyma. *J Magn Reson Imaging* **15**, 679-684, doi:10.1002/jmri.10113 (2002).
- 159 Ohno, Y. *et al.* Pulmonary high-resolution ultrashort TE MR imaging: Comparison with thin-section standard- and low-dose computed tomography for the assessment of pulmonary parenchyma diseases. *J Magn Reson Imaging* **43**, 512-532, doi:10.1002/jmri.25008 (2016).

- 160 Takahashi, M. *et al.* Ultra-short echo time (UTE) MR imaging of the lung: comparison between normal and emphysematous lungs in mutant mice. *J Magn Reson Imaging* **32**, 326-333, doi:10.1002/jmri.22267 (2010).
- 161 Bae, K. *et al.* Comparison of lung imaging using three-dimensional ultrashort echo time and zero echo time sequences: preliminary study. *Eur Radiol* **29**, 2253-2262, doi:10.1007/s00330-018-5889-x (2019).
- 162 Sheikh, K. *et al.* Ultrashort echo time MRI biomarkers of asthma. *J Magn Reson Imaging* **45**, 1204-1215, doi:10.1002/jmri.25503 (2017).
- 163 Bauman, G. *et al.* Non-contrast-enhanced perfusion and ventilation assessment of the human lung by means of fourier decomposition in proton MRI. *Magn Reson Med* **62**, 656-664, doi:10.1002/mrm.22031 (2009).
- 164 Raptis, C. A. *et al.* Building blocks for thoracic MRI: Challenges, sequences, and protocol design. *J Magn Reson Imaging* **50**, 682-701, doi:10.1002/jmri.26677 (2019).
- 165 Kastler, A. Quelques suggestions concernant la production optique et la détection optique d'une inégalité de population des niveaux de quantification spatiale des atomes. Application à l'expérience de Stern et Gerlach et à la résonance magnétique. *J. Phys. Radium* **11**, 255-265, doi:10.1051/jphysrad:01950001106025500 (1950).
- 166 Khan, A. S. *et al.* Enabling Clinical Technologies for Hyperpolarized ^{129}Xe Magnetic Resonance Imaging and Spectroscopy. *Angewandte Chemie International Edition* **60**, 22126-22147, doi:https://doi.org/10.1002/anie.202015200 (2021).
- 167 Barskiy, D. A. *et al.* NMR Hyperpolarization Techniques of Gases. *Chemistry* **23**, 725-751, doi:10.1002/chem.201603884 (2017).
- 168 Oros, A. M. & Shah, N. J. Hyperpolarized xenon in NMR and MRI. *Phys Med Biol* **49**, R105-153, doi:10.1088/0031-9155/49/20/r01 (2004).
- 169 Bouchiat, M. A., Carver, T. R. & Varnum, C. M. Nuclear Polarization in ^3He Gas Induced by Optical Pumping and Dipolar Exchange. *Physical Review Letters* **5**, 373-375, doi:10.1103/PhysRevLett.5.373 (1960).
- 170 Grover, B. Noble-gas NMR detection through noble-gas-rubidium hyperfine contact interaction. *Physical Review Letters* **40**, 391 (1978).
- 171 He, M. *et al.* Dose and pulse sequence considerations for hyperpolarized ^{129}Xe ventilation MRI. *J Magn Reson Imaging* **33**, 877-885 (2015).
- 172 Norquay, G., Collier, G. J., Rao, M., Stewart, N. J. & Wild, J. M. ^{129}Xe -Rb Spin-Exchange Optical Pumping with High Photon Efficiency. *Physical Review Letters* **121**, 153201, doi:10.1103/PhysRevLett.121.153201 (2018).
- 173 Niedbalski, P. J. *et al.* Protocols for multi-site trials using hyperpolarized ^{129}Xe MRI for imaging of ventilation, alveolar-airspace size, and gas exchange: A position paper from the ^{129}Xe MRI clinical trials consortium. *Magnetic resonance in medicine* **86**, 2966-2986, doi:https://doi.org/10.1002/mrm.28985 (2021).
- 174 Walker, T. G. & Happer, W. Spin-exchange optical pumping of noble-gas nuclei. *Reviews of Modern Physics* **69**, 629-642, doi:10.1103/RevModPhys.69.629 (1997).
- 175 Albert, M. S. *et al.* Biological magnetic resonance imaging using laser-polarized ^{129}Xe . *Nature* **370**, 199-201, doi:10.1038/370199a0 (1994).
- 176 Mugler, J. P., 3rd *et al.* MR imaging and spectroscopy using hyperpolarized ^{129}Xe gas: preliminary human results. *Magn Reson Med* **37**, 809-815, doi:10.1002/mrm.1910370602 (1997).

- 177 Kauczor, H. U. *et al.* Imaging of the lungs using ³He MRI: preliminary clinical experience in 18 patients with and without lung disease. *J Magn Reson Imaging* **7**, 538-543, doi:10.1002/jmri.1880070314 (1997).
- 178 Ebert, M. *et al.* Nuclear magnetic resonance imaging with hyperpolarised helium-3. *Lancet* **347**, 1297-1299, doi:10.1016/s0140-6736(96)90940-x (1996).
- 179 MacFall, J. R. *et al.* Human lung air spaces: potential for MR imaging with hyperpolarized He-3. *Radiology* **200**, 553-558 (1996).
- 180 Kauczor, H. U., Chen, X. J., van Beek, E. J. & Schreiber, W. G. Pulmonary ventilation imaged by magnetic resonance: at the doorstep of clinical application. *Eur Respir J* **17**, 1008-1023, doi:10.1183/09031936.01.17510080 (2001).
- 181 Kirby, M., Wheatley, A., McCormack, D. & Parraga, G. Development and application of methods to quantify spatial and temporal hyperpolarized ³He MRI ventilation dynamics: preliminary results in chronic obstructive pulmonary disease. *SPIE Medical Imaging* **7626** (2010).
- 182 Donnelly, L. F. *et al.* Cystic fibrosis: combined hyperpolarized ³He-enhanced and conventional proton MR imaging in the lung--preliminary observations. *Radiology* **212**, 885-889, doi:10.1148/radiology.212.3.r99se20885 (1999).
- 183 Salerno, M. *et al.* Emphysema: hyperpolarized helium 3 diffusion MR imaging of the lungs compared with spirometric indexes--initial experience. *Radiology* **222**, 252-260, doi:10.1148/radiol.2221001834 (2002).
- 184 Ley, S. *et al.* Functional evaluation of emphysema using diffusion-weighted ³Helium-magnetic resonance imaging, high-resolution computed tomography, and lung function tests. *Investigative radiology* **39**, 427-434, doi:10.1097/01.rli.0000129468.79005.1d (2004).
- 185 Woods, J. C. *et al.* Hyperpolarized ³He diffusion MRI and histology in pulmonary emphysema. *Magnetic resonance in medicine* **56**, 1293-1300, doi:10.1002/mrm.21076 (2006).
- 186 Parraga, G. *et al.* Hyperpolarized ³He ventilation defects and apparent diffusion coefficients in chronic obstructive pulmonary disease: preliminary results at 3.0 Tesla. *Investigative radiology* **42**, 384-391, doi:10.1097/01.rli.0000262571.81771.66 (2007).
- 187 de Lange, E. E. *et al.* Evaluation of asthma with hyperpolarized helium-3 MRI: correlation with clinical severity and spirometry. *Chest* **130**, 1055-1062, doi:10.1378/chest.130.4.1055 (2006).
- 188 Coxson, H. O., Leipsic, J., Parraga, G. & Sin, D. D. Using pulmonary imaging to move chronic obstructive pulmonary disease beyond FEV₁. *Am J Respir Crit Care Med* **190**, 135-144, doi:10.1164/rccm.201402-0256PP (2014).
- 189 Lange, P., Halpin, D. M., O'Donnell, D. E. & MacNee, W. Diagnosis, assessment, and phenotyping of COPD: beyond FEV₁. *Int J Chron Obstruct Pulmon Dis* **11 Spec Iss**, 3-12, doi:10.2147/copd.S85976 (2016).
- 190 Leary, D. *et al.* Hyperpolarized ³He magnetic resonance imaging ventilation defects in asthma: relationship to airway mechanics. *Physiological reports* **4**, doi:10.14814/phy2.12761 (2016).
- 191 Eddy, R. L., Westcott, A., Maksym, G. N., Parraga, G. & Dandurand, R. J. Oscillometry and pulmonary magnetic resonance imaging in asthma and COPD. *Physiological reports* **7**, e13955, doi:10.14814/phy2.13955 (2019).

- 192 Kirby, M., Kanhere, N., Etemad-Rezai, R., McCormack, D. G. & Parraga, G. Hyperpolarized helium-3 magnetic resonance imaging of chronic obstructive pulmonary disease exacerbation. *J Magn Reson Imaging* **37**, 1223-1227, doi:10.1002/jmri.23896 (2013).
- 193 Davis, C. *et al.* Ventilation Heterogeneity in Never-smokers and COPD:: Comparison of Pulmonary Functional Magnetic Resonance Imaging with the Poorly Communicating Fraction Derived From Plethysmography. *Acad Radiol* **23**, 398-405, doi:10.1016/j.acra.2015.10.022 (2016).
- 194 Kirby, M. *et al.* COPD: Do Imaging Measurements of Emphysema and Airway Disease Explain Symptoms and Exercise Capacity? *Radiology* **277**, 872-880, doi:10.1148/radiol.2015150037 (2015).
- 195 Kirby, M. *et al.* Pulmonary ventilation visualized using hyperpolarized helium-3 and xenon-129 magnetic resonance imaging: differences in COPD and relationship to emphysema. *J Appl Physiol (1985)* **114**, 707-715, doi:10.1152/japplphysiol.01206.2012 (2013).
- 196 Svenningsen, S., Nair, P., Guo, F., McCormack, D. G. & Parraga, G. Is ventilation heterogeneity related to asthma control? *Eur Respir J* **48**, 370-379, doi:10.1183/13993003.00393-2016 (2016).
- 197 Kowalik, K. *et al.* Persistent ventilation inhomogeneity after an acute exacerbation in preschool children with recurrent wheezing. *Pediatr Allergy Immunol* **31**, 608-615, doi:10.1111/pai.13245 (2020).
- 198 Bourdin, A. *et al.* Nitrogen washout slope in poorly controlled asthma. *Allergy* **61**, 85-89, doi:10.1111/j.1398-9995.2006.00970.x (2006).
- 199 Kirby, M. *et al.* Chronic obstructive pulmonary disease: quantification of bronchodilator effects by using hyperpolarized (3)He MR imaging. *Radiology* **261**, 283-292, doi:10.1148/radiol.11110403 (2011).
- 200 Farahi, N. *et al.* In vivo imaging reveals increased eosinophil uptake in the lungs of obese asthmatic patients. *J Allergy Clin Immunol* **142**, 1659-1662 e1658, doi:10.1016/j.jaci.2018.07.011 (2018).
- 201 Samee, S. *et al.* Imaging the lungs in asthmatic patients by using hyperpolarized helium-3 magnetic resonance: assessment of response to methacholine and exercise challenge. *J Allergy Clin Immunol* **111**, 1205-1211, doi:10.1067/mai.2003.1544 (2003).
- 202 Eddy, R. L., Svenningsen, S., McCormack, D. G. & Parraga, G. What is the minimal clinically important difference for helium-3 magnetic resonance imaging ventilation defects? *Eur Respir J* **51**, doi:10.1183/13993003.00324-2018 (2018).
- 203 Norquay, G., Collier, G., Rao, M., Stewart, N. & Wild, J. Xe 129-Rb Spin-Exchange Optical Pumping with High Photon Efficiency. *Physical review letters* **121**, 153201 (2018).
- 204 Chen, R. Y. *et al.* Tissue-blood partition coefficient for xenon: temperature and hematocrit dependence. *J Appl Physiol Respir Environ Exerc Physiol* **49**, 178-183, doi:10.1152/jappl.1980.49.2.178 (1980).
- 205 Weathersby, P. K. & Homer, L. D. Solubility of inert gases in biological fluids and tissues: a review. *Undersea Biomed Res* **7**, 277-296 (1980).
- 206 Wagshul, M. E. *et al.* In vivo MR imaging and spectroscopy using hyperpolarized 129Xe. *Magn Reson Med* **36**, 183-191, doi:10.1002/mrm.1910360203 (1996).
- 207 Sakai, K. *et al.* Temporal dynamics of hyperpolarized 129Xe resonances in living rats. *J Magn Reson B* **111**, 300-304, doi:10.1006/jmrb.1996.0098 (1996).

- 208 Cleveland, Z. I. *et al.* Hyperpolarized ^{129}Xe MR Imaging of Alveolar Gas Uptake in
Humans. *PLoS one* **5**, e12192, doi:10.1371/journal.pone.0012192 (2010).
- 209 Patz, S. *et al.* Hyperpolarized ^{129}Xe MRI: A viable functional lung imaging modality? *Eur*
J Radiol **64**, 335-344, doi:https://doi.org/10.1016/j.ejrad.2007.08.008 (2007).
- 210 Qing, K. *et al.* Regional mapping of gas uptake by blood and tissue in the human lung using
hyperpolarized xenon- ^{129}Xe MRI. *J Magn Reson Imaging* **39**, 346-359,
doi:10.1002/jmri.24181 (2014).
- 211 Kaushik, S. S. *et al.* Single-breath clinical imaging of hyperpolarized (^{129}Xe) in the
airspaces, barrier, and red blood cells using an interleaved 3D radial 1-point Dixon
acquisition. *Magn Reson Med* **75**, 1434-1443, doi:10.1002/mrm.25675 (2016).
- 212 Ruppert, K. *et al.* Rapid assessment of pulmonary gas transport with hyperpolarized ^{129}Xe
MRI using a 3D radial double golden-means acquisition with variable flip angles. *Magn*
Reson Med **80**, 2439-2448, doi:https://doi.org/10.1002/mrm.27217 (2018).
- 213 Wang, Z. *et al.* Quantitative analysis of hyperpolarized ^{129}Xe gas transfer MRI. *Med Phys*
44, 2415-2428, doi:https://doi.org/10.1002/mp.12264 (2017).
- 214 Bybel, B. *et al.* SPECT/CT imaging: clinical utility of an emerging technology.
Radiographics **28**, 1097-1113, doi:10.1148/rg.284075203 (2008).
- 215 Kapoor, V., McCook, B. M. & Torok, F. S. An introduction to PET-CT imaging.
Radiographics **24**, 523-543, doi:10.1148/rg.242025724 (2004).
- 216 Quick, H. H. Integrated PET/MR. *J Magn Reson Imaging* **39**, 243-258,
doi:10.1002/jmri.24523 (2014).
- 217 Rhodes, C. G. *et al.* Quantification of regional V/Q ratios in humans by use of PET. I.
Theory. *J Appl Physiol* **66**, 1896-1904 (1989).
- 218 Roach, P. J., Schembri, G. P. & Bailey, D. L. V/Q scanning using SPECT and SPECT/CT.
J Nucl Med **54**, 1588-1596, doi:10.2967/jnumed.113.124602 (2013).
- 219 Doi, K. Computer-aided diagnosis in medical imaging: historical review, current status and
future potential. *Computerized medical imaging and graphics : the official journal of the*
Computerized Medical Imaging Society **31**, 198-211,
doi:10.1016/j.compmedimag.2007.02.002 (2007).
- 220 Mishima, M. *et al.* Quantitative assessment of the spatial distribution of low attenuation
areas on X-ray CT using texture analysis in patients with chronic pulmonary emphysema.
Front Med Biol Eng **8**, 19-34 (1997).
- 221 Hoffman, E. A. *et al.* Characterization of the interstitial lung diseases via density-based
and texture-based analysis of computed tomography images of lung structure and function.
Acad Radiol **10**, 1104-1118 (2003).
- 222 Park, Y. S. *et al.* Texture-based quantification of pulmonary emphysema on high-resolution
computed tomography: comparison with density-based quantification and correlation with
pulmonary function test. *Invest Radiol* **43**, 395-402, doi:10.1097/RLI.0b013e31816901c7
(2008).
- 223 Sørensen, L., Shaker, S. B. & de Bruijne, M. Quantitative analysis of pulmonary
emphysema using local binary patterns. *IEEE Trans Med Imaging* **29**, 559-569,
doi:10.1109/tmi.2009.2038575 (2010).
- 224 Ginsburg, S. B. *et al.* Texture-based Quantification of Centrilobular Emphysema and
Centrilobular Nodularity in Longitudinal CT Scans of Current and Former Smokers. *Acad*
Radiol **23**, 1349-1358, doi:10.1016/j.acra.2016.06.002 (2016).

- 225 Ohno, Y. *et al.* Machine learning for lung CT texture analysis: Improvement of inter-observer agreement for radiological finding classification in patients with pulmonary diseases. *Eur J Radiol* **134**, 109410, doi:10.1016/j.ejrad.2020.109410 (2021).
- 226 Risse, F., Pesic, J., Young, S. & Olsson, L. E. A texture analysis approach to quantify ventilation changes in hyperpolarised ³He MRI of the rat lung in an asthma model. *NMR in Biomedicine* **25**, 131-141, doi:https://doi.org/10.1002/nbm.1725 (2012).
- 227 Zha, N. *et al.* Second-order Texture Measurements of (³)He Ventilation MRI: Proof-of-concept Evaluation of Asthma Bronchodilator Response. *Acad Radiol* **23**, 176-185, doi:10.1016/j.acra.2015.10.010 (2016).
- 228 Guo, F. *et al.* Development of a pulmonary imaging biomarker pipeline for phenotyping of chronic lung disease. *J Med Imaging (Bellingham)* **5**, 026002, doi:10.1117/1.Jmi.5.2.026002 (2018).
- 229 Westcott, A., Capaldi, D., McCormack, D., Fenster, A. & Parraga, G. Texture analysis of thoracic CT to predict hyperpolarized gas MRI lung function. *Proc SPIE* (2019).
- 230 Rizzo, S. *et al.* Radiomics: the facts and the challenges of image analysis. *Eur Radiol Exp* **2**, 36, doi:10.1186/s41747-018-0068-z (2018).
- 231 Lubner, M. G., Smith, A. D., Sandrasegaran, K., Sahani, D. V. & Pickhardt, P. J. CT Texture Analysis: Definitions, Applications, Biologic Correlates, and Challenges. *Radiographics* **37**, 1483-1503, doi:10.1148/rg.2017170056 (2017).
- 232 Espinasse, M. *et al.* CT Texture Analysis Challenges: Influence of Acquisition and Reconstruction Parameters: A Comprehensive Review. *Diagnostics (Basel)* **10**, doi:10.3390/diagnostics10050258 (2020).
- 233 Lei, M. *et al.* Benchmarking Various Radiomic Toolkit Features While Applying the Image Biomarker Standardization Initiative toward Clinical Translation of Radiomic Analysis. *J Digit Imaging* **34**, 1156-1170, doi:10.1007/s10278-021-00506-6 (2021).
- 234 Tamura, H., Mori, S. & Yamawaki, T. Textural features corresponding to visual perception. *IEEE Transactions on Systems, man, and cybernetics* **8**, 460-473 (1978).
- 235 Liu, F. & Picard, R. W. Periodicity, directionality, and randomness: Wold features for image modeling and retrieval. *IEEE transactions on pattern analysis and machine intelligence* **18**, 722-733 (1996).
- 236 Galloway, M. M. Texture analysis using gray level run lengths. *Computer Graphics and Image Processing* **4**, 172-179, doi:https://doi.org/10.1016/S0146-664X(75)80008-6 (1975).
- 237 Thawani, R. *et al.* Radiomics and radiogenomics in lung cancer: A review for the clinician. *Lung Cancer* **115**, 34-41, doi:https://doi.org/10.1016/j.lungcan.2017.10.015 (2018).
- 238 Kittler, J., Illingworth, J. & Foglein, J. Threshold Selection Based on a Simple Image Statistic. *Comput Vision Graph* **30**, 125-147, doi:Doi 10.1016/0734-189x(85)90093-3 (1985).
- 239 Sahoo, P. K., Soltani, S., Wong, A. K. C. & Chen, Y. C. A Survey of Thresholding Techniques. *Comput Vision Graph* **41**, 233-260, doi:Doi 10.1016/0734-189x(88)90022-9 (1988).
- 240 Pavlidis, T. & Liow, Y. T. Integrating Region Growing and Edge-Detection. *IEEE transactions on pattern analysis and machine intelligence* **12**, 225-233, doi:Doi 10.1109/34.49050 (1990).
- 241 Haralick, R. M. & Shapiro, L. G. Image Segmentation Techniques. *Comput Vision Graph* **29**, 100-132, doi:Doi 10.1016/S0734-189x(85)90153-7 (1985).

- 242 Beucher, S. & Lantuejoul, C. in *Internaitonal workshop on image processing, real-time*
edge and motion detection (France, 1979).
- 243 Coleman, G. B. & Andrews, H. C. Image Segmentation by Clustering. *P Ieee* **67**, 773-785,
doi:Doi 10.1109/Proc.1979.11327 (1979).
- 244 Bezdek, J. C., Ehrlich, R. & Full, W. Fcm - the Fuzzy C-Means Clustering-Algorithm.
Comput Geosci **10**, 191-203, doi:Doi 10.1016/0098-3004(84)90020-7 (1984).
- 245 McInerney, T. & Terzopoulos, D. Deformable models in medical image analysis.
Proceedings of the IEEE Workshop on Mathematical Methods in Biomedical Image
Analysis, 171-180, doi:Doi 10.1109/Mmbia.1996.534069 (1996).
- 246 Sluimer, I., Prokop, M. & van Ginneken, B. Toward automated segmentation of the
pathological lung in CT. *IEEE transactions on medical imaging* **24**, 1025-1038,
doi:10.1109/TMI.2005.851757 (2005).
- 247 Armato, S. G., 3rd & Sensakovic, W. F. Automated lung segmentation for thoracic CT
impact on computer-aided diagnosis. *Acad Radiol* **11**, 1011-1021,
doi:10.1016/j.acra.2004.06.005 (2004).
- 248 Sun, S., Bauer, C. & Beichel, R. Automated 3-D segmentation of lungs with lung cancer
in CT data using a novel robust active shape model approach. *IEEE transactions on*
medical imaging **31**, 449-460, doi:10.1109/TMI.2011.2171357 (2012).
- 249 Ireland, R. H. *et al.* An image acquisition and registration strategy for the fusion of
hyperpolarized helium-3 MRI and x-ray CT images of the lung. *Phys Med Biol* **53**, 6055-
6063, doi:10.1088/0031-9155/53/21/011 (2008).
- 250 Capaldi, D. P. I. *et al.* Free-breathing Pulmonary MR Imaging to Quantify Regional
Ventilation. *Radiology* **287**, 693-704, doi:10.1148/radiol.2018171993 (2018).
- 251 Guo, F. *et al.* Globally optimal co-segmentation of three-dimensional pulmonary (1)H and
hyperpolarized (3)He MRI with spatial consistence prior. *Med Image Anal* **23**, 43-55,
doi:10.1016/j.media.2015.04.001 (2015).
- 252 Heinrich, M. P. *et al.* MIND: modality independent neighbourhood descriptor for multi-
modal deformable registration. *Med Image Anal* **16**, 1423-1435,
doi:10.1016/j.media.2012.05.008 (2012).
- 253 Klein, S., Staring, M., Murphy, K., Viergever, M. A. & Pluim, J. P. elastix: a toolbox for
intensity-based medical image registration. *IEEE Trans Med Imaging* **29**, 196-205,
doi:10.1109/tmi.2009.2035616 (2010).
- 254 Maes, F., Collignon, A., Vandermeulen, D., Marchal, G. & Suetens, P. Multimodality
image registration by maximization of mutual information. *IEEE Trans Med Imaging* **16**,
187-198, doi:10.1109/42.563664 (1997).
- 255 Nanayakkara, N. D. *et al.* Nonrigid registration of three-dimensional ultrasound and
magnetic resonance images of the carotid arteries. *Med Phys* **36**, 373-385,
doi:10.1118/1.3056458 (2009).
- 256 Haralick, R. M., Shanmugam, K. & Dinstein, I. h. Textural Features for Image
Classification. *IEEE Transactions on Systems, Man and Cybernetics* **SMC-3**, 610-621
(1973).
- 257 Tang, X. Texture information in run-length matrices. *IEEE Trans Image Process* **7**, 1602-
1609, doi:10.1109/83.725367 (1998).
- 258 Depeursinge, A., Foncubierta-Rodriguez, A., Van De Ville, D. & Muller, H. Three-
dimensional solid texture analysis in biomedical imaging: review and opportunities.
Medical image analysis **18**, 176-196, doi:10.1016/j.media.2013.10.005 (2014).

- 259 Bettinelli, A. *et al.* A Novel Benchmarking Approach to Assess the Agreement among Radiomic Tools. *Radiology* **303**, 533-541, doi:10.1148/radiol.211604 (2022).
- 260 Zwanenburg, A. *et al.* The Image Biomarker Standardization Initiative: Standardized Quantitative Radiomics for High-Throughput Image-based Phenotyping. *Radiology* **295**, 328-338, doi:10.1148/radiol.2020191145 (2020).
- 261 Gillies, R. J., Kinahan, P. E. & Hricak, H. Radiomics: Images Are More than Pictures, They Are Data. *Radiology* **278**, 563-577, doi:10.1148/radiol.2015151169 (2016).
- 262 Kursa, M. B. & Rudnicki, W. R. Feature Selection with the Boruta Package. *2010* **36**, 13, doi:10.18637/jss.v036.i11 (2010).
- 263 Makimoto, K. *et al.* Comparison of Feature Selection Methods and Machine Learning Classifiers for Predicting Chronic Obstructive Pulmonary Disease Using Texture-Based CT Lung Radiomic Features. *Acad Radiol* **30**, 900-910, doi:10.1016/j.acra.2022.07.016 (2023).
- 264 Erickson, B. J., Korfiatis, P., Akkus, Z. & Kline, T. L. Machine Learning for Medical Imaging. *Radiographics* **37**, 505-515, doi:10.1148/rg.2017160130 (2017).
- 265 Bian, Z. *et al.* Small airway segmentation in thoracic computed tomography scans: a machine learning approach. *Phys Med Biol* **63**, 155024, doi:10.1088/1361-6560/aad2a1 (2018).
- 266 Da-Ano, R. *et al.* Performance comparison of modified ComBat for harmonization of radiomic features for multicenter studies. *Sci Rep* **10**, 10248, doi:10.1038/s41598-020-66110-w (2020).
- 267 Estépar, R. S. J. Artificial intelligence in functional imaging of the lung. *The British Journal of Radiology* **95**, 20210527, doi:10.1259/bjr.20210527 (2022).
- 268 Giger, M. L. Machine Learning in Medical Imaging. *J Am Coll Radiol* **15**, 512-520, doi:10.1016/j.jacr.2017.12.028 (2018).
- 269 Lee, S. M. *et al.* Deep Learning Applications in Chest Radiography and Computed Tomography: Current State of the Art. *J Thorac Imaging* **34**, 75-85, doi:10.1097/RTI.0000000000000387 (2019).
- 270 Westcott, A. *et al.* Chronic Obstructive Pulmonary Disease: Thoracic CT Texture Analysis and Machine Learning to Predict Pulmonary Ventilation. *Radiology* **293**, 676-684, doi:10.1148/radiol.2019190450 (2019).
- 271 Schiwek, M. *et al.* Quantification of pulmonary perfusion abnormalities using DCE-MRI in COPD: comparison with quantitative CT and pulmonary function. *Eur Radiol* **32**, 1879-1890, doi:10.1007/s00330-021-08229-6 (2022).
- 272 Sutton, R. N. & Hall, E. L. Texture Measures for Automatic Classification of Pulmonary-Disease. *Ieee T Comput C* **21**, 667-+, doi:Doi 10.1109/T-C.1972.223572 (1972).
- 273 Chan, H. P. *et al.* Image feature analysis and computer-aided diagnosis in digital radiography. I. Automated detection of microcalcifications in mammography. *Medical physics* **14**, 538-548, doi:10.1118/1.596065 (1987).
- 274 Katsuragawa, S., Doi, K. & MacMahon, H. Image feature analysis and computer-aided diagnosis in digital radiography: detection and characterization of interstitial lung disease in digital chest radiographs. *Medical physics* **15**, 311-319, doi:10.1118/1.596224 (1988).
- 275 Giger, M. L., Doi, K. & MacMahon, H. Image feature analysis and computer-aided diagnosis in digital radiography. 3. Automated detection of nodules in peripheral lung fields. *Medical physics* **15**, 158-166, doi:10.1118/1.596247 (1988).

- 276 Katsuragawa, S., Doi, K. & MacMahon, H. Image feature analysis and computer-aided diagnosis in digital radiography: classification of normal and abnormal lungs with interstitial disease in chest images. *Medical physics* **16**, 38-44, doi:10.1118/1.596412 (1989).
- 277 Nakamori, N., Doi, K., Sabeti, V. & MacMahon, H. Image feature analysis and computer-aided diagnosis in digital radiography: automated analysis of sizes of heart and lung in chest images. *Medical physics* **17**, 342-350, doi:10.1118/1.596513 (1990).
- 278 Katsuragawa, S., Doi, K., Nakamori, N. & MacMahon, H. Image feature analysis and computer-aided diagnosis in digital radiography: effect of digital parameters on the accuracy of computerized analysis of interstitial disease in digital chest radiographs. *Medical physics* **17**, 72-78, doi:10.1118/1.596530 (1990).
- 279 Sanada, S., Doi, K. & MacMahon, H. Image feature analysis and computer-aided diagnosis in digital radiography: automated delineation of posterior ribs in chest images. *Medical physics* **18**, 964-971, doi:10.1118/1.596611 (1991).
- 280 Sanada, S., Doi, K. & MacMahon, H. Image feature analysis and computer-aided diagnosis in digital radiography: automated detection of pneumothorax in chest images. *Medical physics* **19**, 1153-1160, doi:10.1118/1.596790 (1992).
- 281 Bayramoglu, N., Tiulpin, A., Hirvasniemi, J., Nieminen, M. T. & Saarakkala, S. Adaptive Segmentation of Knee Radiographs for Selecting the Optimal ROI in Texture Analysis. *Osteoarthr Cartil*, doi:10.1016/j.joca.2020.03.006 (2020).
- 282 Yip, S. S. *et al.* Use of registration-based contour propagation in texture analysis for esophageal cancer pathologic response prediction. *Phys Med Biol* **61**, 906-922, doi:10.1088/0031-9155/61/2/906 (2016).
- 283 Ash, S. Y. *et al.* Interstitial Features at Chest CT Enhance the Deleterious Effects of Emphysema in the COPD Gene Cohort. *Radiology* **288**, 600-609, doi:10.1148/radiol.2018172688 (2018).
- 284 Yuan, N. F. *et al.* Unsupervised Learning Identifies Computed Tomographic Measurements as Primary Drivers of Progression, Exacerbation, and Mortality in Chronic Obstructive Pulmonary Disease. *Ann Am Thorac Soc* **19**, 1993-2002, doi:10.1513/AnnalsATS.202110-1127OC (2022).
- 285 Hasenstab, K. A. *et al.* Automated CT Staging of Chronic Obstructive Pulmonary Disease Severity for Predicting Disease Progression and Mortality with a Deep Learning Convolutional Neural Network. *Radiol Cardiothorac Imaging* **3**, e200477, doi:10.1148/ryct.2021200477 (2021).
- 286 Armato, S. G., 3rd *et al.* Automated lung nodule classification following automated nodule detection on CT: a serial approach. *Medical physics* **30**, 1188-1197, doi:10.1118/1.1573210 (2003).
- 287 McNitt-Gray, M. F. *et al.* A pattern classification approach to characterizing solitary pulmonary nodules imaged on high resolution CT: preliminary results. *Medical physics* **26**, 880-888, doi:10.1118/1.598603 (1999).
- 288 Han, F. *et al.* Texture feature analysis for computer-aided diagnosis on pulmonary nodules. *Journal of digital imaging* **28**, 99-115, doi:10.1007/s10278-014-9718-8 (2015).
- 289 Dhara, A. K., Mukhopadhyay, S., Dutta, A., Garg, M. & Khandelwal, N. A Combination of Shape and Texture Features for Classification of Pulmonary Nodules in Lung CT Images. *Journal of digital imaging* **29**, 466-475, doi:10.1007/s10278-015-9857-6 (2016).

- 290 Dilger, S. K. *et al.* Improved pulmonary nodule classification utilizing quantitative lung
parenchyma features. *Journal of medical imaging* **2**, 041004,
doi:10.1117/1.JMI.2.4.041004 (2015).
- 291 Beig, N. *et al.* Perinodular and Intranodular Radiomic Features on Lung CT Images
Distinguish Adenocarcinomas from Granulomas. *Radiology* **290**, 783-792,
doi:10.1148/radiol.2018180910 (2019).
- 292 Sluimer, I. C., Prokop, M., Hartmann, I. & van Ginneken, B. Automated classification of
hyperlucency, fibrosis, ground glass, solid, and focal lesions in high-resolution CT of the
lung. *Medical physics* **33**, 2610-2620, doi:10.1118/1.2207131 (2006).
- 293 Korfiatis, P. *et al.* Texture classification-based segmentation of lung affected by interstitial
pneumonia in high-resolution CT. *Medical physics* **35**, 5290-5302, doi:10.1118/1.3003066
(2008).
- 294 Xu, Y., Sonka, M., McLennan, G., Guo, J. & Hoffman, E. A. MDCT-based 3-D texture
classification of emphysema and early smoking related lung pathologies. *IEEE
transactions on medical imaging* **25**, 464-475, doi:10.1109/TMI.2006.870889 (2006).
- 295 Ginsburg, S. B., Lynch, D. A., Bowler, R. P. & Schroeder, J. D. Automated texture-based
quantification of centrilobular nodularity and centrilobular emphysema in chest CT
images. *Acad Radiol* **19**, 1241-1251, doi:10.1016/j.acra.2012.04.020 (2012).
- 296 Yang, J. *et al.* Unsupervised Discovery of Spatially-Informed Lung Texture Patterns for
Pulmonary Emphysema: The MESA COPD Study. *Medical image computing and
computer-assisted intervention : MICCAI ... International Conference on Medical Image
Computing and Computer-Assisted Intervention* **10433**, 116-124, doi:10.1007/978-3-319-
66182-7_14 (2017).
- 297 Chabat, F., Yang, G. Z. & Hansell, D. M. Obstructive lung diseases: texture classification
for differentiation at CT. *Radiology* **228**, 871-877, doi:10.1148/radiol.2283020505 (2003).
- 298 Spurzem, J. R. & Rennard, S. I. Pathogenesis of COPD. *Semin Respir Crit Care Med* **26**,
142-153, doi:10.1055/s-2005-869535 (2005).
- 299 Saam, B. T. *et al.* MR imaging of diffusion of ³He gas in healthy and diseased lungs. *Magn
Reson Med* **44**, 174-179, doi:10.1002/1522-2594(200008)44:2<174::aid-mrm2>3.0.co;2-4
(2000).
- 300 Mathew, L. *et al.* Hyperpolarized ³He magnetic resonance imaging of chronic obstructive
pulmonary disease: reproducibility at 3.0 tesla. *Acad Radiol* **15**, 1298-1311,
doi:10.1016/j.acra.2008.04.019 (2008).
- 301 Kirby, M. *et al.* Hyperpolarized ³He and ¹²⁹Xe magnetic resonance imaging apparent
diffusion coefficients: physiological relevance in older never- and ex-smokers.
Physiological reports **2**, doi:10.14814/phy2.12068 (2014).
- 302 Kirby, M. *et al.* On the role of abnormal DL(CO) in ex-smokers without airflow limitation:
symptoms, exercise capacity and hyperpolarised helium-3 MRI. *Thorax* **68**, 752-759,
doi:10.1136/thoraxjnl-2012-203108 (2013).
- 303 Miravittles, M. *et al.* Difficulties in differential diagnosis of COPD and asthma in primary
care. *The British journal of general practice : the journal of the Royal College of General
Practitioners* **62**, e68-75, doi:10.3399/bjgp12X625111 (2012).
- 304 Murias, J. M. & Zavorsky, G. S. Short-term variability of nitric oxide diffusing capacity
and its components. *Respir Physiol Neurobiol* **157**, 316-325,
doi:10.1016/j.resp.2006.12.008 (2007).

- 305 Desjardin, A., Creveuil, C., Bergot, E. & Normand, H. Assessment of concordance between diffusion of carbon monoxide through the lung using the 10 s breath-hold method, and the simultaneous NO/CO technique, in healthy participants. *Respir Physiol Neurobiol* **273**, 103319, doi:10.1016/j.resp.2019.103319 (2020).
- 306 Diaz, S. *et al.* Validity of apparent diffusion coefficient hyperpolarized ³He-MRI using MSCT and pulmonary function tests as references. *Eur J Radiol* **71**, 257-263, doi:10.1016/j.ejrad.2008.04.013 (2009).
- 307 Lee, P. N. & Fry, J. S. Systematic review of the evidence relating FEV1 decline to giving up smoking. *BMC medicine* **8**, 84, doi:10.1186/1741-7015-8-84 (2010).

CHAPTER 2

2 MACHINE LEARNING AND CT TEXTURE FEATURES IN EX-SMOKERS WITH NO CT EVIDENCE OF EMPHYSEMA AND MILDLY ABNORMAL DIFFUSING CAPACITY

To better understand the structural determinants of abnormal diffusing capacity in ex-smokers without COPD, we evaluated and compared the sensitivity of CT texture features with established clinical measurements at detecting ex-smokers with mildly abnormal gas-exchange process.

The contents of this chapter were previously published in the Academic Radiology journal: M Sharma, M Kirby, DG McCormack and G Parraga. Machine Learning and CT Texture Features in Ex-smokers with no CT Evidence of Emphysema and Mildly Abnormal Diffusing Capacity. Academic Radiology Journal (2023). This article is available under the terms of the Creative Commons CC BY-NC License.

2.1 Introduction

In some ex-smokers without chronic obstructive pulmonary disease (COPD),¹ the diffusing capacity of the lungs for carbon monoxide (DL_{CO}) can be mildly abnormal.² These are clinically challenging patients that typically lack hallmark COPD characteristics such as symptoms, exercise limitations or quality-of-life impairments, and CT evidence of emphysema.² It remains difficult to explain this mildly abnormal DL_{CO} due to the variability and insensitivity of DL_{CO} measurements,³ reliance on technique and calibration,⁴ and the unusual absence of abnormal cardiovascular or pulmonary measurements in these patients.⁵ Furthermore, because these ex-smokers do not meet COPD criteria, they are systematically excluded from clinical studies. Thus, their longitudinal outcomes, disease progression, and the persistence of abnormalities over time remain poorly understood.

Structural lung changes may take place in the very early stages of COPD and remain undetected by spirometry.⁶ Previously, significant exercise and quality-of-life impairments and abnormal terminal airspace enlargement measured using hyperpolarized ³He MRI apparent diffusion

coefficient (ADC)⁷ were reported in ex-smokers with mildly abnormal DL_{CO}.⁸ These abnormally enlarged terminal airspaces, quantified using ³He MRI and not identified using conventional CT measurements, may point to the underlying pathology responsible for mildly abnormal DL_{CO}. However, hyperpolarized gas MRI is not widely available and a high level of expertise and specialized equipment is required.

In contrast, CT imaging is inexpensive and routinely used as a clinical imaging tool in COPD. Expert radiologists typically look beyond the low attenuation areas for more complex signs of emphysema,⁹ resulting in a stronger association between visual qualitative CT scoring and pulmonary function relative to conventional quantitative CT.¹⁰ Nonetheless, CT images consist of electron densities of parenchymal tissue, providing an opportunity to simultaneously quantify the spatial relationships of voxels and their attenuation values (signal intensity).¹¹ However, current quantitative CT methods are time-consuming and do not capture the full spectrum of spatial information available from visual subtyping of emphysema.

A machine-learning and texture analysis approach¹² has a broad range of utility in medical imaging including image segmentation, classification, registration, and outcome prediction.¹³ Previous work in COPD has shown that CT texture analysis and machine-learning can predict severe COPD exacerbations,¹⁴ progression,¹⁵ Global Initiative for Obstructive Lung Disease (GOLD) grade,¹⁶ and are more strongly associated with lung function than conventional quantitative CT measures.¹⁷

We questioned whether CT texture analysis may help identify patterns that are indicative of mildly abnormal airspace enlargement and diffusing capacity in ex-smokers without conventional spirometry or CT evidence of COPD. Hence, we hypothesized that CT texture analysis and machine-learning models would accurately differentiate ex-smokers with normal from abnormal DL_{CO} (<75%_{pred}). We also aimed to determine whether CT texture features and generated principal

components would outperform established quantitative CT and clinical variables at detecting ex-smokers with abnormal diffusing capacity.

2.2 Methods

2.2.1 Participants

All participants provided written informed consent to a local research ethics board (Institutional Ethics Board #00000984) approved and registered protocol in compliance with Health Canada (clinicaltrials.gov NCT02279329). The Thoracic Imaging Network of Canada (TINCan) study was compliant with the Personal Information Protection and Electronic Documents Act (PIPEDA, Canada) and the Health Insurance Portability and Accountability Act (HIPAA, USA). This study was prospectively planned and performed between 2009 and 2022, and ex-smoker participants were recruited from a tertiary-care academic center and by advertisement in London, Ontario, Canada. We retrospectively evaluated 71 ex-smokers without COPD at baseline, all of whom were 50-85 years of age and had a history of cigarette smoking ≥ 10 pack-years. Ex-smokers were included who ceased smoking ≥ 1 year prior to the study visit, with no maximum cut-off for pack-years. Participants with claustrophobia, COPD according to the GOLD severity criteria,¹ any contraindications for MRI or CT, and current smokers were excluded from this analysis. All evaluations were performed 20 minutes after administering Novo-Salbutamol HFA using a metered dose inhaler (four doses of 100 μg , Teva Novopharm Ltd., Toronto, ON, Canada) through a spacer device (AeroChamber Plus spacer, Trudell Medical International, London, ON, Canada). Participants evaluated in the TINCan study cohort have been previously reported.^{2,18,19}

2.2.2 Pulmonary function tests and questionnaires

Spirometry, plethysmography, and measurement of DL_{CO} were performed according to the American Thoracic Society/European Respiratory Society guidelines²⁰ using a whole-body plethysmography system (MedGraphics Corporation, St Paul, MN, USA) with an attached gas analyzer.² The six-minute walk distance (6MWD) test and St. George's respiratory questionnaire (SGRQ)²¹ were administered under the supervision of study personnel. Participants were dichotomized based on DL_{CO} $\geq 75\%$ _{pred} threshold into normal and abnormal subgroups, as previously defined.^{2,22}

2.2.3 CT acquisition and analysis

Thoracic CT scans were acquired using a 64-slice Lightspeed VCT scanner (GE Healthcare, Milwaukee, WI, USA) (64 \times 0.625 mm, 120 kVp, 100 effective mA, tube rotation time = 500 ms, pitch = 1.0, slice thickness = 1.25 mm, slices = 200-250), as previously described.²³ Images were acquired in the supine position under breath-hold after inhalation of a 1.0 L bag of N₂ from functional residual capacity,¹⁹ for volume-matching to MRI. CT images were reconstructed using a standard convolution kernel to 1.25 mm. Using the ImPACT CT patient dosimetry calculator (based on Health Protection Agency [UK] NRBP-SR250), the total effective dose was estimated as 1.8 mSv. CT data were quantitatively evaluated by a single expert (MS) using VIDAvision software (VIDA Diagnostics Inc., Coralville, IA, USA) to generate relative area of lung less than -950 Hounsfield Units (RA₉₅₀), 15th percentile of the CT density histogram (HU15th Perc), total lung cavity volume, and binary lung mask.

2.2.4 MRI acquisition and analysis

Anatomical proton (^1H) and hyperpolarized ^3He MR images were acquired using a whole-body 3.0 T Discovery MR750 (GE Healthcare, Milwaukee, WI, USA), a whole-body radiofrequency coil and a fast gradient recalled echo (FGRE) sequence with a partial echo implementation (total acquisition time = 16 seconds, repetition time (TR)/echo time (TE)/flip angle = 4.7 ms/1.2 ms/30°, field of view (FOV) = $40 \times 40 \text{ cm}^2$, matrix 256×128 , 14 slices, 15 mm slice thickness, 0 gap), as previously described.¹⁹ Hyperpolarized ^3He MRI was acquired using a linear bird-cage transmit/receive chest coil (RAPID Biomedical GmbH, Wuerzburg, Germany) and a 2D multi-section FGRE sequence (partial echo acquisition; total acquisition time = 11 seconds, TR/TE/flip angle = 3.8 ms/1.0 ms/7°, FOV = $40 \times 40 \text{ cm}^2$, bandwidth = 48.8 kHz; 128×80 matrix, zero padded to 128×128 , partial echo percentage = 62.5%, 15–17 slices, slice thickness = 15 mm, no gap). A turn-key system (HeliSpin™, Polarean Inc, Durham, NC, USA) was used to polarize ^3He gas to 30–40% and doses (5 mL/kg body weight) diluted with N_2 were administered in 1.0 L Tedlar® bags. Hyperpolarized ^3He MRI diffusion-weighted imaging was performed using a 2D multi-slice FGRE (total acquisition time = 14 seconds, TR/TE/flip angle = 7.6 ms/3.7 ms/8°, FOV = $40 \times 40 \text{ cm}^2$, matrix 128×128 , seven slices, 30 mm slice thickness), as previously described,¹⁹ during breath-hold for acquisition of two interleaved images with and without additional diffusion sensitization with $b = 1.6 \text{ sec/cm}^2$ (maximum gradient amplitude [G] = 1.94 G/cm, rise and fall time = 0.5 ms, gradient duration = 0.46 ms, diffusion time = 1.46 ms).

Participants were positioned supine in the MR scanner, and arterial oxygen saturation (SaO_2) was used to monitor arterial blood oxygenation levels during all MRI maneuvers. MR images were analyzed by co-registering the anatomic ^1H and functional ^3He images using a landmark-based registration and a k-means clustering approach was used to generate ventilation clusters, with the

lowest cluster representing ventilation defects, as previously described.¹⁹ Diffusion-weighted images were automatically processed to generate lung ADC images, as previously described.²

2.2.5 CT feature extraction, selection and machine-learning

The complete image analysis and extraction pipeline are depicted in **Figure 2-2**. Briefly, CT images were segmented using VIDAvision (VIDA Diagnostics Inc., Coralville, IA, USA) to obtain the total cavity volume and generate regions of interest (ROI) for feature extraction. Wavelet filtering was used to pre-process the CT images, using four high- and low-pass filter combinations applied to the original image in x - and y -directions for wavelet decomposition.²⁴ Low-pass filtering in both directions (LL) assesses the lowest frequencies, low-pass filtering followed by high-pass filtering (LH) assesses horizontal edges, high-pass filtering followed by low-pass filtering (HL) assesses vertical edges, and high-pass filtering in both (HH) assesses diagonal details. Next, we computed histogram and shape, first-order, and higher-order texture features from gray level run-length, tone-difference, size-zone, neighborhood-dependence, and co-occurrence matrices from the original and pre-processed images using the open-sourced PyRadiomics package (version 2.2.0), compliant with the Image Biomarker Standardization Initiative (IBSI) recommendations.²⁵ All CT images were normalized and a fixed bin number approach was used for voxel intensity quantization into 100 bins (PyRadiomics suggested resulting amount of bins between 30 and 130 after discretization step), as previously described.^{12,26} Gray-level matrices were populated by binning CT data between -300 and -1024 HU, where all voxels with values greater than -300 HU or less than -1024 HU were collapsed into a single bin. All 486 texture features were extracted in a voxel-by-voxel manner using PyRadiomics in Python 3.6.5 environment (Numpy 1.17.4, SimpleITK 1.2.4, PyWavelet 1.0.0).¹²

To maximize the model generalizability and avoid overfitting, a combination of principal component analysis (PCA) and Boruta analysis was implemented for feature selection. PCA is capable of generating principal component scores for each participant using a Varimax rotation method with Kaiser-normalization with multiple iterations. All variables, including the texture features and emergent components generated for every participant, were subjected to Boruta analysis for ranking. Boruta algorithm generated shadow features for comparisons and used a two-step correction for multiple testing, with an optimizable Random Forest classifier for iterations.²⁷ Once all the features and parameters were selected, five-fold cross-validation was performed where all the data were randomly and evenly divided into five groups. Each fold utilizes different combinations of testing and training groups and no information was carried over from training to testing. Single (Naïve Bayes,²⁸ Support Vector Machines,²⁹ Decision Trees,³⁰ K-Nearest Neighbours³⁰) and ensemble (Bagged Trees,³¹ subspace Discriminant,³² subspace K-Nearest Neighbours,³² and Random Under-Sampling Boosted (RUSBoosted) Trees³³) machine-learning classifiers were implemented for dichotomizing ex-smokers with abnormal lung diffusion ($DL_{CO} < 75\%_{pred}$). Machine-learning models were generated using the top-ranking features, selected via Boruta analysis, and also compared with alternative classification models trained exclusively using the emergent component scores from PCA. The data were standardized and a hyperparameter search was performed using MATLAB2021a (Classification Learner App) for each model.

2.2.6 Statistical analysis

Statistical analysis was performed using SPSS Statistics v28.0 (SPSS Inc., Chicago, IL, USA) and GraphPad Prism (Prism v8; La Jolla, CA, USA). The performance of machine-learning models was evaluated using mean cross-validation area under the receiver-operator curve (AUC), sensitivity, specificity, and F1 measure calculated from model's confusion matrix. Shapiro-Wilk

tests were used to determine the normality of the data and non-parametric tests were performed for non-normally distributed data. The p-value significance was determined using the Mann-Whitney U-test for non-parametric data, followed by post-hoc analysis using Holm-Bonferonni corrections. All results were considered statistically significant when the probability of making a Type I error was less than 5% ($p < 0.05$).

2.3 Results

A CONSORT diagram provided in **Figure 2-1** shows that 266 ex-smokers were enrolled and 94 were excluded from analysis due to enrollment in another sub-study ($n = 33$) or due to cancellation or not completing all required tests per protocol ($n = 61$). In addition, 101 participants were excluded following their visit for having COPD ($n = 100$) or having artifacts in acquired images ($n = 1$).

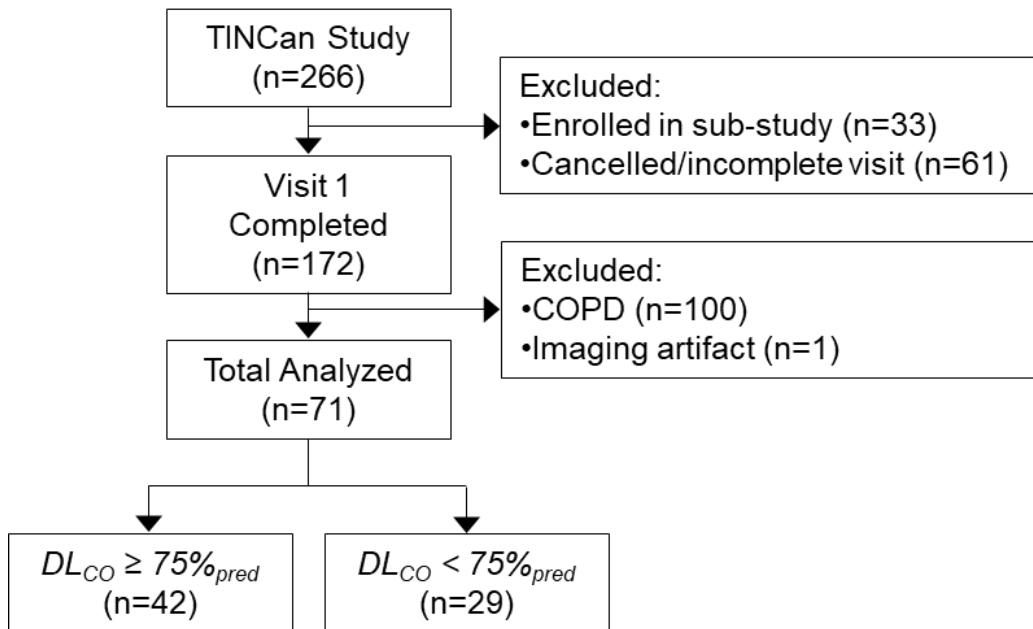


Figure 2-1. CONSORT Flow Diagram

Of the 266 participants enrolled in the TINCan study, 33 were enrolled in a sub-study and 61 either cancelled or did not complete all required tests during Visit 1. Of the 172 participants that completed Visit 1, 100 participants had COPD and one had artifacts present in their images, which were excluded from further analysis. Seventy one ex-smoker participants with Visit 1 were analyzed in this study, of which 42 had $DL_{CO} \geq 75\%_{pred}$ and 29 had $DL_{CO} < 75\%_{pred}$.

2.3.1 Demographics, pulmonary function and imaging measurements

Demographic data and pulmonary function test results for all ex-smokers, and for DL_{CO} subgroups, are provided in **Table 2-1**. Baseline participant demographics and pulmonary function measurements. Imaging measurements are summarized in **Table 2-2**. Imaging measurements of ex-smokers with normal and mildly abnormal DLCO. There were 42 ex-smokers (14 females/28 males, 69 ± 10 years) with normal (DL_{CO} ≥ 75%_{pred}) and 29 ex-smokers (17 females/12 males, 71 ± 9 years) with abnormal DL_{CO} (DL_{CO} < 75%_{pred}). As summarized in **Table 2-1**. Baseline participant demographics and pulmonary function measurements, ex-smokers with DL_{CO} ≥ 75%_{pred} were mostly male (67 % vs 42 %, p = .03), had lesser residual volume to total lung capacity (RV/TLC) ratio (p = .003), SGRQ score (p = .03), MRI ADC (p < 0.001), and greater 6MWD (p < 0.001) compared to those with DL_{CO} < 75%_{pred}. The RV/TLC ratio in five participants from each group (5/42 [12%] vs 5/29 [17%]) was reported RV/TLC > upper limit of normal,³⁴ indicative of plethysmography-based air-trapping. None of the 71 participants had emphysema as defined by RA₉₅₀ > 6.8%.³⁵

Table 2-1. Baseline participant demographics and pulmonary function measurements

Parameter	All Ex-smokers (n=71)	DL _{CO} ≥ 75% _{pred} (n=42)	DL _{CO} < 75% _{pred} (n=29)	p-value
Mean (±SD)				
Age	69 (10)	68 (10)	71 (9)	.2
Female n(%)	31 (43)	14 (33)	17 (58)	.03*
Pack Years	28 (18)	24 (17)	31 (19)	.09
BMI kg/m ²	29 (4)	29 (4)	29 (5)	.3
<i>Pulmonary function and QoL</i>				
FEV ₁ % _{pred}	99 (18)	101 (17)	95 (19)	.1
FVC % _{pred}	92 (17)	94 (15)	87 (20)	.08
FEV ₁ /FVC %	82 (8)	81 (6)	83 (10)	.4
RV % _{pred}	110 (25)	108 (25)	114 (24)	.3
TLC % _{pred}	103 (14)	103 (13)	102 (15)	.8
RV/TLC %	42 (9)	39 (9)	45 (7)	.007*
DL _{CO} % _{pred}	78 (20)	91 (12)	58 (12)	ND
6MWD m	402 (91)	437 (67)	361 (98)	<.001*
SGRQ	24 (22)	19 (20)	31 (22)	.02*

BMI=body mass index; QoL=quality-of-life; FEV₁=forced expiratory volume in 1 second; %_{pred}=percent of predicted value; FVC=forced vital capacity; RV=residual volume; TLC=total

lung capacity; DL_{CO}=diffusing capacity of lung for carbon-monoxide; 6MWD=six minute walk distance; SGRQ=St. George's respiratory questionnaire.

p=uncorrected values showing significant differences between DL_{CO}≥75%_{pred} and DL_{CO}<75%_{pred} groups.

*Indicates a significant difference (p<0.05) between subgroups.

Table 2-2. Imaging measurements of ex-smokers with normal and mildly abnormal DL_{CO}

Parameter Mean (±SD)	All Ex-smokers (n=71)	DL _{CO} ≥75% _{pred} Ex-smokers (n=42)	DL _{CO} <75% _{pred} Ex-smokers (n=29)	p-value
RA ₉₅₀ %	1.2 (1.0)	1.2 (1.1)	1.1 (1.0)	.7
LAC	-2.1 (0.2)	-2.1 (0.2)	-2.0 (0.3)	.1
HU15 th Perc	-888 (22)	-888 (21)	-887 (23)	.8
MRI ADC cm ² /s	0.28 (0.04)	0.26 (0.03)	0.30 (0.03)	<.001*
MRI VDP %	7 (5)	6 (3)	9 (7)	.07
<i>Selected Texture Features</i>				
Shape-M2DDC	290 (31)	297 (34)	279 (22)	.01*
Shape-M3DD	409 (36)	418 (32)	395 (37)	.008*
GLCM-Correlation	.69 (.03)	.68 (.03)	.70 (.03)	.048*
<i>Wavelet-filtered</i>				
HL-FO-Energy	6.5×10 ⁹ (1.3×10 ⁹)	6.7×10 ⁹ (1.3×10 ⁹)	6.3×10 ⁹ (1.5×10 ⁹)	.03*
LL-GLCM-Imc2	.898 (.014)	.895 (.014)	.901 (.013)	.04*
HH-FO-Range	878 (66)	851 (41)	901 (71)	.002*
HH-RLM-HGLRE	2.1×10 ⁵ (.3×10 ⁵)	2.1×10 ⁵ (.2×10 ⁵)	2.3×10 ⁵ (.3×10 ⁵)	.03*

RA₉₅₀=relative area of lung less than -950 Hounsfield Units; LAC=lowest attenuating cluster; HU15th Perc.=15th percentile of the CT density histogram; ADC=apparent diffusion coefficient; VDP=ventilation defect percent; FO=first order features; M2DDC=maximum 2D diameter column; M3DD=maximum 3D diameter; RLM=run length matrix; Imc2=informational measure of correlation; HH=high-high-pass filter; HL=high-low-pass filter; LL=low-low-pass filter; HGLRE=high gray level run emphasis; GLCM=gray level co-occurrence matrix; All texture feature abbreviations and descriptions can be found in Supplementary **Table 2-4** and **Table 2-5**.

P Value=uncorrected values showing significant differences between DL_{CO}≥75%_{pred} and DL_{CO}<75%_{pred} groups.

*Indicates a significant difference (p<0.05) between groups.

2.3.2 Texture feature extraction and selection

Figure 2-2 summarizes the CT texture analysis workflow and supplementary **Table 2-4** and **Table**

2-5 summarize the resulting extracted texture features and their descriptions. **Table 2-2** shows the

subset of seven selected texture features, while supplementary **Table 2-6** summarizes features that

were significantly different between DL_{CO} subgroups. Overall, there were significant differences

observed using seven unfiltered features and 19 wavelet-based texture features extracted from CT

scans, as summarized in supplementary **Table 2-7**.

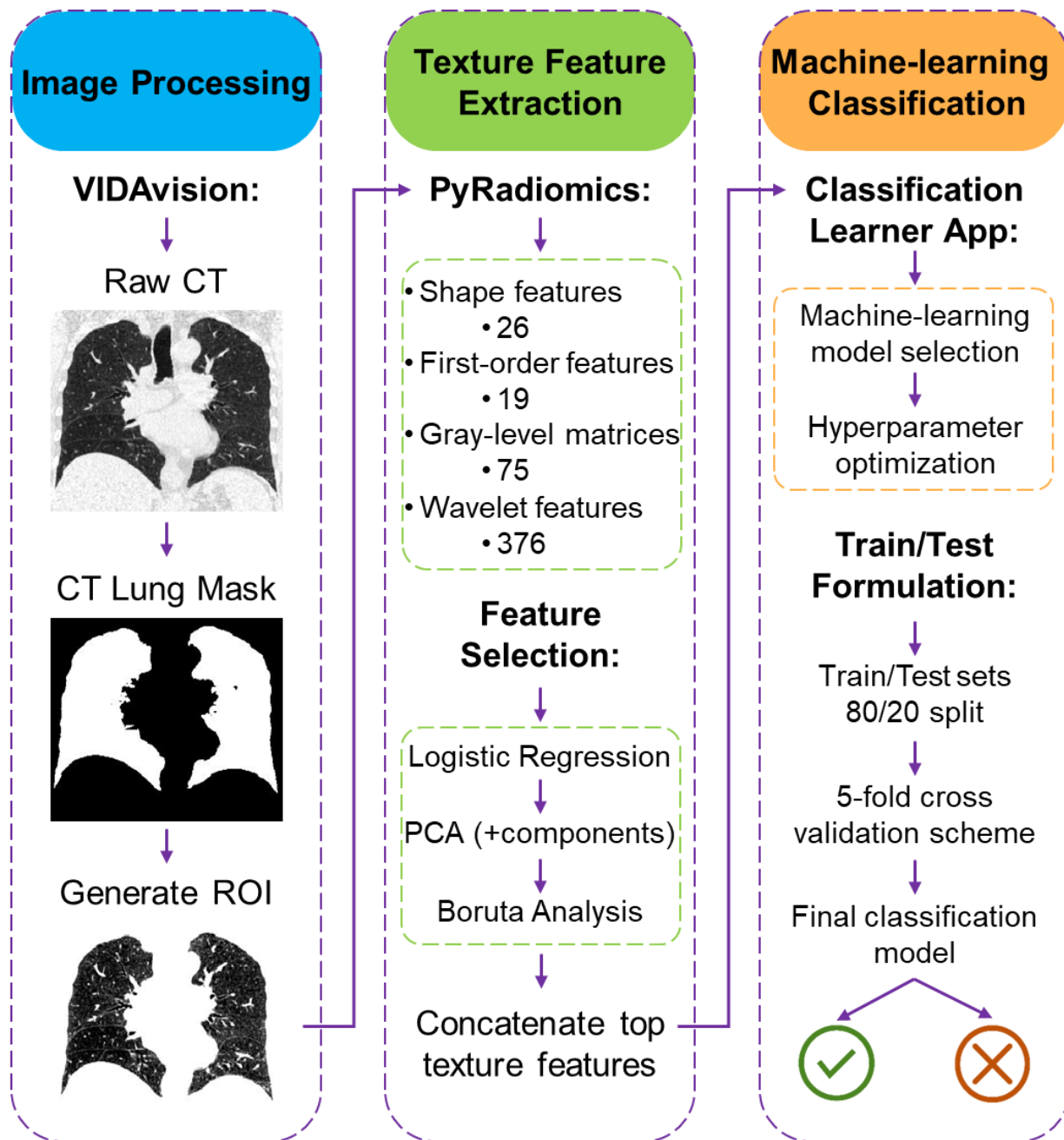


Figure 2-2. Image Processing and Model Generation Pipeline

Thoracic CT images were segmented using commercial software VIDAvision. Raw CT images were multiplied by generated lung mask to obtain regions of interest (ROI), which were analyzed using PyRadiomics platform to calculate first- and higher-order texture features. Feature selection

was performed using the training set, combined with principle component analysis (PCA) and Boruta analysis. Classification learner application was used for model generation. Machine-learning models were trained using a 5-fold cross validation scheme, with 80/20 split for training and testing sets.

Figure 2-3 shows the central slices of diffusion-weighted MRI ADC and CT, along with the corresponding ROI texture homogeneity description, for two representative ex-smokers in each DL_{CO} subgroup. In ex-smokers with normal DL_{CO} (top panel: S53 and S98), there was no CT evidence of emphysema (RA₉₅₀ < 6.8%)³⁵ and the CT texture was visually homogeneous (eg: HH-HGLRE = 192505). In contrast, for ex-smokers with abnormal DL_{CO} (bottom panel: S50 and S72), MRI ADC was abnormal (ADC > 0.25 cm²/s)^{36,37} and there was no CT evidence of emphysema (RA₉₅₀ < 6.8%)³⁵ but CT textures appeared more heterogeneous and visually patchy (eg: HH-HGLRE = 235711).

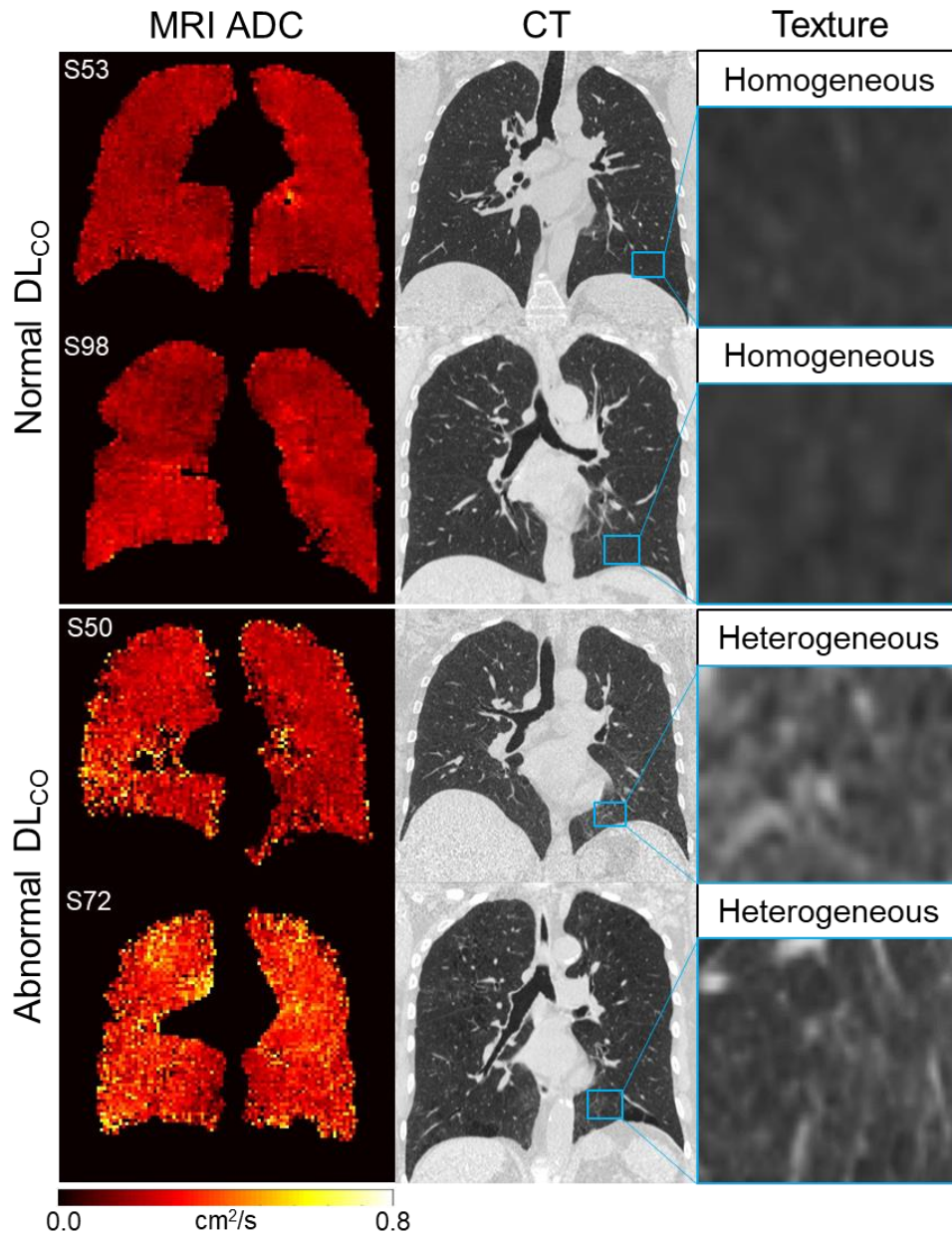


Figure 2-3. Diffusion weighted MRI ADC and CT imaging for representative ex-smokers in normal and abnormal DL_{co} subgroups

Coronal center-slice of ³He MRI ADC, volume-matched coronal center-slice of high-resolution CT imaging and the corresponding qualitative CT texture.

S53: Ex-smoker with normal DL_{co} is a 51 year old female with baseline FEV₁=103%_{pred}, BMI=35kg/m², DL_{co}=86%_{pred}, VDP=3.6%, ADC=0.21cm²/s, RA₉₅₀=0.7%, wavelet-HH-HGLRE=212228, wavelet-HH-FO-Range=834.; S98: Ex-smoker with normal DL_{co} is a 70 year old female with baseline FEV₁=93%_{pred}, BMI=27kg/m², DL_{co}=90%_{pred}, VDP=1.9%, ADC=0.23cm²/s, RA₉₅₀=0.7%, wavelet-HH-HGLRE=192505, wavelet-HH-FO-Range=801.

S50: Ex-smoker with abnormal DL_{co} is a 64 year old female with baseline FEV₁=111%_{pred}, BMI=36kg/m², DL_{co}=60%_{pred}, VDP=4.6%, ADC=0.29cm²/s, RA₉₅₀=1.2%, wavelet-HH-HGLRE=256863, wavelet-HH-FO-Range=914.; S72: Ex-smoker with abnormal DL_{co} is a 76 year old female with baseline FEV₁=116%_{pred}, BMI=26kg/m², DL_{co}=30%_{pred}, VDP=10.3%, ADC=0.36cm²/s, RA₉₅₀=3.5%, wavelet-HH-HGLRE=235711, wavelet-HH-FO-Range=949.

PCA and Boruta analysis were used for dimensionality reduction and feature selection. The first nine components generated from PCA explained >93% of variance in the data, with their constituent texture features and factor loadings summarized in supplementary **Table 2-8**. Boruta analysis (number of trees in the forest =150, maximum iterations =200, maximum tree depth =7 [branches], percentage of shadow feature threshold =95%, alpha =0.05) selected the following texture features and components as input for the models: Shape-based maximum 2D diameter column (M2DDC), Shape-based maximum 3D diameter (M3DD), gray level co-occurrence matrix (GLCM) Correlation, LL GLCM Informational measure of correlation (Imc2), HH gray level run length matrix (GLRLM) high gray level run emphasis (HGLRE), HL first-order energy, HH first-order range and component #9 from PCA. Clinical measurements and CT measurements such as RA₉₅₀, LAC, and HU15th Perc were not selected as they did not rank among the top performing features.

2.3.3 Machine-learning classification

As shown in **Table 2-3**, the best performance was achieved by a logistic regression mixed-model with 87.3% accuracy, AUC of 0.87, 83% sensitivity, 91% specificity and 86% F1 score, calculated from the model's confusion matrix. Overall, linear and single classifiers outperformed ensemble-based models at classifying abnormal diffusing capacity compared to ground-truth. In **Figure 2-4**, independent logistic regression models of abnormal DL_{CO} are shown in receiver operator characteristic (ROC) curves that individually compare the classification power of single clinical (top panel), imaging and textural measurements (bottom panel). The best performing textural feature was wavelet-based HH GLRLM HGLRE (AUC =0.81), while the best imaging measurement was MRI ADC (AUC =0.73), outperforming established CT measures such as RA₉₅₀ (AUC =0.54).

Table 2-3. Machine-learning model classification accuracies

Classifiers	AUC (95% CI)	Sens. (%)	Spec. (%)	F1-score (%)	Acc. (%)
Decision Tree	0.55 (0.50, 0.59)	31	79	57	60
Logistic Regression*	0.87 (0.84, 0.89)	83	91	85	87
Subspace KNN	0.81 (0.78, 0.84)	62	86	75	79
Weighted KNN	0.76 (0.72, 0.80)	66	83	74	77
Linear SVM	0.84 (0.81, 0.87)	76	88	81	82
Quadratic SVM	0.73 (0.68, 0.77)	55	81	67	70
Naïve Bayes	0.71 (0.65, 0.76)	66	69	65	67
Bagged Trees	0.73 (0.67, 0.80)	81	72	71	76
Subspace Discriminant	0.81 (0.78, 0.83)	66	88	77	78
RUSBoosted Trees	0.69 (0.59, 0.77)	55	67	59	62

AUC=area under the receiver-operating curve; CI=confidence interval; Sens.=sensitivity; Spec.=specificity; Acc.=accuracy; KNN=K-nearest neighbours; SVM=support vector machine; RUS=random under sampling.

Selected features used for training the models included: shape-maximum 2D diameter column, shape-maximum 3D diameter, gray level co-occurrence matrix (GLCM)-correlation, high-low-first-order-energy, low-low-GLCM-informational measure of correlation (Imc2), high-high-first-order-range, high-high-gray level run length matrix-high gray level run emphasis (HGLRE) and component #9.

*Indicates the best performing classification model.

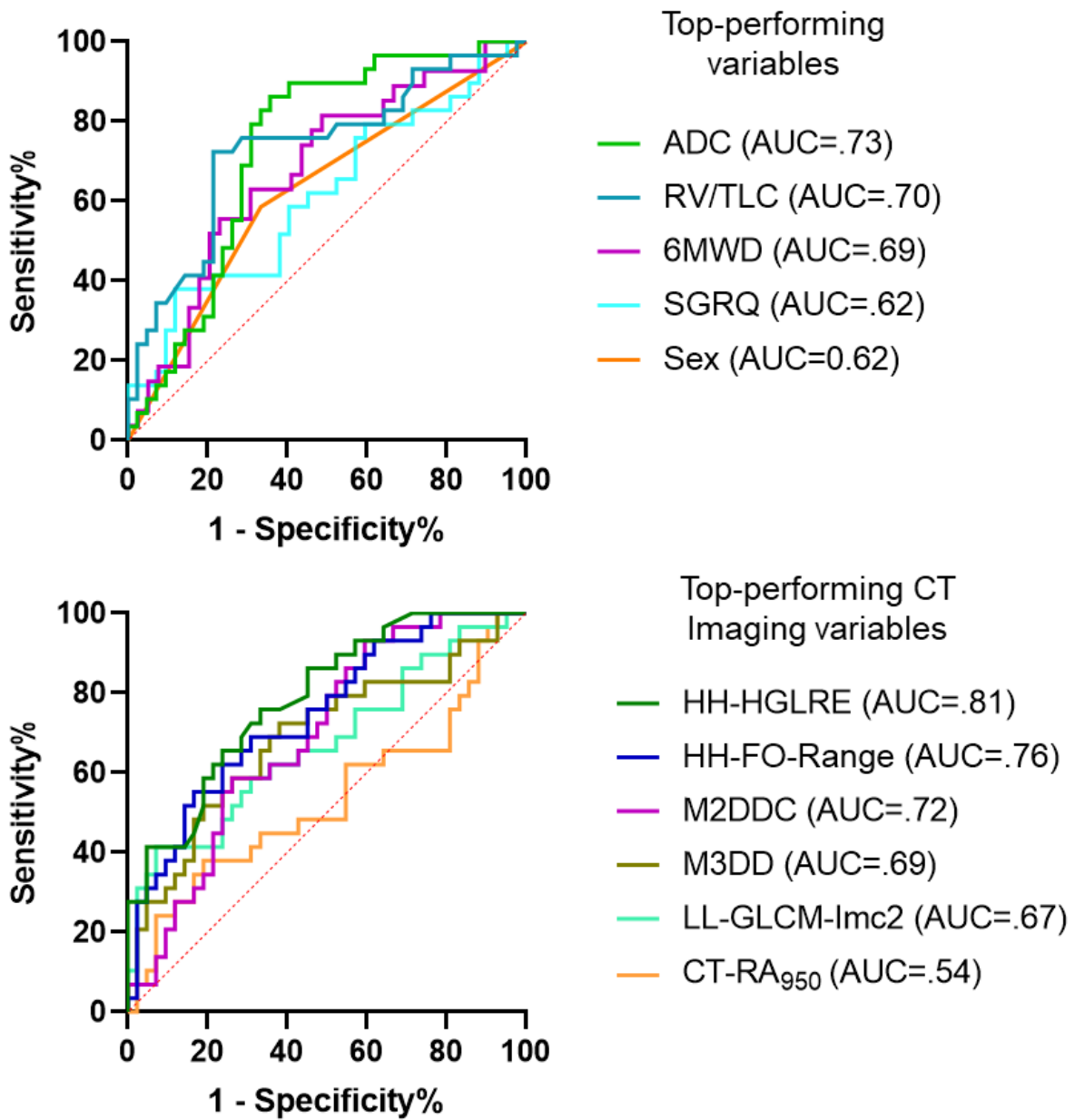


Figure 2-4. Receiver-operator characteristic curves of texture features and clinical variables

Top Panel: Logistic regression analysis of individual top-performing clinical and/or imaging variables at classifying abnormal DL_{CO} observed in ex-smoker participants.

Bottom Panel: Logistic regression of selected top-performing CT imaging and texture features at classifying abnormal DL_{CO}. Individual texture features clearly outperformed conventional variables available to physicians at classifying ex-smokers with abnormal DL_{CO}.

HH=high-high pass filter; *LL*=low-low pass filter; *HGLRE*=high gray level run emphasis; *FO*=first-order; *M2DDC*=maximum 2D diameter column; *M3DDD*=maximum 3D diameter; *GLCM*=gray level co-occurrence matrix; *Imc2*=informational measure of correlation.

An alternative classification model was generated exclusively using the emergent component scores from PCA (**Table 2-8**) for training the models, with results summarized in supplementary **Table 2-9**. Training data were used from selected components #1, #2, #4, #6 and #9 exclusively. Similarly to the previous approach, the best performance was achieved by logistic regression mixed-model with 76% accuracy, with the greatest AUC =0.73 and specificity =78%.

2.3.4 Relationships

Spearman correlations of two top-ranking representative texture features with DL_{CO}, 6MWD, MRI ADC, TLC, RV/TLC, FEV₁, SGRQ and RA₉₅₀ are shown in **Figure 2-5**, with a complete summary of correlations with selected texture features in supplementary **Table 2-10**. The best performing wavelet-based texture feature HH GLRLM HGLRE significantly correlated with 6MWD ($\rho = -.25$, $p = .02$), DL_{CO} ($\rho = -.29$, $p = .02$), and MRI ADC ($\rho = .23$, $p = .048$), while an original CT texture feature shape-based M3DD correlated with TLC ($\rho = .75$, $p = .001$), RV/TLC ($\rho = -.49$, $p = .001$), DL_{CO} ($\rho = .39$, $p = .001$), FEV₁ %_{pred} ($\rho = .31$, $p = .009$), SGRQ score ($\rho = -.26$, $p = .04$), and RA₉₅₀ ($\rho = .24$, $p = .04$). Overall, DL_{CO} was significantly correlated ($p < .05$) with all the selected texture features, and showed the strongest correlations with M3DD ($\rho = .39$, $p = .001$), and diffusion weighted MRI ADC ($\rho = -.44$, $p = .009$), as well as with 6MWD ($\rho = .47$, $p = .001$).

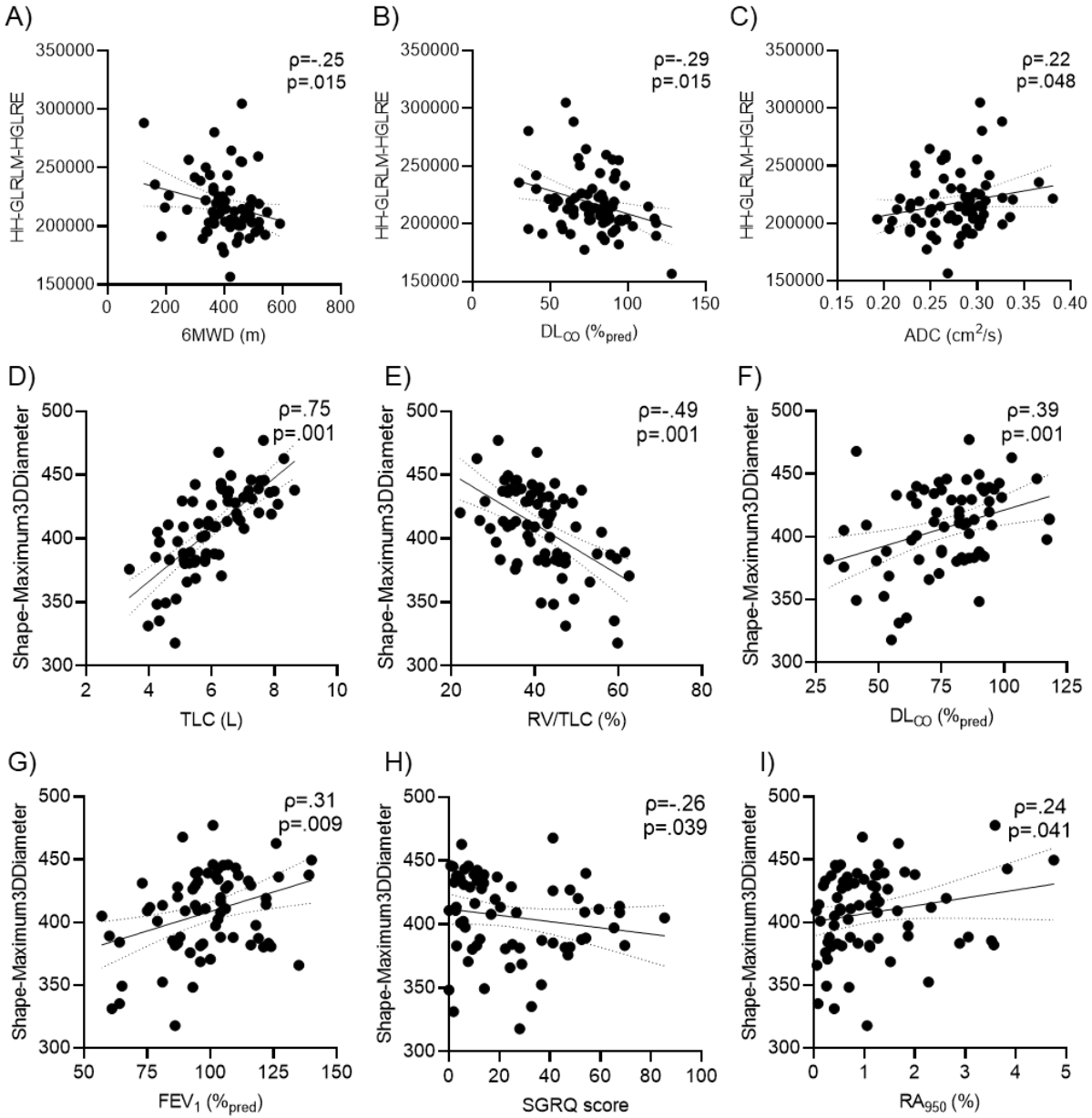


Figure 2-5. Relationships between selected texture features and clinical measurements

Top Panel: A) Spearman correlation for HH-GLRLM-HGLRE with 6MWD ($\rho = -.25$, $p = .02$); B) and with DL_{CO} %pred ($\rho = -.29$, $p = .02$); C) and with MRI-ADC ($\rho = .22$, $p < .05$).

Middle Panel: D) Spearman correlation for Shape-Maximum 3D diameter with TLC ($\rho = .75$, $p = .001$); E) and with RV/TLC ($\rho = -.49$, $p = .001$); F) and with DL_{CO} %pred ($\rho = .39$, $p = .001$).

Bottom Panel: G) Spearman correlation for Shape-Maximum 3D diameter with FEV_1 %predicted ($\rho = .31$, $p = .009$); H) and with SGRQ score ($\rho = -.26$, $p = .04$); I) and with CT- RA_{950} ($\rho = .24$, $p = .04$).

GLCM=gray level co-occurrence matrix; 6MWD=six minute walk distance; ADC=apparent diffusion coefficients; DL_{CO} =diffusing capacity of the lung for carbon monoxide; GLRLM=gray level run length matrix; HGLRE=high gray level run emphasis; TLC=total lung capacity; RV=residual volume; FEV_1 =forced expiratory volume in 1 second; SGRQ=St. George's respiratory questionnaire; RA_{950} = relative area of lung less than -950 Hounsfield Units.

2.4 Discussion

It has been shown that asymptomatic ex-smokers with mildly abnormal DL_{CO} values are at a significantly increased risk of developing COPD within four years.²² In addition, DL_{CO} strongly predicted all-cause mortality in participants with COPD, independent of BODE index and CT measurements.³⁸ Despite this evidence, DL_{CO} is not currently part of the GOLD criteria and cannot be directly inferred from CT. Here, we developed a CT texture analysis pipeline using machine-learning to reveal a subset of CT tissue patterns that could help classify ex-smokers with abnormal DL_{CO} , despite clinically-normal CT and spirometry. We observed that a logistic regression mixed-model trained solely on seven CT texture features outperformed all other models at detecting ex-smokers with abnormal DL_{CO} (87% accuracy). Overall, single machine-learning classifiers outperformed ensemble-based classifiers, consistent with previous findings in COPD,³⁹ indicating the existence of straightforward linear structure-function relationships between CT textures and diffusing capacity. Our findings suggest that texture-based features provide additional information about early structural changes occurring in the lungs, which may be used alongside conventional CT measurements to identify ex-smokers at-risk of developing COPD.

In agreement with machine-learning output, individual AUC-ROC values indicated that selected texture features outperformed standard clinical and quantitative imaging variables available to physicians at detecting ex-smokers with abnormal diffusing capacity. Furthermore, conventional CT measurements such as RA_{950} (AUC =0.54), were outperformed by CT texture features (best performing feature AUC =0.81). Previous studies reported abnormally elevated 3He ADC in asymptomatic ex-smokers without spirometry or CT evidence of COPD.² In prior work, 3He ADC correlated with DL_{CO} , whilst CT RA_{950} did not.^{5,7} Taken together, these findings suggested that elevated 3He ADC may reflect mild emphysema not detected by CT or DL_{CO} . Because of these

previous and compelling results, we included ^3He ADC as a comparator with CT textures. In the current study, ^3He ADC was the strongest (AUC =0.73) individual non-radiomics parameter for differentiating ex-smokers with normal versus abnormal DL_{CO} . However, the relationship between DL_{CO} and other structural and functional markers remains poorly understood. The selected texture features measure the homogeneity and complexity of CT image texture, and were also correlated with established clinical measurements. Together, these results suggest that these features provide unique and clinically-relevant information that could identify ex-smokers with abnormal DL_{CO} , at-risk of progressing to COPD.

Selected texture features M2DDC and M3DD extracted from original unfiltered CT images were related to lung sizes and volumes, as well as CT emphysema, plethysmography-based air-trapping, diffusing capacity, and airflow obstruction. Wavelet-based feature HH GLRLM HGLRE uniquely correlated with DL_{CO} ($\rho = -0.29$, $p = 0.02$) and ADC ($\rho = 0.22$, $p = 0.048$), suggesting that this texture may be related to mild emphysematous disease. In addition, wavelet-based HH-FO-Range was significantly related to plethysmography air-trapping ($\rho = 0.24$, $p = 0.01$), which were both represented in PCA component #9, suggesting that this feature may provide unique information related to mild air-trapping. This also aligns with previous work showing that CT textures predict progression to COPD,¹⁵ and the size and arrangement of emphysematous clusters can differentiate patients even with similar COPD GOLD grade.⁴⁰

We also note that high-pass filtering (HH) generated the highest number of unique texture feature differences, indicating the benefits of pre-processing and assessment of the highest frequencies and diagonal signal variances in the sharpened images. However, the filtered CT images have altered tissue attenuation values, which may not accurately represent patient's lung pathophysiology, and significantly impacts texture feature interpretability and clinical relevance.

In addition, our sub-analysis showed that combining texture features via dimensionality reduction techniques such as PCA may not be beneficial for this specific task. The emphysematous clusters and heterogeneity detected using CT texture features provide additional evidence beyond simple binary CT emphysema or air-trapping measurements. However, individual texture features may not fully capture the heterogeneity present in COPD, hence machine-learning algorithms are instrumental for integrating multiple aspects of the early disease state detected using texture analysis tools. In addition, previous work showed that picking an optimal combination of feature selection and machine-learning algorithms is paramount for accurate radiomics-based predictions in COPD.³⁹

We were surprised to observe significant differences between DL_{CO} subgroups for RV/TLC ratio. Furthermore, 12% of participants with normal DL_{CO} and 17% of participants in the abnormal DL_{CO} subgroup had plethysmography-based air-trapping (RV/TLC>ULN).³⁴ While abnormal ADC in ex-smokers and patients with COPD has largely been attributed to emphysematous destruction,⁴¹ previous work in asthma has demonstrated that abnormal ADC is likely caused by air-trapping.⁴² It has also been shown that air-trapping may aid in early diagnosis of small airways disease,⁴³ and COPD typically starts with the small airways and precedes emphysematous parenchymal destruction.⁴⁴ Worse 6MWD, SGRQ and MRI ADC in ex-smokers with abnormal DL_{CO} are consistent with previous work,² which further underscores the importance of considering air-trapping measurements in relation to the observed ADC abnormalities. The high sensitivity of ADC measurements⁴⁵ also suggests that abnormally enlarged terminal airspaces may be due to mild air-trapping, emphysema, or their combination,⁷ perhaps pointing towards the underlying pathology responsible for mildly abnormal DL_{CO} in this subgroup.

We acknowledge several study limitations. First, our study included a relatively small sample size in comparison to COPD studies such as Genetic Epidemiology of COPD (COPDGene),⁴⁶ Subpopulations and intermediate outcome measures in COPD study (SPIROMICS),⁴⁷ and Evaluation of COPD Longitudinally to Identify Predictive Surrogate End-points (ECLIPSE).⁴⁸ However, we employed statistical techniques to prevent overfitting (5-fold cross-validation, PCA, Boruta Analysis, etc.) and our machine-learning algorithms may be generalized using larger datasets and multicenter data. Second, expiratory CT was not available and we did not make small airways disease measurements, thus we are unable to comment on whether small airway abnormalities have already initiated in these ex-smokers without COPD. Third, CT and MRI were both acquired at the same inspiratory lung volume, however, quantitative measurements are influenced by lung volumes.⁴⁹ Future studies may address this variability via inclusion of standardized features normalized to total lung volume. Fourth, other feature selection methods, such as hybrid feature selection and deep-learning approaches, were not evaluated in this study, although these are less efficient in terms of computational cost and time. Finally, CT images were acquired using the same scanner and protocol, which may lead to weaker generalizability when considering data from other scanners and/or sites.

Until now, it has been impossible to measure mild airspace enlargements using only conventional CT lung tissue attenuation values, and to accurately detect ex-smokers that have an abnormal DL_{CO} by quantifying visually unapparent CT textures. This difficult-to-detect group of at-risk ex-smokers,⁵⁰ with both unrecognized mild emphysema and air-trapping, may be quantifiable through CT tissue-density heterogeneity features alone. This work may bridge the gap between CT and MRI modalities and provide a way to automatically generate sensitive, quantitative measurements of mild parenchymal abnormalities beyond specialized hyperpolarized gas MRI centers. CT

texture measurements provide a way to reveal CT lung pathologies that are not visible to the human eye and may help detect ex-smokers at-risk of developing COPD. This method may also provide subclinical phenotypes responsible for abnormal DL_{CO} in asymptomatic ex-smokers, adding unique clinical information to CT modality for early detection and aggressive intervention for this at-risk group. This is important because quantitative CT is more universally available for clinical measurements and may help explain such at-risk patients in whom typical CT measurements do not help.

2.5 References

- 1 Vestbo, J. *et al.* Global strategy for the diagnosis, management, and prevention of chronic obstructive pulmonary disease: GOLD executive summary. *Am J Respir Crit Care Med* **187**, 347-365, doi:10.1164/rccm.201204-0596PP (2013).
- 2 Kirby, M. *et al.* On the role of abnormal DL(CO) in ex-smokers without airflow limitation: symptoms, exercise capacity and hyperpolarised helium-3 MRI. *Thorax* **68**, 752-759, doi:10.1136/thoraxjnl-2012-203108 (2013).
- 3 Murias, J. M. & Zavorsky, G. S. Short-term variability of nitric oxide diffusing capacity and its components. *Respir Physiol Neurobiol* **157**, 316-325, doi:10.1016/j.resp.2006.12.008 (2007).
- 4 Macintyre, N. *et al.* Standardisation of the single-breath determination of carbon monoxide uptake in the lung. *Eur Respir J* **26**, 720-735, doi:10.1183/09031936.05.00034905 (2005).
- 5 Diaz, S. *et al.* Validity of apparent diffusion coefficient hyperpolarized ³He-MRI using MSCT and pulmonary function tests as references. *Eur J Radiol* **71**, 257-263, doi:10.1016/j.ejrad.2008.04.013 (2009).
- 6 Casanova, C. *et al.* The progression of chronic obstructive pulmonary disease is heterogeneous: the experience of the BODE cohort. *Am J Respir Crit Care Med* **184**, 1015-1021, doi:10.1164/rccm.201105-0831OC (2011).
- 7 Fain, S. B. *et al.* Early emphysematous changes in asymptomatic smokers: detection with ³He MR imaging. *Radiology*. **239**, 875-883 (2006).
- 8 Yablonskiy, D. A., Sukstanskii, A. L. & Quirk, J. D. Diffusion lung imaging with hyperpolarized gas MRI. *NMR in biomedicine* **30**, 10.1002/nbm.3448, doi:10.1002/nbm.3448 (2017).
- 9 Gietema, H. A. *et al.* Quantifying the extent of emphysema: factors associated with radiologists' estimations and quantitative indices of emphysema severity using the ECLIPSE cohort. *Acad Radiol* **18**, 661-671, doi:10.1016/j.acra.2011.01.011 (2011).
- 10 Lynch, D. A. *et al.* CT-based Visual Classification of Emphysema: Association with Mortality in the COPDGene Study. *Radiology* **288**, 859-866, doi:10.1148/radiol.2018172294 (2018).
- 11 Lubner, M. G., Smith, A. D., Sandrasegaran, K., Sahani, D. V. & Pickhardt, P. J. CT Texture Analysis: Definitions, Applications, Biologic Correlates, and Challenges. *Radiographics* **37**, 1483-1503, doi:10.1148/rg.2017170056 (2017).
- 12 van Griethuysen, J. J. M. *et al.* Computational Radiomics System to Decode the Radiographic Phenotype. *Cancer Research* **77**, e104-e107, doi:10.1158/0008-5472.can-17-0339 (2017).
- 13 Thawani, R. *et al.* Radiomics and radiogenomics in lung cancer: A review for the clinician. *Lung Cancer* **115**, 34-41, doi:<https://doi.org/10.1016/j.lungcan.2017.10.015> (2018).
- 14 Hoffman, E. A. *et al.* in *C5. C005 DIAGNOSIS AND PROGNOSIS IN COPD* A1122-A1122.
- 15 Makimoto, K., Hogg, J. C., Bourbeau, J., Tan, W. C. & Kirby, M. CT Imaging With Machine Learning for Predicting Progression to COPD in Individuals at Risk. *Chest*, doi:<https://doi.org/10.1016/j.chest.2023.06.008> (2023).
- 16 Li, Z. *et al.* A Novel CT-Based Radiomics Features Analysis for Identification and Severity Staging of COPD. *Acad Radiol* **29**, 663-673, doi:10.1016/j.acra.2022.01.004 (2022).

- 17 Sørensen, L. *et al.* Chronic Obstructive Pulmonary Disease Quantification Using CT Texture Analysis and Densitometry: Results From the Danish Lung Cancer Screening Trial. *AJR Am J Roentgenol* **214**, 1269-1279, doi:10.2214/ajr.19.22300 (2020).
- 18 Kirby, M. *et al.* Chronic obstructive pulmonary disease: longitudinal hyperpolarized (3)He MR imaging. *Radiology* **256**, 280-289, doi:10.1148/radiol.10091937 (2010).
- 19 Kirby, M. *et al.* Longitudinal Computed Tomography and Magnetic Resonance Imaging of COPD: Thoracic Imaging Network of Canada (TINCan) Study Objectives. *Chronic Obstr Pulm Dis* **1**, 200-211, doi:10.15326/jcopdf.1.2.2014.0136 (2014).
- 20 Miller, M. R. *et al.* Standardisation of spirometry. *Eur Respir J* **26**, 319-338, doi:10.1183/09031936.05.00034805 (2005).
- 21 Jones, P. W., Quirk, F. H., Baveystock, C. M. & Littlejohns, P. A self-complete measure of health status for chronic airflow limitation. The St. George's Respiratory Questionnaire. *Am Rev Respir Dis* **145**, 1321-1327, doi:10.1164/ajrccm/145.6.1321 (1992).
- 22 Harvey, B. G. *et al.* Risk of COPD with obstruction in active smokers with normal spirometry and reduced diffusion capacity. *Eur Respir J* **46**, 1589-1597, doi:10.1183/13993003.02377-2014 (2015).
- 23 Kirby, M. *et al.* Hyperpolarized 3He and 129Xe MR imaging in healthy volunteers and patients with chronic obstructive pulmonary disease. *Radiology* **265**, 600-610, doi:10.1148/radiol.12120485 (2012).
- 24 Rastegar, S. *et al.* Radiomics for classification of bone mineral loss: A machine learning study. *Diagnostic and interventional imaging*, doi:10.1016/j.diii.2020.01.008 (2020).
- 25 Zwanenburg, A. *et al.* The Image Biomarker Standardization Initiative: Standardized Quantitative Radiomics for High-Throughput Image-based Phenotyping. *Radiology* **295**, 328-338, doi:10.1148/radiol.2020191145 (2020).
- 26 Hoebel, K. V. *et al.* Radiomics Repeatability Pitfalls in a Scan-Rescan MRI Study of Glioblastoma. *Radiol Artif Intell* **3**, e190199, doi:10.1148/ryai.2020190199 (2021).
- 27 Kursa, M. B. & Rudnicki, W. R. Feature Selection with the Boruta Package. *2010* **36**, 13, doi:10.18637/jss.v036.i11 (2010).
- 28 Webb, G. I. in *Encyclopedia of Machine Learning* (eds Claude Sammut & Geoffrey I. Webb) 713-714 (Springer US, 2010).
- 29 Cristianini, N. & Ricci, E. in *Encyclopedia of Algorithms* (ed Ming-Yang Kao) 928-932 (Springer US, 2008).
- 30 Quinlan, J. R. Induction of decision trees. *Mach Learn* **1**, 81-106 (1986).
- 31 Breiman, L. Bagging predictors. *Mach Learn* **24**, 123-140 (1996).
- 32 Hastie, T. & Tibshirani, R. in *Proceedings of the 8th International Conference on Neural Information Processing Systems* 409-415 (MIT Press, Denver, Colorado, 1995).
- 33 Seiffert, C., Khoshgoftaar, T. M., Hulse, J. V. & Napolitano, A. RUSBoost: A Hybrid Approach to Alleviating Class Imbalance. *IEEE Trans Syst Man Cybern Syst* **40**, 185-197, doi:10.1109/TSMCA.2009.2029559 (2010).
- 34 Quanjer, P. H. *et al.* Lung volumes and forced ventilatory flows. *Eur Respir J* **6 Suppl 16**, 5-40, doi:10.1183/09041950.005s1693 (1993).
- 35 Lynch, D. A. *et al.* CT-Definable Subtypes of Chronic Obstructive Pulmonary Disease: A Statement of the Fleischner Society. *Radiology* **277**, 192-205, doi:10.1148/radiol.2015141579 (2015).

- 36 Bink, A. *et al.* Clinical aspects of the apparent diffusion coefficient in ³He MRI: Results in healthy volunteers and patients after lung transplantation. *Journal of Magnetic Resonance Imaging* **25**, 1152-1158, doi:<https://doi.org/10.1002/jmri.20933> (2007).
- 37 Sukstanskii, A. L. & Yablonskiy, D. A. In vivo lung morphometry with hyperpolarized ³He diffusion MRI: Theoretical background. *Journal of Magnetic Resonance* **190**, 200-210, doi:<https://doi.org/10.1016/j.jmr.2007.10.015> (2008).
- 38 Balasubramanian, A. *et al.* Diffusing Capacity and Mortality in Chronic Obstructive Pulmonary Disease. *Annals of the American Thoracic Society* **20**, 38-46, doi:10.1513/AnnalsATS.202203-226OC (2023).
- 39 Makimoto, K. *et al.* Comparison of Feature Selection Methods and Machine Learning Classifiers for Predicting Chronic Obstructive Pulmonary Disease Using Texture-Based CT Lung Radiomic Features. *Acad Radiol* **30**, 900-910, doi:10.1016/j.acra.2022.07.016 (2023).
- 40 Virdee, S. *et al.* Spatial Dependence of CT Emphysema in Chronic Obstructive Pulmonary Disease Quantified by Using Join-Count Statistics. *Radiology* **301**, 702-709, doi:10.1148/radiol.2021210198 (2021).
- 41 Fain, S. B. *et al.* Early emphysematous changes in asymptomatic smokers: detection with ³He MR imaging. *Radiology* **239**, 875-883, doi:10.1148/radiol.2393050111 (2006).
- 42 Wang, C. *et al.* Assessment of the lung microstructure in patients with asthma using hyperpolarized ³He diffusion MRI at two time scales: comparison with healthy subjects and patients with COPD. *J Magn Reson Imaging* **28**, 80-88, doi:10.1002/jmri.21408 (2008).
- 43 Stern, E. J. & Frank, M. S. Small-airway diseases of the lungs: findings at expiratory CT. *AJR Am J Roentgenol* **163**, 37-41, doi:10.2214/ajr.163.1.8010242 (1994).
- 44 McDonough, J. E. *et al.* Small-airway obstruction and emphysema in chronic obstructive pulmonary disease. *N Engl J Med* **365**, 1567-1575, doi:10.1056/NEJMoal106955 (2011).
- 45 Woods, J. C. *et al.* Hyperpolarized ³He diffusion MRI and histology in pulmonary emphysema. *Magn Reson Med*. **56**, 1293-1300 (2006).
- 46 Regan, E. A. *et al.* Genetic epidemiology of COPD (COPDGene) study design. *COPD* **7**, 32-43, doi:10.3109/15412550903499522 (2010).
- 47 Couper, D. *et al.* Design of the Subpopulations and Intermediate Outcomes in COPD Study (SPIROMICS). *Thorax* **69**, 491-494, doi:10.1136/thoraxjnl-2013-203897 (2014).
- 48 Vestbo, J. *et al.* Evaluation of COPD Longitudinally to Identify Predictive Surrogate End-points (ECLIPSE). *Eur Respir J* **31**, 869-873, doi:10.1183/09031936.00111707 (2008).
- 49 Madani, A., Van Muylem, A. & Gevenois, P. A. Pulmonary emphysema: effect of lung volume on objective quantification at thin-section CT. *Radiology* **257**, 260-268, doi:10.1148/radiol.10091446 (2010).
- 50 Ni, Y., Yu, Y., Dai, R. & Shi, G. Diffusing capacity in chronic obstructive pulmonary disease assessment: A meta-analysis. *Chron Respir Dis* **18**, 14799731211056340, doi:10.1177/14799731211056340 (2021).

2.6 Supplemental Material

2.6.1 Supplementary Tables

Table 2-4. Texture analysis matrices and CT features extracted from each participant

Category	Level/Order	Description	Texture Features
Intensity histogram (n=19)	First-order	Distribution of pixel or voxel intensities within the image ROI defined by the mask	Energy, Total energy, Entropy, Minimum, Maximum, 10 th , 90 th percentile, Mean, Median, Interquartile range, range, MAD, rMAD, RMS, SD, Skewness, Kurtosis, Variance, Uniformity
Shape-based (n=26)	First-order	2D and 3D size and shape features of the ROI; independent of the pixel or voxel gray level intensity distribution	Mesh volume, Mesh surface, Pixel surface, Perimeter, Perimeter to surface, Surface to volume, Voxel volume, Surface area, SAV, sphericity, Compactness, Spherical disproportion, M2DD, M3DD, M2DDS, M2DDC, M2DDR, Elongation, Flatness, Minor, Major, and Least axis length
GLRLM (n=16)	Second-order	Quantifies consecutive pixels or voxels of the same gray level in a given direction	SRE, LRE, GLN, GLNN, RLN, RLNN, RP, GLV, RV, RE, LGLRE, HGLRE, SRLGLE, SRHGLE, LRLGLE, LRHGLE
GLCM (n=24)	Second-order	Examines the spatial relationship among pixels and defines how frequently pairs of pixels are present in an image in a given direction	Autocorrelation, Joint average, Cluster prominence, Cluster shade, Cluster tendency, Contrast, Correlation, Difference average, Difference entropy, Difference variance, Joint energy, Joint entropy, IMC1, IMC2, IDM, MCC, IDMN, ID, IDN, Inverse variance, Maximum probability, SA, SE, SS
GLSZM (n=16)	Second-order	Quantifies the number of homogeneous connected voxels that share the same gray level intensity in an image	SAE, LAE, GLN, GLNN, SZN, SZNN, ZP, GLV, ZV, ZE, LGLZE, HGLZE, SALGLE, SAHGLE, LALGLE, LAHGLE
NGTDM (n=5)	Second-order	Quantifies the difference between a gray value and the average gray value of its neighbours within a specific distance and direction	Coarseness, Contrast, Busyness, Complexity, Strength
GLDM (n=14)	Second-order	Quantifies the number of connected voxels within a specific distance that are dependent on the center voxel in the ROI of an image	SDE, LDE, GLN, GLNN, DN, DNN, GLV, DV, DE, LGLE, HGLE, SDLGLE, SDHGLE, LDLGLE, LDHGLE
Wavelet-based (n=376)	Higher-order	Applies combinations of high-pass and low-pass wavelet filters to the input image axes to yield the space-frequency decompositions	Four high/low-pass filter combinations applied across the image; Excluding the 16 Shape-based features: $4 \times (19 + 16 + 24 + 16 + 5 + 14) = 376$

n=number of unique extracted texture features; GLRLM=Gray-level Run Length Matrix; GLCM=Gray-level Co-occurrence Matrix; GLSZM= Gray-level Size-zone Matrix; NGTDM= Neighbourhood Gray Tone Difference Matrix; GLDM=Gray-level Dependence Matrix; MAD=Mean Absolute Deviation; rMAD=Robust MAD; RMS=Root Mean Squared; SD=Standard deviation; SAV=Surface area to volume ratio; M3DD=Maximum 3D diameter; M2DDS=Maximum 2D diameter Slice; M2DDC=M2DD Column; M2DDR=M2DD Row; SRE=Short Run Emphasis; LRE=Long Run Emphasis; GLN=Gray Level Non-Uniformity; GLNN=GLN Normalized; RLN=Run Length Non-Uniformity; RLNN=RLN Normalized; RP=Run Percentage; GLV=Gray Level Variance; RV=Run Variance; RE=Run Entropy; LGLRE=Low Gray Level Run Emphasis; HGLRE=High Gray Level Run Emphasis; SRLGLE=Short Run Low Gray Level Emphasis; SRHGLE=Short Run High Gray Level Emphasis; LRLGLE=Long Run Low Gray Level Emphasis; LRHGLE=Long Run High Gray Level Emphasis; IMC=Informational Measure of Correlation; IDM=Inverse Difference Moment; MCC=Maximal Correlation Coefficient; IDMN=IDM Normalized; ID=Inverse Difference; IDN=ID Normalized; SA=Sum Average; SE=Sum Entropy; SS=Sum of Squares; SAE=Small Area Emphasis; LAE=Large Area Emphasis; SZN=Size-Zone Non-Uniformity; SZNN=SZN Normalized; ZP=Zone Percentage; ZV=Zone Variance; ZE=Zone Entropy; LGLZE=Low Gray Level Zone Emphasis; HGLZE=High Gray Level Zone Emphasis; SALGLE=Small Area Low Gray Level Emphasis; SAHGLE=Small Area High Gray Level Emphasis; LALGLE=Large Area Low Gray Level Emphasis; LAHGLE=Large Area High Gray Level Emphasis; SDE=Small Dependence Emphasis; LDE=Large Dependence Emphasis; DN=Dependence Non-Uniformity; DNN=DN Normalized; DV=Dependence Variance; DE=Dependence Entropy; LGLE=Low Gray Level Emphasis; HGLE=High Gray Level Emphasis; SDLGLE=Small Dependence Low Gray Level Emphasis; SDHGLE=Small Dependence High Gray Level Emphasis; LGLGLE=Large Dependence Low Gray Level Emphasis; LDHGLE=Large Dependence High Gray Level Emphasis.

Table 2-5. CT texture feature descriptors for machine-learning modelling

<i>Texture Feature Name</i>	<i>Description</i>
FO-M2DDC	Measures the maximum 2D diameter (Column) defined as the largest pairwise Euclidean distance between ROI surface mesh vertices in the row-slice (coronal) plane
FO-M3DD	Measures the maximum 3D diameter defined as the largest pairwise Euclidean distance between ROI surface mesh vertices. Also known as the Feret Diameter
GLCM-Correlation	Measures the linear dependency of gray level values to their respective voxels in the GLCM
HH-RLM-HGLRE	Measures the distribution of the higher gray-level values, with a higher value indicating a greater concentration of high gray-level values in the image
HH-FO-Range	Measures the distribution of ranges of gray values in the given image region of interest (ROI)
HL-FO-Energy	Measures the magnitude of voxel values in an image and the uniformity of the distribution. Reaches its maximum for a ROI with only one grey level intensity
LL-GLCM-Imc2	Measures the correlation between the probability of grey level distributions between different extraction directions

FO=first order features; GLCM=gray level co-occurrence matrix; Idn=inverse difference normalized; LL=low-low-pass filter; HH=high-high-pass filter; RLM=run length matrix; Imc1=informational measure of correlation; GLDM=gray level dependence matrix; DV=dependence variance.

Table 2-6. Extracted texture feature differences between DL_{CO} subgroups

Parameter	All Ex-smokers (n=71)	DL _{CO} ≥75% _{pred} Ex-smokers (n=42)	DL _{CO} <75% _{pred} Ex-smokers (n=29)	<i>p</i> - value	<i>p</i> -** value
Shape-M2DDC	290 (31)	297 (34)	279 (22)	.01*	.07
Shape-M3DD	409 (36)	418 (32)	395 (37)	.008*	.04*
RLM-LRE	1.071 (.009)	1.081 (.009)	1.057 (.008)	.03*	.06
RLM-Run Percentage	.975 (.003)	.979 (.003)	.971 (.002)	.04*	.1
GLCM-Imc2	.76 (.04)	.73 (.03)	.68 (.04)	.02*	.05
GLCM-Correlation	.69 (.03)	.68 (.03)	.70 (.03)	.048*	.3
GLSZM-ZP	.955 (.007)	.958 (.006)	.951 (.004)	.04*	.05
Wavelet-based Features					
<i>First-Order</i>					
HH-Maximum	410 (44)	393 (33)	420 (42)	.001*	.004*
HH-Minimum	-461 (35)	-455 (24)	-476 (34)	.04*	.07
HH-Range	878 (66)	851 (41)	901 (71)	.002*	.006*
LL-Minimum	-277 (16)	-274 (14)	-283 (16)	.03*	.06
<i>GLRLM</i>					
HH-HGLRE	2.1×10 ⁵ (.3×10 ⁵)	2.1×10 ⁵ (.2×10 ⁵)	2.3×10 ⁵ (.3×10 ⁵)	.03*	.048*
HH-LRHGLE	2.2×10 ⁵ (.3×10 ⁵)	2.2×10 ⁵ (.2×10 ⁵)	2.3×10 ⁵ (.3×10 ⁵)	.047*	.1
HH-SRHGLE	2.1×10 ⁵ (.3×10 ⁵)	2.1×10 ⁵ (.2×10 ⁵)	2.2×10 ⁵ (.3×10 ⁵)	.04*	.07
<i>GLCM</i>					
HH-AC	2.2×10 ⁵ (.3×10 ⁵)	2.1×10 ⁵ (.2×10 ⁵)	2.3×10 ⁵ (.3×10 ⁵)	.04*	.3
HH-SA	927 (66)	918 (43)	948 (67)	.04*	.3
HH-JA	463 (33)	459 (21)	474 (33)	.04*	.3
HH-Imc2	.43 (.03)	.42 (.02)	.44 (.02)	.04*	.3
HH-Idm	.043 (.008)	.044 (.008)	.051 (.009)	.04*	.3
HL-Imc2	.56 (.03)	.56 (.02)	.58 (.03)	.049*	.4
HL-Energy	6.5×10 ⁹ (1.3×10 ⁹)	6.7×10 ⁹ (1.3×10 ⁹)	6.3×10 ⁹ (1.5×10 ⁹)	.03*	.2
LL-Imc2	.898 (.014)	.895 (.014)	.901 (.013)	.04*	.3
<i>GLSZM</i>					
HH-HGLZE	2.2×10 ⁵ (.3×10 ⁵)	2.1×10 ⁵ (.2×10 ⁵)	2.2×10 ⁵ (.3×10 ⁵)	.04*	.08
HH-SAHGLE	2.1×10 ⁵ (.3×10 ⁵)	2.0×10 ⁵ (.2×10 ⁵)	2.2×10 ⁵ (.3×10 ⁵)	.04*	.08
<i>GLDM</i>					
HH-HGLE	2.2×10 ⁵ (.3×10 ⁵)	2.1×10 ⁵ (.2×10 ⁵)	2.3×10 ⁵ (.3×10 ⁵)	.04*	.08
HH-SDHGLE	2.0×10 ⁵ (.3×10 ⁵)	2.0×10 ⁵ (.2×10 ⁵)	2.1×10 ⁵ (.3×10 ⁵)	.048*	.08

FO=first order features; M2DDC=maximum 2D diameter column; M3DD=maximum 3D diameter; RLM=run length matrix; LRE=long run emphasis; Imc2=informational measure of correlation; ZP=zone percentage; HH=high-high-pass filter; HL=high-low-pass filter; LL=low-low-pass filter; HGLRE=high gray level run emphasis; LRHGLE=long run high gray level emphasis; SRHGLE=short run high gray level emphasis; GLCM=gray level co-occurrence matrix; AC=autocorrelation; SA=sum average; JA=joint average; Idm=inverse difference moment; SZM=size-zone matrix; HGLZE=high gray level zone emphasis; SAHGLE=small area high gray level emphasis; GLDM=gray level dependence matrix; HGLE=high gray level emphasis; SDHGLE=small dependence high gray level emphasis; All texture feature abbreviations and descriptions can be found in Table 2-5.

P Value=uncorrected values showing significant differences between DL_{CO}≥75%_{pred} and DL_{CO}<75%_{pred} groups.

*Indicates a significant difference (p<0.05) between groups

*P*** Value=Holm-Bonferroni corrected values showing significant differences between DL_{CO}≥75%_{pred} and DL_{CO}<75%_{pred} groups.

Table 2-7. Distribution of significant texture features based on extraction method and matrices

Matrix Name	Unique Features	Significant features	LH-filter features	HL-filter features	HH-filter features	LL-filter features
First Order	19	0	0	0	3	1
Shape-based	26	2	0	0	0	0
GLCM	24	2	0	2	5	1
GLRLM	16	2	0	0	3	0
GLSZM	16	1	0	0	3	0
NGTDM	5	0	0	0	0	0
GLDM	14	0	0	0	3	0
TOTAL COUNT	120	7	0	2	15	2

GLCM=Gray Level Co-occurrence Matrix; GLRLM=Gray Level Run Length Matrix; GLSZM=Gray Level Size-Zone Matrix; NGTDM=Neighboring Gray Tone Difference Matrix; GLDM=Gray Level Dependence Matrix; Significance level is given by $p < 0.05$.

Table 2-8. Top PCA components from orthogonally rotated correlation matrix

Texture Features	Component								
	1	2	3	4	5	6	7	8	9
Idm	0.990	0.014	-0.005	-0.075	0.051	0.068	0.036	0.000	0.045
LL-SZNU	-0.989	0.027	0.023	0.054	-0.040	-0.064	-0.014	0.029	-0.055
M3DDC	0.984	-0.061	-0.022	0.008	-0.041	-0.010	0.069	-0.040	-0.028
LL-SAE	0.983	-0.062	-0.021	0.008	-0.042	-0.011	0.069	-0.041	-0.028
BMI	0.643	-0.311	0.174	0.252	-0.160	0.045	-0.163	-0.060	-0.272
LL-LDLGLE	-0.004	0.953	0.088	0.186	0.003	0.127	0.029	-0.002	-0.105
RunVariance	0.002	0.952	0.195	0.128	0.054	0.140	-0.047	-0.007	0.032
JointEnergy	-0.003	0.949	0.179	0.095	0.088	0.109	-0.050	0.064	0.100
LAE	-0.119	0.945	0.160	0.167	0.020	0.141	-0.025	-0.015	-0.082
ZoneVariance	-0.113	0.945	0.161	0.169	0.019	0.142	-0.026	-0.016	-0.085
HH-DNU	-0.015	0.107	0.977	0.121	-0.114	0.028	0.004	0.002	-0.020
HH-SZNU	-0.046	0.116	0.974	0.124	-0.118	0.023	0.006	0.000	-0.021
DNU	-0.093	0.086	0.969	0.137	-0.144	0.003	0.008	-0.009	-0.034
SZNU	-0.107	0.109	0.966	0.137	-0.140	0.004	0.009	-0.006	-0.029
TLC	-0.155	0.393	0.732	0.127	0.115	0.144	-0.038	-0.118	0.182
LH-SDHGLE	-0.131	0.169	0.185	0.934	-0.186	0.034	-0.047	0.024	0.029
LH-SA	-0.181	0.173	0.186	0.931	-0.172	0.043	-0.053	0.010	0.005
LH-SAHGLE	-0.158	0.178	0.184	0.929	-0.183	0.033	-0.045	0.022	0.028
LH-HGLRE	-0.183	0.184	0.182	0.925	-0.181	0.031	-0.043	0.019	0.027
HL-SDLGLE	-0.067	-0.096	0.154	0.180	-0.956	0.035	-0.014	-0.033	-0.032
HL-SALGLE	-0.090	-0.089	0.155	0.181	-0.955	0.032	-0.014	-0.031	-0.032
HL-SRLGLE	-0.101	-0.090	0.159	0.181	-0.953	0.029	-0.013	-0.030	-0.032
HL-LGLZE	-0.108	-0.088	0.158	0.181	-0.952	0.028	-0.013	-0.029	-0.032
HH-SDLGLE	-0.016	-0.174	-0.083	-0.058	0.114	-0.968	0.034	0.016	-0.017
HH-SALGLE	-0.087	-0.162	-0.082	-0.054	0.108	-0.967	0.035	0.016	-0.014
HH-SRLGLE	-0.132	-0.158	-0.077	-0.049	0.102	-0.964	0.035	0.015	-0.013
HH-LGLZE	-0.150	-0.155	-0.078	-0.049	0.100	-0.962	0.036	0.015	-0.012
6MWD	0.214	0.146	0.003	-0.179	-0.280	-0.502	-0.341	0.137	0.158
LL-Imc2	-0.214	0.399	-0.073	-0.343	-0.098	-0.233	0.836	-0.071	0.057
HH-HGLRE	0.328	-0.424	0.120	0.305	0.065	0.218	-0.802	0.102	-0.038
Imc2	0.014	0.442	-0.241	-0.388	-0.010	-0.139	0.688	-0.134	0.048
RA ₉₅₀ %	-0.345	-0.260	0.058	0.191	-0.161	0.129	0.616	-0.105	-0.008
HL-CP	0.058	0.151	-0.259	0.120	0.243	-0.166	-0.248	0.802	0.171
LL-DV	0.552	0.054	-0.273	0.003	0.200	-0.046	-0.162	0.664	0.194
Elongation	-0.114	-0.151	-0.146	-0.444	-0.165	-0.098	0.054	0.657	-0.260
Flatness	-0.503	0.022	0.100	0.445	-0.129	-0.043	0.037	0.609	-0.134
HH-Range	0.537	-0.024	0.042	0.053	-0.012	-0.009	0.166	0.236	0.802
RV/TLC %	-0.178	-0.099	-0.334	0.214	0.112	0.097	-0.239	0.487	0.616
LL-Minimum	0.160	-0.069	0.119	0.155	-0.209	-0.186	0.218	0.078	0.506

Idm=inverse difference moment; LL=low-low pass; HH=high-high pass; HL=high-low pass; LH=low-high pass; SZNU=size zone non uniformity; LDLGLE=large dependence low gray level emphasis; SDHGLE=small dependence high gray level emphasis; SA=sum average; SAHGLE=small area high gray level emphasis; HGLRE=high gray level run emphasis; LAE=large area emphasis; DNU=dependence non uniformity; SZNU=size zone non uniformity; TLC=total lung capacity; SALGLE=short area low gray level emphasis; SRLGLE=short run low gray level emphasis; LGLZE=large gray level zone emphasis; 6MWD=six minute walk distance; Imc2=informational measure of correlation; RA₉₅₀=relative area of lung less than -950 Hounsfield Units; CP=cluster prominence; DV=difference variance; RV=residual volume; Following 9 components explain >93% of variance in data and highlighted values show highest texture feature factor loadings that compose the underlying component.

Table 2-9. Machine-learning model accuracies using only PCA and emergent components for classification

Classifiers (n =10)	AUC	Sensitivity(%)	Specificity(%)	Accuracy(%)
Decision Tree	0.57	45.0	66.6	59.7
Logistic Regression*	0.73	74.5	77.7	76.1
Subspace KNN	0.69	76.9	73.5	74.2
Weighted KNN	0.65	50.0	65.3	66.2
Linear SVM	0.71	66.6	71.4	71.0
Quadratic SVM	0.70	57.9	72.1	69.4
Naïve Bayes	0.69	66.6	70.0	69.4
Bagged Trees	0.58	36.8	62.8	54.8
Subspace Discriminant**	0.50	0	62.3	61.3
RUSBoosted Trees	0.63	46.1	69.5	57.5

AUC = Area under the receiver-operating curve; RUS = Random Under-Sampling; KNN = K-Nearest Neighbours; SVM = Support Vector Machines; Training data was used from selected PCA components #1, #2, #4, #6 and #9 exclusively. *Indicates the best performing classification model. **indicates classifiers that failed and classified all subjects as one class.

Table 2-10. Correlations of texture features with clinically-relevant measurements

Parameter	FEV ₁		FVC		FEV ₁ /FVC		RV/TLC		RA ₉₅₀		DL _{CO}		6MWD		SGRQ		ADC		VDP	
	ρ	P	ρ	P	ρ	P	ρ	P	ρ	P	ρ	P	ρ	P	ρ	P	ρ	P	ρ	P
BMI	-0.07	0.56	-0.09	0.50	0.09	0.48	-0.17	0.15	0.22	0.06	0.12	0.33	0.01	0.95	0.15	0.22	0.01	0.93	0.03	0.77
FEV ₁	1.0	-	0.88	0.001	-0.03	0.82	-0.27	0.02	0.03	0.82	0.20	0.09	0.14	0.23	-0.29	0.02	0.07	0.55	-0.11	0.37
FVC	0.88	0.001	1.0	-	-0.26	0.04	-0.25	0.05	0.19	0.13	0.26	0.04	0.19	0.14	-0.28	0.03	0.12	0.35	-0.08	0.55
FEV ₁ /FVC	-0.03	0.82	-0.26	0.04	1.0	-	-0.16	0.20	-0.28	0.02	-0.07	0.55	0.11	0.36	-0.03	0.79	-0.15	0.20	-0.23	0.05
RV/TLC	-0.27	0.02	-0.25	0.04	-0.16	0.20	1.0	-	-0.06	0.62	-0.34	0.001	-0.41	0.001	0.16	0.21	0.18	0.13	0.19	0.12
RA ₉₅₀	0.03	0.82	0.19	0.13	-0.28	0.02	-0.06	0.62	1.0	-	0.06	0.60	-0.17	0.16	0.19	0.12	0.32	0.01	0.13	0.27
DL _{CO}	0.21	0.09	0.26	0.04	-0.07	0.55	-0.34	0.001	0.06	0.60	1.0	-	0.47	0.001	-0.36	0.001	-0.44	0.009	-0.19	0.12
6MWD	0.14	0.23	0.19	0.14	0.11	0.36	-0.41	0.001	-0.17	0.16	0.47	0.001	1.0	-	-0.33	0.01	-0.42	0.001	-0.19	0.11
SGRQ	-0.29	0.02	-0.28	0.03	-0.03	0.79	0.16	0.21	0.19	0.12	-0.36	0.001	-0.33	0.01	1.0	-	0.31	0.01	0.13	0.31
ADC	0.07	0.55	0.12	0.35	-0.15	0.20	0.18	0.13	0.32	0.01	-0.44	0.009	-0.42	0.001	0.31	0.01	1.0	-	0.44	0.001
VDP	-0.11	0.37	-0.08	0.55	-0.23	0.05	0.19	0.12	0.13	0.27	-0.19	0.12	-0.19	0.11	0.13	0.31	0.44	0.001	1.0	-
HH-HGLRE	0.10	0.42	0.16	0.21	0.02	0.87	0.13	0.27	0.17	0.15	-0.29	0.02	-0.25	0.02	0.19	0.12	0.23	0.048	0.19	0.11
HH-Range	-0.11	0.38	-0.04	0.77	-0.01	0.96	0.24	0.009	0.06	0.62	-0.31	0.01	-0.28	0.02	0.24	0.047	0.30	0.02	0.28	0.02
M2DDC	0.26	0.03	0.22	0.07	-0.11	0.34	-0.28	0.02	0.33	0.01	0.33	0.01	0.24	0.04	-0.16	0.21	0.08	0.53	0.20	0.10
M3DD	0.31	0.009	0.32	0.01	-0.18	0.14	-0.49	0.001	0.24	0.04	0.39	0.001	0.13	0.29	-0.26	0.04	-0.01	0.97	0.13	0.29
LL-Imc2	0.01	0.94	-0.12	0.36	0.11	0.35	0.02	0.02	-0.18	0.14	-0.24	0.048	-0.13	0.26	0.17	0.04	0.13	0.30	0.08	0.49

BMI=body mass index; FEV₁=forced expiratory volume in 1 second; %_{pred}=percent of predicted value; FVC=forced vital capacity; RV=residual volume; TLC=total lung capacity; DL_{CO}=diffusing capacity of lung for carbon-monoxide; 6MWD=six minute walk distance; SGRQ=St. George's respiratory questionnaire; RA₉₅₀=relative area of lung less than -950 Hounsfield Units; ADC=apparent diffusion coefficient; VDP=ventilation defect percent. M2DDC=shape-maximum 2D diameter column, M3DD=shape-maximum 3D diameter, GLCM=gray level co-occurrence matrix, HL-energy=high-low-first-order-energy, LL-Imc2=low-low-GLCM-informational measure of correlation, HH-range=high-high-first-order-range, HH-HGLRE=high-high-gray level run length matrix-high gray level run emphasis.

Bolded values indicate a significant correlation (p<0.05) between measurements

CHAPTER 3

3 MACHINE LEARNING AND MR IMAGE TEXTURE ANALYSIS PREDICTS ACCELERATED LUNG FUNCTION DECLINE IN EX-SMOKERS WITH AND WITHOUT COPD

To investigate disease progression in ex-smokers with and without COPD, we evaluated the MRI ventilation measurements and texture features at baseline and 3-year follow-up visit to predict an accelerated lung function decline. The best imaging predictors of worsening were compared and correlated with pulmonary function and quality-of-life measurements in ex-smokers with and without COPD.

The contents of this chapter were submitted to the journal of Medical Imaging: M Sharma, A Fenster, DG McCormack and G Parraga. Machine-learning and Texture Analysis of Hyperpolarized gas MRI Predicts Accelerated Disease Progression Across 3-years in COPD. Submitted to Journal of Medical Imaging. (Manuscript ID: JMI 24004G).

3.1 Introduction

Pulmonary hyperpolarized ^3He gas magnetic resonance imaging (MRI) provides a means to quantify ventilation abnormalities using ventilation defect percent (VDP)¹ that stem from abnormalities in the large and small airways as well as emphysema.² Using forced expiratory volume in 1 s (FEV₁) it is difficult to predict patients with chronic airflow obstruction that will worsen with an accelerated decline in lung function. MRI-VDP measurements were previously shown to progressively worsen in patients with a stable FEV₁ and predict worse outcomes over short time-periods.^{3,4} While spirometry measurements of lung function are straightforward and cost-efficient to implement, they do not provide information about the small airways, which are believed to drive COPD pathogenesis.

In contrast, airway structural changes can be evaluated using established quantitative computed tomography (CT) measurements.⁵ Conversely, MRI VDP¹ provides functional information and has been shown to predict COPD exacerbations⁶ and longitudinal changes in quality of life as well as exercise capacity.⁷ Recent studies have shown that CT radiomics features are associated with

lung function in COPD,⁸ emphysema severity,⁹ and provide complementary information to established quantitative CT measurements.^{10,11} Despite these advantages, current predictive models of COPD progression are usually based on clinical measurements but none incorporate information derived from pulmonary CT or MRI.¹²

Texture analysis provides a unique opportunity to reveal and quantify hyperpolarized ³He MRI ventilation patchiness. Several recent investigations in COPD^{9,11,13} have clearly demonstrated the advantages of using radiomics approaches on CT images. Since binary VDP measurements do not exploit the full spectrum of information and spatial content that is inherent to hyperpolarized gas MRI, our main objective was to develop a texture-based machine learning model to identify ventilation features that can predict patients with an accelerated annual FEV₁ decline. Our secondary objective was to generate novel measurements of MRI ventilation heterogeneity and test their performance at predicting accelerated FEV₁ decline.

In COPD, rapid decliners have been previously defined as patients with a decline in FEV₁ ≥ 40 ^{14,15} or ≥ 60 mL/year.^{11,16-19} In general, the annual FEV₁ decline is larger in patients with mild COPD stages and less pronounced airflow limitation.^{17,19} Therefore, we tested multiple single and ensemble classifiers to determine the best model for predicting COPD patients who would experience an FEV₁ decline ≥ 60 mL/year, over a three-year period. Such predictive models may serve as tools for an early detection of rapidly progressing patients and facilitate early treatment options for this subgroup of patients that are at a higher risk of progressing to a greater disease severity.

3.2 Materials and Methods

3.2.1 Study Design and Participants

All participants provided informed written consent to a study protocol approved by local research ethics board and in compliance with the Health Canada approved and registered protocol²⁰ (clinicaltrials.gov NCT02279329). Inclusion criteria were a history of cigarette smoking >10 pack years, age between 50 and 85 years at baseline. Ex-smoker participants were included who had ceased smoking ≥ 1 -year prior to the study visit, with no cut-off in terms of smoking cessation. COPD subjects were classified according to the Global Initiative for Chronic Obstructive Lung Disease (GOLD) grades.²¹ Participants also completed a longitudinal follow-up visit at 24 \pm 6 months after the baseline visit.²⁰ The CONSORT diagram for the Thoracic Imaging Network of Canada (TINCan) study cohort participants is depicted in **Figure 3-1**.

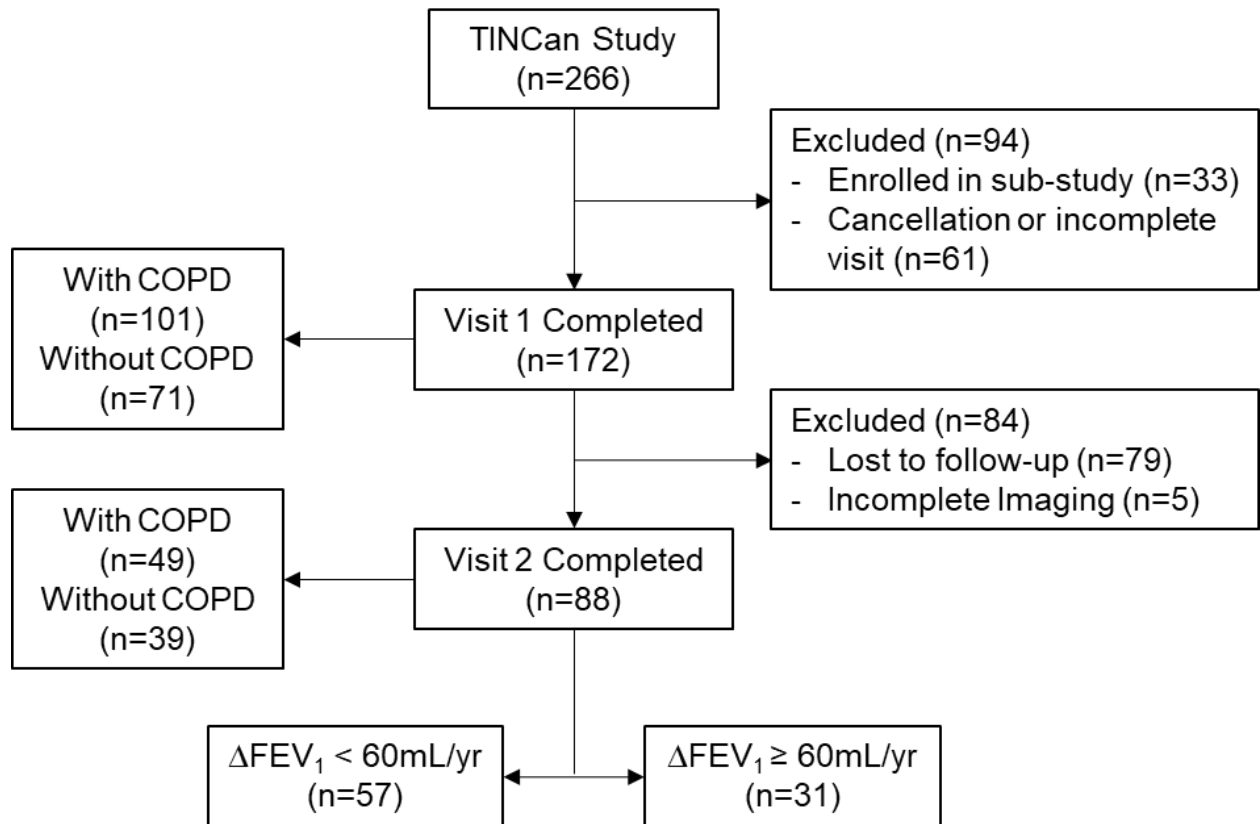


Figure 3-1. CONSORT Flow Diagram

Of the 266 participants enrolled in the TINCan study, 33 were enrolled in a sub-study and 61 either cancelled or did not complete all required tests during Visit 1. Of the 172 participants that completed Visit 1, 79 participants did not complete a 3-year follow-up Visit 2 and five had artifacts present in their images, which were excluded from further analysis. Eighty-eight ex-smoker participants with Visit 1 and Visit 2 data were analyzed in this study, of which 31 had $\Delta\text{FEV}_1 \geq 60\text{mL/year}$ and 57 had $\Delta\text{FEV}_1 < 60\text{mL/year}$.

3.2.2 Pulmonary Function Tests and Image Acquisition

Spirometry, plethysmography, and the diffusing capacity of the lungs for carbon monoxide (DL_{CO}) were measured according to the American Thoracic Society/European Respiratory Society guidelines²² using a whole-body plethysmography system (MedGraphics Corporation, St Paul, MN, USA) and attached gas analyzer.²³ COPD was defined as post-bronchodilator spirometry according to the Global Initiative for Chronic Obstructive Lung Disease (GOLD) criteria.²¹ The 6MWD²⁴ test and St. George's Respiratory Questionnaire (SGRQ)²⁵ were administered under supervision.

Anatomic proton (^1H) and hyperpolarized ^3He MR images were acquired using a whole-body 3.0 Tesla Discovery MR750 system (GE Healthcare, Milwaukee, WI, USA), a whole-body radiofrequency coil and a fast gradient recalled echo (FGRE) sequence with a partial echo implementation, with acquisition parameters as previously described.²⁶ Hyperpolarized ^3He MRI was acquired using a linear bird-cage transmit/receive chest coil (RAPID Biomedical GmbH, Wuerzburg, Germany). A turn-key system (HeliSpinTM, Polarean Inc, Durham, NC, USA) was used to polarize ^3He gas to 30–40% and doses (5 mL/kg body weight) diluted with N_2 were administered in 1.0 L Tedlar® bags. Hyperpolarized ^3He MRI diffusion-weighted imaging was performed using a 2D multi-slice fast gradient-echo method, as previously described,²⁶ during breath-hold for acquisition of two interleaved images with and without additional diffusion sensitization with $b=1.6 \text{ sec/cm}^2$ (maximum gradient amplitude $[G]=1.94 \text{ G/cm}$, rise and fall-time=0.5 ms, gradient duration=0.46 ms, diffusion time=1.46 ms).²⁰ Pulmonary function data and imaging were acquired during both baseline and follow-up visits.

3.2.3 Image Analysis and Proposed Algorithm

Baseline and follow-up visit ^1H and ^3He MR images were processed by a single observer where the thoracic cavity was segmented from the ^1H images using a seeded region-growing algorithm, and the ^3He ventilation region was segmented using k-means clustering.¹ The generated maximum entropy mask was then applied to identify the ventilated region-of-interest (ROI) for feature extraction. Diffusion-weighted images were automatically processed to generate apparent diffusion coefficient (ADC) values and images, as previously described.²³

MRI VDP was generated using a semi-automated segmentation approach, as previously described.¹ Ventilation defect cluster percent (VDCP), which is the sum of ventilation-defect cluster volume normalized to the total lung volume, and defect cluster sizes were generated by an

automated in-house custom-developed algorithm, as described in the prior proceedings paper.²⁷ Briefly, the proposed cluster algorithm iteratively segments unventilated MRI volumes until the maximum sphere fit (or multiple spheres of the same size) within the unventilated volume is identified. This sphere volume(s) is then removed from the non-ventilated region and the process is iteratively repeated until the non-ventilated region is filled by spheres. This is similar in approach to sphere packing previously investigated for radio-surgical treatment planning.²⁸

The approach was implemented using a naïve greedy algorithm where $S = [b_1, b_2, \dots, b_n]$ is a set with n elements, where each element $b_n = B_n(r, l)$ is an open sphere of radius r at locations \vec{l} . Determining the required minimum number of spheres of unequal sizes resulted in the following minimization problem:

$$\min_S \{ \|S\|_0 \} : S \in \mathbf{R}^n \quad (1)$$

Where the cardinality of the set S and $\forall (b \in S) \exists (r, l)$ is minimized. To ensure that the spheres completely fill the unventilated region-of-interest R , and are within the thoracic cavity, several constraints were implemented. First, the intersection between the region that is being filled with spheres (R) and the spheres (b) was set to b . Furthermore, to prevent spheres from overlapping, the overlap between two spheres (b and b') was fixed to result in a null set:

$$b \cap R = b \quad \& \quad b \cap b' = \emptyset \quad (2)$$

A volume constraint was also imposed such that the total volume of spheres was equal to the volume of the specified unventilated region R :

$$\sum_{b \in S} V(b) = V(R) \quad (3)$$

The specified regions were filled with spheres, where the minimum sphere diameter was equal to one voxel ($5 \times 5 \times 5 \text{ mm}^3$), such that the total volume of spheres with diameter equal to one voxel

was equal to be the total residual volume not clustered into large (>one voxel) sphere sizes. To further simplify the problem, there were no location constraints on the sphere spatial position. We used MATLAB R2021a (MathWorks) to solve the minimization problem and generated VDCP in order to calculate cluster-defect-diameter voxel size one (CDD1), which is the cumulative number of defect clusters of one voxel, shown in **Figure 3-2**. Low ventilation cluster (LVC) slopes were also calculated based on the log-log relationship between the cumulative number of spheres and cluster size.^{29,30}

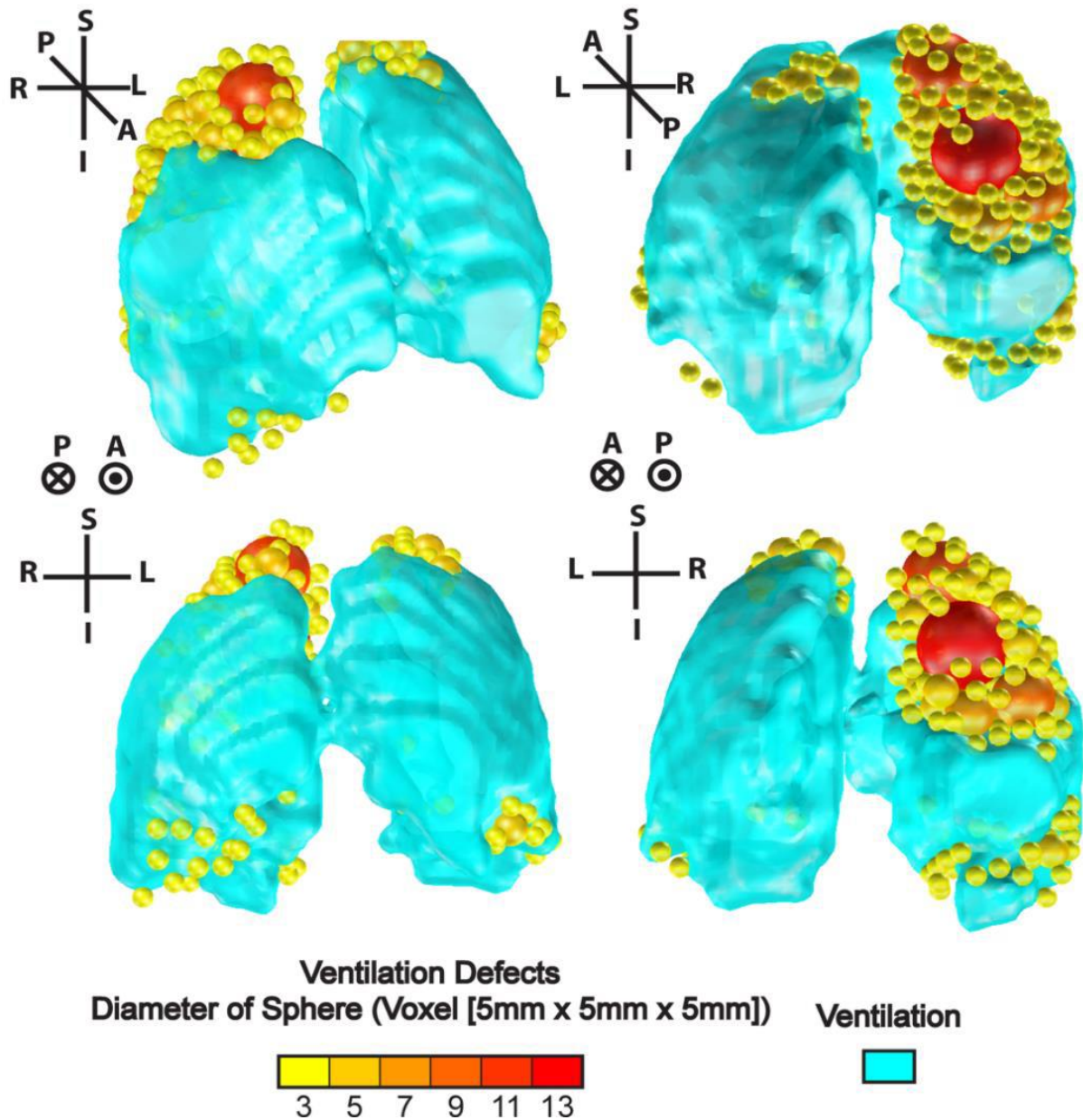


Figure 3-2. Ventilation Defect Cluster Volume Output from Custom-developed Algorithm

A representative 66-year old male ex-smoker participant with COPD: $FEV_1=1.93$ L, $VDP=25\%$, $\Delta FEV_1=-0.22$ L and $\Delta VDP=1\%$ between visits. Three-dimensional isotropic ventilation volume shown in cyan and ventilation defects represented by different sphere sizes ranging from small (yellow=sphere diameters of 3-5 voxels) to large (red=sphere diameters of 9-13 voxels).

Further texture feature extraction was conducted using an open-source PyRadiomics software, detailed in the next section. Unlike the proposed algorithm that analyzes the unventilated region, texture features were extracted from the inhaled hyperpolarized gas distribution within the thoracic cavity.

3.2.4 Feature Extraction and Selection Pipeline

The complete pipeline for processing the baseline and follow-up visit images is summarized in **Figure 3-3**. First, we generate a maximum entropy mask by segmenting the ^3He ventilation image as previously described.¹ We then use a custom-developed algorithm to calculate the ventilation defect clusters, described above, and the PyRadiomics platform³¹ for extracting texture features. Texture features were calculated from gray-level histograms and matrices generated from the ROI of the original image.

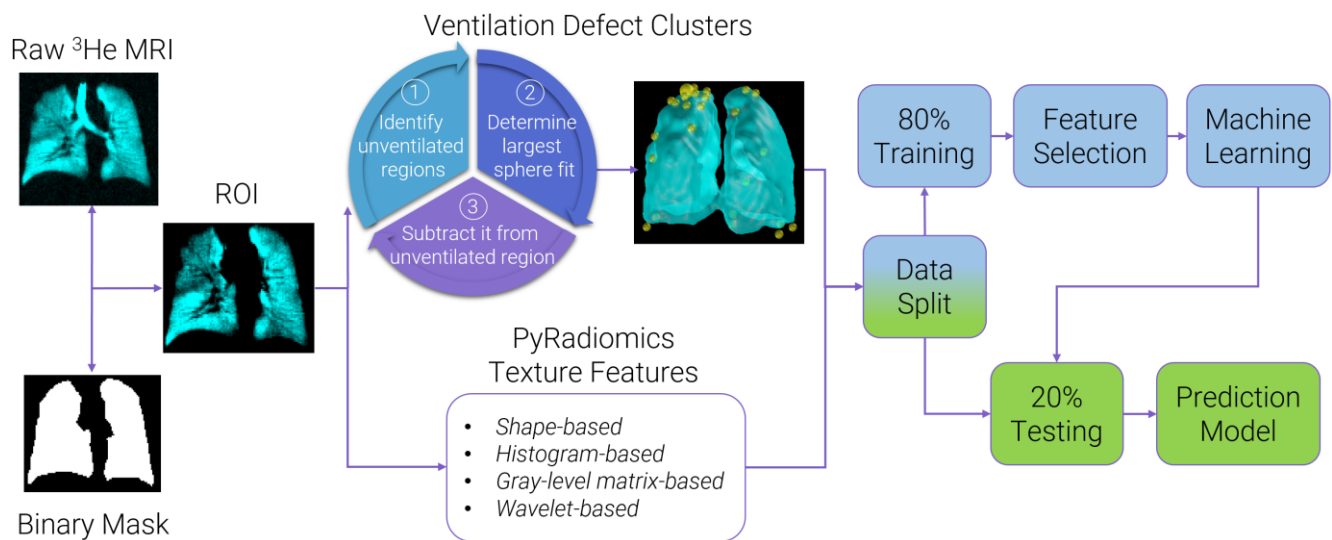


Figure 3-3. Image Processing and Model Generation Pipeline

Hyperpolarized noble gas MR images were analyzed using custom-developed algorithms to calculate ventilation defect clusters and texture features. Raw MR images and corresponding binary lung masks were used to generate the regions-of-interest (ROI), which were analyzed via the PyRadiomics platform to calculate shape, first- and higher-order texture features. Feature selection was performed using the training set, combined with principal component analysis (PCA) and Boruta analysis. Classification learner application was used for model generation, which were trained using a 5-fold cross-validation scheme, with 20% of data reserved for the testing set.

We generated first-order texture features from the gray-level histograms and also evaluated the texture features calculated from run-length, gap-length, co-occurrence, size-zone, dependence and neighborhood gray tone matrices using the PyRadiomics open-sourced platform (version 2.2.0) in Python environment (version 3.7.5).³¹ Image processing filters were also applied for the extraction

of wavelet band-pass filtering texture features. This further quadrupled the number of extracted features due to permutations of high-pass and low-pass filters for wavelet decomposition, resulting in 376 additional MRI texture features. Low-pass filtering in both directions (LL) assesses the lowest frequencies, low-pass filtering followed by high-pass filtering (LH) assesses horizontal edges, high-pass filtering followed by low-pass filtering (HL) assesses vertical edges and high-pass filtering in both directions (HH) assesses diagonal details.³²

The resulting data and 496 extracted features were randomly assigned into training and testing sets with 80%/20% data split. Feature selection was performed on the training set using principal component analysis (PCA) and Boruta analysis to rank and determine texture features significantly contributing to the predictive power of the machine learning models. The Boruta algorithm generated shadow features for comparisons and used a two-step correction for multiple testing, with an optimizable random forest classifier for iterations (number of trees in the forest=200, maximum iterations=300, maximum tree depth=10 [branches], percentage of shadow feature threshold=95%, alpha-level=0.05). We utilized all wavelet band-pass filtering features that were available in the PyRadiomics platform (version 2.2.0), with the detailed mathematical descriptions of all the extracted and selected features provided in **Table 3-5**.³¹

3.2.5 Machine learning and Statistical Analysis

Once all the features and parameters were selected, machine learning models were generated based on 1) Demographic measurements alone; 2) Spirometry measurements alone; 3) Imaging and texture measurements alone; and 4) Combination of all available measurements. Five-fold cross-validation training was performed using several machine learning algorithms including single classifiers and ensemble classifiers to determine the best model for identifying accelerated disease progression. The data were standardized and hyper-parameter optimization was performed through

MATLAB R2021a (Classification Learner App) for each model individually. We compared the performance of multiple machine learning algorithms including variations of: Logistic regression, Naïve Bayes,³³ Support Vector Machines (SVM),³⁴ Decision trees,³⁵ K-nearest neighbours (KNN),³⁶ and four ensemble-classifiers: bagged and boosted trees,³⁷ subspace discriminant,³⁸ subspace K-nearest-neighbours,³⁸ and Random Under-Sampling Boosted (RUSBoosted) Trees. Model performance was evaluated using the mean cross-validation area under the receiver-operator curve (AUC), as well as sensitivity, specificity, and F1-score using the models' confusion matrix. The DeLong's test was used to compare the performance of all machine learning models.³⁹ Statistical analysis was performed using SPSS Statistics v28.0 (IBM Statistics, Armonk, New York, USA). Shapiro-Wilk tests were used to determine the normality of the data and non-parametric tests were performed for data that were not normal. Differences between subject groups were determined using analysis of variance (ANOVA) with post-hoc analysis using the Benjamini-Hochberg correction. The relationship between measurements was determined using Pearson and Spearman coefficients for parametric and non-parametric data, respectively. Results were considered significant when the probability of two-tailed type I error was less than 5% ($p < .05$).

3.3 Results

A CONSORT diagram provided in **Figure 3-1** shows that 266 ex-smokers were enrolled and 94 were excluded from analysis due to enrollment in another sub-study ($n=33$) and due to cancellation or not completing all required tests per protocol ($n=61$). Of the 172 participants that completed Visit 1, 79 participants did not complete a 3-year follow-up visit and five had poor image quality and were excluded from further analysis.

3.3.1 Participant Demographics

We evaluated 88 ex-smoker participants, of which 49 had spirometry evidence of COPD and 39 with no spirometry evidence of COPD. As shown in **Table 3-1**, 57 participants (22 Females/35 Males, 70±9 years) demonstrated a smaller FEV₁ decline (<60mL/year) and 31 participants (7 Females/24 Males, 68±9 years) demonstrated a rapid decline in FEV₁ (≥60mL/year), between baseline and follow-up visit 31 ± 7 months later. At baseline there were significant differences only in forced vital capacity (FVC) between subgroups (FVC L p=.003 and FVC %_{pred} p=.03, respectively). As summarized in **Table 3-2**, these subgroups did not have any statistically significant differences at follow-up.

Table 3-1. Baseline participant demographics and pulmonary function measurements

Parameter	All Participants (n=88)	ΔFEV ₁ <60mL/yr (n=57)	ΔFEV ₁ ≥60mL/yr (n=31)	p-value
Mean (±SD)				
Age	69 (9)	70 (9)	68 (9)	.2
Female n(%)	29 (33)	22 (39)	7 (23)	.1
Height m	169 (8)	168 (8)	171 (7)	.2
BMI kg/m ²	28 (4)	28 (4)	29 (5)	.4
SpO ₂ %	96 (3)	95 (4)	96 (2)	.8
Pack Years	36 (26)	37 (26)	35 (21)	.8
Years Since Quit	15 (13)	14 (14)	16 (13)	.7
<i>Pulmonary function and QoL</i>				
FEV ₁ L	2.3 (0.8)	2.2 (0.8)	2.5 (0.8)	.1
FEV ₁ % _{pred}	84 (26)	82 (26)	86 (27)	.5
FVC L	3.6 (0.9)	3.4 (0.9)	3.9 (0.8)	.003
FVC % _{pred}	95 (17)	92 (16)	100 (17)	.03
FEV ₁ /FVC %	65 (17)	66 (17)	63 (17)	.5
TLC L	6.7 (1.3)	6.5 (1.3)	7.0 (1.2)	.06
TLC % _{pred}	109 (16)	108 (17)	111 (14)	.4
RV/TLC %	43 (10)	45 (10)	42 (9)	.2
DL _{CO} % _{pred}	68 (21)	67 (21)	70 (23)	.6
6MWD m	405 (81)	404 (84)	405 (75)	.9
SGRQ	28 (21)	28 (20)	28 (23)	.9

BMI=body mass index; SpO₂=blood oxygen saturation; QoL=quality-of-life; FEV₁=forced expiratory volume in 1 second; %_{pred}=percent of predicted value; FVC=forced vital capacity; RV=residual volume; TLC=total lung capacity; DL_{CO}=diffusing capacity of lung for carbon-monoxide; 6MWD=six minute walk distance; SGRQ=St. George's respiratory questionnaire. p=uncorrected values showing significant differences between ΔFEV₁ <60mL/yr and ΔFEV₁ ≥60mL/yr groups. Significance level p<0.05.

Table 3-2. Participant demographics and pulmonary function measurements at follow-up visit

Parameter Mean (\pm SD)	All Participants (n=88)	Δ FEV ₁ <60mL/yr (n=57)	Δ FEV ₁ \geq 60mL/yr (n=31)	p-value
Age	72 (9)	73 (9)	70 (9)	.2
Female n(%)	29 (33)	22 (39)	7 (23)	.1
Height m	169 (8)	168 (8)	170 (7)	.2
BMI kg/m ²	28 (4)	28 (4)	29 (5)	.3
SpO ₂ %	95 (3)	95 (4)	95 (2)	.9
Pack Years	36 (26)	37 (26)	35 (21)	.6
Years Since Quit	17 (14)	17 (14)	17 (13)	.9
<i>Pulmonary function and QoL</i>				
FEV ₁ L	2.2 (0.8)	2.2 (0.8)	2.1 (0.7)	.4
FEV ₁ % _{pred}	84 (25)	87 (29)	77 (27)	.07
FVC L	3.3 (0.9)	3.3 (0.9)	3.4 (0.8)	.5
FVC % _{pred}	94 (19)	95 (19)	92 (19)	.4
FEV ₁ /FVC %	65 (16)	66 (17)	62 (17)	.5
TLC L	6.4 (1.3)	6.3 (1.3)	6.6 (1.2)	.3
TLC % _{pred}	105 (16)	105 (17)	106 (14)	.8
RV/TLC %	45 (10)	45 (10)	45 (9)	.7
DL _{CO} % _{pred}	80 (21)	77 (25)	84 (28)	.6
6MWD m	398 (83)	396 (84)	400 (75)	.8
SGRQ	30 (21)	27 (20)	37 (23)	.08

BMI=body mass index; QoL=quality-of-life; SpO₂=blood oxygen saturation; FEV₁=forced expiratory volume in 1 second; %_{pred}=percent of predicted value; FVC=forced vital capacity; RV=residual volume; TLC=total lung capacity; DL_{CO}=diffusing capacity of lung for carbon-monoxide; 6MWD=six minute walk distance; SGRQ=St. George's respiratory questionnaire. p=uncorrected values showing significant differences between Δ FEV₁ <60mL/yr and Δ FEV₁ \geq 60mL/yr groups. Significance level p<0.05.

3.3.2 Imaging Measurements and Texture Features

Table 3-3 summarizes quantitative MR imaging measurements and ranked texture features after feature selection step. Ex-smokers with accelerated lung function decline had significantly different gray level co-occurrence matrix (GLCM)-inverse difference moment normalized (Idmn) feature (p=.048), wavelet-low-low-pass (LL)-size zone matrix (SZM)-low gray level zone emphasis (LGLZE) feature (p=.01), wavelet-LL-run length matrix (RLM)-short run low gray level emphasis (SRLGLE) feature (p=.007), wavelet-LL-gray-level dependence matrix (GLDM)-short distance low gray level emphasis (SDLGLE) feature (p<.001). As summarized in **Table 3-4**, these subgroups did not have any statistically significant differences between imaging measurements at follow-up. **Table 3-5** summarizes the texture feature descriptions and definitions.

Table 3-3. Imaging measurements of participants with stable and accelerated lung function decline

Parameter Mean (±SD)	All Participants (n=88)	ΔFEV₁<60mL/yr (n=57)	ΔFEV₁≥60mL/yr (n=31)	p- value
MRI VDP %	12 (9)	11 (8)	14 (11)	.2
MRI ADC cm ² /s	0.34 (0.10)	0.33 (0.08)	0.36 (0.12)	.1
ΔVDP %	4 (5)	3 (5)	4 (5)	.9
ΔADC cm ² /s	0.02 (0.04)	0.02 (0.04)	0.02 (0.05)	.3
Selected Texture Features				
Shape-MajorAxisLength	98.9 (7.5)	97.7 (7.7)	101.4 (7.1)	.1
CDD1	4771 (3212)	4316 (2751)	5528 (3097)	.1
GLCM-Idn	.956 (.008)	.958 (.008)	.954 (.007)	.095
GLCM-Idmn	.995 (.002)	.995 (.002)	.997 (.001)	.048
<i>Wavelet-filtered</i>				
LL-SZM-LGLZE	.00017 (.00010)	.00015 (.00008)	.00020 (.00010)	.01
LL-RLM-SRLGLE	.00017 (.00009)	.00015 (.00008)	.00020 (.00009)	.007
LL-GLDM-SDLGLE	.00016 (.00007)	.00014 (.00006)	.00019 (.00007)	<.001

MRI VDP=ventilation defect percent; ADC=apparent diffusion coefficient; CDD1=cluster-defect diameter of one voxel; GLCM=gray level co-occurrence matrix; SZM=size zone matrix; RLM=run length matrix; GLDM=gray-level dependence matrix; LL=low-low-pass filter; Idn=inverse difference normalized; Idmn=inverse difference moment normalized; LGLZE=low gray level zone emphasis; SRLGLE=short run low gray level emphasis; SDLGLE=small dependence low gray level emphasis.

p=uncorrected values showing significant differences between ΔFEV₁ <60mL/yr and ΔFEV₁ ≥60mL/yr groups. Significance level p<0.05.

Table 3-4. Imaging measurements of participants with stable and accelerated lung function decline at follow-up visit

Parameter Mean (±SD)	All Participants (n=88)	ΔFEV₁<60mL/yr (n=57)	ΔFEV₁≥60mL/yr (n=31)	p- value
MRI VDP %	16 (13)	15 (9)	18 (14)	.1
MRI ADC cm ² /s	0.35 (0.11)	0.34 (0.07)	0.36 (0.10)	.4
ΔVDP %	4 (5)	3 (5)	4 (5)	.9
ΔADC cm ² /s	0.02 (0.04)	0.02 (0.04)	0.02 (0.05)	.3
Selected Texture Features				
Shape-MajorAxisLength	97.9 (7.7)	97.5 (7.5)	99.8 (7.3)	.6
CDD1	5037 (3866)	4616 (2951)	6128 (3298)	.2
GLCM-Idn	.956 (.008)	.954 (.008)	.957 (.007)	.3
GLCM-Idmn	.995 (.002)	.995 (.002)	.996 (.001)	.1
<i>Wavelet-filtered</i>				
LL-SZM-LGLZE	.00016 (.00010)	.00015 (.00008)	.00019 (.00010)	.2
LL-RLM-SRLGLE	.00016 (.00010)	.00015 (.00008)	.00019 (.00010)	.1
LL-GLDM-SDLGLE	.00015 (.00008)	.00014 (.00007)	.00018 (.00008)	.07

MRI VDP=ventilation defect percent; ADC=apparent diffusion coefficient; CDD1=cluster-defect diameter of one voxel, GLCM=gray level co-occurrence matrix; SZM=size zone matrix; RLM=run length matrix; GLDM=gray-level dependence matrix; LL=low-low-pass filter; Idn=inverse difference normalized; Idmn=inverse difference moment normalized; LGLZE=low gray level zone

*emphasis; SRLGLE=short run low gray level emphasis; SDLGLE=short distance low gray level emphasis.
 p=uncorrected values showing significant differences between $\Delta FEV_1 < 60\text{mL/yr}$ and $\Delta FEV_1 \geq 60\text{mL/yr}$ groups. Significance level $p < 0.05$*

Table 3-5. MRI texture feature descriptors for machine-learning modelling

Texture Feature Name	Description
Shape-Major Axis Length	Measures the largest axis length of the ellipsoid within the ROI, calculated using the largest principal component, generated using the physical coordinates of the voxel centers defining the ROI.
CDD1	Measures the number of spheres with diameter of one voxel that can fit within the unventilated region of the lung, as visualized on hyperpolarized gas MR imaging.
GLCM-Idn	Measures the local homogeneity of an image by normalizing the differences between the neighboring intensity values and dividing over the total number of discrete intensity values.
GLCM-Idmn	Measures the local homogeneity of an image by normalizing the square of the differences between neighboring intensity values and dividing over the square of the total number of discrete intensity values.
LL-SZM-LGLZE	Measures the distribution of low intensity gray-level size zones, with a higher value indicating a greater proportion of low gray-level intensity values and size zones in the image.
LL-RLM-SRLGLE	Measures the joint distribution of shorter run lengths with low gray-level intensity values.
LL-GLDM-SDLGLE	Measures the joint probability distribution of small dependences with low gray-level intensity values.

CDD1=cluster-defect diameter of one voxel; GLCM=gray level co-occurrence matrix; SZM=size zone matrix; RLM=run length matrix; GLDM=gray-level dependence matrix; Idn=inverse difference normalized; Idmn=inverse difference moment normalized; LL=low-low-pass filter; LGLZE=low gray level zone emphasis; SRLGLE=short run low gray level emphasis; SDLGLE=short distance low gray level emphasis.

3.3.3 Machine learning Modeling

As summarized in **Table 3-6**, the best performing machine learning model trained on demographic measurements (Age, Sex, BMI, % SpO₂, Pack years and Years since quit) achieved 64% prediction accuracy. Best performing spirometry model (FVC, TLC, FEV₁, %_{pred} IC, SVC, and RV/TLC) was cosine KNN algorithm with 68% accuracy, which was not statistically different from the models based on demographics measurements. The texture-based model achieved the highest sensitivity (86%) and an 81% accuracy via the ensemble RUSBoosted trees algorithm, exclusively

trained on selected MR image texture features. The combined model achieved the highest accuracy of 82% using the Medium-Gaussian SVM algorithm, trained on FVC, Age, Shape-major axis length, GLCM-Idn, wavelet-LL-SZM-LGLZE, wavelet-LL-GLDM-SDLGLE.

Table 3-6. Machine-learning performance at predicting accelerated lung function decline

Best Performing Models	AUC	Sens. %	Spec. %	F1-score	Acc. %
Demographics model [†] Logistic Regression	0.64	66.7	46.2	75.7	63.6
Spirometry model [‡] Cosine KNN	0.68	68.9	63.6	79.1	68.2
Texture-based model [§] RUSBoosted Trees	0.80	85.7	71.9	85.5	80.7
Combined model [‡] Medium Gaussian SVM	0.81	80.6	85.7	87.1	81.8

*AUC=area under the receiver-operating curve; KNN=K-nearest neighbours; RUS=random under sampling; SVM=support vector machine. *Bold values indicate highest performance in a specific metric.*

[†]Variables used for training included: Age, Sex, BMI, % SpO₂, Pack years and Years since quit.

[‡]Variables used for training included: FVC, TLC, FEV₁, %_{pred} IC, SVC, and RV/TLC.

[§]Features selected for training included: MRI cluster-defect diameter of one voxel (CDD1), Shape-major axis length, Gray Level Co-occurrence Matrix-Inverse difference normalized, Gray Level Co-occurrence Matrix-Inverse difference moment normalized, wavelet-low-low-Size Zone Matrix-Low Gray Level Zone Emphasis, wavelet-low-low-Run Length Matrix-Short Run Low Gray Level Emphasis, wavelet-low-low-Gray Level Dependence Matrix-Small Dependence Low Gray Level Emphasis.

[‡]Combined model included: FVC, Sex, Shape-major axis length, Gray Level Co-occurrence Matrix-Inverse difference normalized, wavelet-low-low-Size Zone Matrix-Low Gray Level Zone Emphasis, wavelet-low-low- Gray Level Dependence Matrix-Small Dependence Low Gray Level Emphasis.

As summarized in **Table 3-7**, the machine learning models trained exclusively on MRI texture features outperformed the machine learning models trained using participant demographic and spirometry measurements ($p < .05$). In addition, the combined model trained on all available measurements also outperformed the demographic and spirometry-based models ($p < .05$); however, the performance of the combined model failed to show a significant difference ($p = .9$) to the machine learning models trained exclusively on MRI texture features.

Table 3-7. DeLong’s test for comparing the models for predicting accelerated disease progression in ex-smokers

Best Model Comparisons	<i>p</i>-value
Demographics model vs Spirometry model	0.7
Demographics model vs Texture-based model	<.001
Demographics model vs Combined model	<.001
Spirometry model vs Texture-based model	.04
Spirometry model vs Combined model	.03
Texture-based model vs Combined model	0.9

Significance level $p < 0.05$.

The ensemble models outperformed the single machine learning models, indicating the presence of more complex and non-linear relationships of texture features and accelerated lung function decline. Logistic regression models for predicting accelerated lung function decline were generated for individual clinical and imaging texture measurements with the receiver-operator characteristic curve AUC, which is summarized in **Figure 3-4**. The best performing clinical measurements for predicting patients with accelerated FEV₁ decline were FVC (AUC=.68) and TLC (AUC=.65). The overall best predictive measurement was wavelet-LL-GLDM-SDLGLE (AUC=.77), which also outperformed standard imaging measurements such as MRI VDP (AUC=.63).

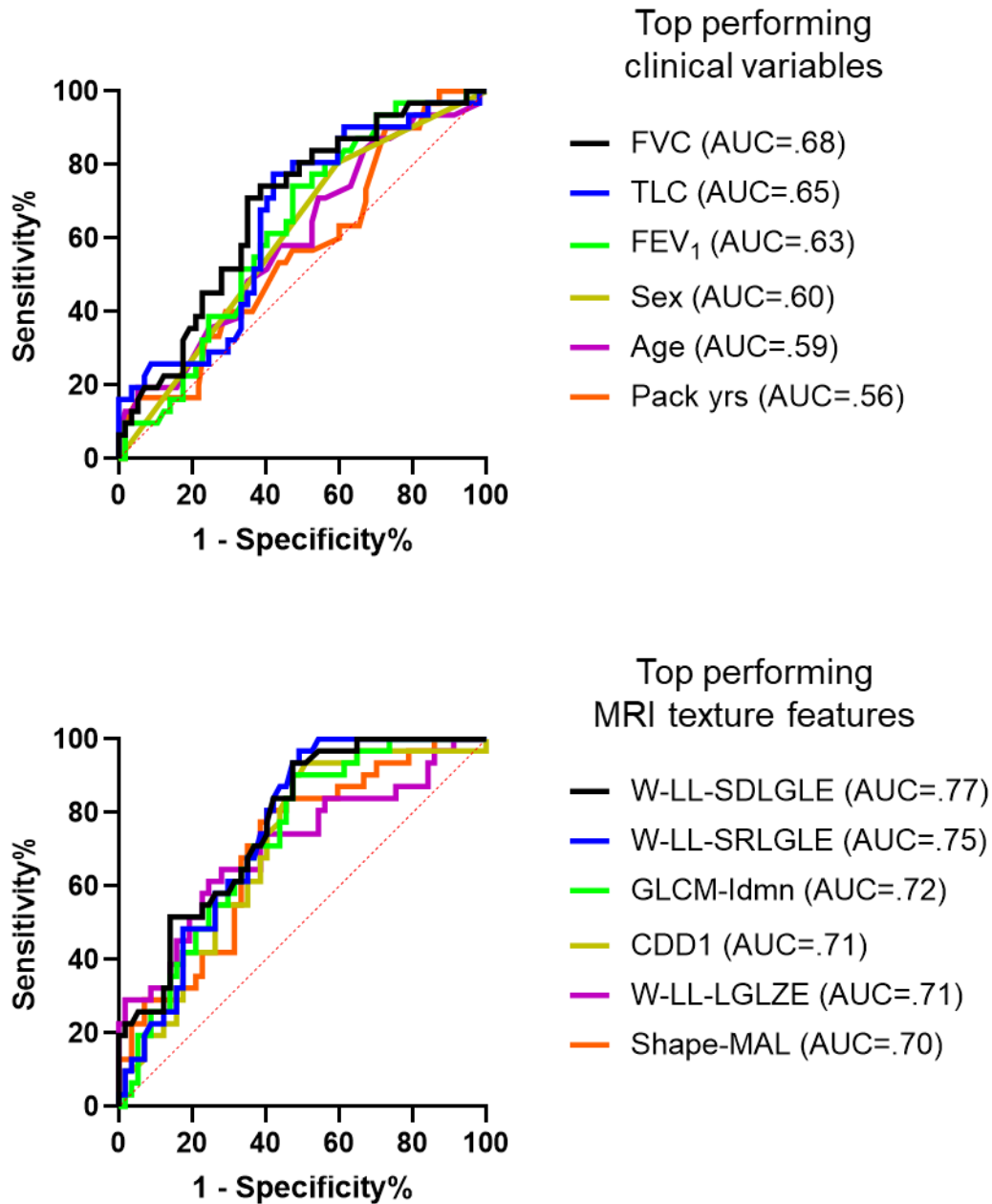


Figure 3-4. Receiver-operator Characteristic Curves of Clinical and Texture Measurements

Top Panel: Logistic regression analysis of individual top-performing demographic and spirometry variables at predicting $\Delta FEV_1 \geq 60\text{mL/year}$ in ex-smoker participants.

Bottom Panel: Logistic regression of selected top-performing MR imaging and texture features at predicting $\Delta FEV_1 \geq 60\text{mL/year}$. Individual texture features clearly outperformed established clinical variables available to physicians at predicting accelerated lung function decline.

FVC=forced vital capacity; TLC=total lung capacity; FEV₁=forced expiratory volume in 1 second; LL=low-low pass filter; SDLGLE=short distance low gray level emphasis; SRLGLE=short run low gray level emphasis; Idmn=inverse difference moment normalized; CDD1=cluster-defect diameter of one voxel; LGLZE=low gray level zone emphasis; MAL=major axis length.

3.3.4 Relationships with Clinical Measurements

Spearman correlations were used to evaluate the relationships between well-established clinical measurements and MRI texture features identified as significant predictors of clinically relevant FEV₁ changes. As shown in **Figure 3-5**, the best performing clinical measurements of FVC and TLC correlated with Δ FEV₁ between visits ($\rho=-.24$, $p=.01$; $\rho=-.23$, $p=.03$, respectively). Similarly, texture features from the original unfiltered image CDD1 and Shape-major axis length correlated with Δ FEV₁ ($\rho=-.20$, $p=.047$; $\rho=-.21$, $p=.046$, respectively). The best performing wavelet-based texture feature LL-GLDM-SDLGLE exhibited the strongest correlation with Δ FEV₁ ($\rho=-.29$, $p=.006$), and only the longitudinal change in this specific texture correlated with the clinically relevant changes in FEV₁ ($\rho=.27$, $p=.041$).

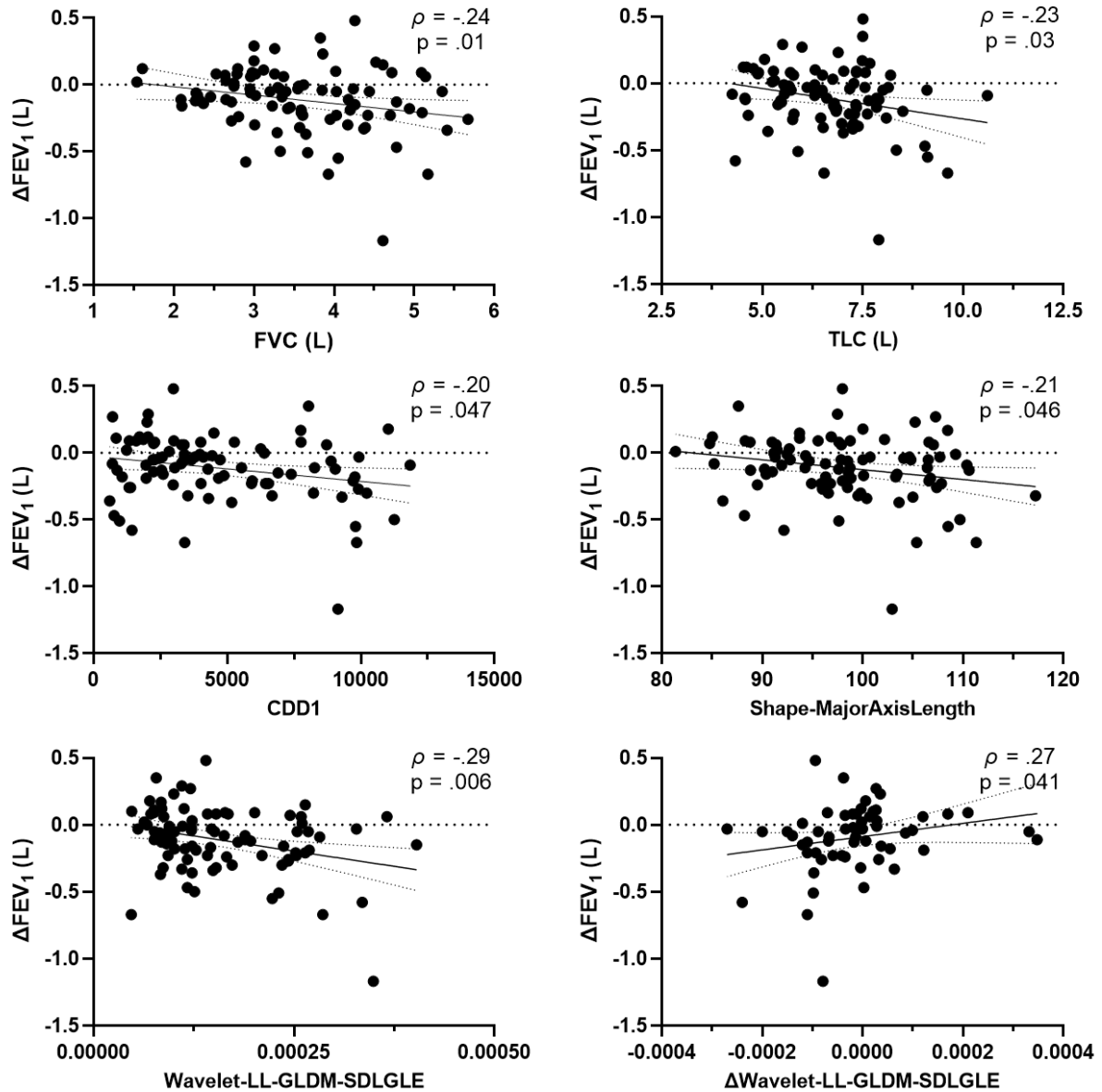


Figure 3-5. Relationships between Selected Texture Features and Change in FEV₁

Top Panel: Spearman correlation for FVC and TLC with ΔFEV_1 ($\rho = -.24$, $p = .01$; $\rho = -.23$, $p = .03$, respectively) between baseline and follow-up visits.

Middle Panel: Spearman correlation for custom CDD1 feature and Shape-Major Axis Length with ΔFEV_1 ($\rho = -.20$, $p = .047$; $\rho = -.21$, $p = .046$, respectively) between baseline and follow-up visits.

Bottom Panel: Spearman correlation for Wavelet-LL-filtered-GLDM-SDLGLE and Δ Wavelet-LL-filtered-GLDM-SDLGLE with ΔFEV_1 ($\rho = -.29$, $p = .006$; $\rho = .27$, $p = .041$, respectively) between baseline and follow-up visits.

FEV₁=forced expiratory volume in 1 second, *FVC*=forced vital capacity, *TLC*=total lung capacity, *CDD1*=cluster-defect diameter of one voxel, *LL*=low-low pass filter, *GLDM*=gray level dependence matrix, *SDLGLE*=short distance low gray level emphasis.

3.4 Discussion

In this study, we developed an MRI texture analysis pipeline to reveal a subset of ventilation patterns that can help predict ex-smokers that will experience accelerated lung function decline. We observed that RUSBoosted trees algorithm trained solely on texture features outperformed all other existing models at predicting clinically relevant change in FEV₁ (81% accuracy). Overall, ensemble machine learning classifiers outperformed single classifiers, indicating the existence of complex non-linear relationships between ventilation patterns and lung function. Our findings suggest that texture-based features provide unique information about early functional changes occurring in the lungs, which may be used alongside established clinical measurements to identify ex-smokers at-risk of accelerated lung function decline.

We identified seven unique texture features residing within hyperpolarized ³He MR ventilation images in order to predict ex-smokers at risk of accelerated lung function decline. Standard MRI-derived measurements were outperformed by MRI texture features during the feature selection step. While model test accuracy was moderate, sensitivity remained high, which underscores the potential of this approach and hyperpolarized noble gas MRI. The values and equations³¹ of extracted LGLZE, SRLGLE and SDLGLE texture features indicate that they collectively measure the distribution of low intensity values, or the clusters and sizes of poorly-ventilated regions. GLCM-Idn and Idmn texture features are measures of heterogeneity and may reflect ventilation patchiness and non-uniformity. The novel extracted CDD1 feature reflects the cumulative number of defect clusters of one voxel in size (5x5x5mm³) and describes defect clusters of low gray-level, or signal void regions. MRI texture analysis provides quantitative information related to the patterns of gas distribution in the ventilated lung; in contrast, the proposed novel measurements

analyze the unventilated regions of the lung, providing a holistic evaluation of the entire thoracic cavity volume on MRI.

Our results showed that MRI ventilation texture features were often selected as the most important features for predicting rapid lung function decline, even in the combined model. Previous studies have shown that CT radiomics features are associated with lung function in COPD,⁸ emphysema severity,⁹ and provide additional complementary information to established quantitative CT measurements.¹⁰ In more recent COPD studies, CT texture features were able to predict rapid lung function decline,¹¹ while the combination of CT and MR imaging texture features were able to predict 10-year mortality risk.⁴⁰ To our knowledge, this study is the first to show that MRI ventilation texture features predict accelerated lung function decline across a relatively short three-year period. Compared to previous studies predicting a clinically-relevant decline in FEV₁ of ≥ 60 mL/year,^{17,18} our proposed model trained exclusively on MRI texture features exhibited a higher performance (AUC=.80) than existing clinical models by Lindberg et al. (AUC=.68)⁴¹ and CT radiomics-based models proposed by Makimoto et al. (AUC=.74).¹¹ Furthermore, the best performing texture feature independently predicted and significantly correlated with longitudinal worsening in lung function. Interestingly, upon investigation only the longitudinal changes in this specific MRI wavelet-based SDLGLE texture feature corresponded and correlated with longitudinal worsening in lung function. We showed that MRI texture features change along with changes in lung function and can differentiate rapid progressors, while previous work showed that MRI textures can also predict future mortality.⁴⁰ Taken together this suggests that MRI texture features offer unique information, not provided by established clinical measurements, and may serve as sensitive imaging biomarkers for early detection of patients at-risk of rapid worsening.

There were several study limitations. Our study included a relatively small sample size and regardless of statistical techniques to prevent overfitting (Univariate analysis, 5-fold cross-validation, Boruta Analysis, etc.), the machine learning classifiers could be optimized using larger datasets in the future. The generalizability could be further enhanced by incorporating an external dataset; thus the generalizability of the machine learning models remains to be evaluated in future studies. Finally, the MR modality use in clinical settings is limited due to the availability and associated costs. Utility of hyperpolarized gas MRI is further limited due to additional personnel and equipment requirements. Therefore, although MRI-derived measurements provide unique prognostic value and are radiation-free, they are not nearly as readily available. However, with the recent FDA regulatory approval for the clinical use of ^{129}Xe and associated equipment, we may see a shift in the near future in the utilization of MRI-derived measurements and biomarkers for evaluating lung diseases.

3.5 Conclusions

For the first time, machine learning and novel texture features from hyperpolarized ^3He MRI ventilation images were used to predict ex-smokers who would experience accelerated FEV_1 decline over a short three-year period. Our work contributes to the growing body of evidence and is an important step for using imaging measurements to generate predictive models of lung function decline in ex-smokers with and without COPD.

3.6 References

- 1 Kirby, M. *et al.* Hyperpolarized ³He magnetic resonance functional imaging semiautomated segmentation. *Acad Radiol* **19**, 141-152, doi:10.1016/j.acra.2011.10.007 (2012).
- 2 Saam, B. T. *et al.* MR imaging of diffusion of ³He gas in healthy and diseased lungs. *Magn Reson Med* **44**, 174-179 (2000).
- 3 Kirby, M. *et al.* Chronic obstructive pulmonary disease: longitudinal hyperpolarized ³He MR imaging. *Radiology* **256**, 280-289 (2010).
- 4 Kirby, M. *et al.* MRI ventilation abnormalities predict quality-of-life and lung function changes in mild-to-moderate COPD: longitudinal TINCan study. *Thorax*, thoraxjnl-2016-209770 (2017).
- 5 Kirby, M. & Smith, B. M. Quantitative CT Scan Imaging of the Airways for Diagnosis and Management of Lung Disease. *Chest* **164**, 1150-1158, doi:10.1016/j.chest.2023.02.044 (2023).
- 6 Kirby, M., Pike, D., Coxson, H. O., McCormack, D. G. & Parraga, G. Hyperpolarized (³)He ventilation defects used to predict pulmonary exacerbations in mild to moderate chronic obstructive pulmonary disease. *Radiology* **273**, 887-896, doi:10.1148/radiol.14140161 (2014).
- 7 Kirby, M. *et al.* Chronic obstructive pulmonary disease: longitudinal hyperpolarized (³)He MR imaging. *Radiology* **256**, 280-289, doi:10.1148/radiol.10091937 (2010).
- 8 Park, Y. S. *et al.* Texture-based quantification of pulmonary emphysema on high-resolution computed tomography: comparison with density-based quantification and correlation with pulmonary function test. *Invest Radiol* **43**, 395-402, doi:10.1097/RLI.0b013e31816901c7 (2008).
- 9 Occhipinti, M. *et al.* Spirometric assessment of emphysema presence and severity as measured by quantitative CT and CT-based radiomics in COPD. *Respir Res* **20**, 101, doi:10.1186/s12931-019-1049-3 (2019).
- 10 Sørensen, L. *et al.* Chronic Obstructive Pulmonary Disease Quantification Using CT Texture Analysis and Densitometry: Results From the Danish Lung Cancer Screening Trial. *AJR Am J Roentgenol* **214**, 1269-1279, doi:10.2214/ajr.19.22300 (2020).
- 11 Makimoto, K., Hogg, J. C., Bourbeau, J., Tan, W. C. & Kirby, M. CT Imaging With Machine Learning for Predicting Progression to COPD in Individuals at Risk. *Chest*, doi:<https://doi.org/10.1016/j.chest.2023.06.008> (2023).
- 12 González, G. *et al.* Disease staging and prognosis in smokers using deep learning in chest computed tomography. *American journal of respiratory and critical care medicine* **197**, 193-203 (2018).
- 13 Li, Z. *et al.* A Novel CT-Based Radiomics Features Analysis for Identification and Severity Staging of COPD. *Acad Radiol* **29**, 663-673, doi:10.1016/j.acra.2022.01.004 (2022).
- 14 Lange, P. *et al.* Lung-Function Trajectories Leading to Chronic Obstructive Pulmonary Disease. *New England Journal of Medicine* **373**, 111-122, doi:doi:10.1056/NEJMoa1411532 (2015).
- 15 Vestbo, J. *et al.* Changes in forced expiratory volume in 1 second over time in COPD. *N Engl J Med* **365**, 1184-1192, doi:10.1056/NEJMoa1105482 (2011).
- 16 Marott, J. L., Ingebrigtsen, T. S., Çolak, Y., Vestbo, J. & Lange, P. Lung Function Trajectories Leading to Chronic Obstructive Pulmonary Disease as Predictors of

- Exacerbations and Mortality. *Am J Respir Crit Care Med* **202**, 210-218, doi:10.1164/rccm.201911-2115OC (2020).
- 17 Tantucci, C. & Modina, D. Lung function decline in COPD. *Int J Chron Obstruct Pulmon Dis* **7**, 95-99, doi:10.2147/copd.S27480 (2012).
- 18 Ramírez-Venegas, A. *et al.* FEV1 decline in patients with chronic obstructive pulmonary disease associated with biomass exposure. *Am J Respir Crit Care Med* **190**, 996-1002, doi:10.1164/rccm.201404-0720OC (2014).
- 19 Lee, H. W. *et al.* Risk Factors of Rapid FEV1 Decline in a Real-World Chronic Obstructive Pulmonary Disease Cohort. *Respiration* **101**, 1078-1087, doi:10.1159/000525871 (2022).
- 20 Kirby, M. *et al.* Longitudinal Computed Tomography and Magnetic Resonance Imaging of COPD: Thoracic Imaging Network of Canada (TINCan) Study Objectives. *Chronic Obstr Pulm Dis* **1**, 200-211, doi:10.15326/jcopdf.1.2.2014.0136 (2014).
- 21 Vestbo, J. *et al.* Global strategy for the diagnosis, management, and prevention of chronic obstructive pulmonary disease: GOLD executive summary. *Am J Respir Crit Care Med* **187**, 347-365, doi:10.1164/rccm.201204-0596PP (2013).
- 22 Miller, M. R. *et al.* Standardisation of spirometry. *Eur Respir J* **26**, 319-338, doi:10.1183/09031936.05.00034805 (2005).
- 23 Kirby, M. *et al.* On the role of abnormal DL(CO) in ex-smokers without airflow limitation: symptoms, exercise capacity and hyperpolarised helium-3 MRI. *Thorax* **68**, 752-759, doi:10.1136/thoraxjnl-2012-203108 (2013).
- 24 Agarwala, P. & Salzman, S. H. Six-Minute Walk Test: Clinical Role, Technique, Coding, and Reimbursement. *Chest* **157**, 603-611, doi:10.1016/j.chest.2019.10.014 (2020).
- 25 Jones, P. W., Quirk, F. H., Baveystock, C. M. & Littlejohns, P. A self-complete measure of health status for chronic airflow limitation. The St. George's Respiratory Questionnaire. *Am Rev Respir Dis* **145**, 1321-1327, doi:10.1164/ajrccm/145.6.1321 (1992).
- 26 Parraga, G. *et al.* Hyperpolarized ³He ventilation defects and apparent diffusion coefficients in chronic obstructive pulmonary disease: preliminary results at 3.0 Tesla. *Invest Radiol* **42**, 384-391, doi:10.1097/01.rli.0000262571.81771.66 (2007).
- 27 Sharma, M., Westcott, A., McCormack, D. & Parraga, G. *Hyperpolarized gas magnetic resonance imaging texture analysis and machine learning to explain accelerated lung function decline in ex-smokers with and without COPD*. Vol. 11600 MI (SPIE, 2021).
- 28 Wang, J. Packing of Unequal Spheres and Automated Radiosurgical Treatment Planning. *Journal of Combinatorial Optimization* **3**, 453-463, doi:10.1023/A:1009831621621 (1999).
- 29 Mishima, M. *et al.* Complexity of terminal airspace geometry assessed by lung computed tomography in normal subjects and patients with chronic obstructive pulmonary disease. *Proceedings of the National Academy of Sciences of the United States of America* **96**, 8829-8834 (1999).
- 30 Capaldi, D. P. *et al.* in *International Society for Magnetic Resonance in Medicine Meeting*.
- 31 van Griethuysen, J. J. M. *et al.* Computational Radiomics System to Decode the Radiographic Phenotype. *Cancer Research* **77**, e104-e107, doi:10.1158/0008-5472.can-17-0339 (2017).
- 32 Rastegar, S. *et al.* Radiomics for classification of bone mineral loss: A machine learning study. *Diagnostic and interventional imaging*, doi:10.1016/j.diii.2020.01.008 (2020).
- 33 Webb, G. I. in *Encyclopedia of Machine Learning* (eds Claude Sammut & Geoffrey I. Webb) 713-714 (Springer US, 2010).

- 34 Cristianini, N. & Ricci, E. in *Encyclopedia of Algorithms* (ed Ming-Yang Kao) 928-932 (Springer US, 2008).
- 35 Quinlan, J. R. Induction of decision trees. *Mach Learn* **1**, 81-106 (1986).
- 36 Cover, T. & Hart, P. Nearest neighbor pattern classification. *IEEE Trans. Inf. Theory* **13**, 21-27 (1967).
- 37 Breiman, L. Bagging predictors. *Mach Learn* **24**, 123-140 (1996).
- 38 Hastie, T. & Tibshirani, R. in *Adv Neural Inf Process Syst.* 409-415.
- 39 DeLong, E. R., DeLong, D. M. & Clarke-Pearson, D. L. Comparing the areas under two or more correlated receiver operating characteristic curves: a nonparametric approach. *Biometrics* **44**, 837-845 (1988).
- 40 Sharma, M., Wyszkievicz, P. V., Matheson, A. M., McCormack, D. G. & Parraga, G. Chest MRI and CT Predictors of 10-Year All-Cause Mortality in COPD. *Copd* **20**, 307-320, doi:10.1080/15412555.2023.2259224 (2023).
- 41 Lindberg, A. *et al.* Decline in FEV1 in relation to incident chronic obstructive pulmonary disease in a cohort with respiratory symptoms. *Copd* **4**, 5-13, doi:10.1080/15412550601168358 (2007).

CHAPTER 4

4 CHEST MRI AND CT PREDICTORS OF 10-YEAR ALL-CAUSE MORTALITY IN COPD

To better understand the predictors of mortality, we evaluated conventional MRI and CT measurements and employed imaging texture analysis to predict all-cause mortality in ex-smokers with and without COPD after 10-years. We investigated if the incorporation of chest MRI and CT texture measurements would provide unique prognostic information and improve mortality risk assessments in these ex-smokers.

The contents of this chapter were previously published in the journal of Chronic Obstructive Pulmonary Disease: M Sharma, PV Wyszkievicz, AM Matheson, DG McCormack and G Parraga. Chest MRI and CT Predictors of 10-Year All-cause Mortality in COPD. Journal of Chronic Obstructive Pulmonary Disease (2023). <https://doi.org/10.1080/15412555.2023.2259224>. This article is available under the terms of the Creative Commons CC BY-NC License.

4.1 Introduction

Chronic obstructive pulmonary disease (COPD) is among the leading causes of global mortality.¹ Currently, mortality risk is predicted using a variety of clinical-based models,²⁻⁴ the most common being the BODE index⁵ (**B**ody-mass-index, **O**bstruction measured via forced-expiratory-volume-in-one-second (FEV₁), **D**yspnea-score and **E**xercise limitation measured via six-minute-walk-distance (6MWD)). A meta-analysis comparing various prognostic clinical models showed that compared to BODE, models based on the Age-Dyspnea-score-FEV₁ (ADO) index⁴ may be stronger, but these were not statistically significantly different at predicting three-year survival.⁶ Decades after the predictions of the Fletcher-Peto model,⁷ the spirometry measurement of FEV₁ remains the clinical measurement of global lung function that helps diagnose and stratify COPD severity.⁸⁻¹⁰

The small airways are considered the major site of airflow limitation in COPD¹¹ and spirometry measured at the mouth is not sensitive to small airway measurements. However, currently chest imaging measurements are not included in clinically-accepted mortality risk assessments,

diagnosis, prognosis, nor staging of COPD. Chest X-ray computed tomography (CT) provides quantitative measurements of airway wall thinning,¹² luminal narrowing and obliteration,¹³ and parenchymal measurements of gas-trapping and terminal airspace enlargement or emphysema.¹⁴ Recent studies stemming from the COPD Genetic Epidemiology study (COPDGene) cohort showed that in ever-smokers with emphysema, emphysema progression over 5-years was associated with all-cause mortality.¹⁵ Emphysema also worsened more quickly in COPD patients with pre-existing emphysema who continued to smoke.¹⁶ In addition, decreased number of distal vascular branches (i.e. pruning) on CT was associated with an increased mortality risk in both COPD and healthy adults.¹⁷ CT measurements of ex vivo lung tissue cores with micro-CT also suggested that COPD may initiate in the small airways and that small airway abnormalities precede the development of emphysema and airflow obstruction.¹⁸⁻²¹

Qualitative visual CT scoring by radiologists shows a stronger association with both pulmonary function and mortality than standard quantitative CT measurements.^{22,23} This could, in part, be explained by visual estimates of emphysema describing both decreased tissue density and complexity of emphysema distribution (and the predominant emphysema type), which may only be identified by a highly-trained chest radiologist.²⁴ Importantly, CT images consist of embedded electron-density textural features, which can be exploited using texture analysis tools to map voxel intensity (attenuation) and spatial relationships²⁵ that are not easily identified by expert observers. In this regard, CT texture analysis and machine-learning tandems have been shown to predict COPD severity,²⁶ progression,²⁷ and showed stronger association with lung function compared to conventional densitometry measures.^{28,29} Imaging textures have also been shown to differentiate emphysema types^{30,31} and provided improved radiological finding assessments as a second-reader.³²

Pulmonary functional magnetic resonance imaging (MRI) using hyperpolarized helium (^3He) and xenon (^{129}Xe) gases provides a way to measure pulmonary microstructure, ventilation, perfusion, and gas-exchange.³³⁻³⁵ In patients with COPD, such MRI measurements of ventilation and parenchyma microstructure^{36,37} are predictive of acute exacerbations,³⁸ airway narrowing and remodeling,³⁹ and symptoms and severity,^{40,41} these measurements also correlate with longitudinal changes in quality-of-life.⁴² Importantly, MRI measurements are sensitive to COPD disease-related changes in patients in whom CT and pulmonary function test results have not changed.^{43,44} In addition, MRI ventilation texture features have been shown to predict longitudinal lung-function decline in ex-smokers with and without COPD.⁴⁵ However, to the best of our knowledge, ventilation and diffusion-weighted MRI measurements and radiomics-based CT/MRI textures have not been investigated for the prediction of 10-year all-cause mortality in ex-smokers with and without COPD.

Given all of this previous evidence, we hypothesized that, regardless of COPD status, incorporating chest MRI and CT measurements and image texture analysis in combination with machine-learning would provide unique prognostic information for mortality risk assessments in ex-smokers. Hence, here we evaluated MRI and CT measurements and employed imaging texture-analysis to predict all-cause mortality in ex-smokers with and without COPD after 10-years.

4.2 Materials and Methods

4.2.1 Study Participants

All participants provided written informed consent to a study protocol approved by a local research ethics board (Institutional Ethics Board #00000984) in compliance with the Health Canada approved and registered protocol (clinicaltrials.gov NCT02279329). All participants were recruited from a tertiary-care academic center and by advertisement in London, Canada between

2009 and 2012 as a convenience sample. These participants were followed for 10-years. Inclusion criteria were age of 50-85 years and a history of cigarette smoking >10 pack-years at baseline visit. Exclusion criteria included current smokers, claustrophobia and any contraindications for MRI or CT. Death dates were obtained from the health electronic record and survival time was calculated from the participant's baseline visit date. Some longitudinal results from this study were previously reported.⁴⁶⁻⁴⁸ In contrast to previous evaluations, this study quantified CT and MR imaging texture features at baseline and their association with 10-year all-cause mortality.

4.2.2 Pulmonary Function Tests and Questionnaires

Spirometry, plethysmography and the diffusing capacity of the lungs for carbon monoxide (DL_{CO}) were measured according to the American Thoracic Society/European Respiratory Society standardization document⁴⁹ using a whole-body plethysmography system (MedGraphics Corporation, St Paul, MN, USA) and attached gas analyzer.⁴⁶ COPD was defined as post-bronchodilator spirometry according to the Global Initiative for Chronic Obstructive Lung Disease (GOLD) criteria.⁵⁰ Abnormal DL_{CO} was defined as DL_{CO} <75%_{pred} as previously reported.⁵¹ The 6MWD⁵² test and St. George's Respiratory Questionnaire (SGRQ)⁵³ were administered under the supervision of study personnel.

4.2.3 CT Acquisition and Analysis

Thoracic CT was acquired using a 64-slice Lightspeed VCT scanner (GE Healthcare, Milwaukee, WI, USA) (64 × 0.625 mm, 120 kVp, 100 effective mA, tube rotation time= 500 ms, pitch= 1.25, reconstructed using a standard convolution kernel to 1.25 mm slice thickness, slices= 200-250), as previously described.⁵⁴ Images were acquired in the supine position under breath-hold after inhalation of a 1L bag of N₂ (from FRC lung volume) in order to match the lung volume for MRI.

Total effective dose was estimated as 1.8 mSv using the ImpACT CT patient dosimetry calculator (Health Protection Agency [UK] NRBP-SR250). CT data were quantitatively evaluated using VIDAvision2.2 software (VIDA Diagnostics Inc., Coralville, IA, USA) to quantify lung density using the relative area of lung less than -950 Hounsfield units (RA_{950}), total lung volume (TLV) and create a binary lung mask. CT vessel measurements were automatically generated using Chest Imaging Platform (Brigham and Women's Hospital, Boston MA).⁵⁵

4.2.4 MRI Acquisition and Analysis

Anatomic proton (^1H) and hyperpolarized ^3He MR images were acquired using a whole-body 3.0 Tesla Discovery MR750 system (GE Healthcare, Milwaukee, WI, USA), a whole-body radiofrequency coil and a fast gradient recalled echo (FGRE) sequence with a partial echo implementation, with acquisition parameters as previously described.⁵⁶ Hyperpolarized ^3He MRI was acquired using a linear bird-cage transmit/receive chest coil (RAPID Biomedical GmbH, Wuerzburg, Germany). A commercial system (HeliSpinTM, Polarean Inc, Durham, NC, USA) was used to polarize ^3He gas to 30–40% and doses (5 mL/kg body weight) diluted with N_2 were administered in 1L Tedlar[®] bags (from FRC lung volume). Hyperpolarized ^3He MRI diffusion-weighted imaging was performed using a 2D multi-slice fast gradient-echo method, as previously described,⁵⁶ during breath-hold for acquisition of two interleaved images with and without additional diffusion sensitization with $b=1.6 \text{ sec/cm}^2$ (maximum gradient amplitude $[G]=1.94 \text{ G/cm}$, rise and fall-time=0.5 ms, gradient duration=0.46 ms, diffusion time=1.46 ms).⁴⁸

MR images were evaluated for the measurement of ventilation defect percent (VDP) using semi-automated custom-built software, as previously described.³⁶ Briefly, the anatomic ^1H and functional ^3He images were first co-registered to segment and remove the large airways (trachea), then a k-means clustering approach was used to generate ventilation clusters, with the lowest

cluster representing ventilation defects as previously described.³⁶ Ventilation abnormalities were quantified as the ventilation defect volume (VDV) and VDP was calculated as VDV normalized to the MRI-measured volume of the thoracic cavity.³⁶ Diffusion-weighted images were automatically processed to generate apparent diffusion coefficient (ADC) values and images, after the removal of the large airways, as previously described.⁴⁶ Abnormal ³He ADC was defined as ADC >0.25 cm²/s, as previously reported.^{57,58}

4.2.5 Texture Feature Extraction, Selection and Machine-learning

CT images were first pre-processed by extracting the lungs and removing the large airways using the binary lung mask generated from the segmented CT images. Signal normalization was applied to the MR images, while a threshold between -1000 Hounsfield Units (HU) and 0 HU was applied to the CT images. The binary mask was applied to the segmented CT images in order to create regions of interest (ROI) for feature extraction. Similarly, the ROI from MR images was generated using the binary lung mask created by co-registering the ¹H and ³He MRI acquisitions, as previously described.⁴⁵ Next, 110 unique, unfiltered texture features were extracted in a voxel-by-voxel manner from CT and MR images using the open-source PyRadiomics platform (version 2.2.0).⁵⁹ For the best compromise between differentiation and resolution, a fixed bin number (FBN) discretization approach⁶⁰ was utilized to extract features between CT and MR modalities and ensure that textures are assessed against similar contrasts within the modality ROI, as previously described.⁶¹ Histogram and shape, first-, and higher-order texture features from run-length, gap-length, size-zone, neighborhood-dependence and co-occurrence matrices were computed. In addition, 376 wavelet-based texture features were extracted using four high- and low-pass filter combinations applied to the original image in x- and y-directions for wavelet decomposition.⁶²

To maximize the model generalizability and avoid overfitting, a combination of principal component analysis (PCA) and Boruta analysis⁶³ were implemented for feature selection. Feature selection step is primarily required for removing any redundant features and/or misleading data for improved modelling accuracy and also used for dimensionality reduction of data, enabling more efficient computations. Feature selection included the generation of nine components from PCA, which explained >94% of the variance in the data. Components were generated using principal component scores for each participant using a Varimax rotation method with Kaiser-normalization that converged after 38 iterations.

All variables in the models, including the texture features and emergent components generated for every participant, were subjected to Boruta analysis for ranking. The Boruta algorithm generated shadow features for comparisons and used a two-step correction for multiple testing, with an optimizable random forest classifier for iterations (number of trees in the forest=150, maximum iterations=200, maximum tree depth=10 [branches], percentage of shadow feature threshold=95%, alpha-level=0.05).

Once all the features and parameters were selected, four machine-learning models were generated using: 1) clinical measurements, 2) imaging measurements, 3) image texture measurements, and 4) a combination of all available measurements. Five-fold cross-validation was performed to avoid overfitting or selection bias of the machine-learning models during the training step. During cross-validation, all participant data (n=162) were randomly and evenly divided into five groups (n=32/33) and for each of the “folds”, one group was withheld for testing and remaining groups were used for training iteratively. Each fold utilized a different combination of testing and training groups in order to avoid data contamination and insure that no information was carried over from training to testing steps. Single (Naïve Bayes,⁶⁴ Support Vector Machines [SVM],⁶⁵ Decision

Trees,⁶⁶ K-Nearest Neighbours [KNN]⁶⁶) and ensemble (Bagged Trees,⁶⁷ subspace Discriminant,⁶⁸ subspace K-Nearest-Neighbours,⁶⁸ and Random Under-Sampling Boosted Trees [RUSBoosted]⁶⁹) machine-learning classifiers were implemented for predicting 10-year all-cause mortality in ex-smokers. Data were standardized and hyperparameter search was performed using MATLAB2021a (Classification Learner App) for every machine-learning model. Classification performance was evaluated using the mean of the respective 5-fold cross-validation area under the receiver-operator characteristic curve (AUC), as well as sensitivity and specificity calculated from model's confusion matrix.

4.2.6 Statistical Analysis

Statistical analysis was performed using SPSS Statistics v28.0 (IBM Statistics, Armonk, New York, USA). Predictors of 10-year all-cause mortality were evaluated using binary logistic regression to generate odds ratios (OR). Shapiro-Wilk tests were used to determine the normality of the data. The p-value significance was determined using the Mann-Whitney U-test for non-parametric data, and a post-hoc analysis using Holm-Bonferroni correction was applied for multiple comparison tests for the selected texture features. Statistical significance was considered using a 5% Type-I error threshold ($p < 0.05$).

4.3 Results

4.3.1 Participant Demographics and Mortality

A CONSORT diagram provided in **Figure 4-1** shows that 266 ex-smokers were enrolled and 99 were excluded from analysis due to enrollment in a sub-study using oscillatory positive expiratory pressure device ($n=33$), due to cancellation or not completing all protocol tests ($n=61$), and due to poor image quality ($n=5$). In addition, five participants were excluded because 10-year follow-up

was outside the Dec 2009-2022 window. As shown in **Figure 4-2**, the last participant enrolled on December 12th 2012 and the mortality data window closed on December 13th, 2022.

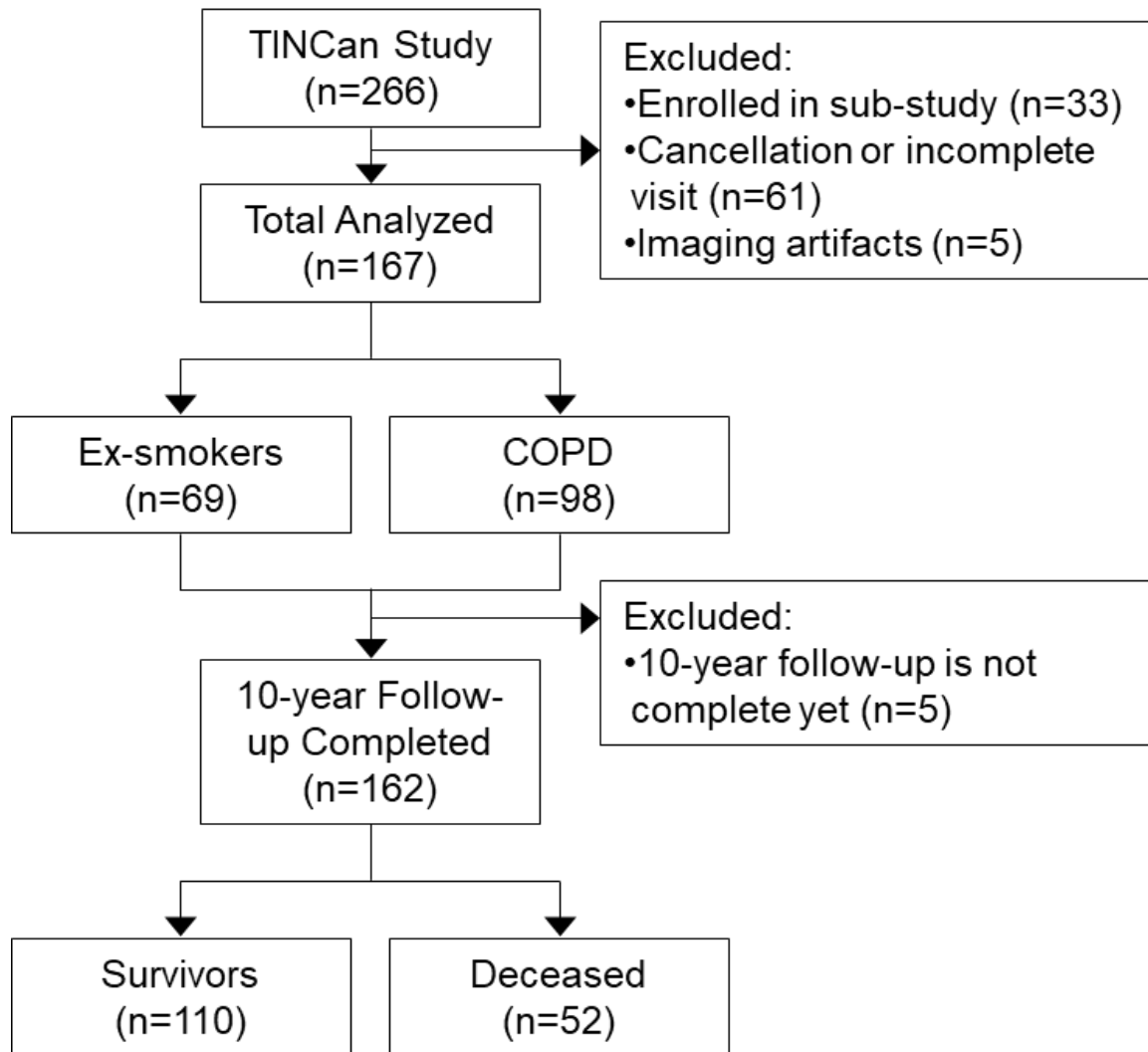


Figure 4-1. CONSORT flow diagram

Of the 266 participants enrolled in the TINCan study, 33 were enrolled in a sub-study, 61 either cancelled or did not complete all required tests during visit 1, and five had CT or MRI artifacts which precluded analysis. Of the 167 participants who completed Visit 1, five were not yet within their 10-year follow-up timeframe. At follow-up, there were 52 deceased participants, of whom 14 were ex-smokers and 38 were ex-smokers with COPD.

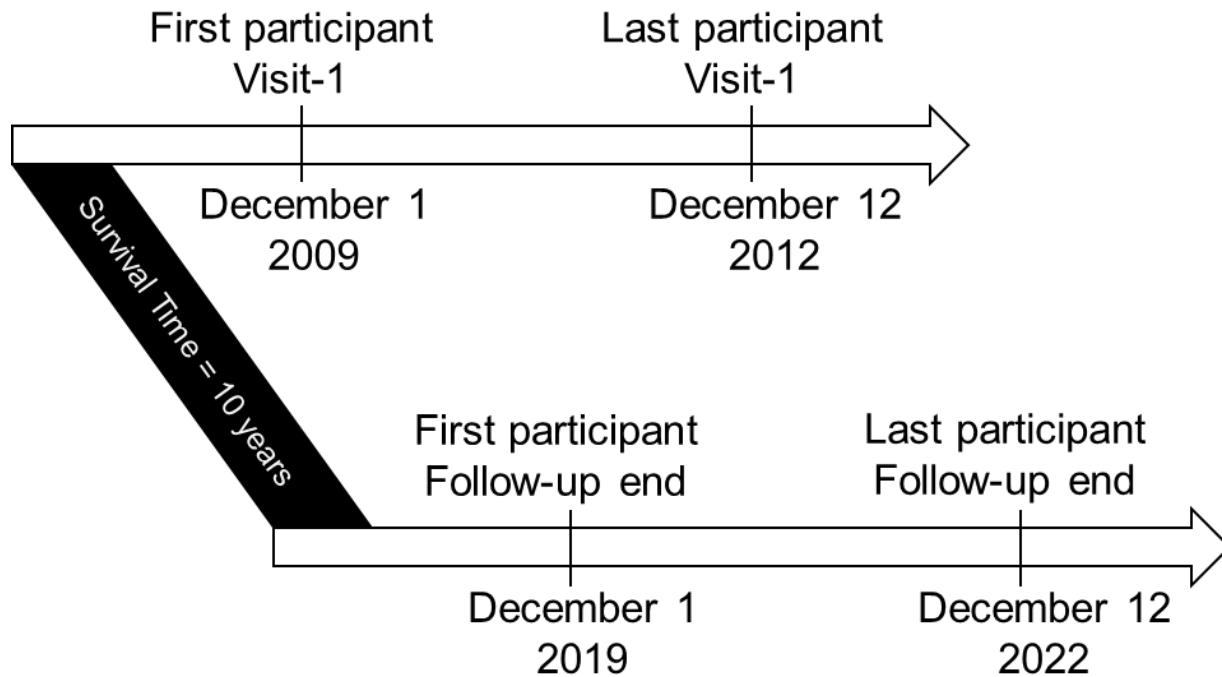


Figure 4-2. Participant enrollment and follow-up timeframe

Arrows showing the timeline of participant enrolment and follow-up period for mortality data collection within 10-years from the initial visit in all ex-smoker participants. Of the 162 ex-smokers analyzed, the first participant completed the baseline visit on December 1st, 2009 and the last participant completed their baseline visit on December 12th, 2012.

Demographic, clinical and imaging data for survivor and deceased ex-smoker subgroups are provided in **Table 4-1** and summarized by COPD status in **Table 4-5** (online supplement). In total, 162 ex-smokers were evaluated, including 93 ex-smokers with spirometry evidence of COPD and 69 ex-smokers without COPD. As shown in **Table 4-1**, 52/162 (32%) ex-smokers died within the 10-year window. Just over half of these (20/52, 53%) had CT evidence of emphysema, defined by the published threshold, $RA_{950} > 6.8\%$.⁷⁰ There were no significant differences between survivors and deceased participants for sex, pack-years, total lung capacity, and the CT measurements of emphysema (lowest attenuating cluster) and the pulmonary vasculature (total blood volume, volume of blood in small and mid-sized vessels).

Table 4-1. Participant demographics, pulmonary function and imaging measurements in survivors and deceased ex-smokers

Parameter mean(±SD)	All (n=162)	Survivors (n=110)	Deceased (n=52)	p-value
Age [years]	71 (9)	69 (9)	73 (8)	.001
Females [n(%)]	62 (37)	42 (36)	20 (38)	.3
Pack Years	39 (25)	37 (23)	41 (27)	.4
BMI [kg/m ²]	28 (4)	28 (4)	26 (5)	.01
FEV ₁ [%pred]	80 (22)	81 (25)	65 (30)	.001
FEV ₁ /FVC	60 (18)	66 (16)	53 (21)	<.001
TLC [L]	6.6 (1.3)	6.7 (1.2)	6.5 (1.5)	.3
RV/TLC	47 (11)	44 (12)	52 (11)	.001
DL _{CO} [%pred]	63 (22)	70 (21)	49 (19)	<.001
6MWD [meters]	384 (97)	407 (81)	335 (104)	<.001
SGRQ [score]	33 (21)	29 (20)	44 (19)	<.001
Without COPD [n(%)]	69 (41)	55 (48)	14 (27)	.007
With COPD [n(%)]	98 (59)	60 (52)	38 (73)	.01
GOLD Severity				
GOLD I [n(%)]	22 (14)	17 (15)	5 (9)	.3
GOLD II [n(%)]	42 (26)	29 (26)	13 (25)	.7
GOLD III [n(%)]	22 (14)	8 (7)	14 (27)	.004
GOLD IV [n(%)]	7 (4)	1 (1)	6 (11)	-
<i>CT and MR Imaging Measurements</i>				
³ He VDP [%]	13 (10)	11 (9)	16 (11)	.002
³ He ADC [cm ² /s]	.35 (.11)	.32 (.09)	.41 (.12)	<.001
HU15 th Percentile	-914 (33)	-908 (29)	-927 (26)	.005
LAC	-1.9 (.3)	-1.9 (.3)	-1.8 (.3)	.1
TBV [ml]	265 (59)	264 (57)	272 (73)	.2
BV ₅ [ml]	115 (28)	117 (26)	109 (31)	.07
BV ₅₋₁₀ [ml]	60 (16)	59 (14)	62 (20)	.3
BV ₁₀ [ml]	89 (32)	86 (3)	101 (4)	.007
BV ₅ /TBV [%]	44 (8)	45 (7)	40 (9)	.003
BV ₅₋₁₀ /TBV [%]	22 (3)	22 (3)	22 (4)	.7
BV ₁₀ /TBV [%]	33 (6)	32 (5)	36 (8)	<.001
RA ₉₅₀ [%]	6.8 (9.2)	4.6 (6.1)	11.7 (12.5)	<.001
Emphysema [n(%)]	50 (31)	30 (25)	20 (53)	.03

BMI=body mass index; FEV₁=forced expiratory volume in 1 second; %_{pred}=percent of predicted value; FVC=forced vital capacity; RV=residual volume; TLC=total lung capacity; DL_{CO}=diffusing capacity of lung for carbon-monoxide; 6MWD=six minute walk distance; SGRQ=St. George's respiratory questionnaire; GOLD= Global Initiative for Chronic Obstructive Lung Disease; TBV=Total blood volume; BV₅=vessel volume for vessels less than 5 mm²; BV₅₋₁₀=vessel volume for vessels between 5-10 mm²; BV₁₀=vessel volume for vessels greater than 10 mm²; LAC=lowest attenuating cluster; RA₉₅₀=relative area of lung less than -950 Hounsfield Units; ADC=apparent diffusion coefficient; VDP=ventilation defect percent.

p=uncorrected values showing significant differences between survivor and deceased ex-smokers.

4.3.2 Texture Extraction and Selection

Table 4-2 shows the six MRI and seven CT texture features which were the highest performing machine-learning predictors of 10-year all-cause mortality. Texture feature predictors were grouped into fine and coarse textures based on their mathematical definitions and are described in **Table 4-6**. As shown in **Table 4-7**, most of these texture features were significantly correlated with clinically-relevant measures (BMI, FEV₁, 6MWD, and SGRQ). **Figure 4-3** and **Figure 4-4** provide context for the CT and MRI textures respectively. **Figure 4-3** shows coronal chest CT slices and in the inserts, representative ROI and example textures. In the survivor with COPD (top panel: S13), there was negligible CT evidence of emphysema (RA₉₅₀=10.8%) and the CT texture was visually homogeneous (eg. GLCM-Imc2=.77) similar to a survivor without COPD (top panel: S11, GLCM-Imc2=.76). In contrast, for the deceased ex-smoker with COPD and quantitative evidence of emphysema (RA₉₅₀=24.9%) (bottom panel: S35, GLCM-Imc2=.84) and deceased ex-smoker with no evidence of COPD (bottom panel: S50, GLCM-Imc2=.82), CT textures appeared patchy and heterogeneously coarse.

Table 4-2. MRI and CT texture features in survivors and deceased ex-smokers

Parameter Mean (±SD)	All (n=162)	Survivors (n=110)	Deceased (n=52)	*p-value
Coarse textures				
MRI FO-Skewness	.77 (.46)	.63 (.38)	1.06 (.49)	<.001
MRI Shape-SVR	.49 (.10)	.47 (.09)	.52 (.13)	.02
MRI W-LL-FO-Kurtosis	3.68 (2.06)	3.25 (0.99)	4.58 (3.17)	.01
MRI W-LL-Cluster Shade	673 (765)	465 (539)	1110 (970)	<.001
MRI W-LL-FO-Skewness	.75 (.47)	.61 (.38)	1.04 (.49)	<.001
MRI GLCM-Idn	.996 (.001)	.996 (.001)	.995 (.001)	<.001
CT Shape-Sphericity	.455 (.069)	.447 (.060)	.473 (.084)	.052
CT RLM-Run Percentage	.944 (.009)	.948 (.010)	.940 (.013)	.001
Fine textures				
CT GLCM-Imc1	-.09 (.03)	-.09 (.02)	-.11 (.02)	<.001
CT GLCM-Imc2	.79 (.06)	.77 (.05)	.82 (.06)	<.001
CT W-HH-GLDM-DV	.80 (0.24)	.74 (0.21)	.92 (0.26)	<.001
CT W-HH-Run Variance	.12 (.05)	.11 (.04)	.15 (.05)	<.001
CT W-LL-GLCM-Imc1	-.12 (.02)	-.12 (.01)	-.14 (.02)	<.001

VDP=ventilation defect percent; ADC=apparent diffusion coefficient; LAC=lowest attenuating cluster; TBV=Total blood volume; BV_5 =vessel volume for vessels less than 5 mm²; BV_{5-10} =vessel volume for vessels between 5-10 mm²; BV_{10} =vessel volume for vessels greater than 10 mm²; RA_{950} =relative area of lung less than -950 Hounsfield Units; FO=first order features; SVR=surface to volume ratio; W=wavelet; GLCM=gray level co-occurrence matrix; Idn=inverse difference normalized; LL=low-low-pass filter; HH=high-high-pass filter; RLM=run length matrix; Imc2=informational measure of correlation; GLDM=gray level dependence matrix; DV=dependence variance; All selected texture feature abbreviations and descriptions can be found in supplementary Table 4-6.

*Holm-Bonferroni corrected *p*-values.

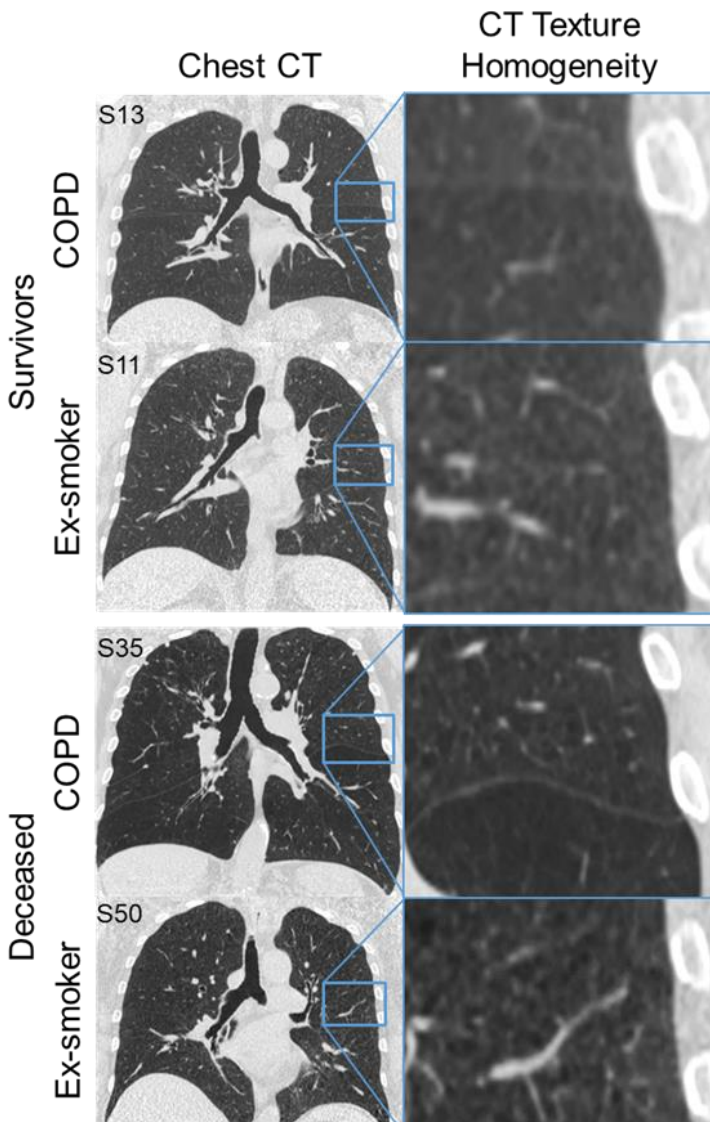


Figure 4-3. Chest CT for representative surviving and deceased ex-smokers with and without COPD

Coronal center-slice of chest CT and the corresponding qualitative CT texture heterogeneity. Top panel: A 63 yo male ex-smoker with COPD: $FEV_1=72\%_{pred}$, $FEV_1/FVC=50$, $BMI=27\text{ kg/m}^2$, $DLCO=79\%_{pred}$, $ADC=0.38\text{ cm}^2/\text{s}$, $VDP=10\%$, $RA_{950}=10.8\%$, $GLCM-Imc2=.77$, $Wavelet-HH-GLDM-DV=.812$; And a 66 yo female ex-smoker: $FEV_1=80\%_{pred}$, $FEV_1/FVC=76$, $BMI=36$

kg/m², DL_{CO}=80%_{pred}, ADC=0.24 cm²/s, VDP=5.4%, RA₉₅₀=2.3%, GLCM-Imc2=.76, Wavelet-HH-GLDM-DV=.766; Bottom panel: A 78 yo male ex-smoker with COPD that died: FEV₁=38%_{pred}, FEV₁/FVC=39, BMI =20 kg/m², DL_{CO}=30%_{pred}, ADC=0.55 cm²/s, VDP=28%, RA₉₅₀=24.9%, GLCM-Imc2=.84, Wavelet-HH-GLDM-DV=1.14; And a 64 yo female ex-smoker that died: FEV₁=111%_{pred}, FEV₁/FVC=82, BMI=36 kg/m², DL_{CO}=68%_{pred}, ADC=0.26 cm²/s, VDP=4.5%, RA₉₅₀=1.2%, GLCM-Imc2=.82, Wavelet-HH-GLDM-DV=1.02.

Figure 4-4 shows coronal MRI ADC and ventilation slices and in the inserts, representative ROI and example MRI ventilation textures. In the representative survivor with COPD (top panel: S13, mean ADC=0.38 cm²/s, VDP= 10%, Wavelet-LL-FO-Skewness=.58) and survivor without COPD (top panel: S11, mean ADC=0.24 cm²/s, VDP=5.4%, Wavelet-LL-FO-Skewness=.81), MRI ventilation textures were visibly homogenous. In contrast, in the deceased ex-smoker with COPD (bottom panel: S35, mean ADC=0.55 cm²/s, VDP=28%, Wavelet-LL-FO-Skewness=2.1) and ex-smoker without COPD (bottom panel S50, mean ADC=0.26 cm²/s, VDP=4.5%, Wavelet-LL-FO-Skewness=1.25), MRI ventilation textures were heterogeneous and patchy.

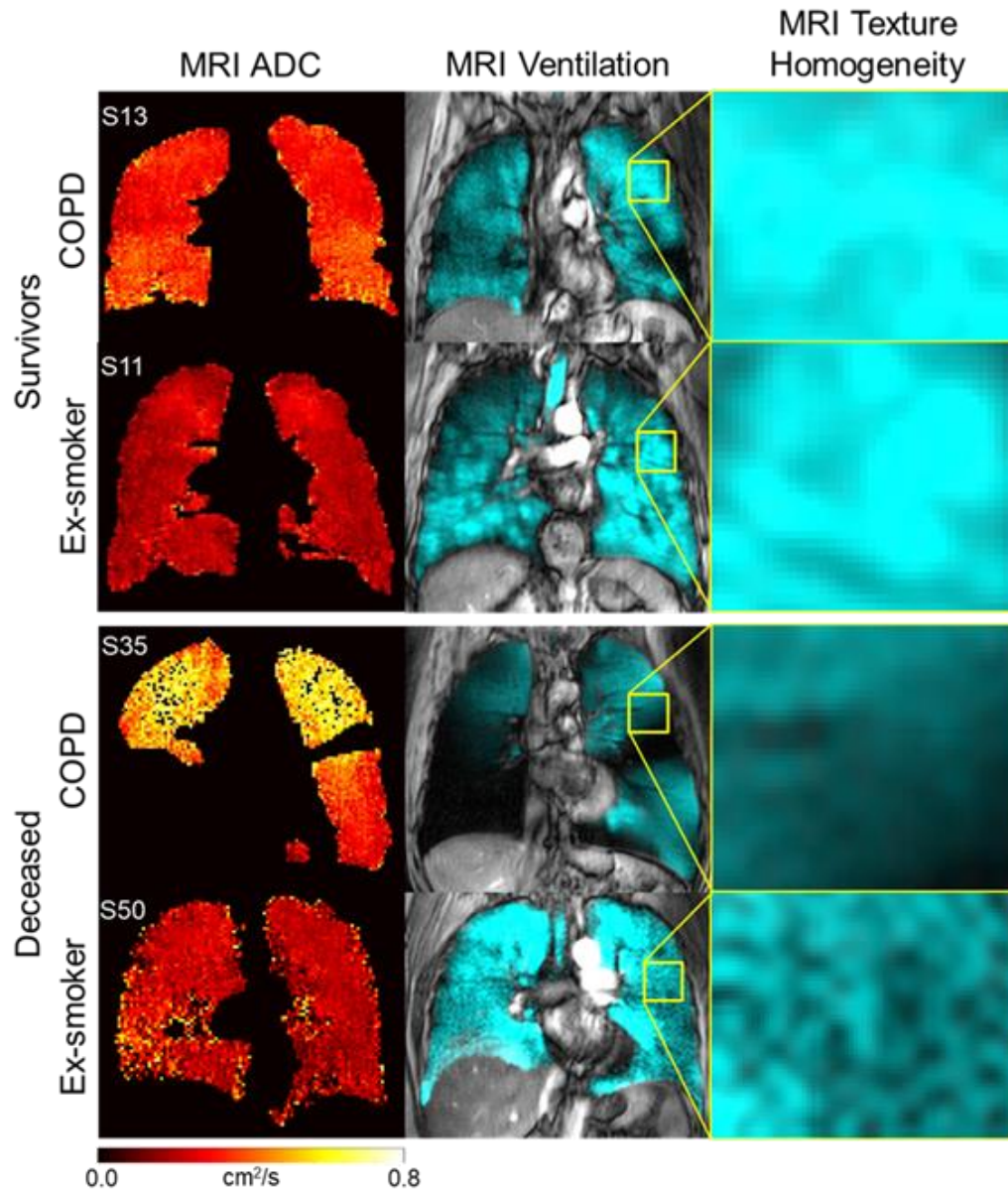


Figure 4-4. Hyperpolarized gas MRI for representative surviving and deceased ex-smokers with and without COPD

Coronal center-slice of MRI ADC and ventilation with corresponding qualitative and quantitative MRI texture heterogeneity. Top panel: A 63 yo male ex-smoker with COPD: $FEV_1=72\%_{pred}$, $FEV_1/FVC=50$, $BMI=27 \text{ kg/m}^2$, $DLCO=79\%_{pred}$, $ADC=0.38 \text{ cm}^2/\text{s}$, $VDP=10\%$, $RA_{950}=10.8\%$, $Shape-SVR=.43$, $Wavelet-LL-Skewness=0.58$; And a 66 yo female ex-smoker: $FEV_1=80\%_{pred}$, $FEV_1/FVC=76$, $BMI=36 \text{ kg/m}^2$, $DLCO=80\%_{pred}$, $ADC=0.24 \text{ cm}^2/\text{s}$, $VDP=5.4\%$, $RA_{950}=2.3\%$, $Shape-SVR=.45$, $Wavelet-LL-Skewness=.81$; Bottom panel: A 78 yo male ex-smoker with COPD that died: $FEV_1=38\%_{pred}$, $FEV_1/FVC=39$, $BMI=20 \text{ kg/m}^2$, $DLCO=30\%_{pred}$, $ADC=0.55 \text{ cm}^2/\text{s}$, $VDP=28\%$, $RA_{950}=24.9\%$, $Shape-SVR=.62$, $Wavelet-LL-Skewness=2.1$; And a 64 yo female ex-smoker that died: $FEV_1=111\%_{pred}$, $FEV_1/FVC=82$, $BMI=36 \text{ kg/m}^2$, $DLCO=68\%_{pred}$, $ADC=0.26 \text{ cm}^2/\text{s}$, $VDP=4.5\%$, $RA_{950}=1.2\%$, $Shape-SVR=.48$, $Wavelet-LL-Skewness=1.25$.

4.3.3 Predicting 10-year All-cause Mortality

As shown in **Table 4-3**, machine-learning prediction models for 10-year all-cause mortality were generated using: 1) clinical measurements, 2) imaging measurements, 3) image texture measurements, and 4) a combination of clinical and imaging measurements. The best performing clinical model (77% accuracy) was based on age, pack years, BMI, FEV₁ %_{pred}, TLC, DL_{CO} %_{pred}, 6MWD and SGRQ score. The best performing imaging-based model (77% accuracy), included MRI VDP and ADC as well as CT HU15th percentile, TBV, BV₅/TBV, BV₁₀, BV₁₀/TBV, and %RA₉₅₀. The predictive model based exclusively on imaging texture features outperformed both clinical and imaging-based models (80% accuracy). Finally, the combined clinical-imaging model had the overall best performance (83% accuracy) which included: DL_{CO}, MRI ADC, as well as MRI and CT texture features.

Table 4-3. Machine-learning performance at predicting all-cause mortality after 10-years

Best Performing Models	AUC	Sensitivity (%)	Specificity (%)	Accuracy (%)
Clinical model†				
Medium Gaussian SVM	0.76	76.8	79.1	77.2
Imaging model‡				
Cosine KNN	0.75	77.7	71.8	76.5
Texture-based model§				
Subspace KNN	0.80	80.4	79.4	80.2
Combined model↓				
Subspace Discriminant	0.82	82.8	84.3	83.3

AUC=area under the receiver-operating curve; KNN=K-nearest neighbours; SVM=support vector machine.

†Variables used for training included: Age, Pack years, BMI, %_{pred} FEV₁, TLC, %_{pred} DL_{CO}, 6MWD and SGRQ score.

‡Variables used for training included: ³He VDP, ³He ADC, HU15th percentile, TBV, BV₅/TBV, BV₁₀, BV₁₀/TBV, and % RA₉₅₀.

§Features selected for training included: MRI wavelet-low-low-First-order-Skewness, MRI wavelet-low-low-kurtosis, CT gray level co-occurrence matrix (GLCM)-informational measure of correlation (Imc2), CT wavelet-high-high-gray-level dependence matrix (GLDM)-dependence variance, CT wavelet-high-high-Run variance, CT wavelet-low-low-first-order-skewness, CT wavelet-low-low-GLCM-Imc1.

↓Combined model included: DL_{CO}, ADC, MRI Wavelet-LL-FO-Skewness, CT LL-GLCM-Imc1, CT Shape-Sphericity, CT Wavelet-HH-GLDM-Dependence variance and MRI Wavelet-LL-FO-Kurtosis.

In **Figure 4-5**, logistic regression models are shown in receiver operator characteristic (ROC) curves of all-cause mortality for individual clinical (top panel), imaging (middle panel) and imaging texture (lower panel) measurements. The best performing individual measurements included DL_{CO} (AUC=.736), MRI ADC (AUC=.738) and CT Wavelet-LL-GLCM-Imc1 (AUC=.787).

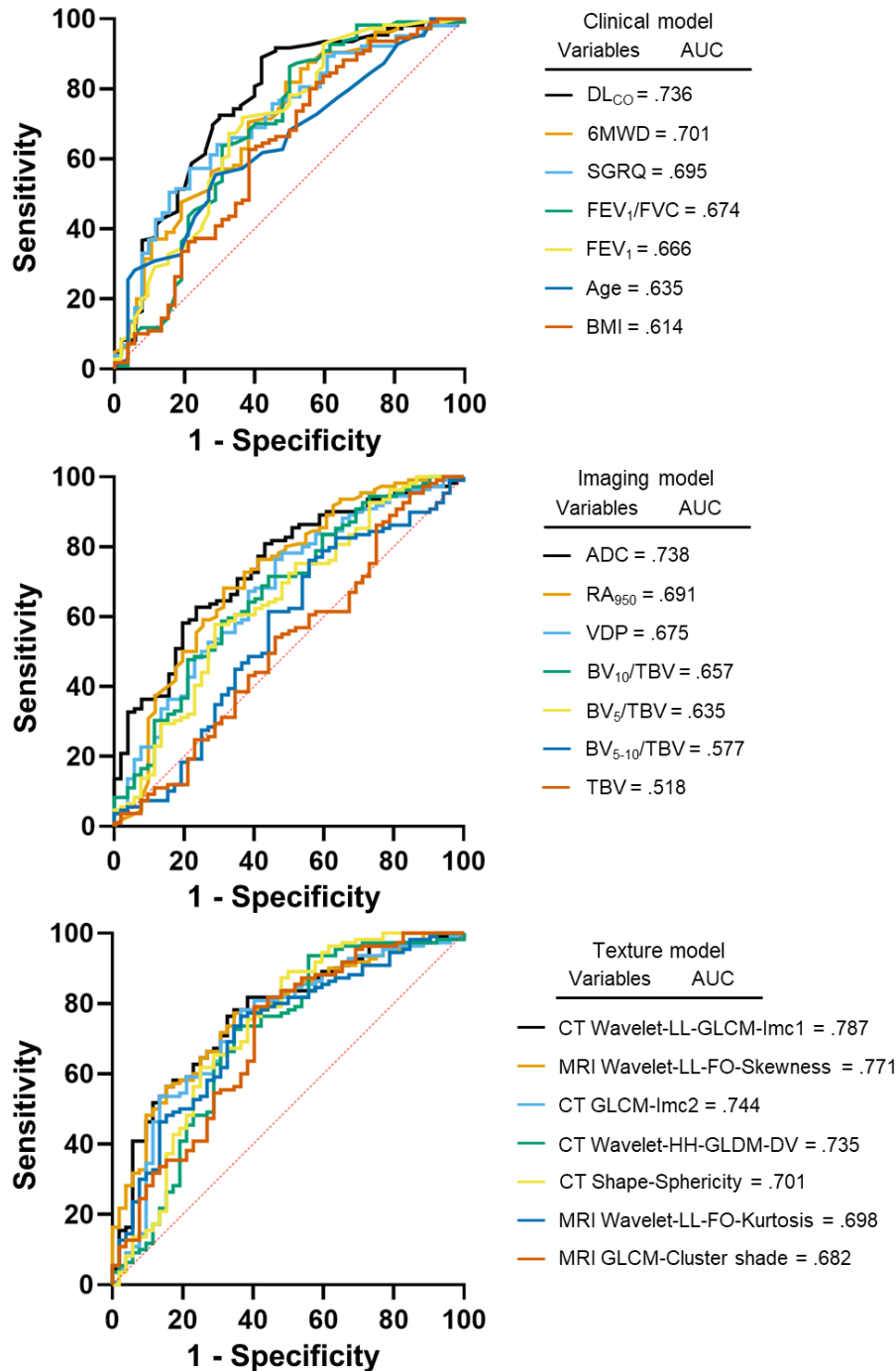


Figure 4-5. Receiver-operator characteristic curves of texture features and clinical variables
 Top Panel: Logistic regression analysis of individual clinical variables at predicting 10-year all-cause mortality in ex-smoker participants. DL_{CO} had the best AUC=.736.
 Middle Panel: Logistic regression analysis of standard imaging measurements at predicting 10-year all-cause mortality in ex-smoker participants. ³He ADC had the best AUC=.738.
 Bottom Panel: Logistic regression analysis of imaging texture features at predicting 10-year all-cause mortality in ex-smoker participants. CT Wavelet-LL-GLCM-Imc1 had best AUC=.787.

Figure 4-6 shows a forest plot for associations adjusted for confounders (age, BMI, sex, and pack-years). The increased risk of 10-year all-cause mortality was strongly associated with the CT texture feature GLCM-Imc2 (OR=3.546 [per 0.1 change], $p=.001$) and MRI ADC (OR=1.843 [per 0.1 cm^2/s change], $p<.001$).

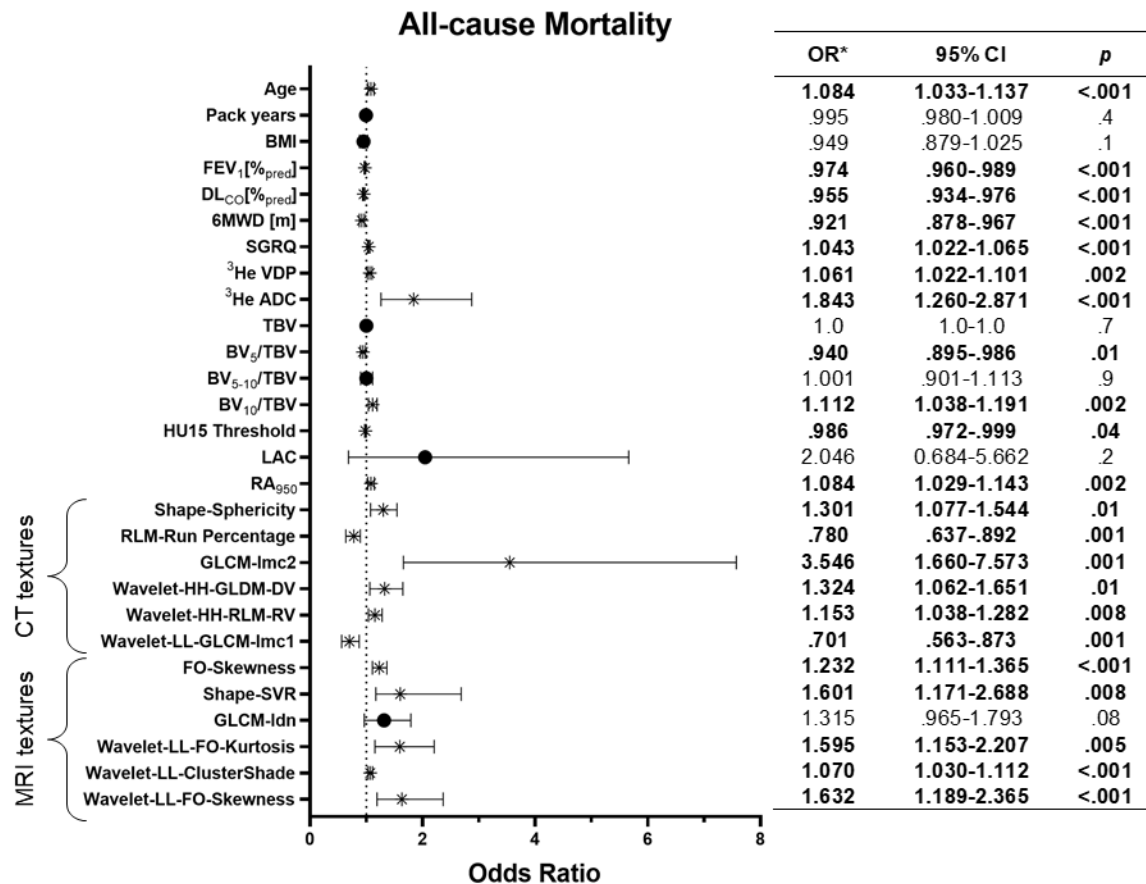


Figure 4-6. Logistic regression models for associations between all-cause mortality and clinical, imaging and textural measurements

All-cause mortality assessment was conducted in 162 ex-smokers, of whom 52 deceased across the longitudinal study duration (10-years). Bolded values indicate categories where 95% CI did not include 1.0 ($P<0.05$). *All odds ratios were adjusted for age, BMI, sex, and pack-years.

GLCM=gray level co-occurrence matrix; 6MWD=six minute walk distance; ADC=apparent diffusion coefficients; DL_{CO}=diffusing capacity of the lung for carbon monoxide; GLDM=gray level dependence matrix; HH=high-high pass filter; LL=low-low pass filter; SVR=Surface volume ratio; DV=dependence variance; RV=run variance; FEV₁=forced expiratory volume in 1 second; FVC=forced vital capacity; SGRQ=St. George's respiratory questionnaire; LAC=lowest attenuating cluster; RA₉₅₀=relative area of lung less than -950 Hounsfield Units; All texture feature abbreviations and descriptions can be found in supplementary Table 4-6.

Kaplan-Meier curves provided in **Figure 4-7** show that ex-smokers with abnormal DL_{CO}, (log-rank $\chi^2=11.95$, $p<.001$), MRI ADC (log-rank $\chi^2=6.38$, $p=.01$) and an MRI texture (highest tertile wavelet-LL-FO-Skewness; $\chi^2=21.81$, $p<.001$) had a significantly greater risk of death.

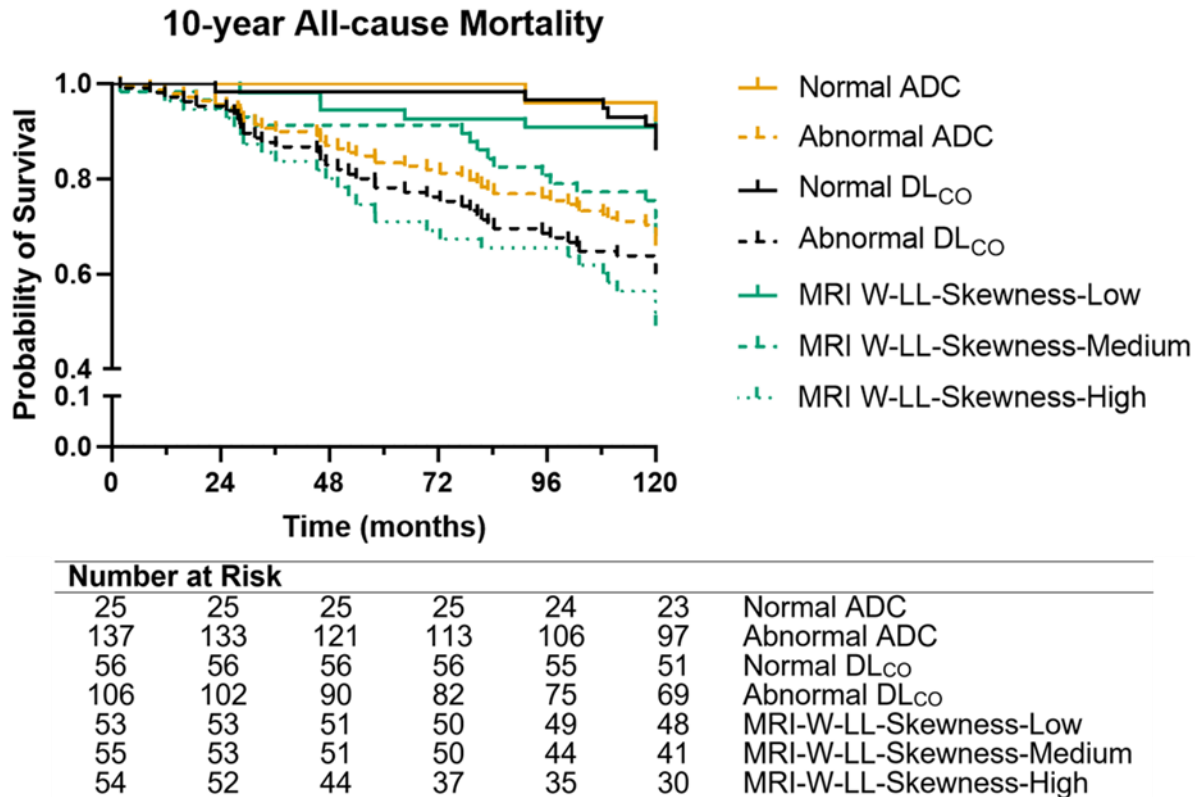


Figure 4-7. Kaplan-Meier survival curves of 10-year all-cause mortality in ex-smokers

Orange: All-cause mortality analysis in ex-smokers with normal vs abnormal MRI ADC

(ADC<0.25cm²/s). Log-rank (Mantel-Cox) test $\chi^2=6.38$; $P=.01$.

Black: All-cause mortality analysis in ex-smokers with normal vs abnormal DL_{CO} (DL_{CO}<75%_{pred}). Log-rank (Mantel-Cox) test $\chi^2=11.95$; $P<.001$.

Green: All-cause mortality analysis in ex-smokers with tertiles of the MRI Wavelet-LL-FO-Skewness texture feature. Log-rank (Mantel-Cox) test across all tertiles: $\chi^2=22.43$; $P<.001$. Log-rank test between tertile-Low and tertile-Medium: $\chi^2=7.86$; $P=.005$. Log-rank test between tertile-Medium and tertile-High: $\chi^2=4.99$; $P=.02$. Log-rank test between tertile-Low and tertile-High: $\chi^2=21.81$; $P<.001$.

Table 4-4 summarizes the best performing measurements in descending order, across the key statistical tests and models generated. The common top performing measurements were DL_{CO}, MRI-ADC, MRI-Wavelet-LL-FO-Skewness and CT-GLCM-Imc2.

Table 4-4. Summary of top performing measurements for the key statistical analyses

<i>Statistical Test</i>	<i>Measurement</i>	<i>Result</i>
ROC analysis	CT-W-GLCM-Imc1	AUC=0.787
	MRI-W-Skewness	AUC=0.771
	CT-GLCM-Imc2	AUC=0.744
	ADC	AUC=0.738
	DL _{CO}	AUC=0.736
	RA ₉₅₀	AUC=0.691
Logistic regression analysis	CT-GLCM-Imc2	OR=3.55
	ADC	OR=1.84
	MRI-W-Skewness	OR=1.63
	MRI-SVR	OR=1.60
	MRI-W-Kurtosis	OR=1.59
	DL _{CO}	OR=0.955
Kaplan-Meier analysis	MRI-W-Skewness	$\chi^2=21.81$ (1 st vs 3 rd tertile)
	CT-GLCM-Imc2	$\chi^2=17.67$ (1 st vs 3 rd tertile)
	DL _{CO}	$\chi^2=11.95$
	ADC	$\chi^2=6.38$
Combined ML model	MRI-W-Skewness	AUC=0.82
	CT W-GLCM-Imc1	Sensitivity=82.8%
	CT Shape-Sphericity	Specificity=84.3%
	CT W-GLDM-Dependence variance	Accuracy=83.3%
	MRI W-FO-Kurtosis	
	ADC DL _{CO}	

ADC=apparent diffusion coefficient; DL_{CO}=diffusing capacity of lung for carbon-monoxide; RA₉₅₀=relative area of lung less than -950 Hounsfield Units; FO=first order features; SVR=surface to volume ratio; W=wavelet; GLCM=gray level co-occurrence matrix; Idn=inverse difference normalized; Imc2=informational measure of correlation; ML=machine-learning; GLDM=gray level dependence matrix; DV=dependence variance; All selected texture feature abbreviations and descriptions can be found in supplementary Table 4-6.

4.4 Discussion

A recent investigation in patients with COPD⁷¹ showed that unsupervised learning of chest CT measurements improved predictions of progression, exacerbation, and mortality risk. Another recent study⁷² showed that machine learning models of clinical and CT imaging measurements outperformed the current standard (BODE and ADO indices) for predicting all-cause mortality. Our investigation focused on predicting 10-year all-cause mortality in ex-smokers at risk of COPD and those with spirometry evidence of COPD and provides a number of key advantages relative to

previous work including: 1) the addition of volume-matched MRI ventilation and ADC measurements, 2) MRI and CT texture features generated from images acquired within a few minutes of one another to capture structural and functional information, 3) inclusion of ex-smokers at-risk of COPD, and, 4) 10-year follow-up.

We applied machine-learning algorithms to generate models for predicting all-cause mortality using clinical, CT, MRI and imaging textures. We observed that a combined model consisting of DL_{CO}, MRI ADC and image textures, outperformed all other models. Surprisingly, none of the individual components of the BODE index were included in the “best performing” model after the feature selection step. Ensemble machine-learning models outperformed single machine-learning models, suggestive of complex, non-linear relationships between the individual imaging textures and mortality.

We were surprised to observe that the strongest individual imaging predictor was MRI ADC (AUC=.74), which outperformed all the individual components of the BODE index (except mMRC which was not measured) and all CT measurements. In fact, mortality risk increased by 84% for every 0.1 cm²/s increase in the ADC value, which underscores the high sensitivity of ADC measurements to terminal airspace enlargement due to air-trapping, emphysema or both.^{43,46} This result also agrees with the COPDGene study results, whereby emphysema progression over 5-years was associated with mortality in ever-smokers with trace emphysema.¹⁵ This result also agrees with the finding that the MRI ADC measurement is highly sensitive to terminal airspace enlargement as previously shown⁴³ and by comparison with histological measurements of the mean linear intercept.⁷³

We observed that one of the “fine” CT textures (GLCM-Imc2) had the strongest independent association with 10-year all-cause mortality, which after adjusting for confounders resulted in a

three-fold increased mortality risk (OR=3.55, p=.001). Such “fine” CT textures may be intuitively considered as reflecting tissue attenuation heterogeneity. To provide context, previous work demonstrated that the spatial arrangement of low attenuating voxels, or the size and arrangement of emphysematous clusters can differentiate patients with similar COPD disease severity.⁷⁴ However, unlike a more commonly used CT measurement of emphysema, RA₉₅₀, CT texture features reflect complex spatial heterogeneity, which may be argued is more sensitive to emphysema^{31,75} and perhaps similar to what is often visually interpreted as emphysema by expert chest CT radiologists.²⁴ In contrast throughout this study, all MRI texture features selected were “coarse” and could be considered as reflecting the compactness and asymmetry of the ventilation distribution in the lungs.

Underscoring the power of MRI and CT measures as predictors of all-cause mortality, forest plots revealed significant associations with mortality for all selected MRI/CT textures, CT vascular measurements and MRI ADC. These results are consistent with those of recent studies reporting that CT emphysema^{15,71,72} and vascular^{17,55,76} measurements are associated with mortality and disease progression in COPD. Our findings contribute to the growing body of evidence about the utility of imaging for the management of patients at risk for, and with, a diagnosis of COPD.

In agreement with the ROC analysis and forest plots, Kaplan-Meier curves revealed that ex-smokers with abnormal DL_{CO}, MRI ADC and a specific MRI texture were at greatest risk of mortality. Of note, across all models, the measurements which remained significant and highly associated with 10-year mortality were DL_{CO}, MRI ADC, MRI Wavelet-LL-FO-Skewness and CT GLCM-Imc2. These consistent observations are indicative of the added-value of imaging measurements and textures for mortality risk assessments in ex-smokers with and without COPD.

We acknowledge a number of study limitations. First, direct comparison of our results with the BODE index should be undertaken with caution because we did not acquire the modified Medical Research Council dyspnea-score component of the BODE index. Second, our study included a relatively small sample size compared to other CT studies.^{77,78} Fortunately, we employed methods to avoid overfitting so the machine-learning methods we used may be generalized with larger datasets and multicenter data in the future. We also acknowledge that lung imaging measurements are influenced by lung volume,⁷⁹ and in this study, data were captured at FRC+1L which for many ex-smokers is within 90% of TLC.^{79,80} Finally, the availability of functional MRI for chest imaging is still limited to research sites. Thus, while such quantitative MR measurements are very helpful, CT measurements are certainly more readily available and generalizable to most clinical centres. Inclusion of at risk ex-smokers may help identify individuals who are at high-risk of death and can potentially be included in clinical trials.⁸¹ It is well established that asymptomatic ex-smokers with mildly abnormal DL_{CO} are at-risk of developing COPD within four years.⁵¹ The abnormal MRI ADC values reported here have been shown to reflect mild air-trapping and/or subclinical emphysema.⁸² Unfortunately, we did not make small airways disease measurements, so we are unable to comment on whether small airway abnormalities have already initiated in these participants with normal spirometry.¹⁸⁻²¹ What we do know is that 14/69 (20%) of ex-smokers and 38/93 (41%) of COPD participants were deceased after 10 years and that similar MRI and CT measurements and textures indicative of emphysema helped explain risk. The results presented here expand on previous CT findings in COPD^{15,17,55,71,72,76} and extend the application of such imaging measurements to ex-smokers without, but at risk of COPD.

4.5 Conclusion

In ex-smokers, regardless of COPD status, DL_{CO}, CT and MR imaging measurements and textures resulted in high accuracy models for predicting mortality risk. Texture measurements provide a way to reveal MRI and CT lung pathologies that are not visible to the human eye and may help predict 10-year all-cause mortality in ex-smokers.

4.6 References

- 1 Adeloye, D. *et al.* Global, regional, and national prevalence of, and risk factors for, chronic obstructive pulmonary disease (COPD) in 2019: a systematic review and modelling analysis. *The Lancet Respiratory Medicine* **10**, 447-458, doi:[https://doi.org/10.1016/S2213-2600\(21\)00511-7](https://doi.org/10.1016/S2213-2600(21)00511-7) (2022).
- 2 Jones, R. C. *et al.* Derivation and Validation of a Composite Index of Severity in Chronic Obstructive Pulmonary Disease. *American Journal of Respiratory and Critical Care Medicine* **180**, 1189-1195, doi:10.1164/rccm.200902-0271OC (2009).
- 3 Mohd Shah, A. *et al.* The SAFE (SGRQ score, air-flow limitation and exercise tolerance) Index: a new composite score for the stratification of severity in chronic obstructive pulmonary disease. *Postgraduate Medical Journal* **83**, 492, doi:10.1136/pgmj.2006.052399 (2007).
- 4 Puhan, M. A. *et al.* Expansion of the prognostic assessment of patients with chronic obstructive pulmonary disease: the updated BODE index and the ADO index. *Lancet* **374**, 704-711, doi:10.1016/s0140-6736(09)61301-5 (2009).
- 5 Celli, B. R. *et al.* The body-mass index, airflow obstruction, dyspnea, and exercise capacity index in chronic obstructive pulmonary disease. *N Engl J Med* **350**, 1005-1012, doi:10.1056/NEJMoa021322 (2004).
- 6 Guerra, B. *et al.* Large-scale external validation and comparison of prognostic models: an application to chronic obstructive pulmonary disease. *BMC Medicine* **16**, 33, doi:10.1186/s12916-018-1013-y (2018).
- 7 Fletcher, C. & Peto, R. The natural history of chronic airflow obstruction. *Br Med J* **1**, 1645-1648, doi:10.1136/bmj.1.6077.1645 (1977).
- 8 Kakavas, S. *et al.* Pulmonary function testing in COPD: looking beyond the curtain of FEV1. *NPJ Prim Care Respir Med* **31**, 23, doi:10.1038/s41533-021-00236-w (2021).
- 9 Singh, D. *et al.* Global Strategy for the Diagnosis, Management, and Prevention of Chronic Obstructive Lung Disease: the GOLD science committee report 2019. *Eur Respir J* **53**, doi:10.1183/13993003.00164-2019 (2019).
- 10 Rabe, K. F. *et al.* Global strategy for the diagnosis, management, and prevention of chronic obstructive pulmonary disease: GOLD executive summary. *Am J Respir Crit Care Med* **176**, 532-555, doi:10.1164/rccm.200703-456SO (2007).
- 11 Burgel, P. R. *et al.* Update on the roles of distal airways in COPD. *Eur Respir Rev* **20**, 7-22, doi:10.1183/09059180.10010610 (2011).
- 12 de Jong, P. A., Muller, N. L., Pare, P. D. & Coxson, H. O. Computed tomographic imaging of the airways: relationship to structure and function. *Eur Respir J* **26**, 140-152, doi:10.1183/09031936.05.00007105 (2005).
- 13 Kirby, M. *et al.* Total Airway Count on Computed Tomography and the Risk of Chronic Obstructive Pulmonary Disease Progression. Findings from a Population-based Study. *Am J Respir Crit Care Med* **197**, 56-65, doi:10.1164/rccm.201704-0692OC (2018).
- 14 Galban, C. J. *et al.* Computed tomography-based biomarker provides unique signature for diagnosis of COPD phenotypes and disease progression. *Nat Med* **18**, 1711-1715, doi:10.1038/nm.2971 (2012).
- 15 Ash, S. Y. *et al.* Relationship between Emphysema Progression at CT and Mortality in Ever-Smokers: Results from the COPDGene and ECLIPSE Cohorts. *Radiology* **299**, 222-231, doi:10.1148/radiol.2021203531 (2021).

- 16 Baraghoshi, D. *et al.* Quantitative CT Evaluation of Emphysema Progression over 10 Years in the COPD Gene Study. *Radiology* **0**, 222786, doi:10.1148/radiol.222786.
- 17 Washko, G. R. *et al.* Arterial Vascular Pruning, Right Ventricular Size, and Clinical Outcomes in Chronic Obstructive Pulmonary Disease. A Longitudinal Observational Study. *Am J Respir Crit Care Med* **200**, 454-461, doi:10.1164/rccm.201811-2063OC (2019).
- 18 Hogg, J. C., McDonough, J. E. & Suzuki, M. Small airway obstruction in COPD: new insights based on micro-CT imaging and MRI imaging. *Chest* **143**, 1436-1443, doi:10.1378/chest.12-1766 (2013).
- 19 McDonough, J. E. *et al.* Small-airway obstruction and emphysema in chronic obstructive pulmonary disease. *N Engl J Med* **365**, 1567-1575, doi:10.1056/NEJMoal106955 (2011).
- 20 Hogg, J. C., Macklem, P. T. & Thurlbeck, W. M. Site and nature of airway obstruction in chronic obstructive lung disease. *N Engl J Med* **278**, 1355-1360, doi:10.1056/nejm196806202782501 (1968).
- 21 Koo, H. K. *et al.* Small airways disease in mild and moderate chronic obstructive pulmonary disease: a cross-sectional study. *Lancet Respir Med* **6**, 591-602, doi:10.1016/s2213-2600(18)30196-6 (2018).
- 22 Ohkubo, H., Nakagawa, H. & Niimi, A. Computer-based quantitative computed tomography image analysis in idiopathic pulmonary fibrosis: A mini review. *Respiratory Investigation* **56**, 5-13, doi:<https://doi.org/10.1016/j.resinv.2017.10.003> (2018).
- 23 Lynch, D. A. *et al.* CT-based Visual Classification of Emphysema: Association with Mortality in the COPD Gene Study. *Radiology* **288**, 859-866, doi:10.1148/radiol.2018172294 (2018).
- 24 Gietema, H. A. *et al.* Quantifying the extent of emphysema: factors associated with radiologists' estimations and quantitative indices of emphysema severity using the ECLIPSE cohort. *Acad Radiol* **18**, 661-671, doi:10.1016/j.acra.2011.01.011 (2011).
- 25 Lubner, M. G., Smith, A. D., Sandrasegaran, K., Sahani, D. V. & Pickhardt, P. J. CT Texture Analysis: Definitions, Applications, Biologic Correlates, and Challenges. *Radiographics* **37**, 1483-1503, doi:10.1148/rg.2017170056 (2017).
- 26 Li, Z. *et al.* A Novel CT-Based Radiomics Features Analysis for Identification and Severity Staging of COPD. *Acad Radiol* **29**, 663-673, doi:10.1016/j.acra.2022.01.004 (2022).
- 27 Makimoto, K., Hogg, J. C., Bourbeau, J., Tan, W. C. & Kirby, M. CT Imaging With Machine Learning for Predicting Progression to COPD in Individuals at Risk. *Chest*, doi:<https://doi.org/10.1016/j.chest.2023.06.008> (2023).
- 28 Sørensen, L. *et al.* Chronic Obstructive Pulmonary Disease Quantification Using CT Texture Analysis and Densitometry: Results From the Danish Lung Cancer Screening Trial. *AJR Am J Roentgenol* **214**, 1269-1279, doi:10.2214/ajr.19.22300 (2020).
- 29 Sørensen, L., Shaker, S. B. & de Bruijne, M. Quantitative analysis of pulmonary emphysema using local binary patterns. *IEEE Trans Med Imaging* **29**, 559-569, doi:10.1109/tmi.2009.2038575 (2010).
- 30 Ginsburg, S. B. *et al.* Texture-based Quantification of Centrilobular Emphysema and Centrilobular Nodularity in Longitudinal CT Scans of Current and Former Smokers. *Acad Radiol* **23**, 1349-1358, doi:10.1016/j.acra.2016.06.002 (2016).
- 31 Park, Y. S. *et al.* Texture-based quantification of pulmonary emphysema on high-resolution computed tomography: comparison with density-based quantification and

- correlation with pulmonary function test. *Invest Radiol* **43**, 395-402, doi:10.1097/RLI.0b013e31816901c7 (2008).
- 32 Ohno, Y. *et al.* Machine learning for lung CT texture analysis: Improvement of inter-observer agreement for radiological finding classification in patients with pulmonary diseases. *Eur J Radiol* **134**, 109410, doi:10.1016/j.ejrad.2020.109410 (2021).
- 33 Sharma, M. *et al.* Quantification of pulmonary functional MRI: state-of-the-art and emerging image processing methods and measurements. *Physics in Medicine & Biology* (2022).
- 34 Adamson, E. B., Ludwig, K. D., Mummy, D. G. & Fain, S. B. Magnetic resonance imaging with hyperpolarized agents: methods and applications. *Phys Med Biol* **62**, R81-R123, doi:10.1088/1361-6560/aa6be8 (2017).
- 35 Ohno, Y. *et al.* Pulmonary Functional Imaging: Part 1-State-of-the-Art Technical and Physiologic Underpinnings. *Radiology* **299**, 508-523, doi:10.1148/radiol.2021203711 (2021).
- 36 Kirby, M. *et al.* Hyperpolarized ³He magnetic resonance functional imaging semiautomated segmentation. *Acad Radiol* **19**, 141-152, doi:10.1016/j.acra.2011.10.007 (2012).
- 37 Sukstanskii, A. L. & Yablonskiy, D. A. Lung morphometry with hyperpolarized ¹²⁹Xe: theoretical background. *Magn Reson Med* **67**, 856-866, doi:10.1002/mrm.23056 (2012).
- 38 Kirby, M., Pike, D., Coxson, H. O., McCormack, D. G. & Parraga, G. Hyperpolarized (³He) ventilation defects used to predict pulmonary exacerbations in mild to moderate chronic obstructive pulmonary disease. *Radiology* **273**, 887-896, doi:10.1148/radiol.14140161 (2014).
- 39 Eddy, R. L. *et al.* Is Computed Tomography Airway Count Related to Asthma Severity and Airway Structure and Function? *Am J Respir Crit Care Med* **201**, 923-933, doi:10.1164/rccm.201908-1552OC (2020).
- 40 de Lange, E. E. *et al.* Evaluation of asthma with hyperpolarized helium-3 MRI: correlation with clinical severity and spirometry. *Chest* **130**, 1055-1062, doi:10.1378/chest.130.4.1055 (2006).
- 41 Davis, C. *et al.* Ventilation Heterogeneity in Never-smokers and COPD:: Comparison of Pulmonary Functional Magnetic Resonance Imaging with the Poorly Communicating Fraction Derived From Plethysmography. *Acad Radiol* **23**, 398-405, doi:10.1016/j.acra.2015.10.022 (2016).
- 42 Kirby, M. *et al.* MRI ventilation abnormalities predict quality-of-life and lung function changes in mild-to-moderate COPD: longitudinal TINCan study. *Thorax* **72**, 475-477, doi:10.1136/thoraxjnl-2016-209770 (2017).
- 43 Fain, S. B. *et al.* Early emphysematous changes in asymptomatic smokers: detection with ³He MR imaging. *Radiology* **239**, 875-883, doi:10.1148/radiol.2393050111 (2006).
- 44 Fain, S., Schiebler, M. L., McCormack, D. G. & Parraga, G. Imaging of lung function using hyperpolarized helium-3 magnetic resonance imaging: Review of current and emerging translational methods and applications. *J Magn Reson Imaging* **32**, 1398-1408, doi:10.1002/jmri.22375 (2010).
- 45 Sharma, M., Westcott, A., McCormack, D. & Parraga, G. *Hyperpolarized gas magnetic resonance imaging texture analysis and machine learning to explain accelerated lung function decline in ex-smokers with and without COPD*. Vol. 11600 MI (SPIE, 2021).

- 46 Kirby, M. *et al.* On the role of abnormal DL(CO) in ex-smokers without airflow limitation: symptoms, exercise capacity and hyperpolarised helium-3 MRI. *Thorax* **68**, 752-759, doi:10.1136/thoraxjnl-2012-203108 (2013).
- 47 Kirby, M. *et al.* Chronic obstructive pulmonary disease: longitudinal hyperpolarized (3)He MR imaging. *Radiology* **256**, 280-289, doi:10.1148/radiol.10091937 (2010).
- 48 Kirby, M. *et al.* Longitudinal Computed Tomography and Magnetic Resonance Imaging of COPD: Thoracic Imaging Network of Canada (TINCan) Study Objectives. *Chronic Obstr Pulm Dis* **1**, 200-211, doi:10.15326/jcopdf.1.2.2014.0136 (2014).
- 49 Miller, M. R. *et al.* Standardisation of spirometry. *Eur Respir J* **26**, 319-338, doi:10.1183/09031936.05.00034805 (2005).
- 50 Vestbo, J. *et al.* Global strategy for the diagnosis, management, and prevention of chronic obstructive pulmonary disease: GOLD executive summary. *Am J Respir Crit Care Med* **187**, 347-365, doi:10.1164/rccm.201204-0596PP (2013).
- 51 Harvey, B. G. *et al.* Risk of COPD with obstruction in active smokers with normal spirometry and reduced diffusion capacity. *Eur Respir J* **46**, 1589-1597, doi:10.1183/13993003.02377-2014 (2015).
- 52 Agarwala, P. & Salzman, S. H. Six-Minute Walk Test: Clinical Role, Technique, Coding, and Reimbursement. *Chest* **157**, 603-611, doi:10.1016/j.chest.2019.10.014 (2020).
- 53 Jones, P. W., Quirk, F. H., Baveystock, C. M. & Littlejohns, P. A self-complete measure of health status for chronic airflow limitation. The St. George's Respiratory Questionnaire. *Am Rev Respir Dis* **145**, 1321-1327, doi:10.1164/ajrccm/145.6.1321 (1992).
- 54 Kirby, M. *et al.* Hyperpolarized 3He and 129Xe MR imaging in healthy volunteers and patients with chronic obstructive pulmonary disease. *Radiology* **265**, 600-610, doi:10.1148/radiol.12120485 (2012).
- 55 Estépar, R. S. *et al.* Computed tomographic measures of pulmonary vascular morphology in smokers and their clinical implications. *Am J Respir Crit Care Med* **188**, 231-239, doi:10.1164/rccm.201301-0162OC (2013).
- 56 Parraga, G. *et al.* Hyperpolarized 3He ventilation defects and apparent diffusion coefficients in chronic obstructive pulmonary disease: preliminary results at 3.0 Tesla. *Invest Radiol* **42**, 384-391, doi:10.1097/01.rli.0000262571.81771.66 (2007).
- 57 Bink, A. *et al.* Clinical aspects of the apparent diffusion coefficient in 3He MRI: Results in healthy volunteers and patients after lung transplantation. *Journal of Magnetic Resonance Imaging* **25**, 1152-1158, doi:<https://doi.org/10.1002/jmri.20933> (2007).
- 58 Sukstanskii, A. L. & Yablonskiy, D. A. In vivo lung morphometry with hyperpolarized 3He diffusion MRI: Theoretical background. *Journal of Magnetic Resonance* **190**, 200-210, doi:<https://doi.org/10.1016/j.jmr.2007.10.015> (2008).
- 59 van Griethuysen, J. J. M. *et al.* Computational Radiomics System to Decode the Radiographic Phenotype. *Cancer Research* **77**, e104-e107, doi:10.1158/0008-5472.can-17-0339 (2017).
- 60 Leijenaar, R. T. *et al.* The effect of SUV discretization in quantitative FDG-PET Radiomics: the need for standardized methodology in tumor texture analysis. *Sci Rep* **5**, 11075, doi:10.1038/srep11075 (2015).
- 61 Zwanenburg, A. *et al.* The Image Biomarker Standardization Initiative: Standardized Quantitative Radiomics for High-Throughput Image-based Phenotyping. *Radiology* **295**, 328-338, doi:10.1148/radiol.2020191145 (2020).

- 62 Rastegar, S. *et al.* Radiomics for classification of bone mineral loss: A machine learning study. *Diagnostic and interventional imaging*, doi:10.1016/j.diii.2020.01.008 (2020).
- 63 Kursu, M. B. & Rudnicki, W. R. Feature Selection with the Boruta Package. *2010* **36**, 13, doi:10.18637/jss.v036.i11 (2010).
- 64 Webb, G. I. in *Encyclopedia of Machine Learning* (eds Claude Sammut & Geoffrey I. Webb) 713-714 (Springer US, 2010).
- 65 Cristianini, N. & Ricci, E. in *Encyclopedia of Algorithms* (ed Ming-Yang Kao) 928-932 (Springer US, 2008).
- 66 Quinlan, J. R. Induction of decision trees. *Mach Learn* **1**, 81-106 (1986).
- 67 Breiman, L. Bagging predictors. *Mach Learn* **24**, 123-140 (1996).
- 68 Hastie, T. & Tibshirani, R. in *Proceedings of the 8th International Conference on Neural Information Processing Systems* 409–415 (MIT Press, Denver, Colorado, 1995).
- 69 Seiffert, C., Khoshgoftaar, T. M., Hulse, J. V. & Napolitano, A. RUSBoost: A Hybrid Approach to Alleviating Class Imbalance. *IEEE Trans Syst Man Cybern Syst* **40**, 185-197, doi:10.1109/TSMCA.2009.2029559 (2010).
- 70 Lynch, D. A. *et al.* CT-Definable Subtypes of Chronic Obstructive Pulmonary Disease: A Statement of the Fleischner Society. *Radiology* **277**, 192-205, doi:10.1148/radiol.2015141579 (2015).
- 71 Yuan, N. F. *et al.* Unsupervised Learning Identifies Computed Tomographic Measurements as Primary Drivers of Progression, Exacerbation, and Mortality in Chronic Obstructive Pulmonary Disease. *Ann Am Thorac Soc* **19**, 1993-2002, doi:10.1513/AnnalsATS.202110-1127OC (2022).
- 72 Moll, M. *et al.* Machine Learning and Prediction of All-Cause Mortality in COPD. *Chest* **158**, 952-964, doi:10.1016/j.chest.2020.02.079 (2020).
- 73 Woods, J. C. *et al.* Hyperpolarized ³He diffusion MRI and histology in pulmonary emphysema. *Magn Reson Med*. **56**, 1293-1300 (2006).
- 74 Virdee, S. *et al.* Spatial Dependence of CT Emphysema in Chronic Obstructive Pulmonary Disease Quantified by Using Joint-Count Statistics. *Radiology* **301**, 702-709, doi:10.1148/radiol.2021210198 (2021).
- 75 Park, J. *et al.* Subtyping COPD by Using Visual and Quantitative CT Imaging Features. *Chest* **157**, 47-60, doi:<https://doi.org/10.1016/j.chest.2019.06.015> (2020).
- 76 Barker, A. L. *et al.* CT Pulmonary Vessels and MRI Ventilation in Chronic Obstructive Pulmonary Disease: Relationship with worsening FEV(1) in the TINCan cohort study. *Acad Radiol* **28**, 495-506, doi:10.1016/j.acra.2020.03.006 (2021).
- 77 Regan, E. A. *et al.* Genetic epidemiology of COPD (COPDGene) study design. *COPD* **7**, 32-43, doi:10.3109/15412550903499522 (2010).
- 78 Vestbo, J. *et al.* Evaluation of COPD Longitudinally to Identify Predictive Surrogate End-points (ECLIPSE). *Eur Respir J* **31**, 869-873, doi:10.1183/09031936.00111707 (2008).
- 79 Madani, A., Van Muylem, A. & Gevenois, P. A. Pulmonary emphysema: effect of lung volume on objective quantification at thin-section CT. *Radiology* **257**, 260-268, doi:10.1148/radiol.10091446 (2010).
- 80 MacNeil, J. L. *et al.* Pulmonary Imaging Phenotypes of Chronic Obstructive Pulmonary Disease Using Multiparametric Response Maps. *Radiology* **295**, 227-236, doi:10.1148/radiol.2020191735 (2020).

- 81 Celli, B. R., Cote, C. G., Lareau, S. C. & Meek, P. M. Predictors of Survival in COPD: more than just the FEV1. *Respir Med* **102 Suppl 1**, S27-35, doi:10.1016/s0954-6111(08)70005-2 (2008).
- 82 Fain, S. B. *et al.* Early emphysematous changes in asymptomatic smokers: detection with ³He MR imaging. *Radiology*. **239**, 875-883 (2006).

4.7 Supplemental Material

4.7.1 Supplementary Tables

Table 4-5. Participant demographics, pulmonary function and imaging by COPD status

Parameter mean(\pm SD)	All (n=162)	COPD (n=93)	Ex-smokers (n=69)	p-value
Age [years]	71 (9)	70 (9)	69 (9)	.2
Females [n(%)]	62 (37)	31 (33)	29 (42)	.3
Pack Years	39 (25)	46 (27)	29 (16)	<.001
BMI [kg/m ²]	28 (4)	26 (4)	29 (4)	<.001
FEV ₁ [% _{pred}]	80 (22)	62 (24)	99 (18)	<.001
FEV ₁ /FVC	60 (18)	50 (12)	80 (6)	<.001
TLC [L]	6.6 (1.3)	7.1 (1.3)	6.1 (1.1)	<.001
RV/TLC	47 (11)	50 (11)	41 (11)	<.001
DL _{CO} [% _{pred}]	63 (22)	54 (20)	78 (20)	<.001
6MWD [meters]	384 (97)	372 (90)	404 (94)	.03
SGRQ [score]	33 (21)	40 (20)	24 (22)	<.001
GOLD Severity				
GOLD I [n(%)]	22 (14)	22 (23)	-	
GOLD II [n(%)]	42 (26)	42 (45)	-	
GOLD III [n(%)]	22 (14)	22 (23)	-	
GOLD IV [n(%)]	7 (4)	7 (7)	-	
<i>CT and MR Imaging Measurements</i>				
³ He VDP [%]	13 (10)	18 (10)	7 (5)	<.001
³ He ADC [cm ² /s]	.35 (.11)	.41 (.10)	.28 (.04)	<.001
HU15 th Percentile	-914 (33)	-934 (25)	-887 (23)	<.001
LAC	-1.9 (.3)	-1.8 (.4)	-2.0 (.3)	.1
TBV [ml]	265 (59)	270 (59)	259 (60)	1.0
BV ₅ [ml]	115 (28)	114 (30)	116 (27)	1.0
BV ₅₋₁₀ [ml]	60 (16)	61 (16)	59 (18)	1.0
BV ₁₀ [ml]	89 (32)	94 (33)	83 (29)	.2
BV ₅ /TBV [%]	44 (8)	42.7 (8.6)	45.5 (7.7)	.2
BV ₅₋₁₀ /TBV [%]	22 (3)	22.4 (3.6)	22.6 (3.4)	1.0
BV ₁₀ /TBV [%]	33 (6)	34.8 (6.7)	31.7 (5.2)	.01
RA ₉₅₀ [%]	6.8 (9.2)	10.9 (10.3)	1.2 (1.1)	.001

BMI=body mass index; FEV₁=forced expiratory volume in 1 second; %_{pred}=percent of predicted value; FVC=forced vital capacity; RV=residual volume; TLC=total lung capacity; DL_{CO}=diffusing capacity of lung for carbon-monoxide; 6MWD=six minute walk distance; SGRQ=St. George's respiratory questionnaire; GOLD= Global Initiative for Chronic Obstructive Lung Disease; TBV=Total blood volume; BV₅=vessel volume for vessels less than 5 mm²; BV₅₋₁₀=vessel volume for vessels between 5-10 mm²; BV₁₀=vessel volume for vessels greater than 10 mm²; LAC=lowest attenuating cluster; RA₉₅₀=relative area of lung less than -950 Hounsfield Units; ADC=apparent diffusion coefficient; VDP=ventilation defect percent.

p=significant difference between ex-smokers with and without COPD

Table 4-6. MRI and CT texture feature descriptors

<i>Texture Feature Name</i>	<i>Description</i>
<i>MRI texture features</i>	
FO-Skewness	Measures asymmetry of the distribution of intensity values about the mean gray level value [<i>coarse</i>]
Shape-SurfaceVolumeRatio	Measures surface area to volume ratio, where a lower value indicates a more compact (sphere-like) shape [<i>coarse</i>]
GLCM-Idn	Measures local homogeneity by normalizing the difference between the neighboring intensity values and dividing by total number of discrete intensity values [<i>coarse</i>]
Wavelet-LL-FO-Kurtosis	Measures the ‘peakedness’ or ‘tailedness’ of the distribution of values in the image ROI [<i>coarse</i>]
Wavelet-LL-Cluster Shade	Measures the skewness for the grey levels from the mean grey level and uniformity of the GLCM [<i>coarse</i>]
Wavelet-LL-FO-Skewness	Measures the asymmetry of the distribution of intensity values about the mean gray level value [<i>coarse</i>]
<i>CT texture features</i>	
Shape-Sphericity	Measures roundness of ROI shape relative to a sphere, where a value of 1 indicates a perfect sphere [<i>coarse</i>]
RLM-Run Percentage	Measures coarseness of the texture via ratio of number of consecutive runs and number of voxels in the ROI [<i>coarse</i>]
GLCM-Imc1	Measures the correlation between the probability of grey level distributions between different directions using the mutual information metric [<i>fine</i>]
GLCM-Imc2	Measures the correlation between the probability of grey level distributions between different extraction directions [<i>fine</i>]
Wavelet-HH-GLDM-DV	Measures the variance of the number of connected voxels within a unit distance that are dependent on the center voxel in the ROI [<i>fine</i>]
Wavelet-HH-Run Variance	Measures the variance in runs for the run lengths, where a run is the length in number of consecutive pixels that have the same gray level value [<i>fine</i>]
Wavelet-LL-GLCM-Imc1	Measures the correlation between the probability of grey level distributions between different directions using mutual information metric [<i>fine</i>]

FO=first order features; GLCM=gray level co-occurrence matrix; Idn=inverse difference normalized; LL=low-low-pass filter; HH=high-high-pass filter; RLM=run length matrix; Imc1=informational measure of correlation; GLDM=gray level dependence matrix; DV=dependence variance.

Table 4-7. Correlations of selected CT and MRI predictor variables in machine-learning models

<i>Selected MRI and CT texture features</i>	BMI		FEV₁ %_{pred}		6MWD		SGRQ	
	ρ	<i>p</i>	ρ	<i>p</i>	ρ	<i>p</i>	ρ	<i>p</i>
FO-Skewness	-.23	.002	-.46	<.001	-.39	<.001	.44	<.001
Shape-SurfaceVolumeRatio	.05	.5	-.50	<.001	-.33	<.001	.41	<.001
GLCM-Idn	-.50	<.001	-.15	.06	-.11	.1	.16	.05
Wavelet-LL-FO-Kurtosis	-.15	.04	-.26	.001	-.34	.001	.29	<.001
Wavelet-LL-Cluster Shade	-.27	<.001	-.43	<.001	-.28	<.001	.37	<.001
Wavelet-LL-FO-Skewness	-.25	<.001	-.50	<.001	-.40	<.001	.45	<.001
CT Shape-Sphericity	-.44	<.001	-.66	<.001	-.23	.003	.37	<.001
CT RLM-Run Percentage	-.26	<.001	-.42	<.001	-.39	.002	.36	<.001
CT GLCM-Imc1	.60	<.001	.58	<.001	.19	.01	-.39	<.001
CT GLCM-Imc2	-.53	<.001	-.57	<.001	-.20	.01	.40	<.001
CT Wavelet-HH-GLDM-DV	-.69	<.001	-.58	<.001	-.17	.03	.32	<.001
CT Wavelet-HH-Run Variance	-.66	<.001	-.60	<.001	-.18	.02	.33	<.001
CT Wavelet-LL-GLCM-Imc1	.55	<.001	.58	<.001	.19	.02	-.39	<.001

p-value represents significance values for spearman correlations; Bolded values are statistically significant (*p*<.05).

BMI=body mass index; FEV₁=forced expiratory volume in 1 second; %_{pred}=percent of predicted value; 6MWD=six minute walk distance; SGRQ=St. George's respiratory questionnaire; FO=first order features; GLCM=gray level co-occurrence matrix; Idn=inverse difference normalized; LL=low-low-pass filter; HH=high-high-pass filter; RLM=run length matrix; Imc1=informational measure of correlation; GLDM=gray level dependence matrix; DV=dependence variance.

CHAPTER 5

5 CONCLUSIONS AND FUTURE DIRECTIONS

*In the final thesis chapter, the motivation and research questions related to this work are summarized, along with important results and conclusions from **Chapters 2 to 4**. The general and specific study limitations are also discussed, with an outline of potential future projects that stem from this thesis.*

5.1 Overview and Research Questions

COPD is characterized by irreversible airflow limitation, and while treatment can alleviate symptoms and provide quality-of-life improvements, they do not resolve the underlying pathologies and cannot fully restore lung function. Thus, the clinical picture is usually progressive with symptoms such as exertional dyspnea and chronic cough. Furthermore, COPD is frequently diagnosed in the later stages when significant irreversible lung damage has already occurred. In this regard, the importance of early detection in COPD is supported by a multitude of studies indicating that timely identification and intervention leads to better outcomes,¹ improved quality-of-life,² and reduced healthcare costs.^{3,4} Early detection also empowers healthcare providers to implement effective strategies, tailor treatment plans, and engage in proactive management to benefit individuals at risk for or diagnosed with COPD. Such preventative measures reduce the frequency and severity of exacerbations,^{5,6} which are strongly associated with long-term patient outcomes and mortality.⁷⁻⁹ However, GOLD/ATS recommendations have been proposed and modified over the decades that now include symptoms severity and exacerbation risk,¹⁰ yet misdiagnosis rates have remained high throughout this period,¹¹⁻¹⁶ indicating there are missing parts to this puzzle. Typically, structure and function of COPD are clinically characterized using the FEV₁ measurement taken at the mouth; while FEV₁ is simple and cost-effective to implement, it does not provide regional measurements of lung function and cannot capture the heterogeneity

of abnormalities present in COPD, specifically the small airway compartment where COPD is believed to initiate.¹⁷⁻²⁰

Quantitative pulmonary imaging methods have been developed to visualize the regional abnormalities directly and quantify the structure and function of the lung. Recent advancements in imaging techniques provide an opportunity for qualitative and quantitative analyses of the lung parenchymal, airways and vascular manifestations of COPD.²¹⁻²³ Pulmonary imaging has been used to provide novel insights into COPD, with 40 years of advances in CT clearly indicating that COPD, in fact, is a heterogeneous disease.²⁴ Currently, the only clinical means for imaging lung ventilation is with lung scintigraphy; however, this method is limited by radiation exposure risks, similar to CT, and also has low spatial resolution.^{25,26} In contrast, hyperpolarized ³He and ¹²⁹Xe MRI provide *in vivo* images of regional gas distribution without imparting any ionizing radiation, with the potential for longitudinal patient monitoring. In COPD, MRI ventilation defects have been shown to be reproducible,^{27,28} reflect airway abnormalities such as narrowing and remodeling,^{29,30} and are associated with disease exacerbations,^{31,32} CT emphysema,³³ symptoms and severity.³⁴⁻³⁶ Many studies have identified the hallmark finding of regional ventilation defects in COPD, even in those with normal clinical measurements, including CT and spirometry.^{34,37-39} Improved characterization of COPD imaging traits is beginning to impact the diagnosis and management of COPD,²⁴ and it is becoming clear that imaging features are important and may even be used for prognostication and longitudinal outcome predictions in COPD.

Image texture analysis tools have been recently investigated in COPD.⁴⁰⁻⁴⁵ These methods have an advantage of providing automatic, continuous and non-categorical measurements that can simultaneously evaluate the signal intensities and their spatial distribution or arrangement of clusters.^{46,47} Unlike the established CT and MR imaging measurements, texture features assess the

full spectrum of information present within the images and can extract additional unique information. MRI texture features have not yet been evaluated in COPD, while CT texture features can predict COPD progression,⁴¹ exacerbations,⁴⁴ severity,⁴⁸ and have shown stronger associations with lung function compared to conventional quantitative CT measures.⁴⁵ Previous studies have shown that the incorporation of structural and functional information from multiple imaging methods^{49,50} and the use of high-level prior knowledge⁵¹ may benefit image analysis. Therefore, the overarching objective of this thesis was to first develop and then apply texture analysis and machine learning pipelines to pulmonary CT and MR images in order to characterize structural and functional lung patterns and predict clinically-relevant outcomes in COPD. The specific research questions were: 1) Can texture analysis identify otherwise “hidden” CT imaging evidence of subclinical parenchymal abnormalities that were detected by MRI ADC in ex-smokers with decreased DL_{CO} but without CT or spirometry evidence of COPD? (**Chapter 2**); 2) Are there visually-unapparent MRI ventilation features that can predict accelerated lung function decline across three years and correlate with clinically-relevant measures, potentially providing insights into underlying mechanisms of disease progression in ex-smokers? (**Chapter 3**); 3) Are there structural CT and functional MR imaging textural features that can improve the performance for predicting all-cause mortality (the ultimate patient outcome) across 10 years in ex-smokers with and without COPD? (**Chapter 4**).

5.2 Summary and Conclusions

In **Chapter 2**, we evaluated 71 ex-smokers without COPD in order to extract CT imaging texture features and apply machine learning algorithms to dichotomize ex-smokers based on abnormal gas exchange. Ex-smokers without COPD often present with a mildly abnormal DL_{CO} and are shown to be at a higher risk of developing COPD.⁵² We developed a CT texture analysis pipeline using

machine learning to detect unexplainably reduced lung diffusion and were able to differentiate ex-smokers with mild emphysematous or gas-trapping abnormalities from regular ex-smokers with 87% accuracy. All available clinical and imaging measurements were outperformed by high-high-pass filter high-gray-level-run-emphasis texture-feature (AUC=0.81), which correlated with DL_{CO} ($\rho=-0.29$, $p=.02$), MRI ADC ($\rho=0.23$, $p=.048$) and 6MWD ($\rho=-0.25$, $p=.02$). These results indicate that an early predictor of COPD development may be detected on a clinically normal CT scan. Identifying these ex-smokers at high risk of worsening to COPD,⁵³ with severe exacerbations,⁵⁴ is critical given the high health-care costs,⁵⁵ and evidence that severe impairments in DL_{CO} are independently associated with increased rates of severe exacerbations requiring an emergency department visit or hospitalization.⁵⁶ Insights from quantitative CT textures into these ex-smokers with MRI evidence of mild emphysema may bridge the gap between modalities and provide subclinical phenotypes responsible for an abnormal DL_{CO} in ex-smokers, adding unique information and clinical utility to a conventional CT scan.

In **Chapter 3**, we retrospectively evaluated 88 ex-smokers with and without COPD and developed another pipeline for extracting unique texture features residing within hyperpolarized ³He MR ventilation images in order to identify COPD participants at risk of accelerated lung function decline, defined by annual FEV₁ worsening ≥ 60 mL/year. Hyperpolarized gas MRI provides highly sensitive and unique microstructural and functional information in COPD,⁵⁷ and can quantify ventilation defects that stem from abnormalities in large and small airways as well as emphysema.⁵⁸ MRI biomarkers are highly reproducible,⁵⁹ associated with clinically-relevant outcomes in COPD⁶⁰, and have shown to detect disease-related changes before computed tomography (CT) or FEV₁ measurements.^{61,62} Unfortunately, current predictive models of COPD progression rarely include MRI-derived measurements and typically use standard clinical

characteristics.^{32,63,64} We generated models to predict FEV₁ decline using demographics, spirometry, and texture features, with the latter yielding an 81% classification accuracy. The combined model achieved the overall best classification accuracy of 82%; however, it was not significantly different from the model trained on MRI texture features alone. A novel imaging measurement was also created, which outperformed clinical variables and independently predicted (AUC=0.71) accelerated lung function decline in ex-smokers. For the first time, machine learning and texture features from hyperpolarized ³He MR images were used to predict ex-smokers who would experience accelerated FEV₁ decline over a short three-year period. Identifying such COPD patients at a higher risk of accelerated disease progression is critical due to observed associations with increased mortality and worse outcomes in these patients.⁵⁴ There is a lack of studies showing that currently developed CT biomarkers reflect changes in outcomes that are important to patients with COPD;^{65,66} while noble gas MRI provides additional information to CT and spirometry, which is important because MRI is acquired without ionizing radiation and can be safely used for longitudinal monitoring in compromised populations.

In **Chapter 4**, we applied, improved, and optimized the methods developed in previous chapters and evaluated baseline CT and MR imaging measurements and texture features in 162 ex-smokers to predict 10-year all-cause mortality risk. Pulmonary imaging measurements have deepened our understanding of COPD by measuring airway and parenchymal pathologic information,^{67,68} which cannot be provided by spirometry. Mortality risk prediction models have been historically developed and widely used for other diseases or processes, but pulmonary imaging measurements are not included in clinically-accepted mortality risk assessments, diagnosis, prognosis, or staging of COPD.⁶⁹ We demonstrated that predictive models incorporating quantitative structural and functional imaging measurements at the site of the pathologies that drive symptoms and

progressive worsening provided more accurate predictions of 10-year all-cause mortality than models trained using clinical features alone (accuracy=83% vs 77%). CT GLCM-Imc2 texture feature had the strongest independent association with mortality, where a unit change in this texture resulted in a 3-fold increase in mortality risk. In addition, Kaplan-Meier survival curves showed that an MRI wavelet-based feature FO-skewness achieved the best mortality risk stratification among all selected predictors. Taken together, these findings suggest that chest CT and MRI texture analysis in combination with machine learning is able to provide additional, unique prognostic information to conventional clinical and imaging measurements that could be leveraged for accurate 10-year all-cause mortality prediction in ex-smokers. Therefore, regardless of COPD status, the inclusion of imaging texture measurements within current clinical models provides unique additional information about disease progression, which can allow for a better understanding and clinical management of COPD. Future work with datasets on the scale needed for regulatory approval is essential, along with methods for texture feature interpretation in clinical research studies and approaches to test the link to underlying pathophysiology.

In summary, we have provided 1) evidence that structural CT texture features can sensitively detect ex-smokers without COPD and/or CT evidence of emphysema that have an abnormal gas-exchange; 2) over a relatively short 3-year period, we showed that MR imaging texture features at baseline predict accelerated lung function decline in ex-smokers with and without COPD and outperform models based on clinical and/or demographic measurements. Evidence was provided that the effect of accelerated lung function decline is reflected in a corresponding change in MRI texture, and 3) evidence to support that CT and MRI texture features provide unique prognostic information for mortality risk assessments, which is not available using established clinical

measures and spirometry. These results indicate the potential for approaches presented in this thesis to be applied for predicting longitudinal and clinically-relevant outcomes in COPD.

5.3 Limitations

5.3.1 Study Specific Limitations

Chapter 2: *Machine Learning and CT Texture Features in Ex-smokers with no CT Evidence of Emphysema and Mildly Abnormal Diffusing Capacity*

The study presented in **Chapter 2** included a relatively small sample size in comparison to other COPD studies,⁷⁰⁻⁷² which have provided hallmark findings responsible for our current understanding of COPD. However, we employed statistical techniques to prevent overfitting (5-fold cross-validation, Regression analysis, principal component analysis, Boruta Analysis, etc.), and our trained machine-learning algorithms may be further generalized using larger datasets and multicenter data. We were unable to comment on whether small airway abnormalities have already been initiated in these ex-smokers without COPD since expiratory CT was not available and small airways disease measurements could not be investigated. Next, the CT images were acquired at the same lung volume as the MR images (FRC+1L); however, it has been established that quantitative imaging measurements are influenced by lung volumes.⁷³ To address this limitation, future studies may include a set of standardized features that are normalized to the total lung volume in an attempt to mitigate this issue. Furthermore, CT images were acquired using the same scanner and protocol, and we did not evaluate the models using data from other scanners or sites, which may lead to weaker generalizability of the models. Therefore, it is necessary to apply this approach to a multi-site dataset in order to fully quantify the translatability of the trained models to clinical settings with diverse scanners. Finally, we did not directly quantify the impact of feature selection methods on model prediction accuracy, and other methods, such as hybrid feature

selection and deep-learning approaches, should be investigated in the future. Such approaches, although more computationally complex and time-consuming, have the ability to provide additional components for generating stronger predictions and potentially improve our understanding of the disease pathology.

Chapter 3: *Machine Learning and MR Image Texture Analysis Predicts Accelerated Lung Function Decline in Ex-smokers with and without COPD*

In the study presented in **Chapter 3**, we were once again limited by the small sample size, particularly due to a high dropout at follow-up. These machine learning classifiers could be better optimized using larger datasets in the future. The generalizability could be further enhanced by incorporating an external dataset and/or with different MRI protocol acquisitions. Furthermore, the TINCan cohort is comprised of a large number of mild to moderate patients compared to the general COPD population. Therefore, the generalizability of the models must also be considered in this context and remains to be validated in future studies. MR image segmentation was conducted by a single experienced observer using a semi-automated approach, which may have an impact on the generation of proposed imaging measurements and texture feature extraction. The generation of such ground-truth data may not be perfect due to the involved user interactions, and as a result, the sources of disagreement between the algorithm and ground-truth data cannot be ascertained. Finally, the availability of functional MRI for chest imaging is currently very limited in a clinical setting, and while such MRI texture measurements are very effective and beneficial, CT measurements are much more readily available.

Chapter 4: *Chest MRI and CT Predictors of 10-year All-cause Mortality in COPD*

In the study presented in **Chapter 4**, a limited number of participants from the TINCan cohort returned for a follow-up visit, and the time to follow-up was relatively short. Another consideration is the follow-up bias and loss to follow-up, where participants who did not return may have been in worse health and/or with comorbidities. Therefore, this study would greatly benefit from a larger sample size and longer follow-up timeframes. Despite a similar emphysema and ventilation defect percent, there may be substantial physiological differences between ex-smokers in the training and testing datasets. Thus, it is difficult to confirm whether the observed reduction in performance from training to testing sets was due to a substantially different disease manifestation or due to suboptimal selection of extraction parameters and overfitting. To address these limitations, we employed several methods to avoid overfitting such that the models used may be generalizable with larger, more heterogeneous datasets, which may allow for a more thorough investigation into the optimal model parameters. Unfortunately, we did not acquire the modified Medical Research Council dyspnea-score component of the BODE index in these ex-smokers. As a result, the direct comparison of our results with the BODE index should be undertaken with caution. We also acknowledge that lung imaging measurements are influenced by lung volume during acquisition;⁷³ however, the imaging data were acquired at FRC+1L lung volume, which for many ex-smokers is within 90% of TLC.^{73,74} Although, abnormal DL_{CO} and MRI ADC values reported here have been shown to reflect mild air-trapping and/or subclinical emphysema,⁷⁵ we did not make small airways disease measurements. Nonetheless, about 20% of ex-smokers and 41% of COPD participants were deceased within 10 years and CT and MR imaging textures indicative of mild emphysema helped explain mortality risk.

5.3.2 General Limitations

This thesis focused on developing and evaluating novel imaging measurements and image processing algorithms for pulmonary MRI and CT. The sample sizes in our TINCan study cohort were small relative to other COPD studies,⁷⁶⁻⁸⁰ and the participants were recruited as a convenience and not a random population-based sample, which may have biased the results to participants with milder COPD and better health. However, study participants who did not return for follow-up reported worse values for pulmonary function, exercise capacity, and quality-of-life at baseline compared to those who returned, suggesting that these results provide a conservative estimate of potential longitudinal differences. We did not have a healthy control population and were unable to capture an equally distributed spectrum of the disease. Heterogeneous study cohorts and diverse datasets may provide better discriminatory ability and enhance machine learning model generalizability. The interpretation of results presented in these preliminary studies must be undertaken with caution in regard to the broader population of COPD patients. Regardless, these exploratory studies provide the foundation for future studies, which should be aimed at evaluating larger groups of patients to confirm the results observed.

One key limitation is that CT was acquired at FRC+1L lung volume, while full inspiratory and expiratory CT images were not acquired; thus, we were unable to quantify CT air-trapping and/or generate CT parametric response maps (PRM)^{74,81} to evaluate the relative contributions of emphysema and air-trapping to disease progression. In addition, the use of MR modality in clinical settings remains very limited due to the availability and associated costs. The utility of hyperpolarized ³He MRI is even further limited due to additional personnel, image processing complexity, equipment requirements, and the depleting global supply of ³He gas. Therefore, although MRI-derived measurements provide unique prognostic value and are radiation-free, they

are not readily available. However, with the recent FDA regulatory approval for the clinical use of ^{129}Xe and associated equipment, we may see a shift in the near future in the utilization of MRI-derived measurements and biomarkers for evaluating lung diseases. Therefore, the results presented in this thesis using ^3He MRI must be compared and validated using equivalent ^{129}Xe MRI measurements; fortunately, preliminary work using ^{129}Xe MRI texture analysis methods has already been conducted and published with several promising results in asthma and COVID-19.^{82,83}

Finally, the developed measurements and methods heavily rely on sophisticated image processing approaches and require substantial computational power, which may impact the clinical translation of the results presented here. This also implies that the proposed methods may be influenced by any errors in the image processing pipeline (particularly segmentation/registration) and, thereby, should be robustly accurate and reproducible. For instance, a semi-automated approach was used for MR image segmentation, which may be influenced by the level of training and subjective user input. This variability in the input images will undoubtedly impact the resultant texture features; however, this can be mitigated by minimizing user interactions and using automated segmentation/registration approaches. We also recognize the lack of normal ranges or measurements in healthy populations as well as a minimal clinically important difference in quantitative texture measurements. These measurements are highly sensitive to signal and spatial variations within the image and, therefore, require robust analyses to determine sensitivity limits, normal versus abnormal ranges of values, as well as characteristic disease features by designing lung phantoms with varying pathologies that are approved by clinicians. Although the differences in texture measurements between patient groups presented in these studies were statistically significant, it is unclear whether these changes are clinically-relevant. Therefore, future studies

should necessarily focus on the validation and standardization of the proposed texture analysis tools, particularly using pulmonary imaging methods.

5.4 Future Directions

5.4.1 Generating synthetic MRI ventilation maps using CT and Deep-learning

Hyperpolarized gas MRI provides valuable insights into lung function yet is not widely available, whereas thoracic CT protocols are cost-effective and universally available.⁸⁴ There is structural information contained in CT, but it is only part of the picture and does not directly inform on lung function. Advanced image registration and processing techniques have been developed to glean functional information from contrast-enhanced dual-energy and multi-volume CT protocols, but despite their recent success, these techniques require specialized, complex analyses and additional scans.⁸⁵ The ability to robustly extract functional information from a single volume, non-contrast-enhanced, breath-hold CT is the next challenge towards broadening the impact of regional functional lung information. Such a prediction model will further deepen our understanding of the interactions between structural and functional determinants of physiological processes.

Recent advances in deep learning using convolutional neural networks (CNN) and generative adversarial networks (GAN) have resulted in ground-breaking performance in various medical imaging applications, including image segmentation and classification.⁸⁶⁻⁹⁰ This success has translated into medical image analysis, where deep learning is being used for tissue classification and, recently, image synthesis.⁹¹ The combination of volume-matched hyperpolarized noble gas MRI and CT provides a unique yet challenging opportunity to predict functional ventilation using information from structural CT. Also, despite the TINCan study cohort not having thousands of images available, the CT and MR images are volume-matched and it does provide benefits as the

data is very focused, extensively studied, and well understood,⁹² thus can adequately serve for this preliminary research. Additionally, utilizing ventilation images as ground-truth provides a more spatially and quantitatively rich measure when compared to training models to predict a single subject measure such as disease stage.

This work will enable a deeper understanding of the structure-function relationships in the ex-smoker cohort by generating functional information from a structural CT image. The underlying principles for the ventilation image synthesis will use texture analysis and combine the knowledge gained from the previous chapters in this thesis in order to generate a predicted lung ventilation map within seconds. The overarching objective will be to develop competing algorithms to classify tissue in a breath-hold CT into well- versus abnormally-ventilated regions and evaluate the accuracy of each model. The specific objectives are to:

- Optimize the existing texture analysis and machine-learning pipeline for classification of abnormal versus well-ventilated tissue from CT images.
- Develop a voxel-wise classification between normal and abnormal ventilation using fully connected CNN and segmented MR images as ground-truth.
- Develop a GAN with input as CT images and volume-matched co-registered MRI ventilation scans as ground-truth.
- Evaluate the outputs of all the approaches by calculating the Dice similarity coefficient (DSC), structural similarity (SSIM) index, and intraclass correlation coefficient (ICC) between the predicted and ground-truth MRI ventilation maps.
- Develop a semantic label fusion method and incorporate the texture-based pipeline output with the CNN layers to generate a superior ventilation map, and then evaluate the new output maps using MRI ground-truth.

Proposed Image Processing Workflow

Thoracic CT volumes will be subdivided into isotropic 15×15×15mm three-dimensional regions of interest (ROI) and labeled as well- or abnormally-ventilated based on co-registered hyperpolarized gas MRI. A set of texture features based on first and second-order statistics will be generated to describe each ROI,^{93,94} which will be used to train a classification model by testing a simple logistic regression, a support vector machine, and a random forest classifier. Another competing method will also be developed in tandem, using Keras with a Tensorflow backend to build a fully convolutional network (CNN) to classify voxels using the entire CT image as the input layer and the binary MR ventilation mask as the output or ground-truth, layer for training. This U-net architecture will utilize transfer learning by building off established networks such as AlexNet before converting the network to focus on segmentation and, finally, fine-tuning for CT classification, as previously described.⁹⁵

The CNN will be built based on the U-net architecture⁹⁶ and will be comprised of two branches: an encoding and a decoding path. Each layer in the two paths will use a 3×3 convolution, a Rectified Linear Unit (ReLU), to introduce nonlinearity, max-pooling/un-pooling, and skip connections between the branches. The encoder branch will be similar to traditional CNNs and will extract a hierarchy of increasingly complex features from the input CT image. The decoding branch will transform the features extracted from the encoding branch and then, step-by-step, will reconstruct a synthetic output image. The network parameters will be optimized using the cross-entropy loss, or log-loss, as the loss function between the predicted ventilation image and corresponding ground-truth ³He MR image. The model based on ROIs will have more training data, due to data augmentation, at the cost of information about the spatial relationships between ROIs. In contrast, the image-to-image synthesis method will be able to account for the relationship between different regions more fully as the neural network is trained on the entire lung volume.

These limitations in both methods can be negated by fusing the labels of the segmented output from the texture-based method with the outputs from the deep-learning-based segmentation method.

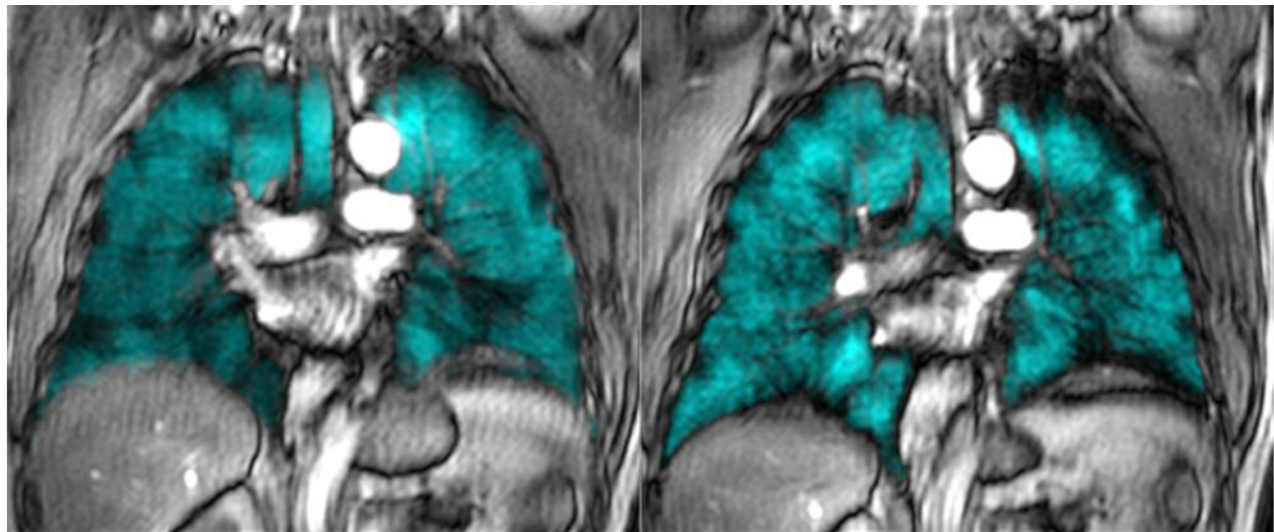
Models will be developed on the same well-characterized set of male and female ex-smokers with and without COPD ($n > 200$), with training/validation/test datasets with 70%/15%/15% split. Shapiro-Wilk tests will be used for checking the normality of the data, non-parametric tests will be used for not normally distributed data, and a one-way ANOVA or a Kruskal-Wallis will be used to look at between-group differences. In cases of multiple significant predictors for ventilation banalization, Boruta Analysis will be deployed to rank the features. The network will be trained using ten-fold cross-validation and evaluated with DSC, SSIM, and ICC measurements between ground-truth and predicted ventilation maps. Additionally, the final generated ventilation maps will be assessed for synthesized VDP measurements and compared to ground-truth MRI VDP.

5.4.2 Texture Analysis and Machine Learning for Predicting Quality-of-life Worsening and Exercise Limitation

CT-based measurements of emphysema and airways disease have shown to provide prognostic information, yet none of the currently developed CT biomarkers are able to reflect longitudinal changes in clinically-relevant outcomes in patients with COPD.² This is important because longitudinal changes in quality-of-life are associated with changes in lung function and mortality. Pulmonary hyperpolarized ^3He MRI provides a way to measure lung ventilation and parenchyma microstructure in patients with COPD, which are associated with COPD outcomes,^{97,98} correlate with longitudinal changes in quality-of-life,⁶⁶ and are sensitive to disease-related changes earlier than either CT or standard pulmonary function tests.^{99,100} Currently, no imaging measurements except VDP have shown to predict changes in quality-of-life.⁶⁶

The 6MWD measurement is associated with worse COPD long-term outcomes, greater risk of exacerbations, and increased mortality. Nevertheless, it remains difficult, if not impossible, to identify the pathological drivers of the 6MWD, which typically is weakly correlated with lung function measurements. To date, there are only a few reliable measurements that may be used to predict the significant risk of reduced exercise capacity in COPD participants.

The pipeline developed in this thesis can be used to extract texture features from participants' ventilation images and predictive models generated for longitudinal worsening in quality-of-life and exercise limitation. Building on the results within this thesis, which focuses on disease progression, a similar evaluation of improvements and response to treatment using clinically-relevant measurements can be conducted. For instance, in patients with asthma, the minimal clinically important difference (MCID) in FEV₁ and asthma quality-of-life questionnaires (AQLQ) can be investigated. Similarly, in patients recovering from COVID-19, the MCID improvements in lung function metrics and perceived quality-of-life measured using SGRQ could be investigated. In COPD, the predictive power of clinical, ventilation imaging, first-, higher-order and, transform texture features⁹ can be evaluated for identifying participants with longitudinal change in SGRQ as well as 6MWD greater than the well-established MCID.^{101,102}



Parameter mean (\pm SD)	Follow-up Visit (28 months)	
	Baseline Visit	Follow-up Visit
VDP (%)	7	9
ADC (cm^2/s)	0.27	0.31
RA ₉₅₀ (%)	3.6	4.2
FEV ₁ (% _{pred})	101	100
FEV ₁ /FVC (% _{pred})	97	96
FO-Skewness	0.877	0.573
Wavelet-LH-Correlation	0.187	0.237
Wavelet-HL-GLCM-Idmn	0.992	0.990
6MWD	404	357
SGRQ	21	29

Figure 5-1. Baseline and follow-up visit ³He MRI ventilation images with associated texture and imaging measurements

A representative 70-year-old male ex-smoker participant without a COPD diagnosis, with 22 pack years and rapid quality-of-life worsening, with no abnormalities in standard imaging and clinical measurements. FO=First-order; LH=low-high pass; HL=High-low pass; GLCM=Gray Level Co-occurrence Matrix.

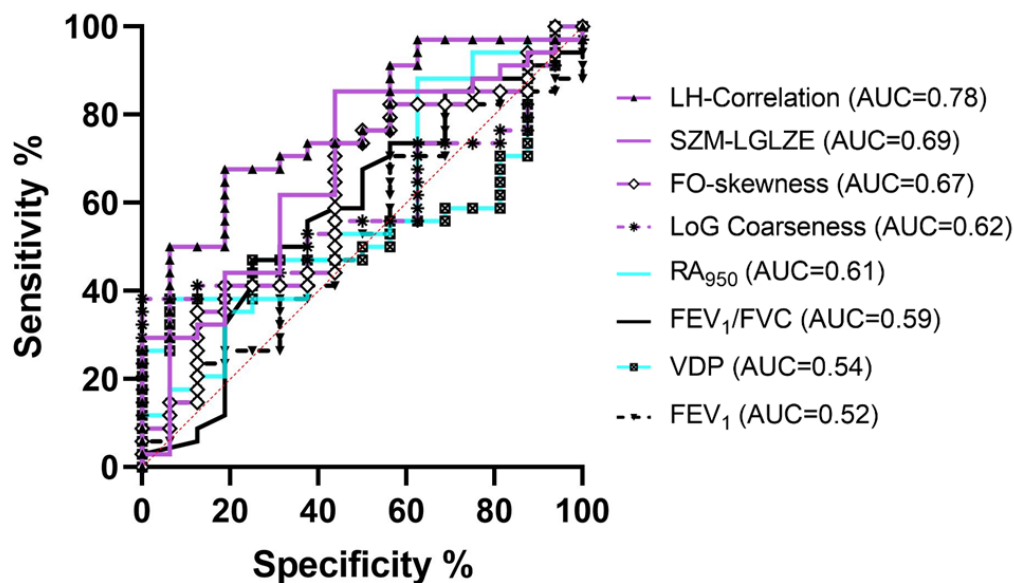


Figure 5-2. Logistic regression analysis of individual ³He MRI ventilation features

The predictors (purple lines) selected for generating machine-learning classification models is compared with standard imaging (cyan) and clinical (black) measurements at predicting MCID change in SGRQ. The above ROC curve represents the predictive power of individual variables used for machine-learning modeling, where individual MRI texture features outperformed standard variables that are available to physicians in a clinical setting.

Overall, the clinical translation of PyRadiomics and radiomic-based analysis faces several potential challenges that need to be addressed for successful integration into clinical practice.

Some of these challenges include: 1) large and diverse datasets, with prospective studies providing evidence on the scale needed for regulatory approval; 2) standardization and reproducibility of radiomic features across different imaging platforms, protocols and software; 3) conducting robust validation studies to demonstrate the clinical utility and predictive value of radiomic features; 4) integrating texture analysis tools into existing clinical workflows and electronic health record systems; 5) addressing regulatory requirements and reimbursement considerations for radiomic analyses in clinical practice; 6) providing education and training to healthcare providers, radiologists, and other stakeholders on the principles and applications of radiomics tools, as well as the interpretation of imaging texture measurements.

5.5 Significance and Impact

COPD is a complex and heterogeneous disease, and it remains difficult to predict patients with obstruction measured using FEV₁ that will experience accelerated disease progression or mortality, which is an ultimate example of a clinical outcome. While spirometry is the cornerstone of COPD diagnosis¹⁰³ and FEV₁ measurements are straightforward and cost-efficient to implement, they cannot directly provide spatial nor functional information about the small-airway compartment that is believed to drive COPD pathogenesis along with emphysema.¹⁰⁴ Therefore, early detection of COPD in patients in the early stages is of paramount importance for several reasons, especially given the historical context of COPD management. Early detection allows for timely intervention and the implementation of strategies to slow the progression of COPD, reduce the frequency and severity of exacerbations, and improve longitudinal outcomes while reducing healthcare costs.^{3,4} However, early detection of COPD has been challenging even using the currently established imaging methods, which are capable of capturing regional measurements of lung function and structure. This is in part because early-stage COPD may go unnoticed due to the absence of prominent symptoms or oversight, while the absence of proactive screening methods further exacerbates the delay in diagnosis. Moreover, COPD lacks highly specific biomarkers for early detection since currently developed measurements do not evaluate the full spectrum of signal and spatial information present within images.

In this thesis, we have developed and evaluated methods for obtaining quantitative CT and MR imaging measurements of structure and function using machine-learning and texture analysis tools. The work presented here confirms that, indeed, there are subtle and unique imaging features that can be automatically quantified and potentially provide valuable insight into disease progression in ex-smokers with and without COPD. I have demonstrated that such imaging texture features

can detect subclinical emphysematous changes on CT and can be used to improve the performance for predicting lung function decline as well as all-cause mortality, which are critical longitudinal outcomes in COPD. I showed that beyond MRI VDP, which quantifies ventilation defects, the quality and heterogeneity of ventilation within the lungs are strong contributing factors when evaluating disease progression. Furthermore, I showed that it is possible to quantify mild airspace enlargements using conventional CT and that clustering of sub-clinical emphysema may provide a better understanding of the underlying pathology responsible for previously undetected abnormal DL_{CO} and MRI ADC. Taken together, the results presented in this thesis suggest that pulmonary imaging textures provide unique sensitive information that can be used to evaluate disease progression and potentially improve clinical decision-making. If these methods become widely accepted, lung imaging will have a greater importance in the early detection of COPD and facilitate timely interventions to impede disease progression.

5.6 References

- 1 Welte, T., Vogelmeier, C. & Papi, A. COPD: early diagnosis and treatment to slow disease progression. *International journal of clinical practice* **69**, 336-349 (2015).
- 2 Maleki-Yazdi, M. R., Lewczuk, C. K., Haddon, J. M., Choudry, N. & Ryan, N. Early detection and impaired quality of life in COPD GOLD stage 0: a pilot study. *COPD: Journal of Chronic Obstructive Pulmonary Disease* **4**, 313-320 (2007).
- 3 Gutiérrez Villegas, C., Paz-Zulueta, M., Herrero-Montes, M., Parás-Bravo, P. & Madrazo Pérez, M. Cost analysis of chronic obstructive pulmonary disease (COPD): a systematic review. *Health Economics Review* **11**, 1-12 (2021).
- 4 Kostikas, K. *et al.* Clinical impact and healthcare resource utilization associated with early versus late COPD diagnosis in patients from UK CPRD database. *International journal of chronic obstructive pulmonary disease*, 1729-1738 (2020).
- 5 Adamson, S. L., Burns, J., Camp, P. G., Sin, D. D. & van Eeden, S. F. Impact of individualized care on readmissions after a hospitalization for acute exacerbation of COPD. *Int J Chron Obstruct Pulmon Dis* **11**, 61-71, doi:10.2147/COPD.S93322 (2016).
- 6 Albert, R. K. *et al.* Azithromycin for prevention of exacerbations of COPD. *N.Engl.J Med.* **365**, 689-698, doi:10.1056/NEJMoa1104623 [doi] (2011).
- 7 Almagro, P. *et al.* Mortality after hospitalization for COPD. *Chest.* **121**, 1441-1448 (2002).
- 8 Cote, C. G. & Celli, B. R. Predictors of mortality in chronic obstructive pulmonary disease. *Clin.Chest Med* **28**, 515-524, v (2007).
- 9 Cote, C. G., Dordelly, L. J. & Celli, B. R. Impact of COPD exacerbations on patient-centered outcomes. *Chest* **131**, 696-704 (2007).
- 10 Venkatesan, P. GOLD COPD report: 2024 update. *The Lancet Respiratory Medicine* **12**, 15-16 (2024).
- 11 Aaron, S. D. *et al.* Diagnostic Instability and Reversals of Chronic Obstructive Pulmonary Disease Diagnosis in Individuals with Mild to Moderate Airflow Obstruction. *Am J Respir Crit Care Med* **196**, 306-314, doi:10.1164/rccm.201612-2531OC (2017).
- 12 Colak, Y., Lokke, A., Marott, J. L., Lange, P. & Vestbo, J. Impact of diagnostic criteria on the prevalence of COPD. *Clin Respir J* **7**, 297-303, doi:10.1111/crj.12007 (2013).
- 13 Elbehairy, A. F. *et al.* Mild chronic obstructive pulmonary disease: why spirometry is not sufficient! *Expert review of respiratory medicine* **11**, 549-563, doi:10.1080/17476348.2017.1334553 (2017).
- 14 Medbo, A. & Melbye, H. Lung function testing in the elderly--can we still use FEV1/FVC<70% as a criterion of COPD? *Respir.Med* **101**, 1097-1105 (2007).
- 15 Nardini, S. *et al.* Accuracy of diagnosis of COPD and factors associated with misdiagnosis in primary care setting. E-DIAL (Early DIAgnosis of obstructive lung disease) study group. *Respiratory Medicine* **143**, 61-66, doi:<https://doi.org/10.1016/j.rmed.2018.08.006> (2018).
- 16 Terence, H., Ruth, P. C., Nagendra, C., Imran, S. & Om, P. K. Under- and over-diagnosis of COPD: a global perspective. *Breathe* **15**, 24, doi:10.1183/20734735.0346-2018 (2019).
- 17 Hogg, J. C., McDonough, J. E. & Suzuki, M. Small airway obstruction in COPD: new insights based on micro-CT imaging and MRI imaging. *Chest* **143**, 1436-1443, doi:10.1378/chest.12-1766 (2013).
- 18 McDonough, J. E. *et al.* Small-airway obstruction and emphysema in chronic obstructive pulmonary disease. *N Engl J Med* **365**, 1567-1575, doi:10.1056/NEJMoa1106955 (2011).

- 19 Hogg, J. C., Macklem, P. T. & Thurlbeck, W. M. Site and nature of airway obstruction in chronic obstructive lung disease. *N Engl J Med* **278**, 1355-1360, doi:10.1056/nejm196806202782501 (1968).
- 20 Koo, H. K. *et al.* Small airways disease in mild and moderate chronic obstructive pulmonary disease: a cross-sectional study. *Lancet Respir Med* **6**, 591-602, doi:10.1016/s2213-2600(18)30196-6 (2018).
- 21 Blanco, I., Piccari, L. & Barbera, J. A. Pulmonary vasculature in COPD: The silent component. *Respirology* **21**, 984-994, doi:10.1111/resp.12772 (2016).
- 22 Hueper, K. *et al.* Pulmonary Microvascular Blood Flow in Mild Chronic Obstructive Pulmonary Disease and Emphysema. The MESA COPD Study. *Am J Respir Crit Care Med* **192**, 570-580, doi:10.1164/rccm.201411-2120OC (2015).
- 23 Synn, A. J. *et al.* Radiographic pulmonary vessel volume, lung function and airways disease in the Framingham Heart Study. *Eur Respir J* **54**, doi:10.1183/13993003.00408-2019 (2019).
- 24 Raouf, S. *et al.* Lung Imaging in COPD Part 1: Clinical Usefulness. *Chest* **164**, 69-84, doi:10.1016/j.chest.2023.03.007 (2023).
- 25 Altes, T. A. *et al.* Ventilation imaging of the lung: comparison of hyperpolarized helium-3 MR imaging with Xe-133 scintigraphy. *Acad.Radiol.* **11**, 729-734 (2004).
- 26 Johns, C. S. *et al.* Lung perfusion: MRI vs. SPECT for screening in suspected chronic thromboembolic pulmonary hypertension. *J Magn Reson Imaging* **46**, 1693-1697, doi:10.1002/jmri.25714 (2017).
- 27 Svenningsen, S. *et al.* Reproducibility of Hyperpolarized (129)Xe MRI Ventilation Defect Percent in Severe Asthma to Evaluate Clinical Trial Feasibility. *Acad Radiol*, doi:10.1016/j.acra.2020.04.025 (2020).
- 28 Zha, W. *et al.* Semiautomated Ventilation Defect Quantification in Exercise-induced Bronchoconstriction Using Hyperpolarized Helium-3 Magnetic Resonance Imaging: A Repeatability Study. *Acad Radiol* **23**, 1104-1114, doi:10.1016/j.acra.2016.04.005 (2016).
- 29 Eddy, R. L., Westcott, A., Maksym, G. N., Parraga, G. & Dandurand, R. J. Oscillometry and pulmonary magnetic resonance imaging in asthma and COPD. *Physiological reports* **7**, e13955, doi:10.14814/phy2.13955 (2019).
- 30 Eddy, R. L. *et al.* Is Computed Tomography Airway Count Related to Asthma Severity and Airway Structure and Function? *Am J Respir Crit Care Med* **201**, 923-933, doi:10.1164/rccm.201908-1552OC (2020).
- 31 Kirby, M., Kanhere, N., Etemad-Rezai, R., McCormack, D. G. & Parraga, G. Hyperpolarized helium-3 magnetic resonance imaging of chronic obstructive pulmonary disease exacerbation. *J Magn Reson Imaging* **37**, 1223-1227, doi:10.1002/jmri.23896 (2013).
- 32 Kirby, M., Pike, D., Coxson, H. O., McCormack, D. G. & Parraga, G. Hyperpolarized (3)He ventilation defects used to predict pulmonary exacerbations in mild to moderate chronic obstructive pulmonary disease. *Radiology* **273**, 887-896, doi:10.1148/radiol.14140161 (2014).
- 33 Kirby, M. *et al.* Pulmonary ventilation visualized using hyperpolarized helium-3 and xenon-129 magnetic resonance imaging: differences in COPD and relationship to emphysema. *J Appl Physiol (1985)* **114**, 707-715, doi:10.1152/jappphysiol.01206.2012 (2013).

- 34 de Lange, E. E. *et al.* Evaluation of asthma with hyperpolarized helium-3 MRI: correlation with clinical severity and spirometry. *Chest* **130**, 1055-1062, doi:10.1378/chest.130.4.1055 (2006).
- 35 Davis, C. *et al.* Ventilation Heterogeneity in Never-smokers and COPD:: Comparison of Pulmonary Functional Magnetic Resonance Imaging with the Poorly Communicating Fraction Derived From Plethysmography. *Acad Radiol* **23**, 398-405, doi:10.1016/j.acra.2015.10.022 (2016).
- 36 Kirby, M. *et al.* COPD: Do Imaging Measurements of Emphysema and Airway Disease Explain Symptoms and Exercise Capacity? *Radiology* **277**, 872-880, doi:10.1148/radiol.2015150037 (2015).
- 37 Coxson, H. O., Leipsic, J., Parraga, G. & Sin, D. D. Using pulmonary imaging to move chronic obstructive pulmonary disease beyond FEV₁. *Am J Respir Crit Care Med* **190**, 135-144, doi:10.1164/rccm.201402-0256PP (2014).
- 38 Lange, P., Halpin, D. M., O'Donnell, D. E. & MacNee, W. Diagnosis, assessment, and phenotyping of COPD: beyond FEV₁. *Int J Chron Obstruct Pulmon Dis* **11 Spec Iss**, 3-12, doi:10.2147/copd.S85976 (2016).
- 39 Leary, D. *et al.* Hyperpolarized 3He magnetic resonance imaging ventilation defects in asthma: relationship to airway mechanics. *Physiological reports* **4**, doi:10.14814/phy2.12761 (2016).
- 40 Makimoto, K. *et al.* Comparison of Feature Selection Methods and Machine Learning Classifiers for Predicting Chronic Obstructive Pulmonary Disease Using Texture-Based CT Lung Radiomic Features. *Acad Radiol* **30**, 900-910, doi:10.1016/j.acra.2022.07.016 (2023).
- 41 Makimoto, K., Hogg, J. C., Bourbeau, J., Tan, W. C. & Kirby, M. CT Imaging With Machine Learning for Predicting Progression to COPD in Individuals at Risk. *Chest*, doi:<https://doi.org/10.1016/j.chest.2023.06.008> (2023).
- 42 Bian, Z. *et al.* Small airway segmentation in thoracic computed tomography scans: a machine learning approach. *Phys Med Biol* **63**, 155024, doi:10.1088/1361-6560/aad2a1 (2018).
- 43 Ginsburg, S. B. *et al.* Texture-based Quantification of Centrilobular Emphysema and Centrilobular Nodularity in Longitudinal CT Scans of Current and Former Smokers. *Acad Radiol* **23**, 1349-1358, doi:10.1016/j.acra.2016.06.002 (2016).
- 44 Hoffman, E. A. *et al.* in *C5. C005 DIAGNOSIS AND PROGNOSIS IN COPD* A1122-A1122.
- 45 Sørensen, L. *et al.* Chronic Obstructive Pulmonary Disease Quantification Using CT Texture Analysis and Densitometry: Results From the Danish Lung Cancer Screening Trial. *AJR Am J Roentgenol* **214**, 1269-1279, doi:10.2214/ajr.19.22300 (2020).
- 46 Depeursinge, A., Al-Kadi, O. S. & Mitchell, J. R. *Biomedical texture analysis: fundamentals, tools and challenges*. (Academic Press, 2017).
- 47 Rizzo, S. *et al.* Radiomics: the facts and the challenges of image analysis. *Eur Radiol Exp* **2**, 36, doi:10.1186/s41747-018-0068-z (2018).
- 48 Li, Z. *et al.* A Novel CT-Based Radiomics Features Analysis for Identification and Severity Staging of COPD. *Acad Radiol* **29**, 663-673, doi:10.1016/j.acra.2022.01.004 (2022).
- 49 Israel, O. *et al.* Combined functional and structural evaluation of cancer patients with a hybrid camera-based PET/CT system using 18F-FDG. *Journal of Nuclear Medicine* **43**, 1129-1136 (2002).

- 50 Bagci, U. *et al.* Joint segmentation of anatomical and functional images: Applications in quantification of lesions from PET, PET-CT, MRI-PET, and MRI-PET-CT images. *Medical image analysis* **17**, 929-945 (2013).
- 51 Cremers, D., Rousson, M. & Deriche, R. A review of statistical approaches to level set segmentation: integrating color, texture, motion and shape. *International journal of computer vision* **72**, 195-215 (2007).
- 52 Dammann, F. *et al.* Diagnostic imaging modalities in head and neck disease. *Deutsches Arzteblatt international* **111**, 417-423, doi:10.3238/arztebl.2014.0417 (2014).
- 53 Harvey, B. G. *et al.* Risk of COPD with obstruction in active smokers with normal spirometry and reduced diffusion capacity. *Eur Respir J* **46**, 1589-1597, doi:10.1183/13993003.02377-2014 (2015).
- 54 Suissa, S., Dell'Aniello, S. & Ernst, P. Long-term natural history of chronic obstructive pulmonary disease: severe exacerbations and mortality. *Thorax* **67**, 957-963, doi:10.1136/thoraxjnl-2011-201518 (2012).
- 55 Ke, X. *et al.* Impact of lung function on exacerbations, health care utilization, and costs among patients with COPD. *Int J Chron Obstruct Pulmon Dis* **11**, 1689-1703, doi:10.2147/copd.S108967 (2016).
- 56 Balasubramanian, A. *et al.* Diffusing Capacity of Carbon Monoxide in Assessment of COPD. *Chest* **156**, 1111-1119, doi:10.1016/j.chest.2019.06.035 (2019).
- 57 Kauczor, H. U., Chen, X. J., van Beek, E. J. & Schreiber, W. G. Pulmonary ventilation imaged by magnetic resonance: at the doorstep of clinical application. *Eur Respir J* **17**, 1008-1023, doi:10.1183/09031936.01.17510080 (2001).
- 58 Saam, B. T. *et al.* MR imaging of diffusion of ³He gas in healthy and diseased lungs. *Magn Reson Med* **44**, 174-179, doi:10.1002/1522-2594(200008)44:2<174::aid-mrm2>3.0.co;2-4 (2000).
- 59 Mathew, L. *et al.* Hyperpolarized ³He magnetic resonance imaging of chronic obstructive pulmonary disease: reproducibility at 3.0 tesla. *Acad Radiol* **15**, 1298-1311, doi:10.1016/j.acra.2008.04.019 (2008).
- 60 Kirby, M. *et al.* Hyperpolarized ³He and ¹²⁹Xe magnetic resonance imaging apparent diffusion coefficients: physiological relevance in older never- and ex-smokers. *Physiological reports* **2**, doi:10.14814/phy2.12068 (2014).
- 61 Fain, S. B. *et al.* Early emphysematous changes in asymptomatic smokers: detection with ³He MR imaging. *Radiology* **239**, 875-883, doi:10.1148/radiol.2393050111 (2006).
- 62 Kirby, M. *et al.* On the role of abnormal DL(CO) in ex-smokers without airflow limitation: symptoms, exercise capacity and hyperpolarised helium-3 MRI. *Thorax* **68**, 752-759, doi:10.1136/thoraxjnl-2012-203108 (2013).
- 63 Matheson, M. C. *et al.* Prediction models for the development of COPD: a systematic review. *Int J Chron Obstruct Pulmon Dis* **13**, 1927 (2018).
- 64 Shah, S. A., Velardo, C., Farmer, A. & Tarassenko, L. Exacerbations in Chronic Obstructive Pulmonary Disease: Identification and Prediction Using a Digital Health System. *J Med Internet Res* **19**, e69, doi:10.2196/jmir.7207 (2017).
- 65 Chapman, K. R. *et al.* Intravenous augmentation treatment and lung density in severe α 1 antitrypsin deficiency (RAPID): a randomised, double-blind, placebo-controlled trial. *Lancet* **386**, 360-368, doi:10.1016/s0140-6736(15)60860-1 (2015).

- 66 Kirby, M. *et al.* MRI ventilation abnormalities predict quality-of-life and lung function changes in mild-to-moderate COPD: longitudinal TINCan study. *Thorax* **72**, 475-477, doi:10.1136/thoraxjnl-2016-209770 (2017).
- 67 Agusti, A. *et al.* Treatable traits: toward precision medicine of chronic airway diseases. *Eur Respir J* **47**, 410-419, doi:10.1183/13993003.01359-2015 (2016).
- 68 Ahumada, S. *et al.* Prevalence of abnormal lung volumes, DLCO and chest HRCT in smokers with normal spirometry. *European Respiratory Journal* **42**, P418 (2013).
- 69 Celli, B. R., Cote, C. G., Lareau, S. C. & Meek, P. M. Predictors of Survival in COPD: more than just the FEV1. *Respir Med* **102 Suppl 1**, S27-35, doi:10.1016/s0954-6111(08)70005-2 (2008).
- 70 Regan, E. A. *et al.* Genetic epidemiology of COPD (COPDGene) study design. *COPD* **7**, 32-43, doi:10.3109/15412550903499522 (2010).
- 71 Couper, D. *et al.* Design of the Subpopulations and Intermediate Outcomes in COPD Study (SPIROMICS). *Thorax* **69**, 491-494, doi:10.1136/thoraxjnl-2013-203897 (2014).
- 72 Vestbo, J. *et al.* Evaluation of COPD Longitudinally to Identify Predictive Surrogate End-points (ECLIPSE). *Eur Respir J* **31**, 869-873, doi:10.1183/09031936.00111707 (2008).
- 73 Madani, A., Van Muylem, A. & Gevenois, P. A. Pulmonary emphysema: effect of lung volume on objective quantification at thin-section CT. *Radiology* **257**, 260-268, doi:10.1148/radiol.10091446 (2010).
- 74 MacNeil, J. L. *et al.* Pulmonary Imaging Phenotypes of Chronic Obstructive Pulmonary Disease Using Multiparametric Response Maps. *Radiology* **295**, 227-236, doi:10.1148/radiol.2020191735 (2020).
- 75 Fain, S. B. *et al.* Early emphysematous changes in asymptomatic smokers: detection with ³He MR imaging. *Radiology*. **239**, 875-883 (2006).
- 76 Han, M. K. *et al.* Association between Emphysema and Chronic Obstructive Pulmonary Disease Outcomes in the COPDGene and SPIROMICS Cohorts: A Post Hoc Analysis of Two Clinical Trials. *Am J Respir Crit Care Med* **198**, 265-267, doi:10.1164/rccm.201801-0051LE (2018).
- 77 Sieren, J. P. *et al.* SPIROMICS Protocol for Multicenter Quantitative Computed Tomography to Phenotype the Lungs. *Am J Respir Crit Care Med* **194**, 794-806, doi:10.1164/rccm.201506-1208PP (2016).
- 78 Ash, S. Y. *et al.* Relationship between Emphysema Progression at CT and Mortality in Ever-Smokers: Results from the COPDGene and ECLIPSE Cohorts. *Radiology* **299**, 222-231, doi:10.1148/radiol.2021203531 (2021).
- 79 Martin, M. *et al.* Ectopic fat accumulation in patients with COPD: an ECLIPSE substudy. *Int J Chron Obstruct Pulmon Dis* **12**, 451-460, doi:10.2147/COPD.S124750 (2017).
- 80 Lowe, K. E. *et al.* COPDGene((R)) 2019: Redefining the Diagnosis of Chronic Obstructive Pulmonary Disease. *Chronic Obstr Pulm Dis* **6**, 384-399, doi:10.15326/jcopdf.6.5.2019.0149 (2019).
- 81 Boes, J. L. *et al.* Parametric response mapping monitors temporal changes on lung CT scans in the subpopulations and intermediate outcome measures in COPD Study (SPIROMICS). *Acad Radiol* **22**, 186-194, doi:10.1016/j.acra.2014.08.015 (2015).
- 82 Guo, F. *et al.* Development of a pulmonary imaging biomarker pipeline for phenotyping of chronic lung disease. *J Med Imaging (Bellingham)* **5**, 026002, doi:10.1117/1.JMI.5.2.026002 (2018).

- 83 McIntosh, M. *et al.* in *International Society for Magnetic Resonance in Medicine Conference 2020*. 192.
- 84 Hoffman, E. A. *et al.* Pulmonary CT and MRI phenotypes that help explain chronic pulmonary obstruction disease pathophysiology and outcomes. *J Magn Reson Imaging* **43**, 544-557, doi:10.1002/jmri.25010 (2016).
- 85 Esteva, A. *et al.* Dermatologist-level classification of skin cancer with deep neural networks. *Nature* **542**, 115-118, doi:10.1038/nature21056 (2017).
- 86 Öztürk, S. a. *Convolutional neural networks for medical image processing applications*. (CRC Press, 2023).
- 87 Heidari, A., Jafari Navimipour, N., Unal, M. & Toumaj, S. The COVID-19 epidemic analysis and diagnosis using deep learning: A systematic literature review and future directions. *Comput Biol Med* **141**, 105141, doi:10.1016/j.compbiomed.2021.105141 (2022).
- 88 Ismael, A. M. & Sengur, A. Deep learning approaches for COVID-19 detection based on chest X-ray images. *Expert Syst Appl* **164**, 114054, doi:10.1016/j.eswa.2020.114054 (2021).
- 89 Capaldi, D. P. I., Guo, F., Xing, L. & Parraga, G. Pulmonary Ventilation Maps Generated with Free-breathing Proton MRI and a Deep Convolutional Neural Network. *Radiology* **298**, 427-438, doi:10.1148/radiol.2020202861 (2021).
- 90 Xu, Y. M. *et al.* Deep Learning in CT Images: Automated Pulmonary Nodule Detection for Subsequent Management Using Convolutional Neural Network. *Cancer Manag Res* **12**, 2979-2992, doi:10.2147/CMAR.S239927 (2020).
- 91 Humphries, S. M., Notary, A. M., Centeno, J. P. & Lynch, D. A. in *TIA-MICCAI 2018*. 319-325 (Springer International Publishing).
- 92 Kirby, M. *et al.* On the role of abnormal DL_{CO} in ex-smokers without airflow limitation: symptoms, exercise capacity and hyperpolarised helium-3 MRI. *Thorax* **68**, 752-759, doi:10.1136/thoraxjnl-2012-203108 (2013).
- 93 Haralick, R. M., Shanmugam, K. & Dinstein, I. Textural Features for Image Classification. *IEEE Trans Image Process*, 610-621 (1973).
- 94 Tang, X. Texture information in run-length matrices. *IEEE Trans Image Process* **7**, 1602-1609, doi:10.1109/83.725367 (1998).
- 95 Shelhamer, E., Long, J. & Darrell, T. Fully Convolutional Networks for Semantic Segmentation. *IEEE transactions on pattern analysis and machine intelligence* **39**, 640-651, doi:10.1109/tpami.2016.2572683 (2017).
- 96 Ronneberger, O., Fischer, P. & Brox, T. U-Net: Convolutional Networks for Biomedical Image Segmentation. *Medical Image Computing and Computer-Assisted Intervention*, 234-241 (2015).
- 97 Woods, J. C. & Conradi, M. S. (3)He diffusion MRI in human lungs. *J Magn Reson* **292**, 90-98, doi:10.1016/j.jmr.2018.04.007 (2018).
- 98 Milne, S. & King, G. G. Advanced imaging in COPD: insights into pulmonary pathophysiology. *J Thorac Dis* **6**, 1570-1585, doi:10.3978/j.issn.2072-1439.2014.11.30 (2014).
- 99 Kirby, M. & Parraga, G. COPD imaging: new tools to tackle an old problem? *COPD* **11**, 477-479, doi:10.3109/15412555.2014.952968 (2014).
- 100 Kirby, M. & Sin, D. D. Imaging End Points in COPD Clinical Trials: Are We There Yet? *Chest* **154**, 3-5, doi:10.1016/j.chest.2018.01.050 (2018).

- 101 Díaz, A. A. *et al.* Emphysema and DLCO predict a clinically important difference for 6MWD decline in COPD. *Respir Med* **109**, 882-889, doi:10.1016/j.rmed.2015.04.009 (2015).
- 102 Jones, P. W. St. George's Respiratory Questionnaire: MCID. *COPD*. **2**, 75-79 (2005).
- 103 Vestbo, J. *et al.* Global strategy for the diagnosis, management, and prevention of chronic obstructive pulmonary disease: GOLD executive summary. *Am J Respir Crit Care Med* **187**, 347-365, doi:10.1164/rccm.201204-0596PP (2013).
- 104 Spurzem, J. R. & Rennard, S. I. Pathogenesis of COPD. *Semin Respir Crit Care Med* **26**, 142-153, doi:10.1055/s-2005-869535 (2005).

APPENDICES

Appendix A – Quantification of Pulmonary Functional MRI: State-of-the-Art and Emerging Image Processing Methods and Measurements

In this review article, we provided a summary of the current state-of-the-art and emerging quantitative image processing methods and measurements, which have advanced or have the potential to provide a better understanding of respiratory disease pathologies.

*The contents of this appendix were previously published in the Physics in Medicine & Biology journal: M Sharma, PV Wyszkievicz, V Desaigoudar, F Guo, DPI Capaldi and G Parraga. Quantification of pulmonary functional MRI: state-of-the-art and emerging image processing methods and measurements. Physics in Medicine & Biology 2022. <https://doi.org/10.1088/1361-6560/ac9510>. Permission to reproduce this article is provided in **Appendix D**.*

RATIONALE

1.1 Background

The structure and the function of our lungs are essential for human life. As the Lung Association clearly states, “*when you can’t breathe, nothing else matters*”.¹ The automatic and rhythmic act of breathing is necessarily driven by networks of neurons in the hindbrain (pons and medulla) that together direct the thoracic and abdominal muscles to actively produce pressure gradients that help move ambient air into and out of the lungs. This activity drives the exchange of oxygen from outside the body with carbon dioxide waste produced inside the body at the alveolar-capillary membrane (~0.2-0.5 μm thickness).² In a healthy human adult, the end of the bronchioles in the lung is where gas-exchange occurs and it involves approximately 300-500 million alveoli, which are themselves completely wrapped in approximately 500-1000 pulmonary capillaries per alveolus.³

The structure and the function of this marvelous system can be captured simultaneously, in real-time, with unprecedented spatial resolution (~1.5mm isotropic voxels with ultra-short echo time [UTE] MRI). For ventilation imaging, pulmonary functional magnetic resonance imaging (PfMRI) methods and measurements can provide ~4x4x10mm voxel resolution. PfMRI is currently

dominated by hyperpolarized gas imaging but involves all pulmonary MRI techniques capable of quantifying lung function. Using such PfMRI approaches, the spatial distribution of pulmonary ventilation and gas-exchange with the pulmonary vascular tree can be non-invasively mapped and measured in three-dimensions (3D), throughout the whole lung or by regions of the lung, including the lung lobes after co-registration with CT. Importantly, this approach does not rely on the use of ionizing radiation because while ^3He and ^{129}Xe atoms can be thermodynamically polarized, their nuclei are stable. Recent reviews⁴⁻¹⁴ have focused on the history and development of MRI hardware and image acquisition methods needed to routinely provide reproducible hyperpolarized ^3He and ^{129}Xe measurements. Until now however, there has been no evaluative review of current image processing methods and the requirements needed to enable rapid, reproducible and physiologically relevant measurements.

1.2 Knowledge gap

Whilst there is international agreement on the need to standardize PfMRI acquisition methods,^{15,16} progress towards standardized image analysis methods including those that employ machine and deep learning has been limited. Hence here we examine and review the quantitative image analysis and processing methods that are required to extract clinically meaningful, reproducible and rapid PfMRI measurements.

1.3 Why read on?

In this invited review we focus on quantitative image processing methods for PfMRI using hyperpolarized noble gases, which has become the dominant acquisition method in the field. We review historical progress and the state-of-the-art applications of these computational techniques to measurements of obstructive lung disease, where arguably, most progress has been made. We will discuss the basic structural and physiologic underpinnings of pulmonary functional imaging

using this modality and highlight the various imaging techniques that have been historically developed to quantify and generate functional biomarkers for ventilation, gas exchange and distribution in the lungs. Throughout the review we summarize the hallmark developments in the image processing and analysis domain, with their current applications, challenges, gaps in knowledge, and future directions of development of these methods for pulmonary imaging. These are discussed in the context of the most common types of obstructive pulmonary diseases, focusing on hyperpolarized gas MRI and image processing techniques for ventilation MRI. We conclude this article with an appraisal of how such quantification methods have helped our understanding of pulmonary diseases and how they can be translated to the clinic and applied for enhanced patient monitoring and management.

II INTRODUCTION

2.1 Pulmonary Structure and Function

In humans, the respiratory system is one of two inter-communicating linearly arranged systems (shown in Figure 1) that ensure blood is oxygenated and circulated to the two actively involved heart and lung organ systems and the rest of the body systems. The heart and lung systems work together at two different frequencies (~ 1 Hz for heart and 0.25 Hz for lungs) to move approximately 6L of blood and 6L of air through the body every minute. Over the course of an 80-year life, the heart will have beaten about 2.5 billion times and the lungs will have taken 640 million breaths.

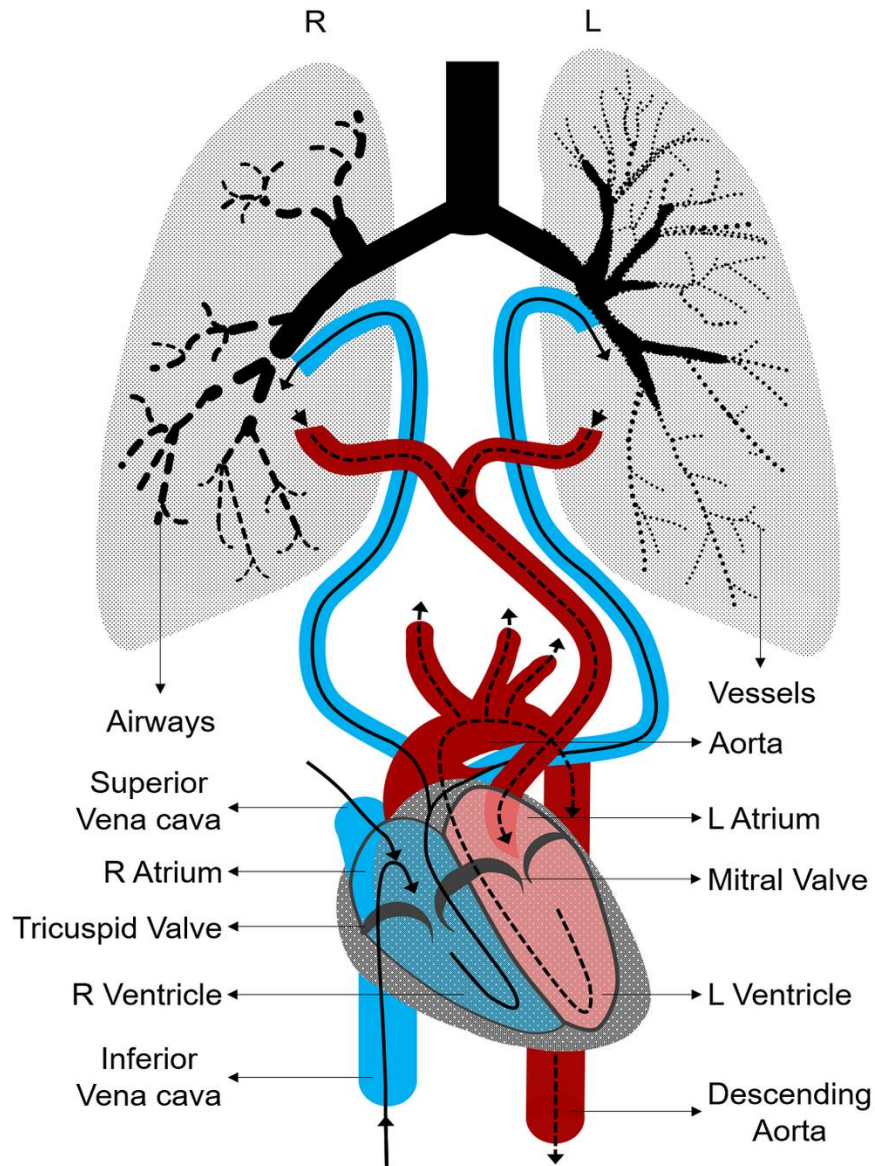


Figure 1. The heart and the lung as interconnected linearly arranged systems

The respiratory and cardiovascular systems are depicted as two inter-communicating linearly arranged systems that collectively enable the blood oxygenation and circulation to the rest of the body systems. The relevant constituents of the heart ensuring the transfer of oxygenated-blood from the lung to the rest of the body are shown.

Here we focus on the adult human lung which is shown in Figure 2 in physiologic schematic and again with an imaging lens in Figure 3. The lungs typically occupy about $30 \times 30 \times 20 \text{ cm}^3$ within the thoracic cavity of a healthy fully-grown adult,¹⁷ as shown in Figure 3. These dimensions vary somewhat, based on sex, body frame size and other factors, but the overarching function of the

lung remains the same- delivery of oxygen to the blood for distribution to the body while simultaneously removing carbon dioxide from the body tissues, back to the environment.

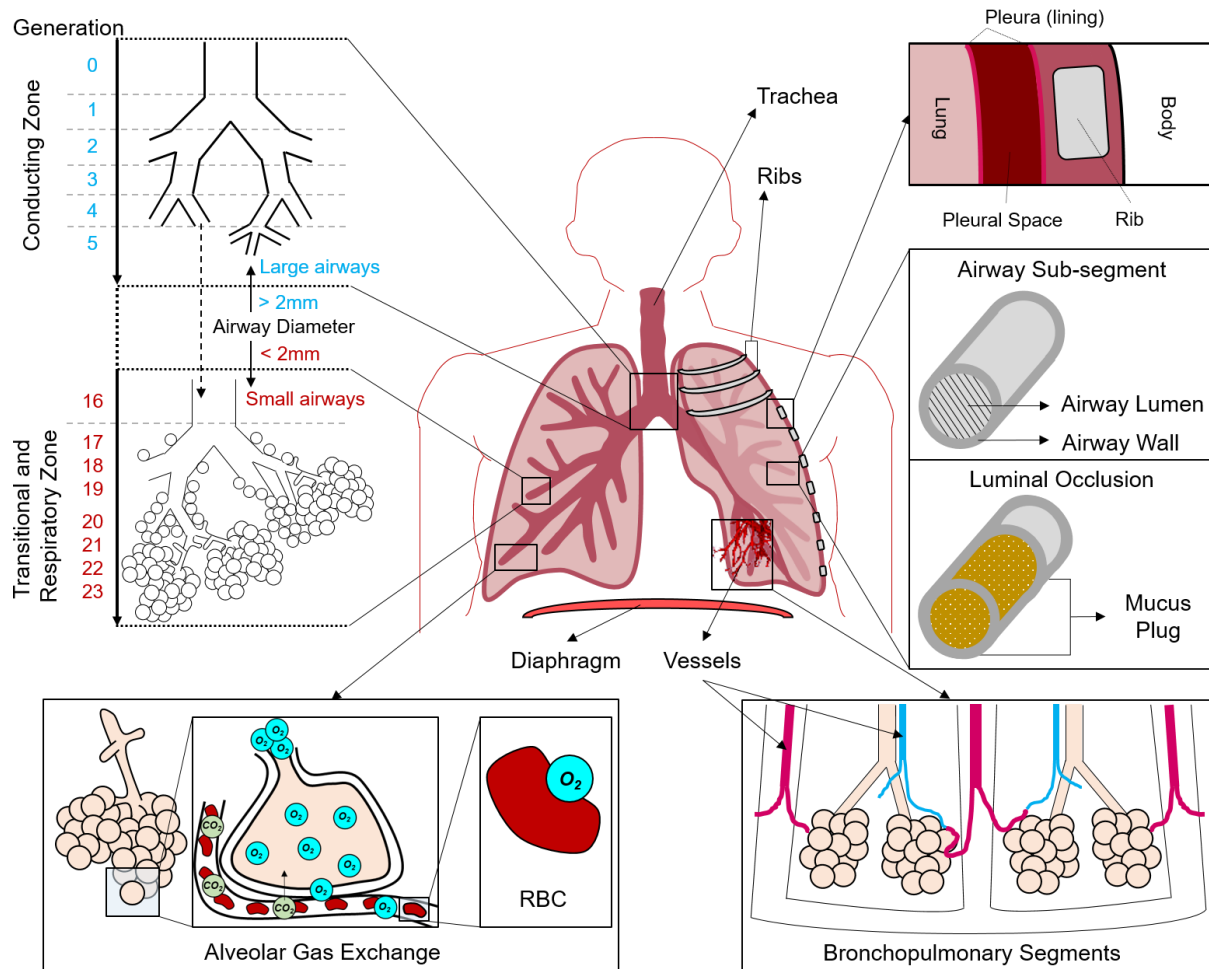


Figure 2. Lung components

Respiratory system structure showing the airway tree generations that provide passage for air to travel from the nose through the large and small airways to the alveoli. Subsegmental airways branch from larger airway segments and are composed of the airway wall and lumen, which may be occluded with a mucus plug. Oxygen binds to the red blood cells in the pulmonary vessels to deliver oxygen into the bloodstream. Bronchopulmonary segments are richly supplied with red blood cells by the segmental bronchi and its vessels, in order to participate in pulmonary gas exchange and perfusion. Oxygen (O_2) travels through the airways into the alveoli where gas exchange occurs and carbon dioxide (CO_2) is removed from the body.

As shown in Figure 2 in the top left panels, air flows and then diffuses through the airway tree, through as few as 10 or as many as 23 branch-point generations. The first 16 generations of the

airway tree, which is the conducting zone where air flows, contain no alveoli and thus are anatomically incapable of gas-exchange with the pulmonary capillary red blood cells (RBC). However, alveoli do populate the terminal airways from the 17th through 19th airway generations in the so-called respiratory bronchioles that constitute the transitional zone, where air moves through the branches via diffusion and not flow. Once air arrives at the 20th to 23rd airway generations, the airway termini are completely populated with alveoli that are available for gas-exchange.¹⁸

As shown in the right panels of Figure 2, the pulmonary arterial tree runs in parallel to the airways and many of the structural properties that affect flow are common to both tree structures. The bronchopulmonary segments and capillary network are richly supplied with blood containing RBC each packed with hemoglobin tetramers. Gas-exchange occurs at the alveolar-capillary tissue membrane, which itself is one cell and ~0.2-0.5 μm thick.² The lungs are also necessarily elastic, allowing for the respiratory system to undergo complex biomechanical changes that enable breathing and highly efficient gas-exchange.

Table 1. Quantitative pulmonary CT and MRI measurements

Method	Measurements	Applications
X-ray CT	-Total airway count (TAC) -Wall area percent (WA%) -Lumen area percent (LA%) -Wall thickness percent (WT%) -Mucus score	-Total number of CT visible airways, related to abnormal airway structure and function ^{19,20} -Airway wall and lumen measures strongly related to airflow obstruction ²¹ -Mucus plugs associated with airflow limitation ^{22,23}
Inspiratory-Expiratory CT	-Relative area of the lung with attenuation < -950 Hounsfield Units (RA ₉₅₀) -Relative area of the lung with attenuation < -856 Hounsfield Units (RA ₈₅₆) -Parametric response map (PRM) -Jacobian determinant (J _{det})	-Inspiratory CT RA ₉₅₀ reflects terminal airspace destruction and emphysema ²⁴ -Expiratory CT RA ₈₅₆ reflects expiratory air trapping, related to small airway obstruction ²⁵ -PRM classifies voxels based on co-registered Insp/Exp attenuation, providing novel emphysema and gas-trapping phenotypes ²⁶ -J _{det} measures local lung expansion and contraction during breathing reflecting lung mechanics ^{27,28}
4D CT	-Deformation anisotropy -Ventilation measure	-Anisotropic deformation quantifies non-linearity and hysteresis of the lung ²⁹ -Deformable image registration of lung voxels from the inhale to the exhale phases to calculate the Jacobian ³⁰
¹ H MRI UTE	Proton density	-Metric for structural tissue density quantification, signal intensity is related to pulmonary function and CT density measurements ^{31,32}
¹ H MRI free breathing Fourier decomposition and other related methods	-Ventilation defect percent (VDP) -Ventilated Volume (VV) -Perfusion defect percent (QDP)	-Fourier decomposition separates signal changes at the breathing frequency from signal changes at the cardiac frequency to generate ventilation and perfusion maps respectively ³³⁻³⁵ -VDP is ratio of ventilation defect volume (VDV) to the thoracic cavity volume; VV is volume of ventilated lung ³⁶ -QDP is the ratio of the perfusion defect volume to the thoracic cavity volume ³⁷
³ He/ ¹²⁹ Xe	-Ventilation defect percent (VDP) -Ventilated Volume (VV) -Ventilation Coefficient of Variation (CV) -Apparent Diffusion Coefficient (ADC)	-VDP is the ratio of ventilation defect volume to the thoracic cavity volume -VV is the volume of ventilated lung ³⁶ -Ventilation CV reflects ventilation heterogeneity ³⁸ -ADC quantifies terminal airspace and alveolar morphology and size, and is related to emphysema ³⁹⁻⁴²
¹²⁹ Xe	-RBC to Gas ratio -Membrane to RBC ratio -Membrane to Gas ratio	-RBC:M is a metric of gas exchange function and parenchymal tissue thickening ⁴³⁻⁴⁵ -RBC:Gas is a metric of gas uptake and perfusion ^{43,46} -M:Gas is a metric of tissue thickening ^{43,47}
Dynamic Contrast Enhanced (DCE) MRI	-Pulmonary blood flow -Perfusion -3D perfusion changes	-Pharmacokinetic analysis of the administered paramagnetic contrast agent ^{48,49} -Can separately assess the macro-and microvasculature when used together with MR angiography ⁵⁰

2.2 Current Clinical Imaging Approaches

2.2.1 Anatomical imaging

As shown in Figure 3 in schematic, the lung may be viewed strictly from an image acquisition framework as five independent pulmonary lobes (three in the right lung and two in the left lung) in three-dimensional (3D) space. When imaging data are acquired in 3D using tomographic methods such as x-ray CT or MRI, the coronal, sagittal and axial views may be independently generated, visualized and evaluated quantitatively. As shown in Table 1, anatomical measurements of the lung airways, blood vessels and parenchyma may be generated using chest CT on a regional (apex, base, central, peripheral), lobar and slice-by-slice basis. CT measurements are related to the airways, including airway lumen area (LA),²¹ airway wall thickness (WT),²¹ total airway count (TAC)^{19,20} and airway wall thickness as a fraction of the total airway area (WT%).²¹ Typical breath-hold CT measurements include the relative area of the lung with attenuation below -950 Hounsfield Units (RA₉₅₀),²⁴ generated from inspiratory CT acquisition, and similarly, the relative area of the lung with attenuation below -856 Hounsfield Units (RA₈₅₆) from expiratory CT.²⁵ Furthermore, parametric response maps (PRM)²⁶ can be generated on a voxel-by-voxel basis by co-registering inspiratory and expiratory CT scans, providing novel emphysema and gas-trapping phenotypes of small airways disease.

The lung parenchyma has a short transverse magnetization relaxation time (T_2), which is the time taken by excited protons to lose phase coherence. This results in a reduction in this transverse magnetization and a much faster MRI signal decay for the lung parenchyma in comparison to other tissues.⁵¹ The difference in magnetic susceptibilities between air and alveolar wall tissue leads to local magnetic field inhomogeneity and results in faster spin dephasing (shorter T_2^*). High spatial resolution images of the lung parenchyma can be obtained by maximizing signal strength and minimizing degradation due to susceptibility dephasing, which can be achieved by minimizing the time between excitation and acquisition of the signal called echo time (TE).⁵² Short,⁵³ ultra-short

(UTE)^{32,54} and zero (ZTE)⁵⁵ echo time ¹H lung MRI as well as advanced MR hardware (such as multi-element RF coil arrays) have since significantly improved the visualization of lung parenchyma, as described in Table 1.

2.2.2 Functional Imaging

Table 1 also provides an overview of pulmonary functional imaging measurements made possible using CT and MRI – although these methods are less-well established for clinical use than anatomic imaging methods. Four-dimensional CT (4DCT) can measure changes in volume by reconstructing images at many points throughout the breathing cycle and has shown that deformation throughout the respiratory cycle is nonlinear and demonstrates hysteresis.⁵⁶ Pulmonary vascular measurements from dynamic perfusion CT can be generated by analyzing the temporal change in injected iodine concentration within the lung parenchyma and vascular spaces as a function of time.^{57,58} Changes throughout the breathing cycle can also be quantified using Oxygen-enhanced (OE) ¹H MRI and Fluorine-19 (¹⁹F) MRI. OE-MRI can provide the combined information about lung ventilation, perfusion from oxygen getting dissolved in blood and oxygen diffusion across the alveolar-capillary membrane.⁵⁹ ¹⁹F-MRI can quantify lung function with only a multinuclear capable MR system with a dedicated ¹⁹F coil, without the need for a specialized polarizer equipment and personnel, which makes it cost efficient and less demanding in research and clinical settings.⁶⁰ PET on its own or in combination with CT and MRI are additional techniques that can be used to evaluate and quantify lung function, perfusion, inflammation, and metabolic changes.⁶¹⁻⁶⁴ Various radiotracers can be used to detect activity of pulmonary inflammation in multiple respiratory diseases,^{62,65,66} but this discussion is beyond the scope of this review.

In breath-hold ventilation MRI, sensitive biomarkers such as ventilation defect percent (VDP),⁶⁷ ventilated volume (VV),⁶⁸ and ventilation coefficient of variation (CV) can be quantified. In contrast to ventilation, CT and MR angiography⁶⁹ as well as dynamic contrast-enhanced (DCE) MR techniques^{48,70} are typically used to visualize vessels and provide functional information on perfusion.^{71,72} Such perfusion measurements are most commonly performed using DCE-MRI, in which pharmacokinetic analysis of the administered paramagnetic contrast agent is used to quantify perfusion, and when used together with MR angiography, these can separately assess the macro- and microvasculature. The ¹²⁹Xe gas has been shown to dissolve in body tissues and the dissolved ¹²⁹Xe exhibits distinctly different resonance frequency shifts for the air spaces, the lung tissues and RBC,⁴³ making it an intriguing alternative technique that may be used clinically in the future.

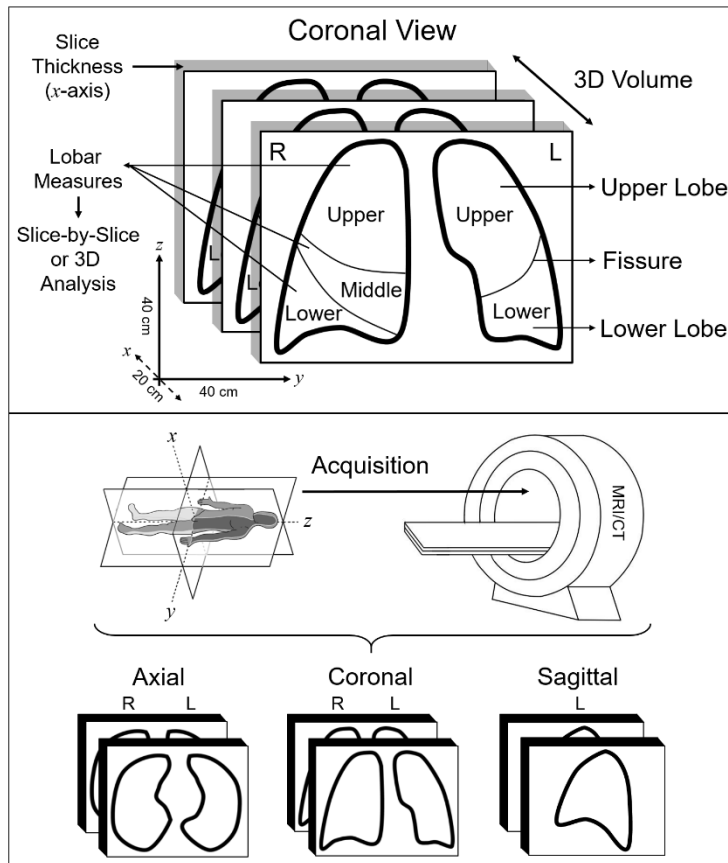


Figure 3. Image acquisition and analysis requirements

Typical coronal field-of-view of 40x40cm in the left-right and superior-inferior directions, with slice thickness shown in the anterior-posterior direction. Three standard acquisition planes are depicted in the coronal (sliced anterior-posterior), sagittal (sliced left-right), and axial planes (superior-inferior). Right and left pulmonary lobes and fissures are shown in coronal view.

2.3 Emerging Functional MRI Methods

2.3.1 *Dynamic and multi-volume ¹H MRI*

The enhancements in spatial resolution due to shorter TE sequences and advancements in MR hardware have also been coincident with new ways to perform free-breathing ¹H MRI to capture dynamic information as well as with multi-volume static breath-hold approaches. One such multi-volume approach utilizes 3D cones UTE sequence to acquire MR images at four lung volumes in order to evaluate the signal changes and generate voxel-wise dynamic proton-density maps that reflect the change of lung signal intensities.⁷³

Analyzing MRI signal variations in the lung resulting from respiration also lies at the heart of Fourier decomposition (FD) MRI, first proposed in 2009.⁷⁴ In FD-MRI, the dynamically acquired images of the lung are elastically registered, preserving the signal variations in the individual voxels from respiration. The time series is then analyzed in the temporal domain, separating the high-frequency signals of pulsating blood from the low-frequency signals of respiratory motion on a voxel-by-voxel level. Finally, the magnitudes of the appropriate respiratory and cardiac peaks of the Fourier spectrum are calculated in order to generate corresponding ventilation and perfusion maps.⁷⁵ The applicability of this method has been demonstrated at 1.5 T,⁷⁴ and using a spoiled-gradient echo (SPGR) sequence at 3 T MR systems.^{34,76-78} Another recently developed method⁷⁹ forgoes FD to obtain specific ventilation maps, using the phase component of the respiratory signal where each imaging time point is linked to a respiratory phase (one cycle $[-\pi, \pi]$) using Hilbert transform.⁸⁰ A 3D dataset for a single respiratory cycle is then created with 10 respiratory-phase

bins, similar to 4DCT.^{81,82} Tidal inspiration and expiration volumes are then co-registered with the reference phase (halfway between these volumes) in order to generate the specific ventilation maps.⁷⁹

In recent years, the development of phase sorting methods according to both the cardiac and ventilation phase has led to developments of self-gated non contrast-enhanced functional lung (SENCEFUL)⁸³ and phase-resolved functional lung (PREFUL) MRI.⁷⁴ SENCEFUL sorts the respiratory phases using a direct current (DC) signal acquired immediately after the signal readout, while PREFUL estimates the respiratory and cardiac phases for each image using the MRI signal of a SPGR sequence and then interpolates the complete respiratory and cardiac cycles. PREFUL and SENCEFUL MRI methods calculate regional flow-volume loops, specific ventilation and perfusion maps,^{84,85} without requiring respiratory bellows.

2.3.2 Hyperpolarized ^3He and ^{129}Xe MRI

Figure 4 outlines the main developments in the historical timeline for hyperpolarized ^3He and ^{129}Xe MRI. As shown in the schematic, spin exchange optical pumping⁸⁶ first reported in 1950s and recently reviewed,⁸⁷⁻⁸⁹ is the method of choice for polarization of noble gases for MRI studies. An intermediary rubidium vapor is exploited where the valence electrons of the rubidium vapor are polarized by absorption of circularly polarized light from the laser source, and it was shown that angular momentum from electron spins could be transferred to nuclear spins of high-pressure noble gases.^{90,91} This technique generates polarizations of about 40–70% for ^3He and 10–40% for ^{129}Xe in a typical dose of 1 L or less for breath-holds.⁹²⁻⁹⁴ This enhances the MRI signal by a factor of up to 100,000 above thermal equilibrium levels.⁹⁵ In 1994,⁹⁶ the first *ex-vivo* hyperpolarized ^{129}Xe MRI study in animals was completed, which initiated a cascade of critical developments in the field,^{97,98} including the first ^3He MRI studies in patients with lung disease in 1996.^{99,100} Most of

the initial human studies were performed using ^3He ,⁷ which has a greater gyromagnetic ratio than ^{129}Xe (-32.434 MHz/T for ^3He vs -11.777 MHz/T for ^{129}Xe) and offered greater polarization and SNR. However, the recent scarcity and corresponding increased price of ^3He gas has driven the development of improved ^{129}Xe gas polarization methods,¹⁰¹ which have become the mainstay method in the field. In 1980,¹⁰² investigations showed that xenon displayed increased solubility in body tissues and blood with increased hematocrit, compared to helium gas, due to its modest Ostwald solubility.^{103,104} Thus, ^{129}Xe is also capable of transmembrane diffusion and in the timeframe of an MRI acquisition it may be independently detected in three pulmonary compartments: the gas, alveoli-capillary membrane and the blood RBC in the capillary network, where it exhibits distinct resonance frequencies. This was initially shown in animal studies,¹⁰⁵ and later demonstrated in human studies.^{13,97,106} In more recent years, the developments in this technique have been focused on visualizing and quantifying lung airspaces, as well as measuring gas exchange and uptake.^{43,106-108} Dissolved-phase MR images are typically quantified in terms of the normalized ratio of the membrane to gas and RBC to gas signal ratio maps, as shown in Table 1. This provides an opportunity to evaluate pulmonary microvasculature and perfusion beyond the larger vessels.^{43,46}

2.4 Chasms and Limitations

MRI offers several important strengths compared to x-ray and nuclear medicine modalities as it provides high soft tissue contrast and is rapid (8-15 seconds in hyperpolarized gas MRI), radiation-free and well-tolerated in acute and chronic/longitudinal investigations, making it well suited for very compromised and/or pediatric populations. MRI signal intensity is derived from multiple factors including acquisition sequence and time, tissue proton density, system gain, local field inhomogeneity. There is a fundamental limitation of conventional ^1H MRI. This stems from the

limited number of spins per unit volume and the millions of air-tissue boundaries which create local field inhomogeneities contributing to a very short T2* (on the order of 0.5–2.5 ms).^{13,109,110} Therefore, such techniques work best at relatively lower magnetic fields (1.5T) because these inherent air-tissue interfaces can create susceptibility artifacts,¹¹¹ whereas depending on the geographical location, the current drive for clinical imaging is headed towards higher (>3T) magnetic field strengths and thus the optimization of protocols at 3T is the next step.^{112,113} Further factors that contribute to the challenges for clinical translation are the limited availability of MR systems in clinical settings, increased expenses for operation and the necessity of additional trained personnel (such as operating polarizer equipment and required MRI coils).

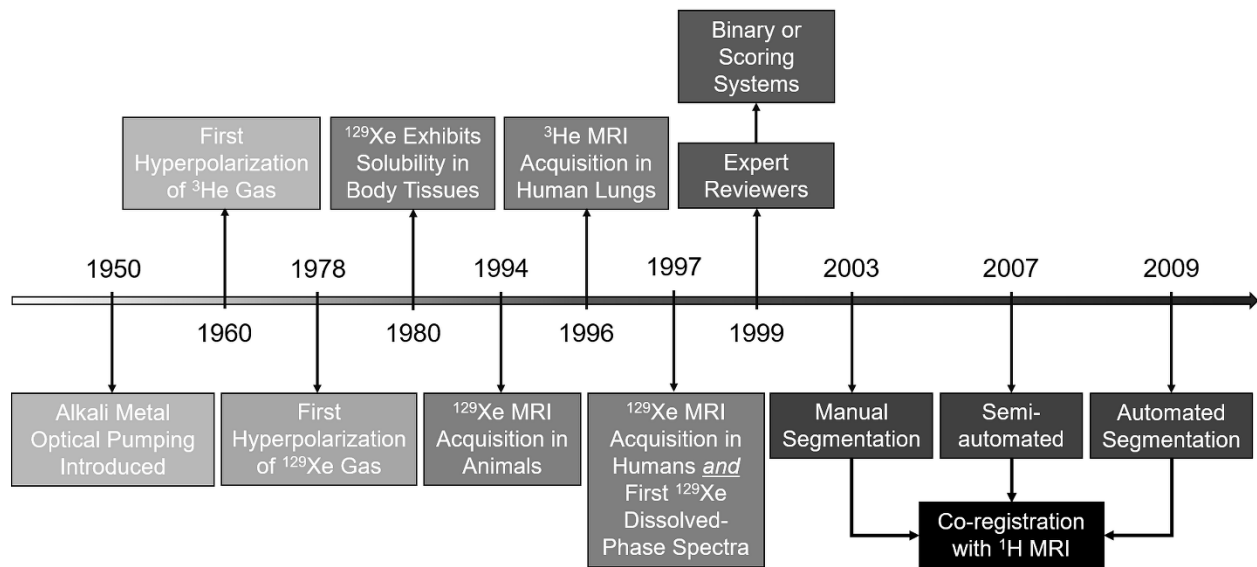


Figure 4. Timeline of key ³He and ¹²⁹Xe MRI developments

A timeline depicting hallmark and key historical developments for quantitative hyperpolarized ¹²⁹Xe/³He MR image evaluation, ranging from the introduction of spin-exchange optical pumping methods for noble gas polarization to the more recent advances in image processing approaches of the ¹²⁹Xe/³He MRI field.

Despite the many applications and benefits of hyperpolarized gas imaging, integration into clinical settings has been limited globally, yet has been performed clinically in United Kingdom.¹¹⁴⁻¹¹⁶ The modality-based extrinsic variation caused due to the diversity of equipment platforms, field

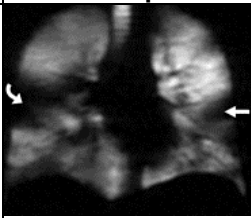
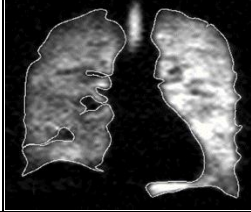
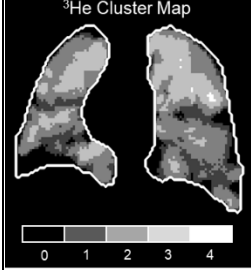
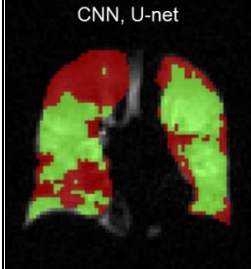
strengths, sequences and protocols represent a major concern in the field. This further exacerbates the diversity of image processing and analysis techniques that are required to process these diverse image acquisitions to quantify biomarkers. ^{129}Xe gas suffers from decreased polarization percentages and yields inferior SNR compared to ^3He gas for imaging.^{87,117} The universal standardization of both the image acquisition, processing methods and regulatory approval for hyperpolarized ^{129}Xe MRI is still pending globally, which constitutes a vital step towards clinical translation since even the level of lung inflation can influence quantitative measurements of lung function.^{118,119} This is especially important as the analysis of hyperpolarized gas images has moved away from initial qualitative visual approaches towards computational, objective and quantitative image processing methods. However, for clinical translation, interpretation of extracted measurements and rigorous mechanistic explanations are of paramount importance for potentially connecting the MRI gas signals and defects to specific structural changes and well-understood, established physiological processes.

III METHODS

3.1 Introduction

The MRI field has been steadily moving away from scoring systems and manual analysis over the past few decades, as depicted in Figure 4, to reliably obtain quantitative measurements. Unlike CT, MRI is attractive for longitudinal studies due to its use of non-ionizing radiation and flexibility for acquiring rapid, dynamic, multidimensional signals in response to changes in lung function by involving complex image processing techniques. Here, we discuss the hallmark approaches used to generate reproducible functional imaging biomarkers, through the lens of the historical timeline of developments in the image processing domain of PfmMRI, as illustrated in Table 2 and Figure 4.

Table 2. Hyperpolarized $^{129}\text{Xe}/^3\text{He}$ MRI segmentation methods

	Example	References	Methods	Strengths	Weaknesses
Reader-based Scoring		Donnelly et al. 1999 - Scoring System ⁶⁸ McMahon et al. 2006 ¹²⁰	Categorical Scoring Systems Expert observers, Radiologists – Defects-based Binary Scoring	-Qualitative assessment of visual ventilation defects -Enables analysis of lung function	-Categorical scores: mild, moderate, severe -Variability and reproducibility of measurements
Manual Segmentation		Woodhouse et al. 2005 ¹²¹	¹ H - Manual segmentation of signal void region ³ He - Mean signal intensity thresholding	-Quantification of ventilation and defect volumes -Continuous variable (%) for assessments	-Reliance on highly trained observers -Relatively long segmentation time
Semi-automated Segmentation		Kirby et al. 2012 ³⁶ Lui et al. 2013 ¹²² Zha et al. 2016 ¹²³ Hughes et al. 2018 ¹²⁴	Hierarchical K-Means Clustering Fuzzy C-Means Adaptive K-Means Spatial Fuzzy C-Means	-High intra- and inter-observer reproducibility -Improvement in segmentation time	-Dependence on expert observers -Intra- and inter-user variability as well as differences in analysis time
Automated Segmentation		Kirby et al. 2010 ⁶⁷ Tustison et al. 2011 ¹²⁵ He et al. 2014 ¹²⁶ Tustison et al. 2019 ¹²⁷	Otsu's Thresholding Multi Atlas-Labeling Histogram Linear-Binning Techniques CNN, U-net architecture	-No reader/user input required for segmentation -Extended the semi-automated method ¹²⁶ -Fully automated and rapid analysis	-Registration step requires a user seed for initiation -Bin thresholds visually estimated -Model complexity and computational power

Manual segmentation figure adapted from Woodhouse et al (2005),¹²¹ Copyright © 2005 John Wiley and Sons Inc. All rights reserved. Automated segmentation figure adapted from Tustison et al (2019),¹²⁷ Copyright © 2019 Elsevier Inc. All rights reserved.

3.2 Qualitative Approaches and Scoring Systems

Today, radiologists use scoring systems to visually score various pulmonary abnormalities (such as emphysema in COPD and Brody score in cystic fibrosis) on CT scans. However, the causes for disagreement between visual scores and quantitative scores remain uncertain.¹²⁸ Visual CT scoring by a radiologist is more indicative of pulmonary function and critical patient outcomes, such as mortality,¹²⁹ compared with quantitative analysis methods, although the superiority of visual scoring over quantitative measurements in predicting mortality has not yet been reported.^{130,131}

Quantitative CT analysis is less time-consuming, more reproducible, correlates with pulmonary function¹³² and is superior to visual scoring for prognosis.¹³³

Reader-based visual scoring was also initially used to quantify the distribution of inhaled hyperpolarized gases. In 1999, researchers developed a scoring system⁶⁸ that was widely adopted for MR images, although other ventilation defect scoring systems were also developed and used.^{134,135} However, the variables reported were categorical (mild, moderate, severe) and were limited to subjective analysis. Intra-/inter-user variability and reproducibility of these measurements remain as significant challenges. Scoring systems also change through time, introducing challenges to retrospective analyses and constraining the future developments to preferentially similar scoring systems with incremental deviations. Deep-learning models may have shed additional light on this problem, since they critically require extremely large datasets with objective, sensitive, accurate and precise labels as ground-truth for algorithm training, but these are not readily available.¹³⁶⁻¹³⁸ The revolutionary merging of structural images for anatomical referencing, such as ¹H MRI or CT, to functional hyperpolarized gas images through co-registration techniques occurred at the start of this century. These in combination with the challenges described above have advanced the development of the field towards rigorous semi- and fully-automated quantification methods.

3.3 MRI and CT Co-Registration

Image registration is primarily used to determine the transform function to map one image onto the domain of the other. Rigid registration methods are limited to rotation, translation, scaling and other linear or affine transformations. These methods are typically used when image acquisition is performed under constant level of lung inflation or breath-hold conditions, such as using a one-liter bag of hyperpolarized gas mixture for functional ventilation or air for ¹H MR acquisition,^{139,140}

simplifying the co-registration. Such intra-modality image registrations are crucial since the co-registered structural image provides the necessary anatomical references and characteristic features to quantify the pulmonary function.

In contrast, elastic or deformable registration with reduced restrictions on the transform function allows local adjustments to register the input images. However, other restrictions in deformable registration tasks may be applied in order to preserve the original structural characteristics and anatomy in the input image. This method deforms acquired images by applying transformations and allows discontinuous sliding window motion, designed to specifically accommodate motion present during respiration.¹⁴¹ These methods are typically used in free-breathing acquisitions or for inter-modality co-registrations, such as between CT and MRI.^{79,142} Several modality-independent methods, where the co-registration is performed by pairing corresponding fiducial points within MR and CT volumes, have been developed.¹⁴³⁻¹⁴⁶ A key feature of elastic registration is the ability to account for differences in local deformations between MRI and CT modalities, which may be caused by one or both modalities, time elapsed between MR and subsequent procedures, as well as warping or scaling changes. Although, it should be noted that some elastic co-registration algorithms may compromise data integrity and change its distribution relative to original image.¹⁴⁷ Nonetheless, the marriage of image registration and segmentation approaches between ¹H and hyperpolarized gas MRI, further discussed in the next section, was pivotal in the development of the field to such extent that these two methods are now considered inseparable for generating reliable and quantifiable measurements in PfmMRI.

The co-registration of a central coronal CT slice with a corresponding static ventilation image can be performed in order to generate a 3D structure-function model automatically, with high-spatial resolution and functional information, as shown in the second-step of Figure 5. This unique method

provides a visual map across the entire lung volume of normally and abnormally functioning areas with either well-ventilated regions or ventilation defects that are localized within the 3D structure of the lung. We note that none of this information can be gleaned using conventional clinical or research methods. A near-automated segmentation and registration technique for inhaled $^3\text{He}/^{129}\text{Xe}$ MRI was developed in 2015¹⁴⁸ by implementing a convex optimization-based co-segmentation approach that exploits image features from both ^1H and $^3\text{He}/^{129}\text{Xe}$ MRI for lung cavity segmentation. This method includes image resampling, $^3\text{He}/^{129}\text{Xe}$ to ^1H rigid registration, user seeding of representative regions to generate the respective probability density functions and max-flow computation with a spatial consistency constraint.¹⁴⁹ This research work was enhanced in 2016 to rapidly segment pulmonary ^1H MRI using a convex optimization-based approach that incorporates the left-to-right lung volume proportion as a constraint for simultaneous left and right lung segmentation.¹⁵⁰ The $^3\text{He}/^{129}\text{Xe}$ and ^1H MRI co-segmentation and the volume-proportion preserved Potts model for left and right lung segmentation approaches were developed based on previous work,¹⁵¹ which provided the theory of max-flow/min-cut algorithms and developed efficient numerical solvers.

The framework, utilized in the third-step of Figure 5, demonstrated strong agreement to expert manual segmentations with clinically acceptable reproducibility, and rapid implementation that aligns with clinical and research requirements.¹⁵⁰ Such automated whole lung, lobar and segmental ventilation quantification methods provide an opportunity to incorporate functional lung biomarkers into clinical research and patient care. The registration of CT and hyperpolarized noble gas MR images has shown great promise by facilitating functionally weighted radiotherapy treatment planning for lung cancer patients¹⁵² while also enabling the differentiation of CT and $^3\text{He}/^{129}\text{Xe}$ MRI measures of ventilation.¹⁵³ This multimodality image registration method can

potentially be deployed in a bronchoscopy suite¹⁵⁴ and provides a unique approach to study and understand the structure-function relationships in obstructive lung diseases. Such methods enable the generation of regional structure-function measurements at lobar and segmental levels, which is not feasible using hyperpolarized gas MR images alone.¹⁴⁷ However, the registration error is a crucial consideration when co-registering MR ventilation images to corresponding anatomic data, which is known to be notoriously difficult to evaluate quantitatively, especially in the presence of significant ventilation defects.¹⁴²

Registration error and its propagation through computational analyses required for generating PfmRI measurements remains a substantial challenge. Most automated image registration algorithms assume that the topology of target and source images is the same, which is frequently not true when considering hyperpolarized gas and ¹H anatomical MR images, especially in patients with severe pulmonary diseases that substantially impact functional lung images. In-terms of manual registration approaches, the inherent spatial co-registration accuracy may be improved by acquiring volume-matched ¹H and hyperpolarized gas MRI in breath-hold conditions,¹⁵⁵ possibly alleviating the need for intricate post-acquisition image registration. Although, studies now suggest that a combination of both neural network-learned descriptors and handcrafted local descriptors and features produce the best registration results;^{138,156} however, machine and deep-learning approaches are infamous for requiring large amounts of carefully sorted training data.

3.4 Segmentation Approaches

Segmentation in essence is pixel-wise annotation of various regions in an input image with categories or labels, and is traditionally performed by experts or radiologists as previously discussed. PfmRI segmentation is an essential step in image analysis to precisely quantify inhaled gas distribution and pulmonary imaging biomarkers. The field used subjective and qualitative

scoring systems^{68,120,121} prior to the development and validation of quantitative MRI biomarkers, whose reproducibility was originally verified.^{123,140,157-159} Most segmentation approaches currently use anatomical data from ¹H MRI to supplement the functional data residing in hyperpolarized gas MRI, which provides an opportunity to quantify inhaled gas ventilation patterns and generate imaging biomarkers, described in Table 1, that are associated with various disease states. As depicted in Figure 4 and Table 2, manual segmentation by expert observers was the successive approach that, for the first time, used ¹H or anatomic MRI in conjunction with hyperpolarized gas MRI by applying various image registration techniques previously discussed. Yet, manual image segmentation still had limitations, such as being labor-intensive, time-consuming, and prone to intra- and inter-observer variability. These limitations restricted PfmRI translation and implementation in large-scale clinical and research studies.³⁶ Moreover, observer expertise and training are always required for manual segmentation, yet segmentations between experts differ.¹⁶⁰

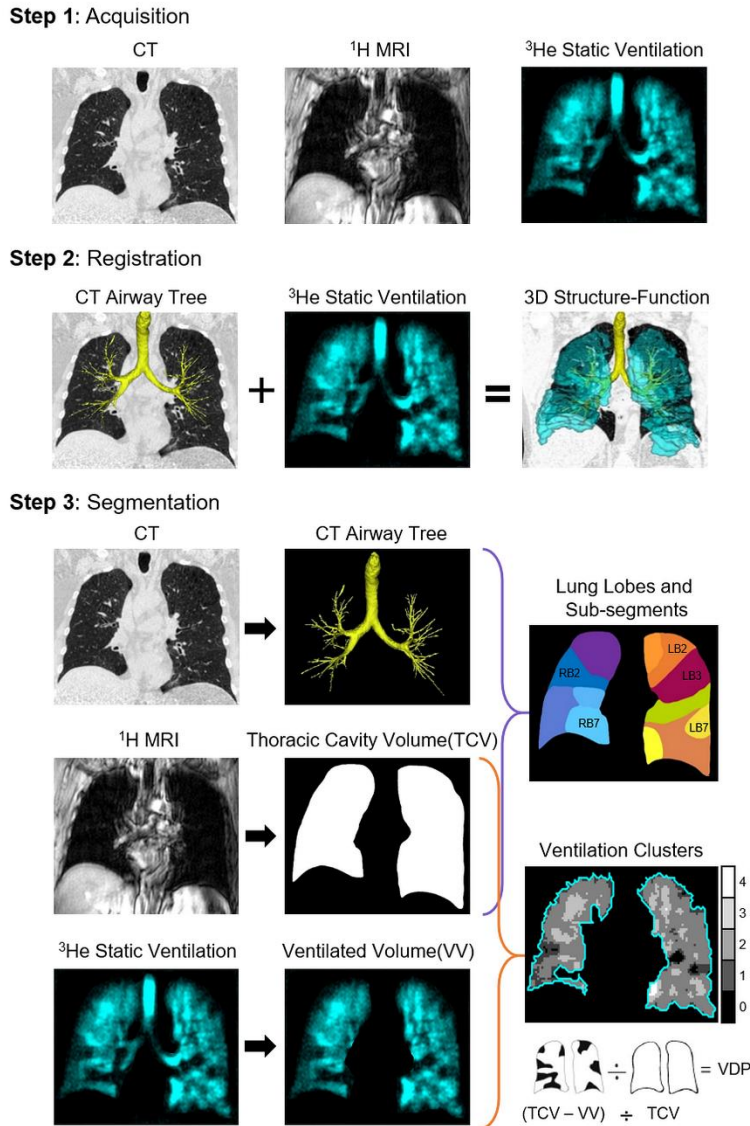


Figure 5. A unified workflow for quantitative PfMRI measurements

Step 1, multi-modality image acquisitions for mapping pulmonary structure-function relationships. Step 2, example of inter-modality registration between CT and pulmonary functional MRI for visualizing structure-function relationships in 3-dimensions (3D).

Step 3, segmenting out the pulmonary function and structural determinants, with structural CT to $^1\text{H MRI}$ inter-modality registration for pulmonary lobar and segmental measurements, and a landmark-based inter-modality registration of ^1H and $^{129}\text{Xe}/^3\text{He}$ MRI for the segmentation of thoracic cavity volume (TCV) and ventilated volume (VV), respectively. This provides a measurement of the ventilation defect percent (VDP) defined as the ratio of ventilation defect volume ($\text{VDV} = \text{TCV} - \text{VV}$) to TCV.

Semi-automated segmentation was the next major development, which has proven to be advantageous over manual methods because of decreased segmentation time and greater intra- and

inter-observer reproducibility of PfMRI biomarker measurements.¹⁵⁷ Briefly described in Table 2, these methods have a greater potential for large-scale multicenter clinical evaluations, where multiple users can generate reliable measurements independent of their experience level. As shown in the schematic diagrams in Figure 5, the quantification and analysis process of acquired multi-modality images involves the essential combined utilization of registration and segmentation techniques, increasingly treated as inseparable for this purpose. Similar to CT airway tree co-registration with PfMRI ventilation images to provide structure–function information by pairing the airways and ventilation abnormalities, ¹H MRI co-registration with hyperpolarized gas MRI is capable of generating lung function biomarkers and regional measures such as ventilated volume (VV),¹⁶¹ and ventilation defect percent (VDP).³⁶

One of the most widely used semi-automated methods was introduced in 2012³⁶ that consists of automatic and semi-automatic segmentations of ¹H and ³He/¹²⁹Xe MR images, with the necessary steps involved depicted in the third-step of Figure 5. Briefly, ¹H MRI anatomical images are segmented using a seeded-region growing algorithm, as the low ¹H density in the lung produces weak MRI signal and thus provides sufficient contrast for the algorithm to automatically segment the thoracic cavity and differentiate ventilation defects from lung edges, although this may be a significant challenge in several disease processes such as fibrosis, mucus, atelectasis, where signal contrast in the lung cavity is not that high.³⁶ ³He/¹²⁹Xe MR images are segmented automatically using a hierarchical K-means clustering algorithm. Expert observers can typically distinguish between four visually apparent classes of ³He/¹²⁹Xe MRI signals, based on the expert chest radiologist’s interpretation of the clinical meaning of the visible signal intensity differences;⁶⁷ this strategy was adopted in a hierarchical K-means clustering method to partition the signal intensities

into four clusters.³⁶ The resulting $^3\text{He}/^{129}\text{Xe}$ clustering and ^1H segmentation maps are registered using a landmark-based affine co-registration approach to quantify MRI ventilation heterogeneity. As indicated in the position paper from the ^{129}Xe MRI Clinical Trials Consortium,⁹⁴ multiple strategies have been employed by researchers to quantify VDP, and one other notable and popular method in the field uses histogram rescaling and binning approach.¹²⁶ Briefly, the binning approach assigns pixels in the ^{129}Xe ventilation scan to specific bins by rescaling the intensity histogram by its top percentile in the range from 0–1. Next, the standard deviation of a healthy reference population distribution¹²⁶ is used to set thresholds for assigning pixels into four clusters referred to as: ventilation defect percentage (VDP), low-, medium, and high- ventilation percentage (LVP, MVP, HVP) respectively.¹⁶² Images are also subjected to two additional corrections: a bias-field correction to account for coil B1 inhomogeneity and an application of a ‘vesselness’ filter to better account for the exclusion of ^{129}Xe signal by the pulmonary vasculature. The bias-correction method assumes a spatially smooth and slowly varying intensity bias across the image, and estimates it using a B-spline approximation, which is iteratively adapted to correct the resulting images. The ‘vesselness’ filter algorithm exploits three properties of the vessel-like structure: intensity difference, tubular shape, and tree-like structure to indicate bifurcation and connectedness. Unlike the previous approach, this vasculature is accounted for when defining the thoracic cavity mask and will not contribute to a false increase in the VDP. However, studies indicate that both methods agree well in quantifying VDP, but there may be variability in LVP and MVP quantification.¹⁶³ Researchers have proposed that an SNR threshold greater than 13.4 may be required for a robust quantification of the ventilated clusters.¹⁶³

These novel methods enable rapid generation of measurements such as $\text{VV}^{121,161}$ and thoracic cavity volume (TCV), which can then be used to determine ventilation defect volume (VDV),¹⁶⁴

from which percentage ventilation volume (PVV)⁶⁸ and VDP^{36,67} can be calculated by normalizing VDV (or VV for calculating PVV) to the TCV obtained from ¹H MRI, as summarized in Figure 5. In particular, the emergent VDP measurement has proven to be a useful imaging biomarker through subsequent studies.^{19,165-167} VDP is highly reproducible across multiple sites^{157,168} and has also shown to detect disease related changes before standardized CT imaging or conventional clinical measures.¹⁶⁹⁻¹⁷¹ However, we must note that segmentation times vary between methods, where manual ³He/¹²⁹Xe segmentation typically requires 60-90 minutes for 8-16 slices with 4-15 mm thicknesses per subject and semi-automated segmentation needs approximately 5-20 minutes of computational time with user input, while automated ¹H as well as ³He/¹²⁹Xe segmentation requires less than 25 seconds for the same task.^{36,120-122,126,127}

Multiple studies have compared the equivalency and repeatability of ³He and ¹²⁹Xe MRI VDP, indicating that both methods show repeatable ventilation defects in asthma,¹⁷² showing repeatability in measures of pre and post-bronchodilator reversibility, and in COPD.^{173,174} However, a bias exists whereby the ¹²⁹Xe MRI VDP in the same individual is greater than the corresponding ³He MRI VDP. This was attributed to the greater density and lower diffusivity of xenon, occluded airspaces, slow filling regions and the snapshot representation of breath-hold imaging.¹⁷⁵ Yet the relationships to lung disease and severity remain equivalent between methods.¹⁷⁴ Therefore, interpretation of VDP is still a debated topic due to the representation of either distinct or a mixture of structural-functional processes.

3.5 Diffusion Weighted Imaging and Alveolar Geometry

Hyperpolarized ³He and ¹²⁹Xe MRI also provides a way to generate alveolar microstructure and diameter measurements through PfmRI methods. In this technique, images are acquired with two different b-values, or with multiple b-values to generate ADC and morphometry measurements.¹⁷⁶

However, due to the breath-hold constraints, compressed sensing acceleration strategies are often deployed.^{177,178} The b-value can be controlled experimentally since it depends on the diffusion gradient strength and the diffusion time. Higher b-values can be obtained by increasing experimental diffusion time or strength of the sensitizing gradient. The terminal airway and alveolar geometry measurements are generated based on the way the random Brownian motion (or diffusion) of noble gas is restricted within the terminal airspaces. The generated MRI apparent diffusion coefficient (ADC)¹⁷⁹ measures the apparent distance of gas molecule diffusion since the free diffusion of the gas is limited by the alveolar walls, resulting in larger diffusion path lengths in enlarged or destroyed terminal acinar units.³⁹

In diffusion weighted imaging, the typically inhaled volume of 0.5 L polarized ³He or ¹²⁹Xe gas is diluted upon inhalation into a ~6 L lung and results in a free diffusivity at atmospheric pressure and temperature of 0.88 cm²/s and 0.14 cm²/s, respectively.¹⁸⁰ It has been shown that the ADC value in healthy subjects increases as they age, which probably reflects the enlargement of the terminal airways and onset of senile emphysema that occurs naturally as we age.¹⁸¹ Additionally, these ADC values can be evaluated across different timescales, where timescales on the order of milliseconds correspond to diffusion within a single alveolus and a timescale on the order of seconds would correspond to diffusion across multiple alveoli. Unfortunately, diffusion weighted imaging method typically requires a longer breath hold or larger voxel sizes than ventilation imaging since multiple b-value images are required to map ADC.

In order to build computational models, various geometric assumptions and simplifications have been developed ranging from simple single branches to full acinar models. The first relationship between ADC values and airway geometry was derived using a simple model where airways were depicted as branches covered with alveoli.¹⁸² Based on previous work,¹⁸³ this method adopted

airway dimensions as the internal airway radius r changing from 250 to 135 μm and the outer radius R (including the sleeve of the alveoli) remaining constant at 350 μm . The authors subsequently simplified this model to a periodic cylinder structure with each alveolus covering a quarter of an annular ring.¹⁸⁴ The modified Weibel geometrical model of lung microstructure at the acinar level was well accepted, while some of the other proposed models developed included the Kitaoka model based on a 3D labyrinth filling a cubic volume,¹⁸⁵ a cylindrical model with semi-spherical alveolar shape and two-dimensional grape-like structures,¹⁸⁶ a porous medium approach,^{187,188} and tree-like branching structures.^{189,190} Despite simple cylindrical models demonstrating ADC values consistent with clinical findings,¹⁸⁴ these are far from accurate models of realistic lung tissue organization as they represent a single airway.

Currently, there are two established models of the whole acinar geometry that have been described for voxel-wise diffusion morphometry analysis. The first method uses a cylindrical model of acinar geometry to estimate alveolar-duct and alveolar dimensions,¹⁹¹ while the other method uses a stretched exponential model to characterize pulmonary morphometry.¹⁹² As a result, parametric maps for airway radii, alveolar depths, and physiologically important parameters such as the alveolar surface area (S_a), lung volume per alveolus (V_a), their ratio (S/V), alveolar number density (N_a) (the number of alveoli per unit lung volume based on geometry) and the mean linear intercept (L_m) can be generated.¹⁹³ Provided that the diffusion time is set to ensure that images are acquired in the proper diffusion regime,¹⁹¹ both models can be used on the same set of diffusion weighted images and have been validated against conventional histology.^{193,194} Unfortunately, the research community has not yet reached an agreement as to which model is preferable, which is a vital aspect for future multi-site studies that involve diffusion morphometry, beyond simple ADC value calculations.

3.6 Machine Learning and Texture Analysis

Here we focus on the clinical research and applications of machine and deep learning in pulmonary functional imaging. For many years the construction of a pattern-recognition or machine-learning systems required considerable knowledge and expertise in the field, and this initially limited the potential of employing conventional machine-learning approaches to process raw data. In addition, heedful engineering of the feature extractor module that would transform the raw pixel data into an appropriate internal representation, such as a feature vector, to be utilized by the pattern recognition and machine-learning systems for subsequent detection or classification of patterns within the input was necessary.¹³⁷ In deep-learning models, a vast number of interconnected simple units or neurons are used to form multiple layers that are capable of extracting abstract features from input images of increasingly sophisticated level of details, auto-generating a representation of the imaging data. Unsupervised machine-learning methods, such as hierarchical k-means clustering already discussed, do not require training on a labeled dataset, while supervised learning methods require large quantities of training data with annotations used as ground-truth.

Currently, one of the most popular architectures is deep convolutional neural networks (CNN) and recurrent neural networks (RNN). These are typically trained end-to-end in a supervised fashion in order to greatly simplify the training process. CNN architectures are most widely used in medical image analysis, although RNN have recently been gaining popularity as well. The recent explosion in popularity of deep-learning approaches may be attributed to the advent of graphics processing units (GPU) for fast computation and the availability of large quantities of data for algorithm training.¹⁹⁵ The tremendous computational power further enabled the development of even more complex and deeper layered networks, ultimately leading to the eruption of state-of-art performance that rivals human expert readers.¹⁹⁶

A novel fully automated functional lung image segmentation method was recently developed,¹²⁷ based on a U-net architecture. This was one of the first efforts of developing deep-learning based methods for functional lung image segmentation, with the proposed image processing pipeline depicted in Figure 6. Briefly, a U-net model architecture is trained on both the ¹H and ventilation images in an offline mode using data augmentation to increase the size of the training data and the robustness of the algorithm. The individual participant image preprocessing modules include MR de-noising and bias correction¹⁹⁷ and merge of ¹H and ventilation images to predict a final ventilation segmentation map.¹²⁷ Due to the sample size requirements of the model, a novel template-based data augmentation approach was also proposed, whereby the imaging data sampled from the population are used to construct a representative template that is optimal in terms of shape and intensity.¹⁹⁸ The template building process also outputs the transformations associated with each individual image, which effectively enables the propagation of an individual training image to every other training image via the template, expanding the size of the training dataset from ‘x’ to ‘x²’. The resulting probability images were compared with other manual and semi-automated methods utilized in the field, with the proposed method outperforming the competition in terms of spatial agreement/overlap and computational time.¹²⁷

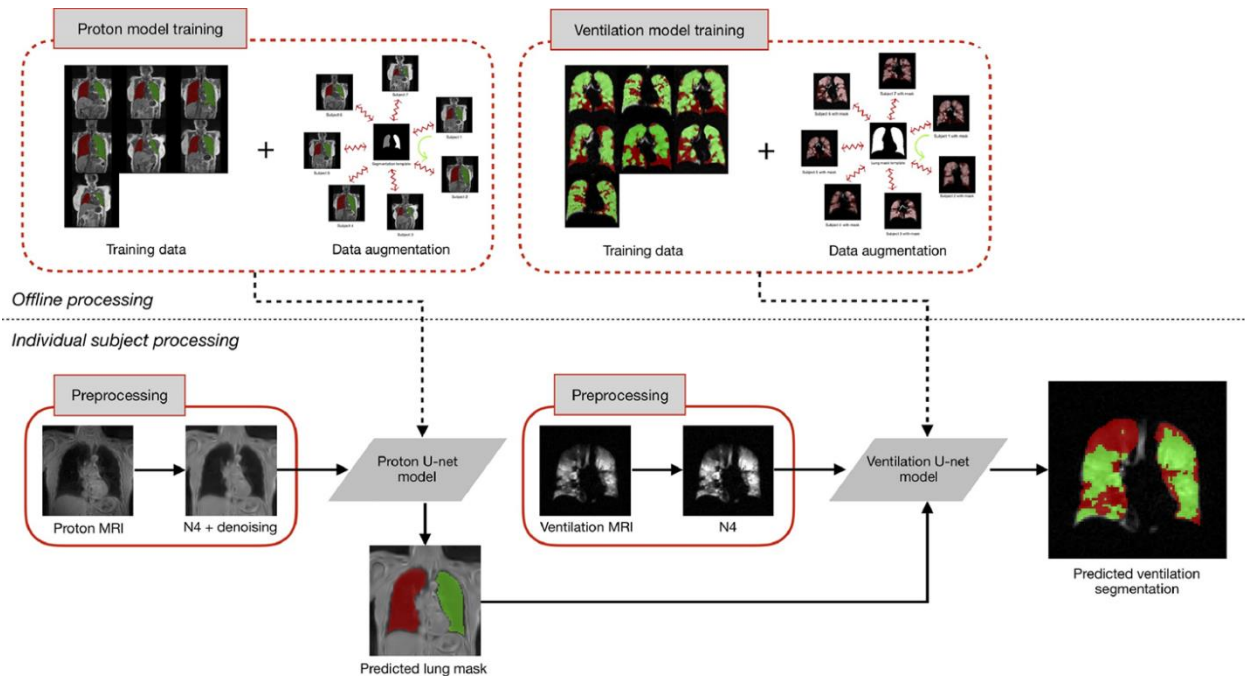


Figure 6. Deep learning driven fully-automated registration-segmentation pipeline

Offline training of U-net models for both ^1H and $^{129}\text{Xe}/^3\text{He}$ MRI was performed using template-based data augmentation and multiple atlas-labelling approach. Individual subject image processing includes MR denoising and N4 bias correction. In ventilation image processing, the ^1H mask is included as a separate channel, merged with the ventilation model to predict the segmented ventilation map. Adapted from Tustison et al (2019),¹²⁷ Copyright © 2019 Elsevier Inc. All rights reserved.

Texture analysis generates quantitative features, which are descriptors extracted from the images by software implementing mathematical algorithms.¹⁹⁹ They exhibit different levels of complexity and express properties firstly of the tissue or region shape and the voxel intensity histogram, secondarily of the spatial arrangement of the intensity values at voxel level (the texture).²⁰⁰ Features can be extracted either directly from the images (such as first-order, shape-based features and second-order features using various gray level matrices) or after applying different filters or transforms (such as Gaussian filters, wavelet transforms, Laplacian transforms, fractal analysis, etc.).^{200,201} Many of the extracted features would typically be redundant. Therefore, initial efforts should focus on identifying appropriate endpoints with a potential clinical application, to select information useful for a specific task via feature selection and dimensionality reduction

methods.^{136,137,202} The applications of such techniques in hyperpolarized gas MRI have been scarce. In 2012, texture analysis was shown to quantify changes in hyperpolarized ³He MRI ventilation after therapeutic intervention in rat asthma-model²⁰³ and this has more recently been implemented in humans.²⁰⁴⁻²⁰⁶ Due to advancements in computational hardware, it is now possible to combine texture analysis and machine-learning classifiers in order to generate predictive models.

Texture analysis of CT images has established that gray level run length matrix-based texture features^{200,207} extracted from CT volumes of interest are able to predict regional ventilation, and the predicted VDP strongly correlates with ground-truth ³He MRI VDP.²⁰⁶ A more recent method²⁰⁸ using a U-net architecture was developed to estimate hyperpolarized ³He MRI ventilation maps from free-breathing ¹H MRI after respiratory phase sorting and interpolation, discussed previously.⁷⁹ Predicted ventilation maps of participants with diverse pulmonary pathologic findings used in this study showed strong correlations with ³He MRI and pulmonary function measurements, with a strong spatial agreement of ventilation defects.²⁰⁸ Other deep learning approaches also demonstrated this promising potential to offer patient-specific information from structural modalities on pulmonary functional impairments.²⁰⁹⁻²¹³ These hallmark developments and increasing automation seen in segmentation and quantification methods hold key strengths while at the same time address some of the weaknesses of the predecessor methods, although limitations still remain.

In texture analysis, different measuring techniques produce different patterns in texture and these may vary across various centers and manufacturers, implying that texture features can be reliably used at one center with a specific imaging protocol but the same analysis methodology may not be directly applied to images acquired at different centers with different protocols.²¹⁴ Several attempts

by international research groups are underway to harmonize and standardize the texture feature extraction and analysis process.²¹⁵⁻²¹⁷ The most common challenges for machine and deep-learning applications include the high computational cost, the lack of model interpretability (the black-box problem), and the lack of standardized data and accompanying labels. Although these are very important challenges, here we focus on more specific challenges in the context of pulmonary MR images as the intrinsic patient variability (such as patient position, lung sizes and heterogeneity) and the diversity of equipment and protocols indicate a major concern in the field. There is a large diversity in targeted ventilation and defect shapes for segmentation due to their heterogeneous appearances on MRI as well as different patient positions. The global and local context is typically needed to perform accurate segmentation and multi-stream algorithms with randomly sampled patches or different scales are used. In order to leverage both the global and local context in tissue segmentation, applications of U-net and similar architectures have been successfully deployed.

An additional challenge for functional lung MRI segmentation is the class imbalance, as most voxels/pixels in an image are from the non-diseased class (ventilation) and the ventilation class is usually composed of multiple clusters ranging from hypo-ventilation to hyper-ventilation.⁶⁷ This can be combatted with modifications to the loss function with a greater weight for the specificity to make it less sensitive to the data imbalance, or alternatively, using data augmentation with the imbalanced class (non-ventilated versus ventilated regions) of the data. Another aspect to be discussed is model hyper-parameter optimization (for example, learning rate, dropout rate, etc.), which can help squeeze out extra performance from a given network. Unfortunately, no clear recipe can be given to obtain the best set of hyper-parameters as it is a highly empirical exercise. Random search based on intuition works quite well and is perhaps the most common approach, where researchers¹³⁷ have identified and provided several suggestions for successful

implementation. Detailed reviews of the deep-learning research related to the lung image analysis applications, such as reconstruction, segmentation, registration and image synthesis have been recently published.^{138,218-220} Nonetheless, the major challenge is the development of models that can leverage the full imaging data available in 3D, with further validation studies in different populations, and global standardization of the image processing methods without significantly increasing the computational complexity in order to facilitate successful clinical translation.

3.7 Spectroscopic Quantification

As the field rapidly transitions back toward ^{129}Xe MRI due to the scarcity and costs associated with ^3He research, the use of ^{129}Xe presents a great opportunity to quantify alveolar tissue density and xenon dissolved in blood due to the modest Ostwald solubility of xenon gas.¹⁰² Xenon can bind to the hemoglobin in red blood cells in a manner similar to oxygen, and when dissolved, it exhibits distinctly different resonance frequency shifts for the xenon gas in the ventilated airspaces, xenon dissolved in the lung tissues and xenon dissolved in the RBC.⁴³ Most of the inhaled ^{129}Xe remains in the lung airspaces, while about 1-2% of the noble gas diffuses into the membrane and the RBC, dubbed dissolved-phase xenon.²²¹ The gas phase peak of ^{129}Xe spectrum is set at 0 ppm and is commonly used as the reference frequency; the smaller spectral peaks are at approximately 198 ppm for xenon dissolved in the lung tissue and 218 ppm for the xenon dissolved in the RBC.⁴³ Therefore, the dissolved-phase signal and gas-phase signal can be differentiated using interleaved excitations, and analysis techniques may also be used to separate the dissolved-phase signals at their distinct frequency peaks and generate maps of alveolar tissue density and RBC distribution. Currently, there is a discrepancy in spectroscopic quantification that is performed differently by various research sites in the field. The choice of reference frequency is still up for debate, although the 0 ppm for the gas peak may become a convention and used as a reference frequency for other

phases of interest.²²² Furthermore, even the number of pulmonary dissolved peaks is currently a debatable topic.²²³ There are also differences in the selection of curve fitting techniques, either in the time or the frequency domain. When curve fitting performed in the time domain, no line-broadening or zero-padding is needed.²²² Decomposition of a free induction decay (FID) into a series of additive Lorentzian components yields parameters such as amplitude, starting phase, resonant frequency and linewidth. These parameters are typically fitted to minimize the least squares error of the complex data using a trust-region-reflective algorithm.²²⁴ Additional components can be included until the residual error between measured and fitted data is unrelated. Alternative methods to fitting the data in time domain using a Lorentzian function have been developed, for instance a Voigt function for the various peak shapes may be used in order to determine spectroscopic gaseous contamination parameters.²²⁵

Tissue damage detected using hyperpolarized ^{129}Xe MRI has also been validated histologically.^{226,227} Dissolved-phase images have been interpreted as representing combined gas uptake and transport since there is a continual exchange of atoms between the airspaces and dissolved compartments, which also results in diffusion-limited localization where the ^{129}Xe signal is restricted to the gas exchange units in the lung and the capillary beds. There is a small frequency gap between the two smaller peaks (20 ppm) and it is challenging to separate them. In ^1H MRI, a similar problem exists for separating the adjacent water and fat peaks which was resolved via precise timing using the Dixon method.²²⁸ FID-based chemical shift imaging with Cartesian phase encoding enables spatially-resolved spectra acquisitions, but the speed and spatial resolution remained a limitation. The Dixon technique was successfully implemented to separate the two ^{129}Xe dissolved-phase resonances from each another using RF pulses designed to maximize the signal from phase. Dixon methods require calibration of the scan on a per-patient basis to ensure

that maximum signal is acquired and the sequence is properly timed (TE) to acquire data when tissue membrane and RBC signals are 90° out of phase.⁴³ However, the 1-point Dixon method of imaging gas exchange provides only a single static “snapshot” of the gas uptake process, which is inherently dynamic.

An alternative approach was developed based on iterative decomposition of water and fat with echo asymmetry and least-squared estimation (IDEAL).^{107,229-232} This technique does not require the assumption that tissue membrane and RBC signals are 90° out of phase but may sacrifice the comparatively high spatial resolution provided by 1-point Dixon imaging. Multi-echo techniques are more robust and achieve temporal sampling of gas exchange while maintaining sufficient spatial resolution. This is required to fully quantify the complex dynamics of the gas exchange process. Recent efforts have been focused on characterization of dissolved-phase resonance lineshapes,²³³ chemical shift reference,²²² and novel techniques for imaging of the cardiogenic oscillations of the ¹²⁹Xe RBC resonance.^{223,234} However, there are substantial limitations of the technique that need to be addressed. These include the high degree of undersampling, excitation pulse design, disregard of local phase variations, and chemical-shift-induced phase evolution during the radial read-out.^{94,235}

Images are typically quantified in terms of the normalized ratio of the alveolar-capillary membrane to gas and RBC to gas signal ratio maps on a voxel-by-voxel basis, and frequency distribution histograms analyses. Thus, a greater signal in the ventilation histograms would indicate a better ventilation, and a greater signal in the RBC histograms would indicate a better gas exchange into the RBC. In the alveolar-capillary membrane, a lower signal would suggest the presence of emphysema whereas a higher signal would indicate fibrotic thickening of the capillary bed.⁴⁷ The ratio of ¹²⁹Xe MRI signal intensity in the alveolar-capillary tissue to the signal intensity in the RBC

has been postulated to reflect pulmonary gas transfer efficiency, and such novel emergent hyperpolarized noble gas MRI measurements provide a unique opportunity for the evaluation of pulmonary microvasculature beyond only the larger vessels.

IV PHYSIOLOGIC RELEVANCE AND FUTURE DIRECTIONS

4.1 Inhaled gas Distribution and Ventilation

Numerous pivotal studies have identified the hallmark finding of regional ventilation defects or ventilation heterogeneity in patients with asthma and chronic obstructive pulmonary disease (COPD), even in participants who report normal or nearly normal clinical measurements including CT and spirometry.^{135,171,236,237} This PfmRI finding is important because it showed, for the first time, the impact of highly sensitive regional functional measurements that enhanced our understanding of pulmonary diseases and the contribution of the small airways, which cannot be directly measured using CT or spirometry. In particular, ventilation defects and heterogeneity have shown to be robust and reproducible measures¹⁵⁷ that are correlated with a multitude of clinically meaningful measurements.

In COPD patients, hyperpolarized ^3He and ^{129}Xe MRI VDP reflects airway abnormalities such as narrowing and remodeling,^{19,165} and is associated with disease exacerbations,^{166,167} symptoms and severity,^{135,238,239} CT-derived emphysema measurements,¹⁷⁵ and strongly correlates with lung clearance index,²⁴⁰ which is thought to be reflective of ventilation heterogeneity caused by small airway abnormalities, even in those with normal spirometry.^{40,241} In asthma, studies have identified a multitude of defect shapes using hyperpolarized gas MRI but in particular, the wedge- and pyramidal-shaped ventilation defects resulting from abnormalities in the bronchopulmonary segments shown in Figure 2, are correlated with asthma symptoms and severity.^{134,135,161,242} Importantly, in patients with asthma, ventilation is characteristically heterogeneous compared with

healthy volunteers.^{38,135,243} Larger and more numerous ventilation defects are present in older asthma patients, with worse airway remodeling,²⁴⁴ and these defects correlated with asthma control and quality-of-life.²⁴⁰ Ventilation defects are also sensitive to bronchodilation for both asthma and COPD patients,²⁴⁵ and to bronchoconstriction in asthma patients.^{246,247} The minimal-clinically-important-difference (MCID) in VDP has been established on the basis of ACQ score as an anchor and using the standard error of measurement (SEM) to estimate the distribution-based MCID for VDV. In contrast with gold-standard forced-expiratory volume in one second (FEV₁), which is dominated by the large airways, MRI is sensitive to all airways. The MCID was found to be 2-4% for VDP (anchor-based) and 110-200 mL for VDV (distribution-based),²⁴⁸ which is similar to FEV₁ MCID in asthma at 110–200 mL.²⁴⁹ All of these findings suggest that PfmRI may be used to evaluate the consequences of structural abnormalities and reveal the underlying pathophysiological causes of lung diseases.

The image processing framework, described in Figure 5, provides a unique opportunity to not only improve our understanding of disease pathogenesis by potentially incorporating lung functional biomarkers into clinical research and patient care, but also develop optimal localized therapy options for patients with respiratory diseases. For instance, airway bronchial thermoplasty, although invasive, may be considered for asthma patients in whom therapy approaches have not resulted in improved disease control.²⁵⁰ In COPD, surgical intervention may be performed to remove diseased tissue in order to maximize the efficiency of the lung because hyper-inflated tissue and bullae compress surrounding healthy tissue, which reduces lung function.²⁵¹ Hence, functional-avoidance in management and treatment planning for such patients is an important avenue that can be strengthened using PfmRI measurements. Hyperpolarized gas MRI is beautifully positioned to identify low-functioning regions, and clinical trials are currently

underway to evaluate the ^{129}Xe MRI measurements of lung function (taken together with perfusion, alveolar microstructure and collateral ventilation) in advance of resection, bronchial thermoplasty and lung transplantation in cancer.²⁵²⁻²⁵⁵

The results of several ventilation studies have clearly demonstrated the advantages and clinical applications of this technology, showing significant correlations between ventilation biomarkers and conventionally measured pulmonary function in patients with COPD,²⁴⁵ asthma,²⁵⁶ and cystic fibrosis (CF).⁶ CF was initially evaluated using ^3He MRI⁶⁸ and more recently, ^{129}Xe MRI in mild CF patients revealed ventilation defects, even in those with normal spirometry.²⁵⁷ Both ^{129}Xe and ^3He MRI methods showed early detection of CF, prior to abnormalities in CT and LCI,^{258,259} and were sensitive to disease progression.^{257,260} The feasibility of ^{129}Xe MRI was also demonstrated as an endpoint when standard clinical measurements do not detect disease. Since nearly all pulmonary disorders are heterogeneously distributed in the lung, the ability of pulmonary functional imaging tools to spatially map and quantify the regional distribution of pulmonary ventilation (and probe functional processes even at the level of alveolar-capillary units) provides clinically applicable information not available through conventional pulmonary function tests, which provide only global measurements. Future implementation of these image processing tools to obtain on-demand quantifiable functional measurements are likely to substantially benefit the field, and efforts for clinical integration of these tools have already begun.^{261,262}

4.2 Alveolar-Capillary Interface

PfMRI provides a way to generate volume-averaged measurements that stem from sub-voxel compartments including the alveolar space,^{47,263} the alveolar-capillary boundary^{45,105,264} and ^{129}Xe bound to hemoglobin in the RBC.^{43,107,265} Pathological findings from histological analyses have shown that COPD stage progression is strongly associated with thickening of the airway wall and

its compartments by remodeling or repair process,²⁶⁶ including emphysematous changes,²⁶⁷⁻²⁷⁰ and that small airways become occluded by inflammatory exudates resulting in mucus plugs as COPD progresses.²⁷¹ Histology analysis additionally suggest that airway inflammation and remodeling in asthma may cause airway wall thickening and induces increased airway smooth muscle mass that may generate asthma symptoms.²⁷² Diffusion weighted imaging during breath-hold enables measurements of ADC,¹⁹³ a sensitive marker of alveolar enlargement, which is significantly increased in subjects with emphysema,^{169,273,274} idiopathic pulmonary fibrosis,²⁷⁵ lymphangiomyomatosis,²⁷⁶ congenital diaphragmatic hernia,²⁷⁷ and bronchopulmonary dysplasia.²⁷⁸ PfmRI ADC measures the apparent diffusion distance of the noble gases, whose inherent diffusion or Brownian motion is restricted by the alveolar wall and the terminal airspaces.¹⁹³ ³He MRI ADC in the lungs was shown to be related with the surface area to lung volume ratio (S/V) and L_m measurements, validated using histology.²²⁷ This technique has demonstrated high reproducibility,^{139,279} and was also used to validate ¹²⁹Xe ADC measurements.¹⁶⁸

While both noble gases provide MRI ADC biomarker related to emphysema, the ¹²⁹Xe acquisition uniquely provides measurements of alveolar-capillary membrane thickness^{45,105} due to its modest Ostwald solubility as previously discussed.^{103,104} Recent studies have now suggested that a decreased ratio of the ¹²⁹Xe MRI signal intensity in the alveolar-capillary interface to the signal intensity in the RBC may reflect diminished pulmonary gas transfer efficiency.^{43,221,264} Furthermore, alveolar thickness can be quantified by fitting the signals acquired over time to mathematical models of alveolar geometry to obtain alveolar thickness based on diffusion properties of the tissue.²⁸⁰⁻²⁸² This emergent technique of ¹²⁹Xe MRI provides a unique opportunity

to non-invasively estimate the alveolar thickness, which previously could only be measured using histologic analyses and invasive biopsy methods.²⁸⁰⁻²⁸²

In pulmonary fibrosis patients, dissolved-phase ^{129}Xe MRI revealed that the RBC to membrane ratio was much lower than in healthy controls. This suggests either a reduced RBC signal and/or that the ^{129}Xe signal was enhanced in the alveolar tissue membrane^{221,280} which is normally thickened in patients with fibrosis. Quantification of the differences in ^{129}Xe signal in RBC and membrane is performed by generating ratio maps, which showed that a combination of normal ventilation and high membrane signal was common in pulmonary fibrosis patients.⁴⁶ The regions with decreased RBC-to-membrane signal correspond to greater CT density, suggesting the presence of fibrotic tissue that supports the notion that there is a relationship between the presence of fibrosis and a low RBC-to-membrane ratio.⁴³ Furthermore, ^{129}Xe RBC to membrane ratio has also shown to be sensitive to short-term disease progression in idiopathic pulmonary fibrosis.²⁸³ ^{129}Xe MRI also revealed abnormal regions not observed using standard CT⁴³ which suggests that ^{129}Xe MRI is sensitive to early-stage and subclinical alveolar thickening that is not revealed by CT.

A lower signal intensity in the ratio of membrane and RBC distributions relative to the gas was observed in COPD patients with multiple characteristic ventilation defects.⁴⁶ Emphysema in such patients typically causes parenchymal destruction that may explain the observed lower dissolved-phase signal intensity relative to the gas signal. This is further supported by preliminary studies that reported decreased RBC-to-gas ratios and abnormal mean MRI-ADC in severe COPD patients.^{45,107} Due to the radiation-free nature of this method, there is a great opportunity for its implementation in larger-scale clinical studies of ^{129}Xe gas-exchange MRI in obstructive and interstitial lung diseases. Unlike phase-resolved and Fourier-decomposition based ^1H MRI

methods that measure signal changes at the cardiac frequency, dissolved-phase ^{129}Xe MRI is capable of capturing microvasculature changes at the capillary level (without requiring contrast injection like in DCE-MRI) and consequently measures a different part of the vascular process. Therefore, this relatively recent method holds a unique and unexplored value for the field, and also provides an exciting opportunity for visualizing the entire gas exchange process in the lung.

4.3 Future Clinical Translation

Image processing applications have substantially enhanced our understanding of lung disease. MRI-derived biomarkers correlate well with clinical measures of lung disease pathology, which in some cases correspond to disease state and progression better than well-established clinical measures. Despite this, clinical translation has been minimal and to date has occurred only in the United Kingdom.¹¹⁴⁻¹¹⁶ Several technical limitations and major challenges remain to be addressed for universal, widespread clinical translation.

First, the image acquisition and analysis must be standardized, which has been recently initiated.⁹⁴ The parameters for image acquisition such as the level of lung inflation can influence quantitative measurements of lung function.¹¹⁸ Moreover, the research conducted and methods of analysis used are typically developed in-house using varied MRI software and hardware, which leads to non-standardized measurements in the field.²⁸⁴ Stemming from this is the need for validation of such MRI-derived measurements, as well as the subsequent establishment of ranges of normal values, which is currently lacking and needs to be further investigated.¹¹⁸ Interpretation of extracted measurements and rigorous mechanistic explanations are still needed to connect MRI gas signals and defects to specific structural changes and well-understood, established physiologic processes. There is a prevalence of unfamiliarity among clinicians with hyperpolarized noble gas MRI measurements and a comprehensive, interdisciplinary approach connecting the physicists,

physiologists, and clinicians will be essential for clinical translation. The efficient integration into routine clinical workflow would also require specialized polarization equipment, as well as the training and knowledge of image analysis software for automated or manual quantification and interpretation.

In Figure 7, we highlight a pipeline and propose several approaches for potential integration of these complex image processing methods discussed thus far into the clinical workflow. The first module deals with the input of the imaging data, which can consist of a ^1H scan, a calibration scan for dissolved phase imaging, and all hyperpolarized ^{129}Xe MRI acquisitions. There is also an option for including imaging using other modalities, which can be co-registered with functional MR images for a detailed interpretation of the structure-function relationships. This step would require MR trained personnel for acquisition and transfer of data. The next module operates using the information from the previous module and completes most of the image processing in an automated manner. The images are then used for registration, total lung volume segmentation and quantification of the gas distribution. This can be done: A) on a virtual server or a cloud-based system for offline image processing, which benefits from substantial computational power for very rapid analysis, or B) on a tablet or laptop for real-time analysis and bed-side visualization of results using an embedded graphical user interface. When using a cloud-based server, the final module documents and stores the reports for physician interpretation of results. On the other hand, the tablet-based approach allows for real-time interpretation of results, where the main function of the final module is report generation for continuing care. Centralized implementation of this pipeline and its rapid and automated outputs can be leveraged for secure generation of patient reports online or offline without the need for human intervention. Similar software platforms and environments

should be further investigated and developed to integrate various automated image processing pipelines for routine clinical use.

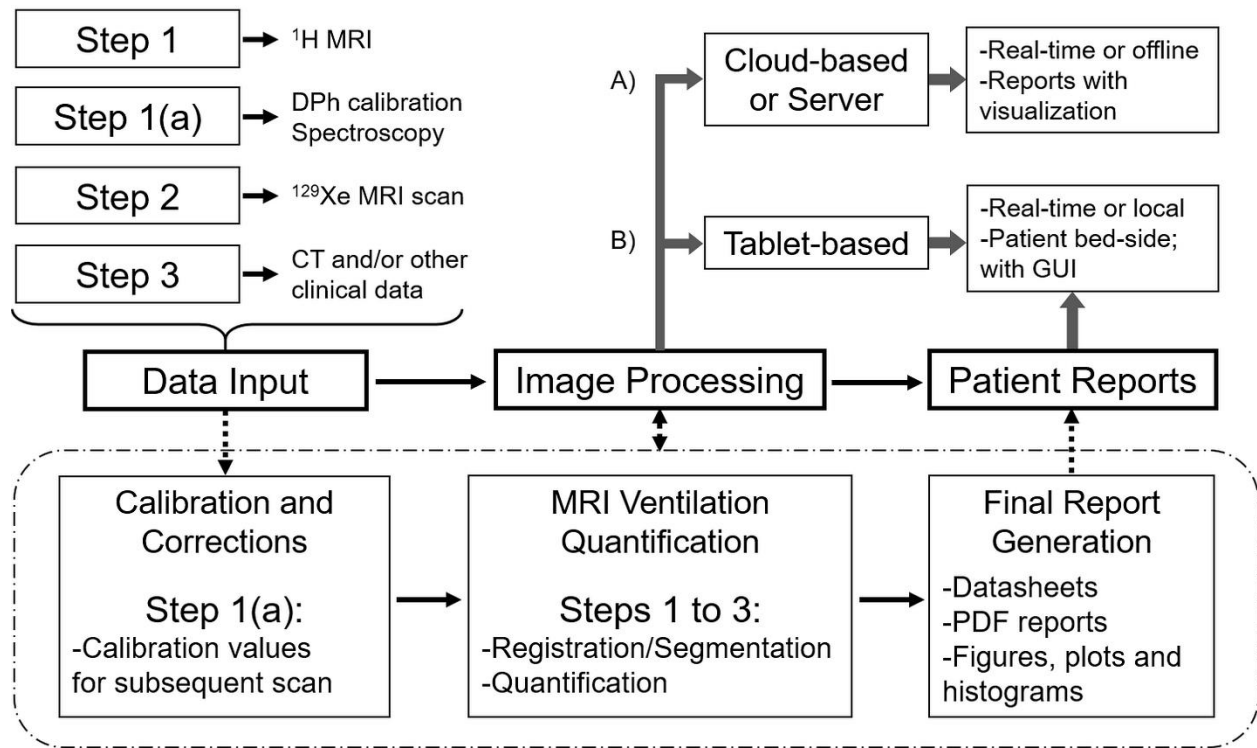


Figure 7: Schematic diagram of a pipeline for real-time image processing and quantitative reporting of ^{129}Xe MRI ventilation, ^{129}Xe MRI gas exchange and CT- $^{129}\text{Xe}/^3\text{He}$ structure-function relationships

Proposed pipeline consists of three modules: 1) Data input module for calibration of ^{129}Xe dissolved phase spectroscopy. 2) Image processing module for registration, segmentation and ventilation quantification from ^1H - ^{129}Xe MRI. 3) Patient report generation module for physician interpretation and continuing care.

Despite these challenges, there is now a surmounting evidence about the various advantages and utility of imaging biomarkers in observational and interventional studies that is enabled through PfMRI. There still exists a great opportunity for collaboration and standardization between the pulmonary and other research sites, vendors and clinical trial sponsors to address the current limitations and move past them into a brighter future. In general, the field currently lacks large scale multi-center repeatability studies and this should likely be the main focus of future research conducted in the field, given the substantial benefits of PfMRI methods. Currently, it is very likely

that in the near future different techniques will have different applications that would depend on the availability of required hardware equipment and MR system model and type since access to advanced MR technologies is not necessarily consistent within the disease populations. Alternatively, the long term future seems to be headed towards an establishment of a single method for quantifying various pulmonary functional measurements using MRI, such as ventilation, perfusion, etc. Although this may require a strong clinical motivation for such measurements that would likely come from applications in pediatric populations. The ongoing dissemination of PfMRI methods beyond the specialized centers where they were developed would enable a better characterization of the strengths and weaknesses of methods that have been discussed throughout the review.

In recent years, the advent of improved polarizer technology for ^{129}Xe gas^{93,285} had accelerated the research in the field and enabled an even greater diversity of applications of hyperpolarized gas MRI.^{4,87} Current improvements in commercial availability of noble gas hyperpolarization methods and greater polarization levels with reduced gas doses and isotopic ratio, make the translation of ^{129}Xe ventilation imaging to the clinic economically feasible. Furthermore, the lung is known to be over-engineered to perform daily tasks, which results in patients often not experiencing symptoms until the disease is in later and more severe stages. This provides a unique venue for PfMRI to step-in with its great advantage in early detection, monitoring and also in enhanced phenotyping of patients once they are diagnosed.

Currently, the gap between research workbench and clinical workflow translation of MRI methods is still significant, primarily due to the small-scale collaborations typically found in most clinics and academic centers. Thus, multicenter large-scale clinical trials and collaborations are required to bridge this gap by providing large amounts of data required to fully understand and validate

PfMRI biomarkers. As the coronavirus disease 2019 (COVID-19) pandemic is currently unfolding, there is a great opportunity to unite the lung imaging community through global collaborations and highlight the role of functional imaging by integrating and applying novel PfMRI biomarkers to enhance our understanding of this disease.²⁸⁶⁻²⁸⁸ We are approaching the threshold for widespread implementation of the necessary steps towards the validation and translation of clinically meaningful PfMRI biomarkers into clinical settings globally, with an ultimate objective to improve patient outcomes. With the ongoing attempts for regulatory approval of ¹²⁹Xe and the required polarization equipment, currently under FDA review, this should be possible in North America within the next 2-3 years.

V CONCLUSIONS

For at least 30 years, chest CT imaging has been the clinical imaging mainstay for pulmonary disease diagnosis and monitoring. In the past decade or so, PfMRI methods have been developed that provide a way to visualize and quantify MR-visible inhaled gas as it flows and then diffuses to the terminal airways and alveoli, across the alveolar tissue to the capillaries and into red blood cells. While much of the focus has been on image acquisition and polarization improvements, PfMRI image processing methods have also been developed for the regional quantification of pulmonary ventilation, gas-exchange and perfusion.

The results of such image processing developments have generated novel pulmonary biomarkers, some of which are now regarded as hallmark features of obstructive lung disease.^{157-159,245} Now, research must focus on how this new information about mechanisms and physiology can be used in clinical workflows towards improving patient outcomes^{8,16,166,169} including those potential approaches^{261,262} summarized here. The development and validation of rapid, reproducible, point-of-care quantitative methods embedded within clinical workflows is aimed at leading to new

treatments, and to improved outcomes including quality-of-life in patients with various pulmonary diseases.

REFERENCES

- 1 American-Lung-Association. *About the American Lung Association*, <<https://web.archive.org/web/20130629130704/http://www.lung.org/about-us/>> (2001).
- 2 D’Agnillo, F., Zhang, X. & Williams, M. C. Structural Integrity of the Alveolar–Capillary Barrier in Cynomolgus Monkeys Challenged with Fully Virulent and Toxin-Deficient Strains of *Bacillus anthracis*. *The American Journal of Pathology* **190**, 2095-2110, doi:<https://doi.org/10.1016/j.ajpath.2020.06.007> (2020).
- 3 Willführ, A. *et al.* Estimation of the number of alveolar capillaries by the Euler number (Euler-Poincaré characteristic). *Am J Physiol Lung Cell Mol Physiol* **309**, L1286-1293, doi:[10.1152/ajplung.00410.2014](https://doi.org/10.1152/ajplung.00410.2014) (2015).
- 4 Adamson, E. B., Ludwig, K. D., Mummy, D. G. & Fain, S. B. Magnetic resonance imaging with hyperpolarized agents: methods and applications. *Phys Med Biol* **62**, R81-R123, doi:[10.1088/1361-6560/aa6be8](https://doi.org/10.1088/1361-6560/aa6be8) (2017).
- 5 Bruegel, M. *et al.* MRI of the lung: value of different turbo spin-echo, single-shot turbo spin-echo, and 3D gradient-echo pulse sequences for the detection of pulmonary metastases. *J Magn Reson Imaging* **25**, 73-81, doi:[10.1002/jmri.20824](https://doi.org/10.1002/jmri.20824) (2007).
- 6 Fain, S., Schiebler, M. L., McCormack, D. G. & Parraga, G. Imaging of lung function using hyperpolarized helium-3 magnetic resonance imaging: Review of current and emerging translational methods and applications. *J Magn Reson Imaging* **32**, 1398-1408, doi:[10.1002/jmri.22375](https://doi.org/10.1002/jmri.22375) (2010).
- 7 Kauczor, H. U., Chen, X. J., van Beek, E. J. & Schreiber, W. G. Pulmonary ventilation imaged by magnetic resonance: at the doorstep of clinical application. *Eur Respir J* **17**, 1008-1023, doi:[10.1183/09031936.01.17510080](https://doi.org/10.1183/09031936.01.17510080) (2001).
- 8 Kirby, M. *et al.* Management of COPD: Is there a role for quantitative imaging? *Eur J Radiol* **86**, 335-342, doi:[10.1016/j.ejrad.2016.08.022](https://doi.org/10.1016/j.ejrad.2016.08.022) (2017).
- 9 Liu, Z., Araki, T., Okajima, Y., Albert, M. & Hatabu, H. Pulmonary hyperpolarized noble gas MRI: Recent advances and perspectives in clinical application. *Eur J Radiol* **83**, 1282-1291, doi:<https://doi.org/10.1016/j.ejrad.2014.04.014> (2014).
- 10 Möller, H. E. *et al.* MRI of the lungs using hyperpolarized noble gases. *Magn Reson Med* **47**, 1029-1051, doi:[10.1002/mrm.10173](https://doi.org/10.1002/mrm.10173) (2002).
- 11 Ohno, Y. *et al.* Pulmonary Functional Imaging: Part 1—State-of-the-Art Technical and Physiologic Underpinnings. *Radiology* **299**, 508-523, doi:[10.1148/radiol.2021203711](https://doi.org/10.1148/radiol.2021203711) (2021).
- 12 Salerno, M. *et al.* Hyperpolarized noble gas MR imaging of the lung: Potential clinical applications. *Eur J Radiol* **40**, 33-44, doi:[https://doi.org/10.1016/S0720-048X\(01\)00347-3](https://doi.org/10.1016/S0720-048X(01)00347-3) (2001).
- 13 Patz, S. *et al.* Hyperpolarized ¹²⁹Xe MRI: A viable functional lung imaging modality? *Eur J Radiol* **64**, 335-344, doi:<https://doi.org/10.1016/j.ejrad.2007.08.008> (2007).
- 14 Wald, L. L. Ultimate MRI. *J Magn Reson* **306**, 139-144, doi:[10.1016/j.jmr.2019.07.016](https://doi.org/10.1016/j.jmr.2019.07.016) (2019).
- 15 Hatabu, H. *et al.* Expanding Applications of Pulmonary MRI in the Clinical Evaluation of Lung Disorders: Fleischner Society Position Paper. *Radiology* **297**, 286-301, doi:[10.1148/radiol.2020201138](https://doi.org/10.1148/radiol.2020201138) (2020).

- 16 Gefter, W. B. *et al.* Pulmonary Functional Imaging: Part 2-State-of-the-Art Clinical Applications and Opportunities for Improved Patient Care. *Radiology* **299**, 524-538, doi:10.1148/radiol.2021204033 (2021).
- 17 Kramer, G. H., Capello, K., Bearrs, B., Lauzon, A. & Normandeau, L. LINEAR DIMENSIONS AND VOLUMES OF HUMAN LUNGS OBTAINED FROM CT IMAGES. *Health Physics* **102**, 378-383, doi:10.1097/HP.0b013e31823a13f1 (2012).
- 18 Tschirren, J., McLennan, G., Palágyi, K., Hoffman, E. A. & Sonka, M. Matching and anatomical labeling of human airway tree. *IEEE transactions on medical imaging* **24**, 1540-1547, doi:10.1109/TMI.2005.857653 (2005).
- 19 Eddy, R. L. *et al.* Is Computed Tomography Airway Count Related to Asthma Severity and Airway Structure and Function? *Am J Respir Crit Care Med* **201**, 923-933, doi:10.1164/rccm.201908-1552OC (2020).
- 20 Kirby, M. *et al.* Total Airway Count on Computed Tomography and the Risk of Chronic Obstructive Pulmonary Disease Progression. Findings from a Population-based Study. *Am J Respir Crit Care Med* **197**, 56-65, doi:10.1164/rccm.201704-0692OC (2018).
- 21 de Jong, P. A., Muller, N. L., Pare, P. D. & Coxson, H. O. Computed tomographic imaging of the airways: relationship to structure and function. *Eur Respir J* **26**, 140-152, doi:10.1183/09031936.05.00007105 (2005).
- 22 Dunican, E. M. *et al.* Mucus plugs in patients with asthma linked to eosinophilia and airflow obstruction. *J Clin Invest* **128**, 997-1009, doi:10.1172/jci95693 (2018).
- 23 Dunican, E. M. *et al.* Mucus Plugs and Emphysema in the Pathophysiology of Airflow Obstruction and Hypoxemia in Smokers. *Am J Respir Crit Care Med* **203**, 957-968, doi:10.1164/rccm.202006-2248OC (2021).
- 24 Gevenois, P. A. *et al.* Comparison of computed density and microscopic morphometry in pulmonary emphysema. *Am J Respir Crit Care Med* **154**, 187-192, doi:10.1164/ajrccm.154.1.8680679 (1996).
- 25 Schroeder, J. D. *et al.* Relationships between airflow obstruction and quantitative CT measurements of emphysema, air trapping, and airways in subjects with and without chronic obstructive pulmonary disease. *AJR Am J Roentgenol* **201**, W460-470, doi:10.2214/AJR.12.10102 (2013).
- 26 Galban, C. J. *et al.* Computed tomography-based biomarker provides unique signature for diagnosis of COPD phenotypes and disease progression. *Nat Med* **18**, 1711-1715, doi:10.1038/nm.2971 (2012).
- 27 Choi, S. *et al.* Registration-based assessment of regional lung function via volumetric CT images of normal subjects vs. severe asthmatics. *J Appl Physiol (1985)* **115**, 730-742, doi:10.1152/jappphysiol.00113.2013 (2013).
- 28 Bodduluri, S. *et al.* Biomechanical CT metrics are associated with patient outcomes in COPD. *Thorax* **72**, 409-414, doi:10.1136/thoraxjnl-2016-209544 (2017).
- 29 Jahani, N. *et al.* A four-dimensional computed tomography comparison of healthy and asthmatic human lungs. *J Biomech* **56**, 102-110, doi:10.1016/j.jbiomech.2017.03.012 (2017).
- 30 Reinhardt, J. M. *et al.* Registration-based estimates of local lung tissue expansion compared to xenon CT measures of specific ventilation. *Med Image Anal* **12**, 752-763, doi:https://doi.org/10.1016/j.media.2008.03.007 (2008).

- 31 Ma, W. *et al.* Ultra-short echo-time pulmonary MRI: evaluation and reproducibility in COPD subjects with and without bronchiectasis. *J Magn Reson Imaging* **41**, 1465-1474, doi:10.1002/jmri.24680 (2015).
- 32 Takahashi, M. *et al.* Ultra-short echo time (UTE) MR imaging of the lung: comparison between normal and emphysematous lungs in mutant mice. *J Magn Reson Imaging* **32**, 326-333, doi:10.1002/jmri.22267 (2010).
- 33 Voskresbenzev, A. & Vogel-Claussen, J. Proton MRI of the Lung: How to Tame Scarce Protons and Fast Signal Decay. *Journal of Magnetic Resonance Imaging* **53**, 1344-1357, doi:https://doi.org/10.1002/jmri.27122 (2021).
- 34 Capaldi, D. P. *et al.* Free-breathing pulmonary ¹H and Hyperpolarized ³He MRI: comparison in COPD and bronchiectasis. *Acad Radiol* **22**, 320-329, doi:10.1016/j.acra.2014.10.003 (2015).
- 35 Biederer, J. *et al.* MRI of the lung (3/3)-current applications and future perspectives. *Insights Imaging* **3**, 373-386, doi:10.1007/s13244-011-0142-z (2012).
- 36 Kirby, M. *et al.* Hyperpolarized ³He magnetic resonance functional imaging semiautomated segmentation. *Acad Radiol* **19**, 141-152, doi:10.1016/j.acra.2011.10.007 (2012).
- 37 Bauman, G. & Eichinger, M. Ventilation and perfusion magnetic resonance imaging of the lung. *Pol J Radiol* **77**, 37-46, doi:10.12659/pjr.882579 (2012).
- 38 Tzeng, Y. S., Lutchen, K. & Albert, M. The difference in ventilation heterogeneity between asthmatic and healthy subjects quantified using hyperpolarized ³He MRI. *J Appl Physiol (1985)* **106**, 813-822, doi:10.1152/jappphysiol.01133.2007 (2009).
- 39 Diaz, S. *et al.* Validity of apparent diffusion coefficient hyperpolarized ³He-MRI using MSCT and pulmonary function tests as references. *Eur J Radiol* **71**, 257-263, doi:10.1016/j.ejrad.2008.04.013 (2009).
- 40 Bourdin, A. *et al.* Nitrogen washout slope in poorly controlled asthma. *Allergy* **61**, 85-89, doi:10.1111/j.1398-9995.2006.00970.x (2006).
- 41 Safavi, S. *et al.* Evaluating post-bronchodilator response in well-controlled paediatric severe asthma using hyperpolarised ¹²⁹Xe-MRI: A pilot study. *Respir Med* **180**, 106368, doi:10.1016/j.rmed.2021.106368 (2021).
- 42 Maunder, A. *et al.* MR properties of (19) F C(3) F(8) gas in the lungs of healthy volunteers: T2* and apparent diffusion coefficient at 1.5T and T2* at 3T. *Magn Reson Med* **85**, 1561-1570, doi:10.1002/mrm.28511 (2021).
- 43 Kaushik, S. S. *et al.* Single-breath clinical imaging of hyperpolarized (¹²⁹Xe) in the airspaces, barrier, and red blood cells using an interleaved 3D radial 1-point Dixon acquisition. *Magn Reson Med* **75**, 1434-1443, doi:10.1002/mrm.25675 (2016).
- 44 Ruppert, K., Brookeman, J. R., Hagspiel, K. D. & Mugler, J. P., 3rd. Probing lung physiology with xenon polarization transfer contrast (XTC). *Magn Reson Med* **44**, 349-357, doi:10.1002/1522-2594(200009)44:3<349::aid-mrm2>3.0.co;2-j (2000).
- 45 Qing, K. *et al.* Assessment of lung function in asthma and COPD using hyperpolarized ¹²⁹Xe chemical shift saturation recovery spectroscopy and dissolved-phase MRI. *NMR Biomed* **27**, 1490-1501, doi:10.1002/nbm.3179 (2014).
- 46 Wang, Z. *et al.* Quantitative analysis of hyperpolarized ¹²⁹Xe gas transfer MRI. *Med Phys* **44**, 2415-2428, doi:https://doi.org/10.1002/mp.12264 (2017).

- 47 Wang, J. M. *et al.* Using hyperpolarized ^{129}Xe MRI to quantify regional gas transfer in idiopathic pulmonary fibrosis. *Thorax* **73**, 21, doi:10.1136/thoraxjnl-2017-210070 (2018).
- 48 Yankeelov, T. E. & Gore, J. C. Dynamic Contrast Enhanced Magnetic Resonance Imaging in Oncology: Theory, Data Acquisition, Analysis, and Examples. *Curr Med Imaging Rev* **3**, 91-107, doi:10.2174/157340507780619179 (2009).
- 49 Johns, C. S. *et al.* Pulmonary MR angiography and perfusion imaging-A review of methods and applications. *Eur J Radiol* **86**, 361-370, doi:10.1016/j.ejrad.2016.10.003 (2017).
- 50 Johns, C. S. *et al.* Lung perfusion: MRI vs. SPECT for screening in suspected chronic thromboembolic pulmonary hypertension. *J Magn Reson Imaging* **46**, 1693-1697, doi:10.1002/jmri.25714 (2017).
- 51 Bergin, C. J., Pauly, J. M. & Macovski, A. Lung parenchyma: projection reconstruction MR imaging. *Radiology* **179**, 777-781, doi:10.1148/radiology.179.3.2027991 (1991).
- 52 Bergin, C. J., Glover, G. M. & Pauly, J. Magnetic resonance imaging of lung parenchyma. *J Thorac Imaging* **8**, 12-17 (1993).
- 53 Gold, G. E. *et al.* Short echo time MR spectroscopic imaging of the lung parenchyma. *J Magn Reson Imaging* **15**, 679-684, doi:10.1002/jmri.10113 (2002).
- 54 Ohno, Y. *et al.* Pulmonary high-resolution ultrashort TE MR imaging: Comparison with thin-section standard- and low-dose computed tomography for the assessment of pulmonary parenchyma diseases. *J Magn Reson Imaging* **43**, 512-532, doi:10.1002/jmri.25008 (2016).
- 55 Bae, K. *et al.* Comparison of lung imaging using three-dimensional ultrashort echo time and zero echo time sequences: preliminary study. *European radiology* **29**, 2253-2262, doi:10.1007/s00330-018-5889-x (2019).
- 56 Jahani, N. *et al.* A four-dimensional computed tomography comparison of healthy and asthmatic human lungs. *Journal of biomechanics* **56**, 102-110, doi:10.1016/j.jbiomech.2017.03.012 (2017).
- 57 Wildberger, J. E. *et al.* Multislice computed tomography perfusion imaging for visualization of acute pulmonary embolism: animal experience. *European radiology* **15**, 1378-1386, doi:10.1007/s00330-005-2718-9 (2005).
- 58 Grob, D. *et al.* Imaging of pulmonary perfusion using subtraction CT angiography is feasible in clinical practice. *European radiology* **29**, 1408-1414, doi:10.1007/s00330-018-5740-4 (2019).
- 59 Loffler, R. *et al.* Optimization and evaluation of the signal intensity change in multisection oxygen-enhanced MR lung imaging. *Magn Reson Med* **43**, 860-866, doi:10.1002/1522-2594(200006)43:6<860::aid-mrm12>3.0.co;2-c (2000).
- 60 Couch, M. J. *et al.* Pulmonary Ultrashort Echo Time ^{19}F MR Imaging with Inhaled Fluorinated Gas Mixtures in Healthy Volunteers: Feasibility. *Radiology* **269**, 903-909, doi:10.1148/radiol.13130609 (2013).
- 61 Nobashi, T. *et al.* ^{18}F -FDG Uptake in Less Affected Lung Field Provides Prognostic Stratification in Patients with Interstitial Lung Disease. *J Nucl Med* **57**, 1899-1904, doi:10.2967/jnumed.116.174946 (2016).
- 62 Hofman, M. S. *et al.* ^{68}Ga PET/CT ventilation-perfusion imaging for pulmonary embolism: a pilot study with comparison to conventional scintigraphy. *J Nucl Med* **52**, 1513-1519, doi:10.2967/jnumed.111.093344 (2011).

- 63 Le Roux, P. Y., Hicks, R. J., Siva, S. & Hofman, M. S. PET/CT Lung Ventilation and Perfusion Scanning using Galligas and Gallium-68-MAA. *Semin Nucl Med* **49**, 71-81, doi:10.1053/j.semnuclmed.2018.10.013 (2019).
- 64 Hatori, A. *et al.* PET imaging of lung inflammation with [18F]FEDAC, a radioligand for translocator protein (18 kDa). *PLoS one* **7**, e45065, doi:10.1371/journal.pone.0045065 (2012).
- 65 Largeau, B., Dupont, A. C., Guilloteau, D., Santiago-Ribeiro, M. J. & Arlicot, N. TSPO PET Imaging: From Microglial Activation to Peripheral Sterile Inflammatory Diseases? *Contrast Media Mol Imaging* **2017**, 6592139, doi:10.1155/2017/6592139 (2017).
- 66 Zhang, Z. *et al.* Positron Emission Tomography Imaging with 2-[18F]F-p-Aminobenzoic Acid Detects Staphylococcus aureus Infections and Monitors Drug Response. *ACS Infectious Diseases* **4**, 1635-1644, doi:10.1021/acsinfecdis.8b00182 (2018).
- 67 Kirby, M., Wheatley, A., McCormack, D. & Parraga, G. Development and application of methods to quantify spatial and temporal hyperpolarized 3He MRI ventilation dynamics: preliminary results in chronic obstructive pulmonary disease. *SPIE Medical Imaging* **7626** (2010).
- 68 Donnelly, L. F. *et al.* Cystic fibrosis: combined hyperpolarized 3He-enhanced and conventional proton MR imaging in the lung--preliminary observations. *Radiology* **212**, 885-889, doi:10.1148/radiology.212.3.r99se20885 (1999).
- 69 Meaney, J. F. M., Prince, M. R., Nostrant, T. T. & Stanley, J. C. Gadolinium-enhanced MR angiography of visceral arteries in patients with suspected chronic mesenteric ischemia. *Journal of Magnetic Resonance Imaging* **7**, 171-176, doi:https://doi.org/10.1002/jmri.1880070126 (1997).
- 70 Tofts, P. S. *et al.* Estimating kinetic parameters from dynamic contrast-enhanced T(1)-weighted MRI of a diffusible tracer: standardized quantities and symbols. *J Magn Reson Imaging* **10**, 223-232, doi:10.1002/(sici)1522-2586(199909)10:3<223::aid-jmri2>3.0.co;2-s (1999).
- 71 Kearon, C. Natural history of venous thromboembolism. *Circulation* **107**, I22-30, doi:10.1161/01.Cir.0000078464.82671.78 (2003).
- 72 Hatabu, H. *et al.* Pulmonary perfusion: qualitative assessment with dynamic contrast-enhanced MRI using ultra-short TE and inversion recovery turbo FLASH. *Magn Reson Med* **36**, 503-508, doi:10.1002/mrm.1910360402 (1996).
- 73 Sheikh, K. *et al.* Ultrashort echo time MRI biomarkers of asthma. *J Magn Reson Imaging* **45**, 1204-1215, doi:10.1002/jmri.25503 (2017).
- 74 Bauman, G. *et al.* Non-contrast-enhanced perfusion and ventilation assessment of the human lung by means of fourier decomposition in proton MRI. *Magn Reson Med* **62**, 656-664, doi:10.1002/mrm.22031 (2009).
- 75 Raptis, C. A. *et al.* Building blocks for thoracic MRI: Challenges, sequences, and protocol design. *J Magn Reson Imaging* **50**, 682-701, doi:10.1002/jmri.26677 (2019).
- 76 Capaldi, D. P. I. *et al.* Free-breathing Functional Pulmonary MRI: Response to Bronchodilator and Bronchoprovocation in Severe Asthma. *Acad Radiol* **24**, 1268-1276, doi:10.1016/j.acra.2017.04.012 (2017).
- 77 Voskresbenzev, A., Gutberlet, M., Kaireit, T. F., Wacker, F. & Vogel-Claussen, J. Low-pass imaging of dynamic acquisitions (LIDA) with a group-oriented registration (GOREG) for proton MR imaging of lung ventilation. *Magn Reson Med* **78**, 1496-1505, doi:10.1002/mrm.26526 (2017).

- 78 Bauman, G., Pusterla, O. & Bieri, O. Functional lung imaging with transient spoiled gradient echo. *Magn Reson Med* **81**, 1915-1923, doi:10.1002/mrm.27535 (2019).
- 79 Capaldi, D. P. I. *et al.* Free-breathing Pulmonary MR Imaging to Quantify Regional Ventilation. *Radiology* **287**, 693-704, doi:10.1148/radiol.2018171993 (2018).
- 80 Harrison, S. J. *et al.* A Hilbert-based method for processing respiratory timeseries. *Neuroimage* **230**, 117787, doi:10.1016/j.neuroimage.2021.117787 (2021).
- 81 Vedam, S. S. *et al.* Acquiring a four-dimensional computed tomography dataset using an external respiratory signal. *Phys Med Biol* **48**, 45-62, doi:10.1088/0031-9155/48/1/304 (2003).
- 82 Yamamoto, T. *et al.* 4D CT lung ventilation images are affected by the 4D CT sorting method. *Med Phys* **40**, 101907-101907, doi:10.1118/1.4820538 (2013).
- 83 Fischer, A. *et al.* Self-gated Non-Contrast-Enhanced FUncTional Lung imaging (SENCEFUL) using a quasi-random fast low-angle shot (FLASH) sequence and proton MRI. *NMR Biomed* **27**, 907-917, doi:10.1002/nbm.3134 (2014).
- 84 Voskresenzev, A. *et al.* Feasibility of quantitative regional ventilation and perfusion mapping with phase-resolved functional lung (PREFUL) MRI in healthy volunteers and COPD, CTEPH, and CF patients. *Magn Reson Med* **79**, 2306-2314, doi:10.1002/mrm.26893 (2018).
- 85 Moher Alsady, T. *et al.* MRI-derived regional flow-volume loop parameters detect early-stage chronic lung allograft dysfunction. *J Magn Reson Imaging* **50**, 1873-1882, doi:10.1002/jmri.26799 (2019).
- 86 Kastler, A. Quelques suggestions concernant la production optique et la détection optique d'une inégalité de population des niveaux de quantification spatiale des atomes. Application à l'expérience de Stern et Gerlach et à la résonance magnétique. *J. Phys. Radium* **11**, 255-265, doi:10.1051/jphysrad:01950001106025500 (1950).
- 87 Khan, A. S. *et al.* Enabling Clinical Technologies for Hyperpolarized ^{129}Xe Magnetic Resonance Imaging and Spectroscopy. *Angewandte Chemie International Edition* **60**, 22126-22147, doi:https://doi.org/10.1002/anie.202015200 (2021).
- 88 Barskiy, D. A. *et al.* NMR Hyperpolarization Techniques of Gases. *Chemistry* **23**, 725-751, doi:10.1002/chem.201603884 (2017).
- 89 Oros, A. M. & Shah, N. J. Hyperpolarized xenon in NMR and MRI. *Phys Med Biol* **49**, R105-153, doi:10.1088/0031-9155/49/20/r01 (2004).
- 90 Bouchiat, M. A., Carver, T. R. & Varnum, C. M. Nuclear Polarization in ^3He Gas Induced by Optical Pumping and Dipolar Exchange. *Physical Review Letters* **5**, 373-375, doi:10.1103/PhysRevLett.5.373 (1960).
- 91 Grover, B. Noble-gas NMR detection through noble-gas-rubidium hyperfine contact interaction. *Physical Review Letters* **40**, 391 (1978).
- 92 He, M. *et al.* Dose and pulse sequence considerations for hyperpolarized ^{129}Xe ventilation MRI. *Magnetic resonance imaging* **33**, 877-885 (2015).
- 93 Norquay, G., Collier, G. J., Rao, M., Stewart, N. J. & Wild, J. M. ^{129}Xe -Rb Spin-Exchange Optical Pumping with High Photon Efficiency. *Physical Review Letters* **121**, 153201, doi:10.1103/PhysRevLett.121.153201 (2018).
- 94 Niedbalski, P. J. *et al.* Protocols for multi-site trials using hyperpolarized ^{129}Xe MRI for imaging of ventilation, alveolar-airspace size, and gas exchange: A position paper from the ^{129}Xe MRI clinical trials consortium. *Magn Reson Med* **86**, 2966-2986, doi:https://doi.org/10.1002/mrm.28985 (2021).

- 95 Walker, T. G. & Happer, W. Spin-exchange optical pumping of noble-gas nuclei. *Reviews of Modern Physics* **69**, 629-642, doi:10.1103/RevModPhys.69.629 (1997).
- 96 Albert, M. S. *et al.* Biological magnetic resonance imaging using laser-polarized ^{129}Xe . *Nature* **370**, 199-201, doi:10.1038/370199a0 (1994).
- 97 Mugler, J. P., 3rd *et al.* MR imaging and spectroscopy using hyperpolarized ^{129}Xe gas: preliminary human results. *Magn Reson Med* **37**, 809-815, doi:10.1002/mrm.1910370602 (1997).
- 98 Kauczor, H. U. *et al.* Imaging of the lungs using ^3He MRI: preliminary clinical experience in 18 patients with and without lung disease. *J Magn Reson Imaging* **7**, 538-543, doi:10.1002/jmri.1880070314 (1997).
- 99 Ebert, M. *et al.* Nuclear magnetic resonance imaging with hyperpolarised helium-3. *Lancet* **347**, 1297-1299, doi:10.1016/s0140-6736(96)90940-x (1996).
- 100 MacFall, J. R. *et al.* Human lung air spaces: potential for MR imaging with hyperpolarized He-3. *Radiology* **200**, 553-558 (1996).
- 101 Norquay, G., Collier, G., Rao, M., Stewart, N. & Wild, J. Xe ^{129}Rb Spin-Exchange Optical Pumping with High Photon Efficiency. *Physical review letters* **121**, 153201 (2018).
- 102 Chen, R. Y. *et al.* Tissue-blood partition coefficient for xenon: temperature and hematocrit dependence. *J Appl Physiol Respir Environ Exerc Physiol* **49**, 178-183, doi:10.1152/jappl.1980.49.2.178 (1980).
- 103 Weathersby, P. K. & Homer, L. D. Solubility of inert gases in biological fluids and tissues: a review. *Undersea Biomed Res* **7**, 277-296 (1980).
- 104 Wagshul, M. E. *et al.* In vivo MR imaging and spectroscopy using hyperpolarized ^{129}Xe . *Magn Reson Med* **36**, 183-191, doi:10.1002/mrm.1910360203 (1996).
- 105 Sakai, K. *et al.* Temporal dynamics of hyperpolarized ^{129}Xe resonances in living rats. *J Magn Reson B* **111**, 300-304, doi:10.1006/jmrb.1996.0098 (1996).
- 106 Cleveland, Z. I. *et al.* Hyperpolarized ^{129}Xe MR Imaging of Alveolar Gas Uptake in Humans. *PloS one* **5**, e12192, doi:10.1371/journal.pone.0012192 (2010).
- 107 Qing, K. *et al.* Regional mapping of gas uptake by blood and tissue in the human lung using hyperpolarized xenon-129 MRI. *J Magn Reson Imaging* **39**, 346-359, doi:10.1002/jmri.24181 (2014).
- 108 Ruppert, K. *et al.* Rapid assessment of pulmonary gas transport with hyperpolarized ^{129}Xe MRI using a 3D radial double golden-means acquisition with variable flip angles. *Magn Reson Med* **80**, 2439-2448, doi:https://doi.org/10.1002/mrm.27217 (2018).
- 109 Stock, K. W., Chen, Q., Hatabu, H. & Edelman, R. R. Magnetic resonance T2* measurements of the normal human lung in vivo with ultra-short echo times. *Magn Reson Imaging* **17**, 997-1000, doi:10.1016/s0730-725x(99)00047-8 (1999).
- 110 Yu, J., Xue, Y. & Song, H. K. Comparison of lung T2* during free-breathing at 1.5 T and 3.0 T with ultrashort echo time imaging. *Magn Reson Med* **66**, 248-254, doi:10.1002/mrm.22829 (2011).
- 111 Krupa, K. & Bekiesińska-Figatowska, M. Artifacts in magnetic resonance imaging. *Pol J Radiol* **80**, 93-106, doi:10.12659/PJR.892628 (2015).
- 112 Duwell, S. H. *et al.* Musculoskeletal MR imaging at 4 T and at 1.5 T: comparison of relaxation times and image contrast. *Radiology* **196**, 551-555, doi:10.1148/radiology.196.2.7617876 (1995).

- 113 Duewell, S., Wolff, S. D., Wen, H., Balaban, R. S. & Jezzard, P. MR imaging contrast in human brain tissue: assessment and optimization at 4 T. *Radiology* **199**, 780-786, doi:10.1148/radiology.199.3.8638005 (1996).
- 114 Wild, J. *et al.* Hyperpolarised gas MR lung imaging – Breaks through to clinical practice. *European Respiratory Journal* **46**, OA4992, doi:10.1183/13993003.congress-2015.OA4992 (2015).
- 115 Mussell, G. T. *et al.* Xenon ventilation MRI in difficult asthma: initial experience in a clinical setting. *ERJ Open Res* **7**, doi:10.1183/23120541.00785-2020 (2021).
- 116 Stewart, N. J. *et al.* Lung MRI with hyperpolarised gases: current & future clinical perspectives. *The British Journal of Radiology* **95**, 20210207, doi:10.1259/bjr.20210207 (2022).
- 117 Mugler, J. P., 3rd & Altes, T. A. Hyperpolarized ¹²⁹Xe MRI of the human lung. *J Magn Reson Imaging* **37**, 313-331, doi:10.1002/jmri.23844 (2013).
- 118 Hoffman, E. A. *et al.* Pulmonary CT and MRI phenotypes that help explain chronic pulmonary obstruction disease pathophysiology and outcomes. *J Magn Reson Imaging* **43**, 544-557, doi:10.1002/jmri.25010 (2016).
- 119 Hughes, P. J. C. *et al.* Assessment of the influence of lung inflation state on the quantitative parameters derived from hyperpolarized gas lung ventilation MRI in healthy volunteers. *J Appl Physiol* **126**, 183-192, doi:10.1152/jappphysiol.00464.2018 (2019).
- 120 McMahon, C. J. *et al.* Hyperpolarized ³helium magnetic resonance ventilation imaging of the lung in cystic fibrosis: comparison with high resolution CT and spirometry. *European radiology* **16**, 2483-2490, doi:10.1007/s00330-006-0311-5 (2006).
- 121 Woodhouse, N. *et al.* Combined helium-3/proton magnetic resonance imaging measurement of ventilated lung volumes in smokers compared to never-smokers. *J Magn Reson Imaging* **21**, 365-369, doi:10.1002/jmri.20290 (2005).
- 122 Lui, J. K. *et al.* Semiautomatic segmentation of ventilated airspaces in healthy and asthmatic subjects using hyperpolarized ³He MRI. *Comput Math Methods Med* **2013**, 624683, doi:10.1155/2013/624683 (2013).
- 123 Zha, W. *et al.* Semiautomated Ventilation Defect Quantification in Exercise-induced Bronchoconstriction Using Hyperpolarized Helium-3 Magnetic Resonance Imaging: A Repeatability Study. *Acad Radiol* **23**, 1104-1114, doi:10.1016/j.acra.2016.04.005 (2016).
- 124 Hughes, P. J. C. *et al.* Spatial fuzzy c-means thresholding for semiautomated calculation of percentage lung ventilated volume from hyperpolarized gas and (1) H MRI. *J Magn Reson Imaging* **47**, 640-646, doi:10.1002/jmri.25804 (2018).
- 125 Tustison, N. J. *et al.* Ventilation-based segmentation of the lungs using hyperpolarized (³He) MRI. *J Magn Reson Imaging* **34**, 831-841, doi:10.1002/jmri.22738 (2011).
- 126 He, M. *et al.* Extending semiautomatic ventilation defect analysis for hyperpolarized (¹²⁹Xe) ventilation MRI. *Acad Radiol* **21**, 1530-1541, doi:10.1016/j.acra.2014.07.017 (2014).
- 127 Tustison, N. J. *et al.* Convolutional Neural Networks with Template-Based Data Augmentation for Functional Lung Image Quantification. *Acad Radiol* **26**, 412-423, doi:10.1016/j.acra.2018.08.003 (2019).
- 128 Zurawska, J. H. *et al.* What to Do When a Smoker's CT Scan Is “Normal”? Implications for Lung Cancer Screening. *Chest* **141**, 1147-1152, doi:https://doi.org/10.1378/chest.11-1863 (2012).

- 129 Ohkubo, H., Nakagawa, H. & Niimi, A. Computer-based quantitative computed tomography image analysis in idiopathic pulmonary fibrosis: A mini review. *Respiratory Investigation* **56**, 5-13, doi:https://doi.org/10.1016/j.resinv.2017.10.003 (2018).
- 130 Colombi, D. *et al.* Visual vs Fully Automatic Histogram-Based Assessment of Idiopathic Pulmonary Fibrosis (IPF) Progression Using Sequential Multidetector Computed Tomography (MDCT). *PloS one* **10**, e0130653, doi:10.1371/journal.pone.0130653 (2015).
- 131 Best, A. C. *et al.* Idiopathic Pulmonary Fibrosis: Physiologic Tests, Quantitative CT Indexes, and CT Visual Scores as Predictors of Mortality. *Radiology* **246**, 935-940, doi:10.1148/radiol.2463062200 (2008).
- 132 Jacob, J. *et al.* Automated Quantitative Computed Tomography Versus Visual Computed Tomography Scoring in Idiopathic Pulmonary Fibrosis: Validation Against Pulmonary Function. *Journal of Thoracic Imaging* **31**, 304-311, doi:10.1097/rti.0000000000000220 (2016).
- 133 Jacob, J. *et al.* Mortality prediction in idiopathic pulmonary fibrosis: evaluation of computer-based CT analysis with conventional severity measures. *Eur Respir J* **49**, doi:10.1183/13993003.01011-2016 (2017).
- 134 Altes, T. A. *et al.* Hyperpolarized ³He MR lung ventilation imaging in asthmatics: preliminary findings. *J Magn Reson Imaging* **13**, 378-384, doi:10.1002/jmri.1054 (2001).
- 135 de Lange, E. E. *et al.* Evaluation of asthma with hyperpolarized helium-3 MRI: correlation with clinical severity and spirometry. *Chest* **130**, 1055-1062, doi:10.1378/chest.130.4.1055 (2006).
- 136 Giger, M. L. Machine Learning in Medical Imaging. *J Am Coll Radiol* **15**, 512-520, doi:10.1016/j.jacr.2017.12.028 (2018).
- 137 LeCun, Y., Bengio, Y. & Hinton, G. Deep learning. *Nature* **521**, 436-444, doi:10.1038/nature14539 (2015).
- 138 Astley, J. R., Wild, J. M. & Tahir, B. A. Deep learning in structural and functional lung image analysis. *The British Journal of Radiology* **0**, 20201107, doi:10.1259/bjr.20201107 (2021).
- 139 Parraga, G. *et al.* Hyperpolarized ³He ventilation defects and apparent diffusion coefficients in chronic obstructive pulmonary disease: preliminary results at 3.0 Tesla. *Invest Radiol* **42**, 384-391, doi:10.1097/01.rli.0000262571.81771.66 (2007).
- 140 Parraga, G., Mathew, L., Etemad-Rezai, R., McCormack, D. G. & Santyr, G. E. Hyperpolarized ³He magnetic resonance imaging of ventilation defects in healthy elderly volunteers: initial findings at 3.0 Tesla. *Acad Radiol* **15**, 776-785, doi:10.1016/j.acra.2008.03.003 (2008).
- 141 Schmidt-Richberg, A., Werner, R., Handels, H. & Ehrhardt, J. Estimation of slipping organ motion by registration with direction-dependent regularization. *Medical Image Anal.* **16**, 150-159, doi:10.1016/j.media.2011.06.007 (2012).
- 142 Ireland, R. H. *et al.* An image acquisition and registration strategy for the fusion of hyperpolarized helium-3 MRI and x-ray CT images of the lung. *Phys Med Biol* **53**, 6055-6063, doi:10.1088/0031-9155/53/21/011 (2008).
- 143 Heinrich, M. P. *et al.* MIND: modality independent neighbourhood descriptor for multi-modal deformable registration. *Med Image Anal* **16**, 1423-1435, doi:10.1016/j.media.2012.05.008 (2012).

- 144 Klein, S., Staring, M., Murphy, K., Viergever, M. A. & Pluim, J. P. elastix: a toolbox for intensity-based medical image registration. *IEEE Trans Med Imaging* **29**, 196-205, doi:10.1109/tmi.2009.2035616 (2010).
- 145 Maes, F., Collignon, A., Vandermeulen, D., Marchal, G. & Suetens, P. Multimodality image registration by maximization of mutual information. *IEEE Trans Med Imaging* **16**, 187-198, doi:10.1109/42.563664 (1997).
- 146 Nanayakkara, N. D. *et al.* Nonrigid registration of three-dimensional ultrasound and magnetic resonance images of the carotid arteries. *Med Phys* **36**, 373-385, doi:10.1118/1.3056458 (2009).
- 147 Tahir, B. A. *et al.* A method for quantitative analysis of regional lung ventilation using deformable image registration of CT and hybrid hyperpolarized gas/¹H MRI. *Phys Med Biol* **59**, 7267-7277, doi:10.1088/0031-9155/59/23/7267 (2014).
- 148 Guo, F. *et al.* Globally optimal co-segmentation of three-dimensional pulmonary (¹H and hyperpolarized (³He MRI with spatial consistence prior. *Med Image Anal* **23**, 43-55, doi:10.1016/j.media.2015.04.001 (2015).
- 149 Yuan, J., Bae, E. & Tai, X. in *2010 IEEE Computer Society Conference on Computer Vision and Pattern Recognition*. 2217-2224.
- 150 Guo, F. *et al.* Anatomical pulmonary magnetic resonance imaging segmentation for regional structure-function measurements of asthma. *Med Phys* **43**, 2911-2926, doi:10.1118/1.4948999 (2016).
- 151 Yuan, J., Bae, E., Tai, X. & Boykov, Y. in *ECCV*.
- 152 Ireland, R. H. *et al.* Feasibility of image registration and intensity-modulated radiotherapy planning with hyperpolarized helium-3 magnetic resonance imaging for non-small-cell lung cancer. *Int J Radiat Oncol Biol Phys* **68**, 273-281, doi:10.1016/j.ijrobp.2006.12.068 (2007).
- 153 Mathew, L. *et al.* Hyperpolarized (³He magnetic resonance imaging: comparison with four-dimensional x-ray computed tomography imaging in lung cancer. *Acad Radiol* **19**, 1546-1553, doi:10.1016/j.acra.2012.08.007 (2012).
- 154 Guo, F. *et al.* Thoracic CT-MRI coregistration for regional pulmonary structure-function measurements of obstructive lung disease. *Med Phys* **44**, 1718-1733, doi:10.1002/mp.12160 (2017).
- 155 Wild, J. M. *et al.* Synchronous acquisition of hyperpolarised ³He and ¹H MR images of the lungs – maximising mutual anatomical and functional information. *NMR Biomed* **24**, 130-134, doi:https://doi.org/10.1002/nbm.1565 (2011).
- 156 Blendowski, M. & Heinrich, M. P. Combining MRF-based deformable registration and deep binary 3D-CNN descriptors for large lung motion estimation in COPD patients. *International Journal of Computer Assisted Radiology and Surgery* **14**, 43-52, doi:10.1007/s11548-018-1888-2 (2019).
- 157 Mathew, L. *et al.* Hyperpolarized ³He magnetic resonance imaging of chronic obstructive pulmonary disease: reproducibility at 3.0 tesla. *Acad Radiol* **15**, 1298-1311, doi:10.1016/j.acra.2008.04.019 (2008).
- 158 Sheikh, K., Coxson, H. O. & Parraga, G. This is what COPD looks like. *Respirology* **21**, 224-236, doi:10.1111/resp.12611 (2016).
- 159 Svenningsen, S. *et al.* Reproducibility of Hyperpolarized (¹²⁹Xe MRI Ventilation Defect Percent in Severe Asthma to Evaluate Clinical Trial Feasibility. *Acad Radiol* **28**, 817-826, doi:10.1016/j.acra.2020.04.025 (2021).

- 160 Waring, J., Lindvall, C. & Umeton, R. Automated machine learning: Review of the state-of-the-art and opportunities for healthcare. *Artif Intell Med* **104**, 101822, doi:10.1016/j.artmed.2020.101822 (2020).
- 161 de Lange, E. E. *et al.* Changes in regional airflow obstruction over time in the lungs of patients with asthma: evaluation with ³He MR imaging. *Radiology* **250**, 567-575, doi:10.1148/radiol.2502080188 (2009).
- 162 He, M., Driehuys, B., Que, L. G. & Huang, Y. T. Using Hyperpolarized (¹²⁹Xe) MRI to Quantify the Pulmonary Ventilation Distribution. *Acad Radiol* **23**, 1521-1531, doi:10.1016/j.acra.2016.07.014 (2016).
- 163 He, M. *et al.* A Comparison of Two Hyperpolarized (¹²⁹Xe) MRI Ventilation Quantification Pipelines: The Effect of Signal to Noise Ratio. *Acad Radiol* **26**, 949-959, doi:10.1016/j.acra.2018.08.015 (2019).
- 164 Fain, S. B. *et al.* Evaluation of structure-function relationships in asthma using multidetector CT and hyperpolarized He-3 MRI. *Acad Radiol* **15**, 753-762, doi:10.1016/j.acra.2007.10.019 (2008).
- 165 Eddy, R. L., Westcott, A., Maksym, G. N., Parraga, G. & Dandurand, R. J. Oscillometry and pulmonary magnetic resonance imaging in asthma and COPD. *Physiol Rep* **7**, e13955, doi:10.14814/phy2.13955 (2019).
- 166 Kirby, M., Kanhere, N., Etemad-Rezai, R., McCormack, D. G. & Parraga, G. Hyperpolarized helium-3 magnetic resonance imaging of chronic obstructive pulmonary disease exacerbation. *J Magn Reson Imaging* **37**, 1223-1227, doi:10.1002/jmri.23896 (2013).
- 167 Kirby, M., Pike, D., Coxson, H. O., McCormack, D. G. & Parraga, G. Hyperpolarized (³He) ventilation defects used to predict pulmonary exacerbations in mild to moderate chronic obstructive pulmonary disease. *Radiology* **273**, 887-896, doi:10.1148/radiol.14140161 (2014).
- 168 Kirby, M. *et al.* Hyperpolarized ³He and ¹²⁹Xe magnetic resonance imaging apparent diffusion coefficients: physiological relevance in older never- and ex-smokers. *Physiol Rep* **2**, doi:10.14814/phy2.12068 (2014).
- 169 Fain, S. B. *et al.* Early emphysematous changes in asymptomatic smokers: detection with ³He MR imaging. *Radiology* **239**, 875-883, doi:10.1148/radiol.2393050111 (2006).
- 170 Kirby, M. *et al.* On the role of abnormal DL(CO) in ex-smokers without airflow limitation: symptoms, exercise capacity and hyperpolarised helium-3 MRI. *Thorax* **68**, 752-759, doi:10.1136/thoraxjnl-2012-203108 (2013).
- 171 Coxson, H. O., Leipsic, J., Parraga, G. & Sin, D. D. Using pulmonary imaging to move chronic obstructive pulmonary disease beyond FEV₁. *Am J Respir Crit Care Med* **190**, 135-144, doi:10.1164/rccm.201402-0256PP (2014).
- 172 Svenningsen, S. *et al.* Hyperpolarized (³ He and (¹²⁹ Xe) MRI: differences in asthma before bronchodilation. *J Magn Reson Imaging* **38**, 1521-1530, doi:10.1002/jmri.24111 (2013).
- 173 Kirby, M. *et al.* Hyperpolarized ³He and ¹²⁹Xe MR imaging in healthy volunteers and patients with chronic obstructive pulmonary disease. *Radiology* **265**, 600-610, doi:10.1148/radiol.12120485 (2012).
- 174 Stewart, N. J. *et al.* Comparison of (³) He and (¹²⁹) Xe MRI for evaluation of lung microstructure and ventilation at 1.5T. *J Magn Reson Imaging* **48**, 632-642, doi:10.1002/jmri.25992 (2018).

- 175 Kirby, M. *et al.* Pulmonary ventilation visualized using hyperpolarized helium-3 and xenon-129 magnetic resonance imaging: differences in COPD and relationship to emphysema. *J Appl Physiol (1985)* **114**, 707-715, doi:10.1152/jappphysiol.01206.2012 (2013).
- 176 Chan, H. F., Stewart, N. J., Norquay, G., Collier, G. J. & Wild, J. M. 3D diffusion-weighted (129) Xe MRI for whole lung morphometry. *Magn Reson Med* **79**, 2986-2995, doi:10.1002/mrm.26960 (2018).
- 177 Zhang, H. *et al.* Lung morphometry using hyperpolarized (129) Xe multi-b diffusion MRI with compressed sensing in healthy subjects and patients with COPD. *Med Phys* **45**, 3097-3108, doi:10.1002/mp.12944 (2018).
- 178 Qing, K. *et al.* Rapid acquisition of helium-3 and proton three-dimensional image sets of the human lung in a single breath-hold using compressed sensing. *Magn Reson Med* **74**, 1110-1115, doi:https://doi.org/10.1002/mrm.25499 (2015).
- 179 Yablonskiy, D. A. *et al.* Quantitative in vivo assessment of lung microstructure at the alveolar level with hyperpolarized 3He diffusion MRI. *Proc Natl Acad Sci U S A* **99**, 3111-3116, doi:10.1073/pnas.052594699 (2002).
- 180 Miller, G. W., Carl, M., Mata, J. F., Cates, G. D., Jr. & Mugler, J. P., 3rd. Simulations of short-time diffusivity in lung airspaces and implications for S/V measurements using hyperpolarized-gas MRI. *IEEE Trans Med Imaging* **26**, 1456-1463, doi:10.1109/tmi.2007.903192 (2007).
- 181 Altes, T. A., Mata, J., de Lange, E. E., Brookeman, J. R. & Mugler, J. P., 3rd. Assessment of lung development using hyperpolarized helium-3 diffusion MR imaging. *J Magn Reson Imaging* **24**, 1277-1283, doi:10.1002/jmri.20723 (2006).
- 182 Woods, J. C. *et al.* Magnetization tagging decay to measure long-range 3He diffusion in healthy and emphysematous canine lungs. *Magn Reson Med* **51**, 1002-1008, doi:https://doi.org/10.1002/mrm.20070 (2004).
- 183 Haefeli-Bleuer, B. & Weibel, E. R. Morphometry of the human pulmonary acinus. *The Anatomical Record* **220**, 401-414, doi:https://doi.org/10.1002/ar.1092200410 (1988).
- 184 Sukstanskii, A. L. & Yablonskiy, D. A. In vivo lung morphometry with hyperpolarized 3He diffusion MRI: Theoretical background. *Journal of Magnetic Resonance* **190**, 200-210, doi:https://doi.org/10.1016/j.jmr.2007.10.015 (2008).
- 185 Kitaoka, H., Tamura, S. & Takaki, R. A three-dimensional model of the human pulmonary acinus. *J Appl Physiol (1985)* **88**, 2260-2268, doi:10.1152/jappl.2000.88.6.2260 (2000).
- 186 Fichele, S. *et al.* Finite-difference simulations of 3He diffusion in 3D alveolar ducts: comparison with the "cylinder model". *Magn Reson Med* **52**, 917-920, doi:10.1002/mrm.20213 (2004).
- 187 Mair, R. W. *et al.* Pulsed-field-gradient measurements of time-dependent gas diffusion. *J Magn Reson* **135**, 478-486, doi:10.1006/jmre.1998.1588 (1998).
- 188 Mair, R. W. *et al.* Probing porous media with gas diffusion NMR. *Phys Rev Lett* **83**, 3324-3327, doi:10.1103/PhysRevLett.83.3324 (1999).
- 189 Verbanck, S. & Paiva, M. Model simulations of gas mixing and ventilation distribution in the human lung. *J Appl Physiol (1985)* **69**, 2269-2279, doi:10.1152/jappl.1990.69.6.2269 (1990).
- 190 Verbanck, S. & Paiva, M. Simulation of the apparent diffusion of helium-3 in the human acinus. *J Appl Physiol (1985)* **103**, 249-254, doi:10.1152/jappphysiol.01384.2006 (2007).

- 191 Sukstanskii, A. L. & Yablonskiy, D. A. Lung morphometry with hyperpolarized ^{129}Xe :
theoretical background. *Magn Reson Med* **67**, 856-866, doi:10.1002/mrm.23056 (2012).
- 192 Parra-Robles, J., Marshall, H., Hartley, R., Brightling, C. E. & Wild, J. in *Proceedings of
the 22nd Annual Meeting of ISMRM, Milan, Italy*. 3529.
- 193 Yablonskiy, D. A. *et al.* Quantification of lung microstructure with hyperpolarized ^3He
diffusion MRI. *J Appl Physiol* (1985) **107**, 1258-1265,
doi:10.1152/jappphysiol.00386.2009 (2009).
- 194 Chan, H. F., Collier, G. J., Parra-Robles, J. & Wild, J. M. Finite element simulations of
hyperpolarized gas DWI in micro-CT meshes of acinar airways: validating the cylinder
and stretched exponential models of lung microstructural length scales. *Magn Reson Med*
86, 514-525, doi:10.1002/mrm.28703 (2021).
- 195 Raina, R., Madhavan, A. & Ng, A. Y. in *Proceedings of the 26th Annual International
Conference on Machine Learning* 873–880 (Association for Computing Machinery,
Montreal, Quebec, Canada, 2009).
- 196 Rajpurkar, P. *et al.* Deep learning for chest radiograph diagnosis: A retrospective
comparison of the CheXNeXt algorithm to practicing radiologists. *PLOS Medicine* **15**,
e1002686, doi:10.1371/journal.pmed.1002686 (2018).
- 197 Tustison, N. J. *et al.* N4ITK: Improved N3 Bias Correction. *IEEE Transactions on Medical
Imaging* **29**, 1310-1320, doi:10.1109/TMI.2010.2046908 (2010).
- 198 Avants, B. B. *et al.* The optimal template effect in hippocampus studies of diseased
populations. *NeuroImage* **49**, 2457-2466,
doi:<https://doi.org/10.1016/j.neuroimage.2009.09.062> (2010).
- 199 Rizzo, S. *et al.* Radiomics: the facts and the challenges of image analysis. *Eur Radiol Exp*
2, 36, doi:10.1186/s41747-018-0068-z (2018).
- 200 Haralick, R. M., Shanmugam, K. & Dinstein, I. Textural Features for Image Classification.
IEEE Trans Image Process, 610-621 (1973).
- 201 Tang, X. Texture information in run-length matrices. *IEEE Trans Image Process* **7**, 1602-
1609, doi:10.1109/83.725367 (1998).
- 202 Parmar, C., Grossmann, P., Bussink, J., Lambin, P. & Aerts, H. Machine Learning methods
for Quantitative Radiomic Biomarkers. *Sci Rep* **5**, 13087, doi:10.1038/srep13087 (2015).
- 203 Risse, F., Pesic, J., Young, S. & Olsson, L. E. A texture analysis approach to quantify
ventilation changes in hyperpolarised ^3He MRI of the rat lung in an asthma model. *NMR
Biomed* **25**, 131-141, doi:<https://doi.org/10.1002/nbm.1725> (2012).
- 204 Zha, N. *et al.* Second-order Texture Measurements of (^3He) Ventilation MRI: Proof-of-
concept Evaluation of Asthma Bronchodilator Response. *Acad Radiol* **23**, 176-185,
doi:10.1016/j.acra.2015.10.010 (2016).
- 205 Schiwek, M. *et al.* Quantification of pulmonary perfusion abnormalities using DCE-MRI
in COPD: comparison with quantitative CT and pulmonary function. *European radiology*
32, 1879-1890, doi:10.1007/s00330-021-08229-6 (2022).
- 206 Westcott, A. *et al.* Chronic Obstructive Pulmonary Disease: Thoracic CT Texture Analysis
and Machine Learning to Predict Pulmonary Ventilation. *Radiology* **0**, 190450,
doi:10.1148/radiol.2019190450 (2019).
- 207 Galloway, M. M. Texture analysis using gray level run lengths. *Computer Graphics and
Image Processing* **4**, 172-179, doi:[https://doi.org/10.1016/S0146-664X\(75\)80008-6](https://doi.org/10.1016/S0146-664X(75)80008-6)
(1975).

- 208 Capaldi, D. P. I., Guo, F., Xing, L. & Parraga, G. Pulmonary Ventilation Maps Generated with Free-breathing Proton MRI and a Deep Convolutional Neural Network. *Radiology* **298**, 427-438, doi:10.1148/radiol.2020202861 (2021).
- 209 Gerard, S. E., Reinhardt, J. M., Christensen, G. E. & Estépar, R. S. J. in *2020 IEEE 17th International Symposium on Biomedical Imaging (ISBI)*. 1856-1860.
- 210 Zhong, Y. *et al.* Technical Note: Deriving ventilation imaging from 4DCT by deep convolutional neural network. *Med Phys* **46**, 2323-2329, doi:<https://doi.org/10.1002/mp.13421> (2019).
- 211 Porter, E. M. *et al.* Synthetic pulmonary perfusion images from 4DCT for functional avoidance using deep learning. *Phys Med Biol* **66**, doi:10.1088/1361-6560/ac16ec (2021).
- 212 Ren, G. *et al.* Investigation of a Novel Deep Learning-Based Computed Tomography Perfusion Mapping Framework for Functional Lung Avoidance Radiotherapy. *Front Oncol* **11**, 644703, doi:10.3389/fonc.2021.644703 (2021).
- 213 Estépar, R. S. J. Artificial intelligence in functional imaging of the lung. *The British Journal of Radiology* **95**, 20210527, doi:10.1259/bjr.20210527 (2022).
- 214 Mayerhoefer, M. E., Szomolanyi, P., Jirak, D., Materka, A. & Trattnig, S. Effects of MRI acquisition parameter variations and protocol heterogeneity on the results of texture analysis and pattern discrimination: an application-oriented study. *Med Phys* **36**, 1236-1243, doi:10.1118/1.3081408 (2009).
- 215 Zwanenburg, A. *et al.* The Image Biomarker Standardization Initiative: Standardized Quantitative Radiomics for High-Throughput Image-based Phenotyping. *Radiology* **295**, 328-338, doi:10.1148/radiol.2020191145 (2020).
- 216 Lei, M. *et al.* Benchmarking Various Radiomic Toolkit Features While Applying the Image Biomarker Standardization Initiative toward Clinical Translation of Radiomic Analysis. *J Digit Imaging* **34**, 1156-1170, doi:10.1007/s10278-021-00506-6 (2021).
- 217 Rai, R. *et al.* Multicenter evaluation of MRI-based radiomic features: A phantom study. *Med Phys* **47**, 3054-3063, doi:10.1002/mp.14173 (2020).
- 218 Duan, C. *et al.* Fast and accurate reconstruction of human lung gas MRI with deep learning. *Magn Reson Med* **82**, 2273-2285, doi:10.1002/mrm.27889 (2019).
- 219 Hou, K.-Y., Lu, H.-Y. & Yang, C.-C. Applying MRI Intensity Normalization on Non-Bone Tissues to Facilitate Pseudo-CT Synthesis from MRI. *Diagnostics* **11**, 816 (2021).
- 220 Olberg, S. *et al.* Deep Learning-Based Pseudo CT Reconstruction for MR Only-Guided Radiation Therapy of Lung SBRT. *International Journal of Radiation Oncology*Biophysics* **102**, e309-e310, doi:<https://doi.org/10.1016/j.ijrobp.2018.07.969> (2018).
- 221 Kaushik, S. S. *et al.* Measuring diffusion limitation with a perfusion-limited gas--hyperpolarized ¹²⁹Xe gas-transfer spectroscopy in patients with idiopathic pulmonary fibrosis. *J Appl Physiol (1985)* **117**, 577-585, doi:10.1152/jappphysiol.00326.2014 (2014).
- 222 Virgincar, R. S. *et al.* Establishing an accurate gas phase reference frequency to quantify ¹²⁹Xe chemical shifts in vivo. *Magn Reson Med* **77**, 1438-1445, doi:<https://doi.org/10.1002/mrm.26229> (2017).
- 223 Bier, E. A. *et al.* A protocol for quantifying cardiogenic oscillations in dynamic (129) Xe gas exchange spectroscopy: The effects of idiopathic pulmonary fibrosis. *NMR Biomed* **32**, e4029, doi:10.1002/nbm.4029 (2019).

- 224 Coleman, T. F. & Li, Y. An interior trust region approach for nonlinear minimization subject to bounds. *SIAM Journal on optimization* **6**, 418-445 (1996).
- 225 Willmerring, M. M., Cleveland, Z. I., Walkup, L. L. & Woods, J. C. Removal of off-resonance xenon gas artifacts in pulmonary gas-transfer MRI. *Magn Reson Med* **86**, 907-915, doi:<https://doi.org/10.1002/mrm.28737> (2021).
- 226 Driehuys, B. *et al.* Imaging alveolar–capillary gas transfer using hyperpolarized ¹²⁹Xe MRI. *Proceedings of the National Academy of Sciences* **103**, 18278-18283, doi:10.1073/pnas.0608458103 (2006).
- 227 Woods, J. C. *et al.* Hyperpolarized ³He diffusion MRI and histology in pulmonary emphysema. *Magn Reson Med* **56**, 1293-1300, doi:10.1002/mrm.21076 (2006).
- 228 Dixon, W. T. Simple proton spectroscopic imaging. *Radiology* **153**, 189-194, doi:10.1148/radiology.153.1.6089263 (1984).
- 229 Kammerman, J. *et al.* Transverse relaxation rates of pulmonary dissolved-phase Hyperpolarized (129) Xe as a biomarker of lung injury in idiopathic pulmonary fibrosis. *Magn Reson Med* **84**, 1857-1867, doi:10.1002/mrm.28246 (2020).
- 230 Collier, G. J. *et al.* Dissolved (129) Xe lung MRI with four-echo 3D radial spectroscopic imaging: Quantification of regional gas transfer in idiopathic pulmonary fibrosis. *Magn Reson Med* **85**, 2622-2633, doi:10.1002/mrm.28609 (2021).
- 231 Doganay, O. *et al.* Magnetic resonance imaging of the time course of hyperpolarized (129)Xe gas exchange in the human lungs and heart. *European radiology* **29**, 2283-2292, doi:10.1007/s00330-018-5853-9 (2019).
- 232 Zanette, B. & Santyr, G. Accelerated interleaved spiral-IDEAL imaging of hyperpolarized (129) Xe for parametric gas exchange mapping in humans. *Magn Reson Med* **82**, 1113-1119, doi:10.1002/mrm.27765 (2019).
- 233 Robertson, S. H. *et al.* Uncovering a third dissolved-phase 129 Xe resonance in the human lung: Quantifying spectroscopic features in healthy subjects and patients with idiopathic pulmonary fibrosis. *Magn Reson Med* **78**, 1306-1315 (2017).
- 234 Norquay, G., Leung, G., Stewart, N. J., Wolber, J. & Wild, J. M. 129Xe chemical shift in human blood and pulmonary blood oxygenation measurement in humans using hyperpolarized 129Xe NMR. *Magn Reson Med* **77**, 1399-1408 (2017).
- 235 Marshall, H. *et al.* In vivo methods and applications of xenon-129 magnetic resonance. *Progress in Nuclear Magnetic Resonance Spectroscopy* **122**, 42-62, doi:<https://doi.org/10.1016/j.pnmrs.2020.11.002> (2021).
- 236 Lange, P., Halpin, D. M., O'Donnell, D. E. & MacNee, W. Diagnosis, assessment, and phenotyping of COPD: beyond FEV₁. *Int J Chron Obstruct Pulmon Dis* **11 Spec Iss**, 3-12, doi:10.2147/copd.S85976 (2016).
- 237 Leary, D. *et al.* Hyperpolarized ³He magnetic resonance imaging ventilation defects in asthma: relationship to airway mechanics. *Physiol Rep* **4**, doi:10.14814/phy2.12761 (2016).
- 238 Davis, C. *et al.* Ventilation Heterogeneity in Never-smokers and COPD:: Comparison of Pulmonary Functional Magnetic Resonance Imaging with the Poorly Communicating Fraction Derived From Plethysmography. *Acad Radiol* **23**, 398-405, doi:10.1016/j.acra.2015.10.022 (2016).
- 239 Kirby, M. *et al.* COPD: Do Imaging Measurements of Emphysema and Airway Disease Explain Symptoms and Exercise Capacity? *Radiology* **277**, 872-880, doi:10.1148/radiol.2015150037 (2015).

- 240 Svenningsen, S., Nair, P., Guo, F., McCormack, D. G. & Parraga, G. Is ventilation heterogeneity related to asthma control? *Eur Respir J* **48**, 370-379, doi:10.1183/13993003.00393-2016 (2016).
- 241 Kowalik, K. *et al.* Persistent ventilation inhomogeneity after an acute exacerbation in preschool children with recurrent wheezing. *Pediatr Allergy Immunol* **31**, 608-615, doi:10.1111/pai.13245 (2020).
- 242 Altes, T. A. *et al.* Clinical correlates of lung ventilation defects in asthmatic children. *J Allergy Clin Immunol* **137**, 789-796 e787, doi:10.1016/j.jaci.2015.08.045 (2016).
- 243 Teague, W. G., Tustison, N. J. & Altes, T. A. Ventilation heterogeneity in asthma. *J Asthma* **51**, 677-684, doi:10.3109/02770903.2014.914535 (2014).
- 244 Svenningsen, S. *et al.* What are ventilation defects in asthma? *Thorax* **69**, 63-71, doi:10.1136/thoraxjnl-2013-203711 (2014).
- 245 Kirby, M. *et al.* Chronic obstructive pulmonary disease: quantification of bronchodilator effects by using hyperpolarized (3)He MR imaging. *Radiology* **261**, 283-292, doi:10.1148/radiol.11110403 (2011).
- 246 Farahi, N. *et al.* In vivo imaging reveals increased eosinophil uptake in the lungs of obese asthmatic patients. *J Allergy Clin Immunol* **142**, 1659-1662 e1658, doi:10.1016/j.jaci.2018.07.011 (2018).
- 247 Samee, S. *et al.* Imaging the lungs in asthmatic patients by using hyperpolarized helium-3 magnetic resonance: assessment of response to methacholine and exercise challenge. *J Allergy Clin Immunol* **111**, 1205-1211, doi:10.1067/mai.2003.1544 (2003).
- 248 Eddy, R. L., Svenningsen, S., McCormack, D. G. & Parraga, G. What is the minimal clinically important difference for helium-3 magnetic resonance imaging ventilation defects? *Eur Respir J* **51**, doi:10.1183/13993003.00324-2018 (2018).
- 249 Eddy, R., Svenningsen, S. L., McCormack, D. G. & Parraga, G. Determining the Minimal Clinically Important Difference: MRI Ventilation Defect Percent in Asthmatics. *D28. RESPIRATORY DISEASE DIAGNOSIS: PULMONARY FUNCTION TESTING AND IMAGING*, A6381-A6381, doi:10.1164/ajrccm-conference.2018.197.1_MeetingAbstracts.A6381 (2018).
- 250 Thomen, R. P. *et al.* Regional ventilation changes in severe asthma after bronchial thermoplasty with (3)He MR imaging and CT. *Radiology* **274**, 250-259, doi:10.1148/radiol.14140080 (2015).
- 251 Schipper, P. H. *et al.* Outcomes after resection of giant emphysematous bullae. *Ann Thorac Surg* **78**, 976-982; discussion 976-982, doi:10.1016/j.athoracsur.2004.04.005 (2004).
- 252 Hall, C. S. *et al.* Single-Session Bronchial Thermoplasty Guided by (129)Xe Magnetic Resonance Imaging. A Pilot Randomized Controlled Clinical Trial. *Am J Respir Crit Care Med* **202**, 524-534, doi:10.1164/rccm.201905-1021OC (2020).
- 253 Svenningsen, S. *et al.* Bronchial thermoplasty guided by hyperpolarised gas magnetic resonance imaging in adults with severe asthma: a 1-year pilot randomised trial. *ERJ Open Research* **7**, 00268-02021, doi:10.1183/23120541.00268-2021 (2021).
- 254 Svenningsen, S., Haider, E. A., Eddy, R. L., Parraga, G. & Nair, P. Normalisation of MRI ventilation heterogeneity in severe asthma by dupilumab. *Thorax*, doi:10.1136/thoraxjnl-2019-213415 (2019).
- 255 Rankine, L. J. *et al.* Correlation of Regional Lung Ventilation and Gas Transfer to Red Blood Cells: Implications for Functional-Avoidance Radiation Therapy Planning.

- International Journal of Radiation Oncology*Biography*Physics* **101**, 1113-1122, doi:https://doi.org/10.1016/j.ijrobp.2018.04.017 (2018).
- 256 Eddy, R. L., Svenningsen, S., Licskai, C., McCormack, D. G. & Parraga, G. Hyperpolarized Helium 3 MRI in Mild-to-Moderate Asthma: Prediction of Postbronchodilator Reversibility. *Radiology*, 190420, doi:10.1148/radiol.2019190420 (2019).
- 257 Thomen, R. P. *et al.* Hyperpolarized (129)Xe for investigation of mild cystic fibrosis lung disease in pediatric patients. *J Cyst Fibros* **16**, 275-282, doi:10.1016/j.jcf.2016.07.008 (2017).
- 258 Marshall, H. *et al.* Detection of early subclinical lung disease in children with cystic fibrosis by lung ventilation imaging with hyperpolarised gas MRI. *Thorax* **72**, 760-762, doi:10.1136/thoraxjnl-2016-208948 (2017).
- 259 Kanhere, N. *et al.* Correlation of Lung Clearance Index with Hyperpolarized (129)Xe Magnetic Resonance Imaging in Pediatric Subjects with Cystic Fibrosis. *Am J Respir Crit Care Med* **196**, 1073-1075, doi:10.1164/rccm.201611-2228LE (2017).
- 260 Smith, L. *et al.* Longitudinal Assessment of Children with Mild Cystic Fibrosis Using Hyperpolarized Gas Lung Magnetic Resonance Imaging and Lung Clearance Index. *American Journal of Respiratory and Critical Care Medicine* **197**, 397-400, doi:10.1164/rccm.201705-0894LE (2018).
- 261 Wang, Z. *et al.* A Real-Time Centralized Pipeline for Reconstructing and Quantifying Hyperpolarized 129Xe Gas Exchange MRI. *Proceeding of ISMRM*, 1728 (2019).
- 262 Guo, F. *et al.* Development of a pulmonary imaging biomarker pipeline for phenotyping of chronic lung disease. *J Med Imaging (Bellingham)* **5**, 026002, doi:10.1117/1.JMI.5.2.026002 (2018).
- 263 Saam, B. T. *et al.* MR imaging of diffusion of 3He gas in healthy and diseased lungs. *Magn Reson Med* **44**, 174-179, doi:10.1002/1522-2594(200008)44:2<174::aid-mrm2>3.0.co;2-4 (2000).
- 264 Wang, Z. *et al.* Using hyperpolarized (129)Xe gas-exchange MRI to model the regional airspace, membrane, and capillary contributions to diffusing capacity. *J Appl Physiol (1985)* **130**, 1398-1409, doi:10.1152/jappphysiol.00702.2020 (2021).
- 265 Tseng, C. H. *et al.* NMR of laser-polarized 129Xe in blood foam. *J Magn Reson* **126**, 79-86, doi:10.1006/jmre.1997.1145 (1997).
- 266 Hogg, J. C. *et al.* The Nature of Small-Airway Obstruction in Chronic Obstructive Pulmonary Disease. *N Engl J Med* **350**, 2645-2653, doi:10.1056/NEJMoa032158 (2004).
- 267 Berg, K. & Wright, J. L. The Pathology of Chronic Obstructive Pulmonary Disease: Progress in the 20th and 21st Centuries. *Archives of Pathology & Laboratory Medicine* **140**, 1423-1428, doi:10.5858/arpa.2015-0455-RS (2016).
- 268 Leopold, J. G. & Gough, J. The centrilobular form of hypertrophic emphysema and its relation to chronic bronchitis. *Thorax* **12**, 219-235, doi:10.1136/thx.12.3.219 (1957).
- 269 Ochs, M. & Mühlfeld, C. Quantitative microscopy of the lung: a problem-based approach. Part 1: basic principles of lung stereology. *Am J Physiol Lung Cell Mol Physiol* **305**, L15-22, doi:10.1152/ajplung.00429.2012 (2013).
- 270 Ley, S. *et al.* Functional evaluation of emphysema using diffusion-weighted 3Helium-magnetic resonance imaging, high-resolution computed tomography, and lung function tests. *Invest Radiol* **39**, 427-434, doi:10.1097/01.rli.0000129468.79005.1d (2004).

- 271 Hogg, J. C. Pathophysiology of airflow limitation in chronic obstructive pulmonary
disease. *Lancet* **364**, 709-721, doi:10.1016/s0140-6736(04)16900-6 (2004).
- 272 Kudo, M., Ishigatsubo, Y. & Aoki, I. Pathology of asthma. *Front Microbiol* **4**, 263-263,
doi:10.3389/fmicb.2013.00263 (2013).
- 273 Chen, X. J. *et al.* Spatially resolved measurements of hyperpolarized gas properties in the
lung in vivo. Part I: diffusion coefficient. *Magn Reson Med* **42**, 721-728,
doi:10.1002/(sici)1522-2594(199910)42:4<721::aid-mrm14>3.0.co;2-d (1999).
- 274 Kirby, M. *et al.* Chronic obstructive pulmonary disease: longitudinal hyperpolarized (3)He
MR imaging. *Radiology* **256**, 280-289, doi:10.1148/radiol.10091937 (2010).
- 275 Chan, H. F. *et al.* Airway Microstructure in Idiopathic Pulmonary Fibrosis: Assessment at
Hyperpolarized (3)He Diffusion-weighted MRI. *Radiology* **291**, 223-229,
doi:10.1148/radiol.2019181714 (2019).
- 276 Walkup, L. L. *et al.* Cyst Ventilation Heterogeneity and Alveolar Airspace Dilation as
Early Disease Markers in Lymphangiomyomatosis. *Ann Am Thorac Soc* **16**, 1008-
1016, doi:10.1513/AnnalsATS.201812-880OC (2019).
- 277 Spoel, M. *et al.* Pulmonary ventilation and micro-structural findings in congenital
diaphragmatic hernia. *Pediatric Pulmonology* **51**, 517-524,
doi:https://doi.org/10.1002/ppul.23325 (2016).
- 278 Flors, L. *et al.* Hyperpolarized Helium-3 Diffusion-weighted Magnetic Resonance Imaging
Detects Abnormalities of Lung Structure in Children With Bronchopulmonary Dysplasia.
J Thorac Imaging **32**, 323-332, doi:10.1097/rti.0000000000000244 (2017).
- 279 Morbach, A. E. *et al.* Diffusion-weighted MRI of the lung with hyperpolarized helium-3:
a study of reproducibility. *J Magn Reson Imaging* **21**, 765-774, doi:10.1002/jmri.20300
(2005).
- 280 Stewart, N. J. *et al.* Experimental validation of the hyperpolarized (129) Xe chemical shift
saturation recovery technique in healthy volunteers and subjects with interstitial lung
disease. *Magn Reson Med* **74**, 196-207, doi:10.1002/mrm.25400 (2015).
- 281 Stewart, N. J. *et al.* Reproducibility of quantitative indices of lung function and
microstructure from (129) Xe chemical shift saturation recovery (CSSR) MR spectroscopy.
Magn Reson Med **77**, 2107-2113, doi:10.1002/mrm.26310 (2017).
- 282 Chang, Y. V. MOXE: A model of gas exchange for hyperpolarized 129Xe magnetic
resonance of the lung. *Magn Reson Med* **69**, 884-890,
doi:https://doi.org/10.1002/mrm.24304 (2013).
- 283 Weatherley, N. D. *et al.* Hyperpolarised xenon magnetic resonance spectroscopy for the
longitudinal assessment of changes in gas diffusion in IPF. *Thorax* **74**, 500-502,
doi:10.1136/thoraxjnl-2018-211851 (2019).
- 284 Couch, M. J. *et al.* A two-center analysis of hyperpolarized 129Xe lung MRI in stable
pediatric cystic fibrosis: Potential as a biomarker for multi-site trials. *Journal of Cystic
Fibrosis* **18**, 728-733, doi:https://doi.org/10.1016/j.jcf.2019.03.005 (2019).
- 285 Stewart, N. J., Norquay, G., Griffiths, P. D. & Wild, J. M. Feasibility of human lung
ventilation imaging using highly polarized naturally abundant xenon and optimized three-
dimensional steady-state free precession. *Magn Reson Med* **74**, 346-352,
doi:https://doi.org/10.1002/mrm.25732 (2015).
- 286 Kooner, H. K. *et al.* (129)Xe MRI ventilation defects in ever-hospitalised and never-
hospitalised people with post-acute COVID-19 syndrome. *BMJ Open Respir Res* **9**,
doi:10.1136/bmjresp-2022-001235 (2022).

- 287 Li, H. *et al.* Damaged lung gas exchange function of discharged COVID-19 patients detected by hyperpolarized (129)Xe MRI. *Sci Adv* **7**, doi:10.1126/sciadv.abc8180 (2021).
- 288 Grist, J. T. *et al.* Lung Abnormalities Depicted with Hyperpolarized Xenon MRI in Patients with Long COVID. *Radiology*, 220069, doi:10.1148/radiol.220069 (2022).

Appendix B – Hyperpolarized Gas Magnetic Resonance Imaging Texture Analysis and Machine Learning to explain Accelerated Lung Function Decline in Ex-smokers with and without COPD

In this proof-of-concept study, we developed and evaluated a novel MRI ventilation measurement alongside texture features to predict ex-smokers with and without COPD that will experience an accelerated lung function decline across 3-years.

*The contents of this appendix were previously published in the proceedings of the international society for optics and photonics (SPIE): M Sharma, AR Westcott, DG McCormack and G Parraga. Hyperpolarized gas magnetic resonance imaging texture analysis and machine learning to explain accelerated lung function decline in ex-smokers with and without COPD. Proc. SPIE 11600, Medical Imaging 2021: Biomedical Applications in Molecular, Structural, and Functional Imaging, 116000E (14 February 2021). <https://doi.org/10.1117/12.2580451>. Permission to reproduce this article is provided in **Appendix D**.*

INTRODUCTION

Pulmonary hyperpolarized ^3He gas magnetic resonance imaging (MRI) provides a way to quantify ventilation abnormalities using ventilation defect percent (VDP)¹ that stem from abnormalities in the large and small airways as well as emphysema.² It is difficult to predict those with obstruction measured using forced expiratory volume in 1 s (FEV_1) that will worsen to Chronic Obstructive Pulmonary Disease (COPD). MRI-VDP measurements were previously shown to progressively worsen in FEV_1 stable patients and predict worse outcomes over short time-periods.^{3,4} While spirometry measurements of lung function are straightforward and cost-efficient to implement, they do not provide information about the small airways, which are believed to drive COPD pathogenesis. In contrast, MRI VDP,¹ has been shown to predict COPD exacerbations⁵ and longitudinal changes in quality of life as well as exercise capacity.⁶ Despite these advantages, current predictive models of COPD progression are usually based on clinical measurements but none incorporate information derived from pulmonary computed tomography (CT)⁷ or MRI.⁵

Texture analysis provides a unique opportunity to reveal and quantify hyperpolarized ^3He MRI ventilation patchiness. This approach shows promise for data classification,⁸ tumor segmentation,⁹ image registration¹⁰ and outcome predictions.¹¹ Since VDP measurements do not fully exploit the full information and spatial content that is inherent to hyperpolarized gas MRI, our main objective was to develop a novel texture-based machine-learning model to identify ventilation features that can predict patients with accelerated annual FEV_1 decline. To achieve this we tested multiple single and ensemble classifiers to determine the best model for predicting COPD patients who would experience an FEV_1 decline $>30\text{ml/year}$ ¹² over a three year period. Such predictive models may serve as tools for an early detection of rapidly-progressing patients and facilitate timely treatment for this subgroup of patients that are at a higher risk of progressing to a greater disease severity.

MATERIALS AND METHODS

Study participants and image acquisition

Pipeline performance was evaluated using 42 subjects with and without COPD diagnosis including at-risk ex-smokers and elderly never-smokers that provided informed written consent to a study protocol approved by research ethics board and Health Canada.¹³ Inclusion criteria were a history of cigarette smoking >10 pack years, age between 50 and 85 years at baseline. Ex-smoker participants had ceased smoking ≥ 1 -year prior to the study visit with no cut-off in terms of ceasing smoking. COPD subjects were classified according to the Global Initiative for Chronic Obstructive Lung Disease (GOLD) grades.¹⁴ Long-term follow-up was prospectively planned for 24 ± 6 months and 120 ± 12 months after the baseline visit.¹³ ^1H and ^3He MRI was performed on a 3T whole-body system (MR750 Discovery, GEHC, Milwaukee, WI) as previously described.¹³ The consort diagram for the TINCan study cohort participants is shown in Figure 1 below.

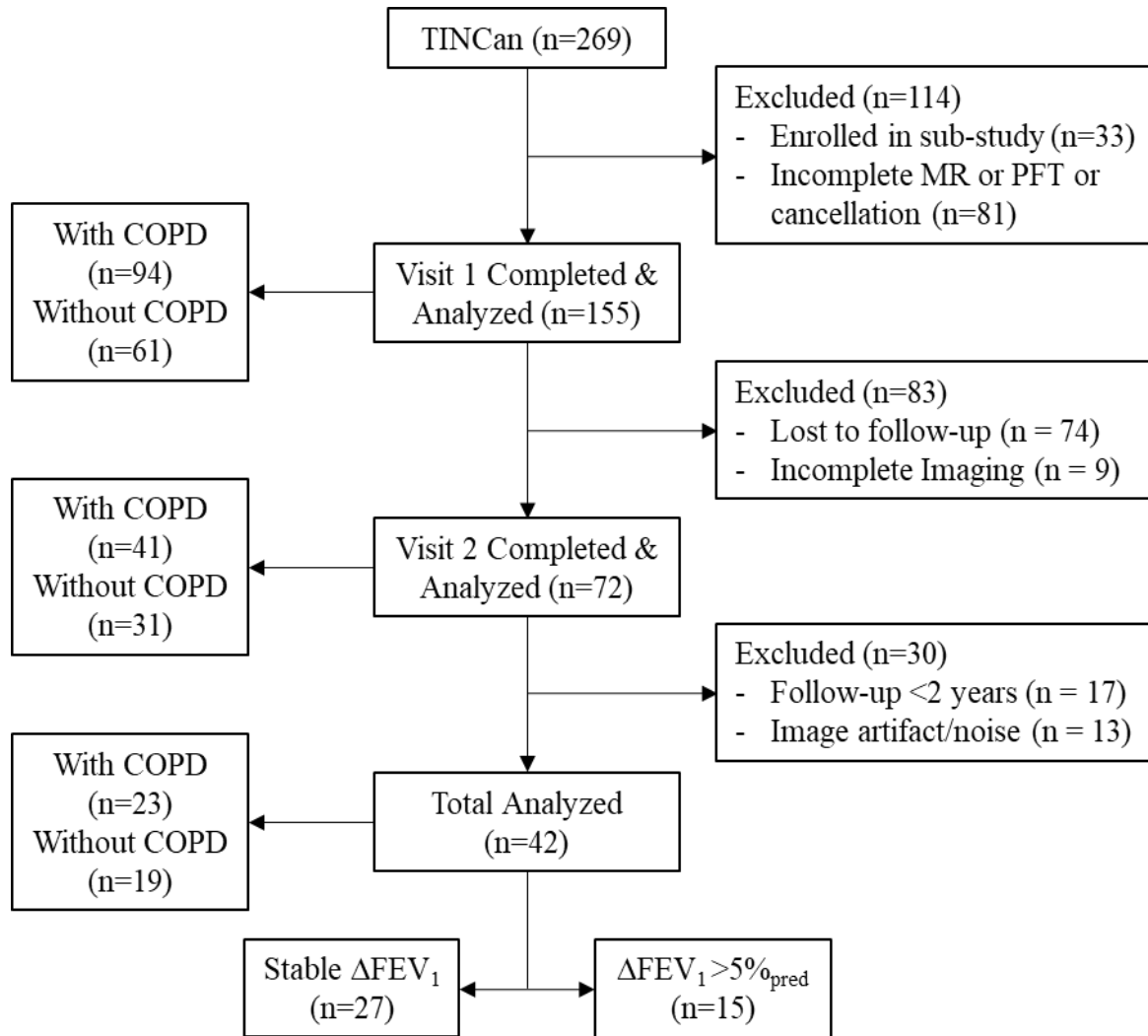


Figure 1. Consort diagram for participants from the TINCan study cohort (January 2010–February 2017).

Proposed extraction pipeline

The proposed pipeline is summarized in Figure 2. First we generate a maximum entropy mask by segmenting the ^3He ventilation image as previously described.¹ We then use a custom-built algorithm to calculate ventilation defect clusters and PyRadiomics platform¹⁵ for extracting texture features. The data was split into a 70% training set, a 15% validation set and the remaining 15% was used as the testing set. Feature selection was performed on the training set using principle component analysis (PCA) and logistic regression to determine significant features contributing to the machine learning models. Significant features were tested and applied to final machine learning predictive models from the validation set. The performance of machine learning algorithms in the 5-fold cross validation training and testing set were evaluated and compared via receiver operating characteristic curves.

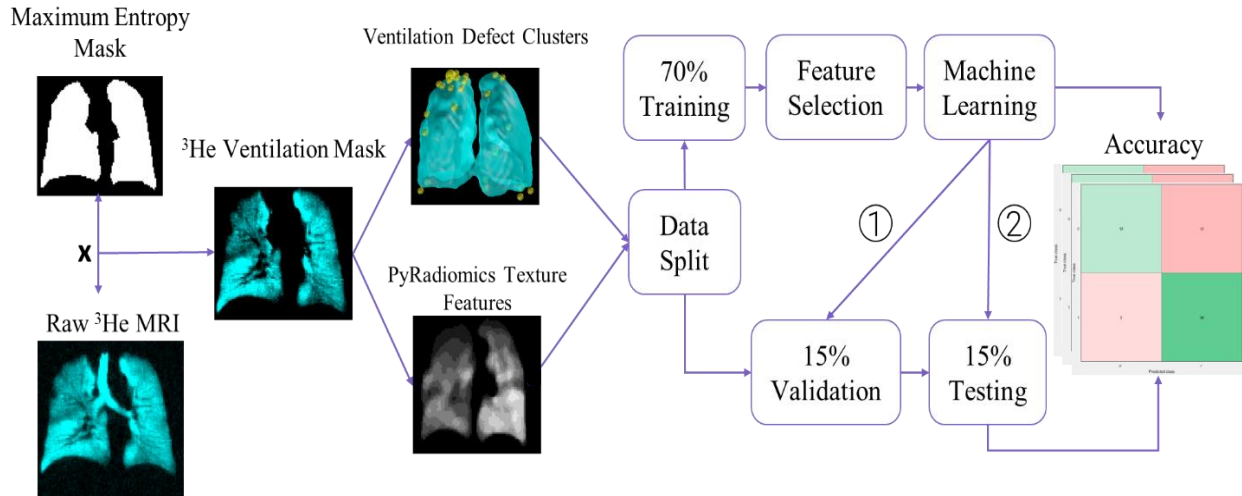


Figure 2. Overview of the proposed texture-based image processing pipeline for hyperpolarized gas MRI.

Image analysis and custom algorithm

^1H and ^3He MR images were segmented by a single observer where the thoracic cavity was segmented from the ^1H images using a seeded region-growing algorithm, and the ^3He ventilation was segmented using k-means clustering.¹ The generated maximum entropy mask was then applied to identify the ventilated region of interest (ROI) for feature extraction.

Ventilation-defect-percent (VDP) was generated by a semi-automated segmentation using a custom-built software, as previously described.¹ Ventilation-defect-cluster-percent (VDCP) was generated by an automated custom-built algorithm that was previously presented at an international conference.¹⁶ The approach was implemented using a naïve greedy algorithm where $S = [b_1, b_2, \dots, b_n]$ is a set with n elements, where each element $b_n = B_n(r, l)$ is an open sphere of radius r at locations l . Determining the required minimum number of spheres of unequal sizes resulted in the following minimization problem:

$$\min_S \{ \|S\|_0 \} : S \in \mathbf{R}^n \quad (1)$$

Where the cardinality of the set S and $\forall (b \in S) \exists (r, l)$ is minimized. To ensure that the spheres completely fill the region of interest R , (ventilation defect) a constraint was implemented so that the intersection between the region filled with spheres R and the spheres b is just b and to prevent overlap between two spheres (b and b'), this was set to result in the null set:

$$b \cap R = b \quad \& \quad b \cap b' = \emptyset \quad (2)$$

A volume constraint was also imposed so that the total volume of spheres was equal to the volume of the specified region R :

$$\sum_{b \in S} V(b) = V(R) \quad (3)$$

We then used MATLAB R2019a (MathWorks) to solve the minimization problem and generated VDCP, which is the sum of ventilation-defect cluster volume normalized to the total lung volume. From VDCP we calculated cluster-defect-diameter voxel size one (CDD1) which is the cumulative number of defect clusters of one voxel ($5 \times 5 \times 5 \text{ mm}^3$), shown in Figure 3 below. Low ventilation cluster (LVC) slopes were also calculated based on the log-log relationship between the cumulative number of spheres and cluster size (LVC).¹⁷

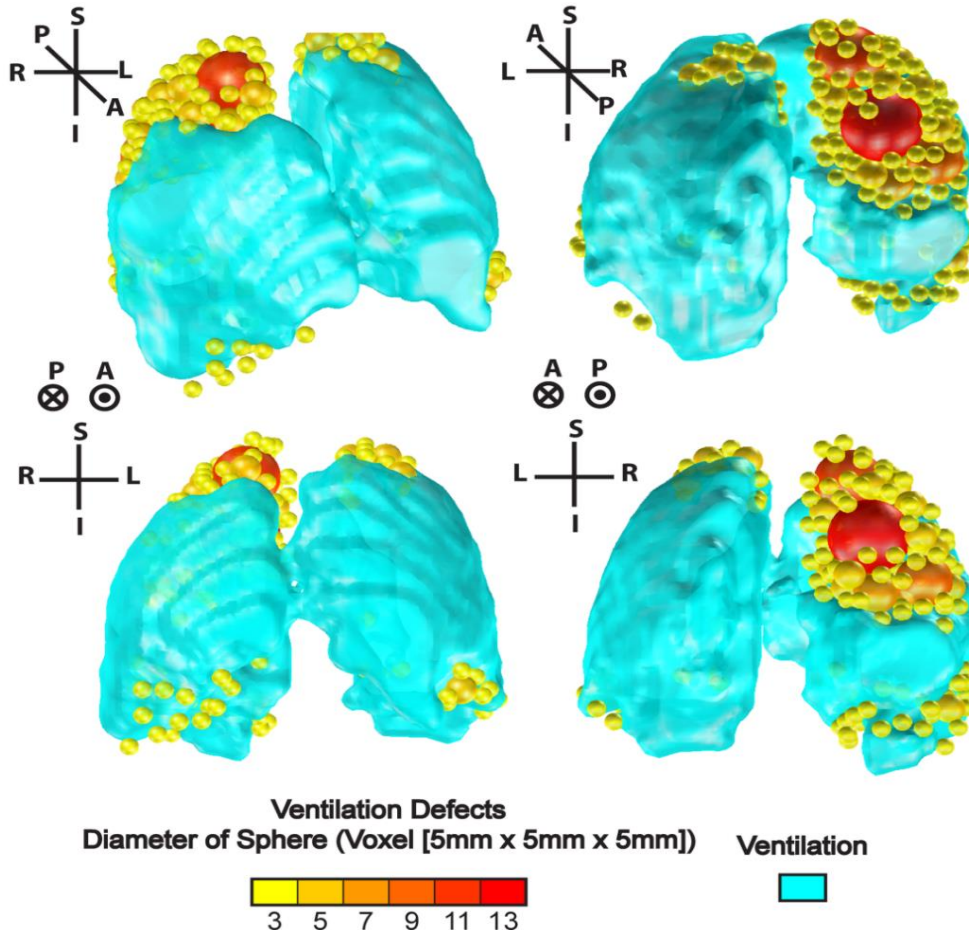


Figure 3. Ventilation defect cluster volume output from custom-built algorithm in MATLAB (R2019a).

Further texture feature extraction was conducted using a well-tested radiomic software called PyRadiomics, detailed in the next section. We utilized all available higher-order texture features as well as wavelet band-pass filtering features that were available in the PyRadiomics platform (version 2.2.0) and the detailed mathematical descriptions of all the features are provided online.¹⁵

Feature extraction and Statistics

Texture features were calculated and extracted from gray-level histograms and the gray-level matrices generated from the ROI of the original image. We evaluated first-order texture features from the gray-level histogram such as mean, range, minimum, standard deviation, etc. We also evaluated the texture features calculated from run-length, gap-length, size-zone, dependence and co-occurrence matrices using the open-sourced PyRadiomics platform (version 2.2.0) in Python environment.¹⁵ Image filters were also applied for the extraction of wavelet band-pass filtering texture features that further quadrupled the number of extracted features due to permutations of high-pass and low-pass filters for wavelet decomposition, resulting in 368 additional texture features. Low-pass filtering in both directions (LL)

assesses the lowest frequencies, low-pass filtering followed by high-pass filtering (LH) assesses horizontal edges, high-pass filtering followed by low-pass filtering (HL) assesses vertical edges and high-pass filtering in both directions (HH) assesses diagonal details.⁸ The resulting 474 features underwent PCA and forward selection logistic regression analysis to identify factors contributing to the predictive power of the models and for simultaneously generating components that comprised from a combination of texture features with a commonality. Shapiro-Wilk tests were used to determine the normality of the data and non-parametric tests were performed for not normally distributed data. Differences between subject groups were determined using analysis of variance (ANOVA) with post-hoc analysis using the Benjamini-Hochberg correction. The relationship between measurements was determined using Pearson and Spearman coefficients for parametric and nonparametric data, respectively. Results were considered significant when the probability of two-tailed type I error was less than 5% ($p < .05$). All of the statistical analysis was performed using SPSS Statistics v26.0 (SPSS Inc., Chicago, Illinois, USA).

Machine learning algorithms

The entire texture dataset was randomly split into training/validation/testing sets in 70/15/15 percent distribution. Once all the features were extracted and selected, 5-fold cross-validation training was performed using a number of machine learning algorithms including four types of single classifiers and four ensemble classifiers in an attempt to determine best model for identifying accelerated disease progression. The data were standardized and hyper-parameter optimization was performed through MATLAB R2019a (Classification Learner Application) for each model individually. We compared the performance of multiple machine learning algorithms including variations of: Naïve Bayes,¹⁸ Support Vector Machines,¹⁹ Decision trees,²⁰ K-nearest neighbours,²¹ and four ensemble-classifiers: bagged trees²² subspace discriminant,²³ subspace K-nearest-neighbours (subspace KNN),²³ and Random Under-Sampling Boosted Trees (RUSBoosted). Model performance was evaluated using the mean cross-validation area under the receiver-operator curve (AUC), as well as sensitivity and specificity using the confusion matrix outputs.

RESULTS

Subject demographics and significant features

We evaluated 42 participants who were ex-smokers including 23 participants with spirometry evidence of COPD and 19 with no spirometry evidence of COPD. As shown in Table 1, 27 participants (9 Females/18 Males, 66±7 years) reported stable FEV₁ decline and 15 participants (5 Females/10 Males, 71±8 years) reported a rapid decline in FEV₁ greater than -30ml/year, or about -5%_{pred} decline, between baseline and follow-up visit 30 ± 8 months later. There were 11 significantly different texture features out of 120 unique extracted features and only four of them significantly contributed to the accuracy of the models. The p-value was corrected using the Mann-Whitney U test and also corrected for false discovery rate using the Benjamini-Hochberg correction. The dichotomized group differences and significantly different texture features that also contributed to the machine-learning models are shown in Table 1.

Table 1. Demographics and texture features by subgroup.

Parameter Mean (±SD)	Stable FEV ₁ (n=27)	Change in FEV ₁ >5% (n=15)	Sig. Difference (p-value)
Age	66 (7)	71 (8)	0.64
# Females (%)	9 (30)	5 (33)	ND
Pack Years	49 (29)	50 (27)	0.79
BMI kg/m ²	28.1 (3.8)	28.3 (4.5)	0.65
FEV ₁ % _{pred}	82 (25)	71 (25)	0.16
FEV ₁ /FVC % _{pred}	85 (22)	77 (25)	0.09
DLCO % _{pred}	66 (20)	59 (22)	0.06
³ He VDP %	11 (8)	16 (9)	0.03
CDD1	4935 (1000)	7293 (1000)	<0.01
FO-Minimum	85 (57)	48 (41)	0.03
SZM-LGLZE	0.0003(0.0002)	0.0004(0.0002)	0.04
RLM-Run Percentage	0.997 (0.009)	0.985 (0.009)	0.05

BMI=Body Mass Index; FVC=Forced Vital Capacity; DL_{CO}=Diffusing capacity of lung for Carbon-monoxide; ³He-VDP=ventilation defect percent; CDD1=Cluster defect diameter size 1 voxel; FO =First-Order features; SZM =Size-Zone Matrix; LGLZE = Low Gray Level Zone Emphasis; RLM =Run Length Matrix.

Feature selection and component generation

Feature extraction was performed using a custom-built algorithm as well as PyRadiomics.¹⁵ All the extracted features underwent PCA followed by forward selection multivariate logistic regression analysis for determination of significantly different features. PCA was used to generate component scores for each subject, where the emergent components consist of factor loadings from original texture features and the first 7 components explained >90% of the variance in the entire data set, shown in Table 2. The emergent components were orthogonal to one another and were designed so as to maximize their own factor loadings while minimizing it for other components. A score was also generated for each of the components on a per patient basis and resulting components #1 and #6 contributed to model prediction accuracy, in addition to texture features shown in Table 1.

Table 2. Resultant components from orthogonally rotated correlation matrix from PCA (SPSS).

Texture Features	Component						
	1	2	3	4	5	6	7
SALGLE	0.931	0.321	-0.045	-0.101	-0.011	-0.088	-0.026
LGLZE	0.930	0.320	-0.046	-0.101	-0.013	-0.093	-0.023
SDLGLE	0.930	0.322	-0.043	-0.107	-0.008	-0.086	-0.032
Autocorrelation	0.930	0.320	-0.046	-0.103	-0.014	-0.090	-0.024
Zone Variance	-0.291	-0.935	0.074	0.055	0.033	0.007	-0.015
LAE	-0.333	-0.924	0.081	0.066	0.027	-0.010	-0.027
Maximum Probability	-0.219	-0.918	0.004	0.044	0.062	0.170	-0.063
SZNU	-0.007	0.158	0.972	0.067	0.097	-0.062	-0.033
DNU	-0.135	-0.131	0.961	0.089	0.106	-0.068	0.035
RLNU	0.039	0.228	0.959	0.054	0.097	-0.055	0.027
Idm	-0.166	-0.364	0.267	0.804	0.029	-0.073	0.111
Idmn	-0.229	-0.265	0.325	0.785	0.055	-0.103	0.028
Cluster Shade	0.356	0.237	-0.089	0.692	-0.065	0.370	0.012
Maximum2DDiameterSlice	-0.138	0.001	0.223	0.047	0.869	0.122	0.111
Maximum3DDiameter	-0.134	0.055	0.195	0.026	0.820	0.065	0.077
Flatness	-0.017	-0.065	0.359	0.025	-0.799	-0.103	0.056
Sphericity	0.138	0.098	0.014	-0.142	-0.269	-0.892	0.043
Surface Volume Ratio	-0.046	0.037	-0.376	0.067	0.189	0.857	-0.078
Correlation	0.092	-0.317	0.091	0.440	-0.380	-0.184	0.607

SALGLE =Small Area Low GrayLevel Emphasis; LGLZE =Low GrayLevel Zone Emphasis; SDLGLE =Small- Dependence Low GrayLevel Emphasis; LAE =Large Area Emphasis; DNU =Dependence Non-Uniformity; RLNU =Run Length Non-Uniformity; SZNU =Size Zone Non-Uniformity; Idm =Inverse Difference Moment. The bolded values show highest factor loadings that explain and constitute the underlying component.

Machine learning models

The entire extracted texture data was randomly split into training/validation/testing sets in 70/15/15 percent distribution. Once all the features were extracted and selected, a 5-fold cross-validation training was performed using four types of single classifiers and four ensemble classifiers, with their prediction performances shown in Table 3 below. The ensemble classifiers outperformed single classifiers, with Bagged trees algorithm providing nearly 85% classification accuracy. The bagged-trees model was the most sensitive, specific and had the best AUC metric out of all tested models and is depicted in Figure 4. Multi-variate modelling revealed that CDD1, FO-Minimum, LGLZE and Run Percentage features are significant contributors to predictions of a clinically relevant change in FEV₁ in these ex-smokers.

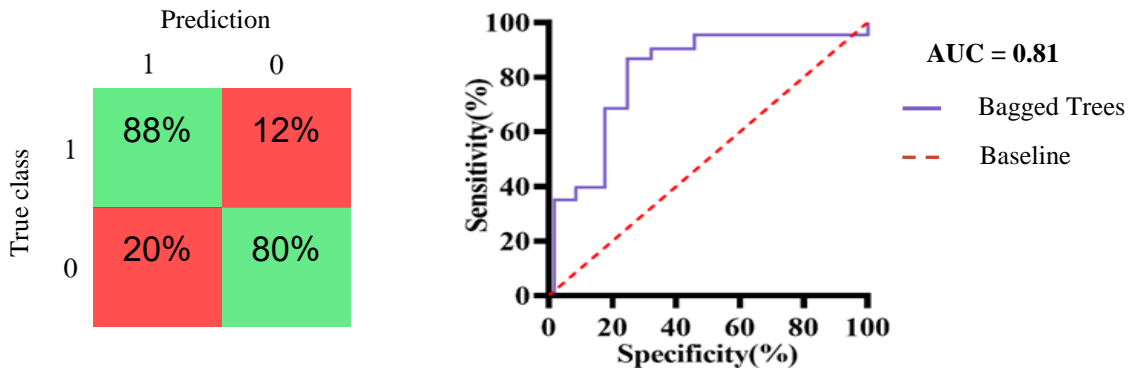


Figure 4. ROC curve and confusion matrix of the best performing model utilizing bagged-trees.

Table 3. Performance of single and ensemble machine-learning models trained using all selected texture features.

Model Name (n =10)	AUC	Sensitivity (%)	Specificity (%)	Accuracy (%)
Logistic Regression	0.76	83.6	75.0	81.4
Decision Trees*	0.53	75.0	0	75.0
Naïve Bayes	0.63	78.3	42.8	66.3
Medium KNN	0.75	78.3	75.0	77.9
Bagged Trees	0.81	87.5	80.0	84.6
Boosted Trees	0.73	78.3	54.6	77.9
Subspace Discriminant	0.72	74.1	63.6	73.7
Subspace KNN	0.79	80.0	75.0	78.3
RUSBoosted Trees	0.63	78.3	21.4	76.7
Fine Gaussian SVM	0.73	83.6	66.6	79.1

AUC = Area under the receiver-operating curve; RUS = Random Under Sampling; KNN = K-Nearest Neighbours; SVM = Support Vector Machines; *indicates classifiers that simply predicted all subjects as one class.

Alternative predictive models were also tested using only the emergent components as inputs to the machine learning algorithms. The resultant model classification accuracy was lower than using the selected texture features individually. Addition of generated components to extracted texture feature increased the model performance with components #1 and #6 selected as significant predictors. The highest performance achieved by models trained on PCA components was Medium-KNN with a 75.6% accuracy and AUC of 0.70 as shown in Table 4 below.

Table 4. Performance of single and ensemble machine-learning models trained only on selected PCA components.

Model Name (n =10)	AUC	Sensitivity (%)	Specificity (%)	Accuracy (%)
Logistic Regression	0.68	74.1	40.5	70.9
Decision Trees*	0.56	75.0	0	75.0
Naïve Bayes	0.66	74.1	36.3	69.8
Medium KNN	0.70	78.3	56.5	75.6
Bagged Trees	0.65	78.3	43.2	73.7
Boosted Trees	0.58	72.3	10.0	66.3
Subspace Discriminant	0.62	74.1	17.0	69.8
Subspace KNN	0.67	80.0	40.5	73.7
RUSBoosted Trees	0.63	75.0	34.3	62.8

AUC = Area under the receiver-operating curve; RUS = Random Under Sampling; KNN = K-Nearest Neighbours; SVM = Support Vector Machines; *indicates classifiers that simply predicted all subjects as one class.

Correlations with clinical measurements

The texture features identified as significant predictors of clinically relevant FEV₁ changes were correlated with well-established clinical measurements. Spearman's correlations between the hyperpolarized ³He MRI and pulmonary function measurements with a sample texture feature of GLSZM-LGLZE are shown in Figure 5 below. All other significant texture features except FO-Minimum, provided weak-to-moderate correlations ($r=0.2-0.5$, $p<.05$) with the established clinical measurements. The generated texture components #1 and #6 from PCA did not show significant correlations with majority of the clinically relevant measurements shown below.

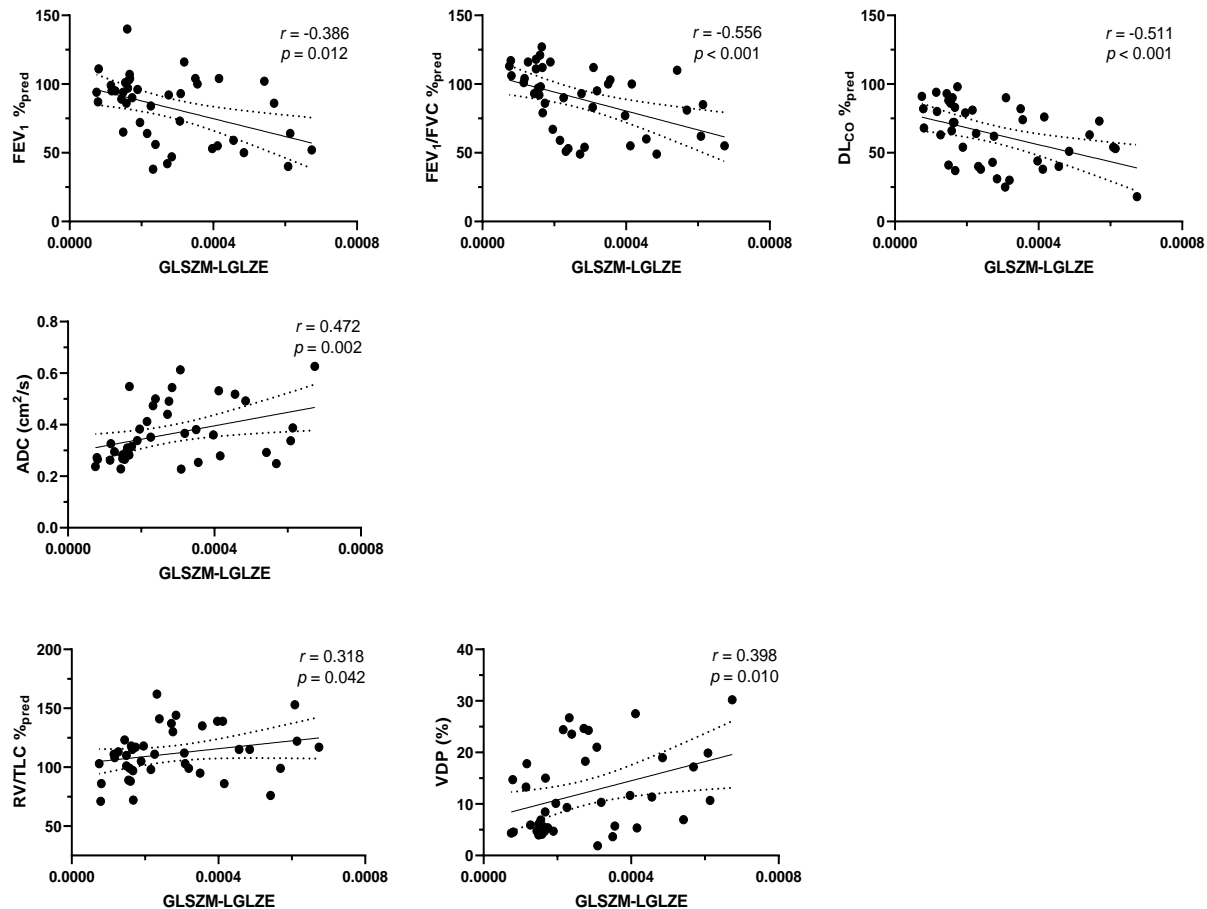


Figure 5. Spearman correlations of LGLZE texture feature with MRI and lung function measurements.

NEW OR BREAKTHROUGH WORK TO BE PRESENTED

For the first time, machine learning and texture features from hyperpolarized ³He MRI ventilation images were used to predict ex-smokers who would experience accelerated FEV₁ decline over a short three-year period. This is an important first step in generating predictive models of pulmonary function decline in ex-smokers with and without COPD, which has not been possible so far.

DISCUSSION AND CONCLUSION

In this study, we developed a pipeline to identify unique texture features residing within hyperpolarized ^3He MR ventilation images in order to identify ex-smokers at risk of accelerated lung function decline. While model test accuracy was moderate, sensitivity remained high, which underscores the potential of this approach and hyperpolarized noble gas MRI. Standard MRI-derived measurements were outperformed by MRI-derived texture features during the feature selection step. From Tables 3 & 4, using individual texture features for training has generated a superior predictive model (85%) compared to models including only generated components from PCA (76%). Extracted CDD1 feature reflects the cumulative number of defect clusters of one voxel ($5 \times 5 \times 5 \text{mm}^3$) and described defect clusters ~ 1 voxel, and of low gray-level, or small to no signal, based on the values and equations¹⁵ of extracted FO-minimum, LGLZE and run percentage texture features which were all significant predictors of accelerated FEV₁ decline in ex-smokers. Features extracted directly from the original images were correlated with well-established clinical measurements shown using LGLZE texture feature in Figure 5. All higher-order texture features significantly correlated with these clinically relevant measurements, whereas the first-order statistical features and the generated components #1 and #6 did not show correlations, suggesting that higher-order features can potentially become imaging markers that can significantly correlate and independently predict clinically relevant endpoints.

Future work will include a more robust analysis of extraction parameters and relative stability of extracted textures, using a larger and more heterogeneous dataset to improve performance and clinical efficacy of the pipeline. The developed algorithms use a computationally expensive optimization approach through the naïve greedy algorithm, whereas alternatives such as dynamic parallel processing²⁴ will also be explored. We will implement Boruta analysis for the feature selection step and also compare multiple feature selection approaches to increase the classification accuracy of the machine-learning models. Boruta analysis uses a random forest classifier for performing iterations of features considered all together and also uses a two-step correction for multiple testing. This allows all features that carry information usable for prediction to be identified, rather than finding a potential compact subset of features for which classifiers have minimal error.

REFERENCES

- [1] Kirby, M. *et al.* "Hyperpolarized ^3He magnetic resonance functional imaging semiautomated segmentation." *Acad Radiol* **19**, 141-152, doi:10.1016/j.acra.2011.10.007 (2012).
- [2] Saam, B. T. *et al.* "MR imaging of diffusion of ^3He gas in healthy and diseased lungs." *Magn Reson Med* **44**, 174-179 (2000).
- [3] Kirby, M. *et al.* "Chronic obstructive pulmonary disease: longitudinal hyperpolarized ^3He MR imaging." *Radiology* **256**, 280-289 (2010).
- [4] Kirby, M. *et al.* "MRI ventilation abnormalities predict quality-of-life and lung function changes in mild-to-moderate COPD: longitudinal TINCan study." *Thorax*, thoraxjnl-2016-209770 (2017).
- [5] Kirby, M., Pike, D., Coxson, H. O., McCormack, D. G. & Parraga, G. "Hyperpolarized (^3He) ventilation defects used to predict pulmonary exacerbations in mild to moderate chronic obstructive pulmonary disease." *Radiology* **273**, 887-896, doi:10.1148/radiol.14140161 (2014).
- [6] Kirby, M. *et al.* "Chronic obstructive pulmonary disease: longitudinal hyperpolarized (^3He) MR imaging." *Radiology* **256**, 280-289, doi:10.1148/radiol.10091937 (2010).
- [7] González, G. *et al.* "Disease staging and prognosis in smokers using deep learning in chest computed tomography." *Am J Respir Crit Care Med* **197**, 193-203 (2018).
- [8] Rastegar, S. *et al.* "Radiomics for classification of bone mineral loss: A machine learning study." *Diagn Interv Imaging*, doi:10.1016/j.diii.2020.01.008 (2020).
- [9] Bayramoglu, N., "Tiulpin, A., Hirvasniemi, J., Nieminen, M. T. & Saarakkala, S. Adaptive Segmentation of Knee Radiographs for Selecting the Optimal ROI in Texture Analysis." *Osteoarthritis Cartil* doi:10.1016/j.joca.2020.03.006 (2020).
- [10] Yip, S. S. *et al.* "Use of registration-based contour propagation in texture analysis for esophageal cancer pathologic response prediction." *Phys Med Biol* **61**, 906-922, doi:10.1088/0031-9155/61/2/906 (2016).
- [11] Chaddad, A., Sabri, S., Niazi, T. & Abdulkarim, B. "Prediction of survival with multi-scale radiomic analysis in glioblastoma patients." *Med Biol Eng Comput* **56**, 2287-2300, doi:10.1007/s11517-018-1858-4 (2018).

- [12] Lee, P. N. & Fry, J. S. "Systematic review of the evidence relating FEV1 decline to giving up smoking." *BMC Med* **8**, 84, doi:10.1186/1741-7015-8-84 (2010).
- [13] Kirby, M. *et al.* "Longitudinal Computed Tomography and Magnetic Resonance Imaging of COPD: Thoracic Imaging Network of Canada (TINCan) Study Objectives." *Chronic Obstr Pulm Dis* **1**, 200-211, doi:10.15326/jcopdf.1.2.2014.0136 (2014).
- [14] Vestbo, J. *et al.* "Global strategy for the diagnosis, management, and prevention of chronic obstructive pulmonary disease: GOLD executive summary." *Am J Respir Crit Care Med* **187**, 347-365, doi:10.1164/rccm.201204-0596PP (2013).
- [15] van Griethuysen, J. J. M. *et al.* "Computational Radiomics System to Decode the Radiographic Phenotype." *Cancer Research* **77**, e104-e107, doi:10.1158/0008-5472.can-17-0339 (2017).
- [16] Capaldi, D. P. *et al.* "MRI Measurements of Regional Ventilation Heterogeneity: Ventilation Defect Clusters " *Proc. ISMRM* **23**, 3969-3992 (2015).
- [17] Mishima, M. *et al.* "Complexity of terminal airspace geometry assessed by lung computed tomography in normal subjects and patients with chronic obstructive pulmonary disease." *Proceedings of the National Academy of Sciences of the United States of America* **96**, 8829-8834 (1999).
- [18] Webb, G. I., [Encyclopedia of Machine Learning], Springer US, 713-714 (2010).
- [19] Cristianini, N. and Ricci, E., [Encyclopedia of Algorithms], Springer US, 928-932 (2008).
- [20] Quinlan, J. R. "Induction of decision trees." *Mach Learn* **1**, 81-106 (1986).
- [21] Cover, T. & Hart, P. "Nearest neighbor pattern classification." *IEEE Trans. Inf. Theory* **13**, 21-27 (1967).
- [22] Breiman, L. "Bagging predictors." *Mach Learn* **24**, 123-140 (1996).
- [23] Hastie, T. & Tibshirani, R., "Discriminant adaptive nearest neighbor classification and regression." *Proc. Adv Neural Inf Process Syst.* **8**, 409-415 (1995).
- [24] He, S. *et al.* "Dataset for reservoir impoundment operation coupling parallel dynamic programming with importance sampling and successive approximation." *Data Brief* **26**, 104440-104440, doi:10.1016/j.dib.2019.104440 (2019).

Appendix C – Don't Forget the Kids!: Novel Pulmonary MRI and AI of Neonatal Lung Disease

In this editorial, we critically evaluated a provided comments on an innovative deep learning ensemble approach for pulmonary MRI segmentation in neonates, where custom intensity-spatial-distribution features were evaluated.

*The contents of this appendix were previously published in the Radiology: Artificial Intelligence journal as editorial commentary: G Parraga and M Sharma. Don't forget the kids! Novel pulmonary MRI and AI of neonatal lung disease. Radiology: Artificial Intelligence (2023). <https://doi.org/10.1148/ryai.230400>. Permission to reproduce this article was granted by the Radiological Society of North America (RSNA) and is provided in **Appendix D**.*

Neonatal pulmonary disease, including bronchopulmonary dysplasia (BPD), is the final frontier for modern medical imaging. Neonatal lungs are tiny and, in cases that require hospital-based care, usually they are not fully developed. Neonates themselves cannot respond to instructions or lie still easily; those who are acutely ill need critical care support. The structure and function of the respiratory system at birth and at hospital discharge play an enormous role in the long-term achievement of optimal lung structure and function in growing children as they approach adulthood (1). In other words, the impact of neonatal care can last a lifetime.

Unfortunately, the diagnosis of lung abnormalities in premature and full-term neonates still relies mainly on clinical signs and observations, which typically are managed in the intensive care unit with the aid of chest radiography. Repeat chest CT generally is not performed because of the risk of ionizing radiation to patients who are so early in life. As such, it remains difficult to provide a framework to understand potential long-term outcomes and prognoses so that the parents of neonatal patients can plan for expected hurdles and aftereffects.

Into this clinical care gulf has emerged a cadre of pioneering researchers and clinicians dedicated to improving neonatal imaging using the radiation-free methods of US (2) and MRI (3). They bring the hope that if we discover and develop novel ways to rapidly acquire whole-lung images with clinically meaningful data, better outcomes and a better understanding of future outcomes will emerge.

Free-breathing hydrogen 1 (^1H) MRI methods can generate simulated ventilation and perfusion maps based on the small periodic change in ^1H signal intensity that occurs as the lungs fill and empty with air during tidal breathing (4). Another method, based on ultra-low- and zero-echo-time methods (5,6), has been developed to visualize the structural information, including airways and parenchyma, similar to chest CT images (7). These techniques have been studied in children, including neonates (8,9), but generally remain in the research domain. Image analysis and interpretation can be quite involved for quantitative results and have not yet been translated to clinical use.

In this issue of *Radiology: Artificial Intelligence*, Mairhörmann and Castelblanco and colleagues (10) address these limitations head on. The authors employed an innovative deep learning ensemble approach for pulmonary MRI segmentation, with multiple cross-validation schemes to avoid overfitting. In combination with custom intensity-spatial-distribution features, the ensemble

deep learning convolutional neural network models were highly consistent with expert MRI neonatal lung segmentations (cross-validation volumetric Dice coefficient = 0.91). Their model performed segmentation without time-consuming expert observer interaction, which provides a very large advantage. The authors evaluated neonates from two different study cohorts. Three expert observers performed manual MRI annotations, and two trained experts evaluated morphologic abnormalities. In addition to segmentation, a three-dimensional (3D) reconstruction approach quantified MRI features, including lung volume, surface, shape, and intensity. These 3D MRI features were highly accurate as compared with the reference standard (clinical diagnosis) for differentiating neonates with and without BPD; the area under the receiver operating characteristic curve (AUC) was 0.92 ± 0.02 for diagnosing BPD.

Although these results are worth considering for clinical applications, unfortunately the 3D MRI lung features alone did not outperform patient and clinical features. Supplementary analysis that ranked all features revealed that clinical measurements, such as gestational age, outperformed the MRI lung features. From a clinical and patient-centered perspective, it is important to note that the 3D MRI features, such as lung volume normalized by birth weight, correlated with continuous BPD indicators such as duration of mechanical ventilation ($\rho = 0.74$, $P < .001$) and oxygen supplementation ($\rho = 0.66$, $P < .001$). There is room for optimism that this approach is on the right track.

Certainly, these results take us some distance toward a future where MRI becomes a mainstay imaging method in neonates. In general, however, artificial intelligence (AI) segmentation approaches are not intuitive, and, in many cases, the clinical relevance of the algorithm output is not directly relatable or obviously relevant to the clinical problem. For implementation in clinical workflows, such approaches need to be more than highly accurate and rapid, but also trustworthy, transparent, interpretable, and explainable. Ultimately, as clinicians and radiologists, we want to understand more deeply how AI algorithms can improve patient care within clinical workflows.

Future work likely will focus on developing standardized methods to improve interpretability of AI-generated predictions and their relationship with disease pathologies. In addition, model performance measures will need to be developed to reflect what is most important to neonatal patients and their parents, namely whether the use of an AI approach results in changes to patient care that improve long-term outcomes. Fortunately, the proposed MRI features extracted here correlated with key BPD indicators and added unique information to predict BPD severity. Hence, the algorithmic results were certainly relatable to BPD, and the approach was not completely a "black box."

In summary, the study by Mairhörmann and Castelblanco and colleagues addresses an important clinical challenge in neonatal medicine and radiology by automating MRI lung segmentation and enabling rapid generation of quantitative MRI features. Automated segmentation and extraction of imaging features helped predict the development of BPD and its severity. To accelerate clinical translation, prospective studies should investigate relationships between algorithmic outputs and long-term clinical outcomes. As researchers continue to develop novel combinations of MRI and AI methods dedicated to neonatal health, it becomes less likely that we will forget the kids!

REFERENCES

1. Martinez FD . Early-Life Origins of Chronic Obstructive Pulmonary Disease . *N Engl J Med* 2016. ; 375 (9): 871 – 878.
2. Loi B , Vigo G , Baraldi E , et al. . Lung Ultrasound to Monitor Extremely Preterm Infants and Predict Bronchopulmonary Dysplasia. A Multicenter Longitudinal Cohort Study . *Am J Respir Crit Care Med* 2021. ; 203 (11): 1398 – 1409.
3. Walkup LL , Higano NS , Woods JC . Structural and Functional Pulmonary Magnetic Resonance Imaging in Pediatrics-From the Neonate to the Young Adult . *Acad Radiol* 2019. ; 26 (3): 424 – 430.
4. Bauman G , Puderbach M , Deimling M , et al. . Non-contrast-enhanced perfusion and ventilation assessment of the human lung by means of fourier decomposition in proton MRI . *Magn Reson Med* 2009. ; 62 (3): 656 – 664.
5. Johnson KM , Fain SB , Schiebler ML , Nagle S . Optimized 3D ultrashort echo time pulmonary MRI . *Magn Reson Med* 2013. ; 70 (5): 1241 – 1250.
6. Gibiino F , Sacolick L , Menini A , Landini L , Wiesinger F . Free-breathing, zero-TE MR lung imaging . *MAGMA* 2015. ; 28 (3): 207 – 215.
7. Higano NS , Fleck RJ , Spielberg DR , et al. . Quantification of neonatal lung parenchymal density via ultrashort echo time MRI with comparison to CT . *J Magn Reson Imaging* 2017. ; 46 (4): 992 – 1000.
8. Higano NS , Spielberg DR , Fleck RJ , et al. . Neonatal Pulmonary Magnetic Resonance Imaging of Bronchopulmonary Dysplasia Predicts Short-Term Clinical Outcomes . *Am J Respir Crit Care Med* 2018. ; 198 (10): 1302 – 1311.
9. Walkup LL , Tkach JA , Higano NS , et al. . Quantitative Magnetic Resonance Imaging of Bronchopulmonary Dysplasia in the Neonatal Intensive Care Unit Environment . *Am J Respir Crit Care Med* 2015. ; 192 (10): 1215 – 1222.
10. Mairhörmann B , Castelblanco A , Häfner F , et al. . Automated MRI Lung Segmentation and 3D Morphologic Features for Quantification of Neonatal Lung Disease . *Radiol Artif Intell* 2023. ; 5 (6): e220239.

Appendix D – Permission for Reproduction of Scientific Articles

Chapter 2 was published under Open Access in the journal of Academic Radiology. As author of the original article, I do not require permission beyond citing the original source.



Sign In/Register



Machine Learning and CT Texture Features in Ex-smokers with no CT Evidence of Emphysema and Mildly Abnormal Diffusing Capacity

Author: Maksym Sharma, Miranda Kirby, David G. McCormack, Grace Parraga

Publication: Academic Radiology

Publisher: Elsevier

Date: Available online 30 December 2023

© 2023 The Association of University Radiologists. Published by Elsevier Inc. All rights reserved.

Journal Author Rights

Please note that, as the author of this Elsevier article, you retain the right to include it in a thesis or dissertation, provided it is not published commercially. Permission is not required, but please ensure that you reference the journal as the original source. For more information on this and on your other retained rights, please visit: <https://www.elsevier.com/about/our-business/policies/copyright/#Author-rights>

BACK

CLOSE WINDOW

Chapter 4 was published under Open Access in the journal of Chronic Obstructive Pulmonary Disease. As author of the original article, I do not require permission beyond citing the original source.

Home > All Journals > COPD: Journal of Chronic Obstructive Pulmonary Disease > List of Issues > Volume 20, Issue 1 > Chest MRI and CT Predictors of 10-Year A ...

COPD: Journal of Chronic Obstructive Pulmonary Disease >
Volume 20, 2023 - Issue 1

Open access

900 0
Views CrossRef citations to date | Altmetric

Research Article

Chest MRI and CT Predictors of 10-Year All-Cause Mortality in COPD

Maksym Sharma, Paulina V. Wyszkievicz, Alexander M. Matheson, David G. McCormack & Grace Parraga

Pages 307-320 | Received 11 May 2023, Accepted 11 Sep 2023, Published online: 22 Sep 2023

Cite this article <https://doi.org/10.1080/15412555.2023.2259224> 

[Full Article](#) [Figures & data](#) [References](#) [Supplemental](#) [Citations](#) [Metrics](#) [Licensing](#) [Reprints & Permissions](#) [View PDF](#) [View EPUB](#)

Reprints and Permissions

This is an open access article distributed under the terms of the Creative Commons CC BY license, which permits unrestricted use, distribution, reproduction in any medium, provided the original work is properly cited.

You are not required to obtain permission to reuse this article in part or whole.

Appendix A – Quantification of Pulmonary Functional MRI: State-of-the-Art and Emerging Image Processing Methods and Measurements – Review article was published under CCBY 4.0 license in an Open Access *Physics in Medicine & Biology* journal. As author of the original article, I do not require permission beyond citing the original source.

1/28/24, 12:45 PM

marketplace.copyright.com/rs-ui-web/mp/search/all/10.1088/1361-6560/2Fac9510



All types 10.1088/1361-6560/ac9510 [Advanced Search](#) [Search Tips](#)

Filter your results:
No filters are available

> 0 publications and 1 articles/chapters matched your search term(s)
< Hide filters

Article/Chapter Results

Sort by Relevance ▾

Quantification of pulmonary functional MRI: state-of-the-art and emerging image processing methods and measurements

Sharma, Maksym; Wyszklewicz, Paulina Victoria; Desai, Goudar, Vedanth; Guo, Fumin; ...More *Physics in Medicine & Biology*, 21 Nov 2022, Vol. 67, Issue 22, pages 22TR01 - ...

ISSN: 00319155
DOI: 10.1088/1361-6560/ac9510
PMID: 36162409
Publisher: IOP Publishing; Ediciones Universidad de Navarra
Language: English
Country: United Kingdom of Great Britain and Northern Ireland
URL: <https://iopscience.iop.org/article/10.1088/1361-6560/ac9510>

[Details >](#)

[Request Reprints/ePrints](#) | [Request Single Copy](#) | [Open Access - Creative Commons CC BY 4.0](#)

Appendix B – Hyperpolarized Gas Magnetic Resonance Imaging Texture Analysis and Machine Learning to explain Accelerated Lung Function Decline in Ex-smokers with and without COPD – Article was reproduced with the permission granted by the international society for optics and photonics (SPIE).

1/31/24, 12:48 PM

marketplace.copyright.com/rs-ui-web/mp/license/d1c72aa2-2f38-47f7-8087-53f372a3eddb/268efe69-bcd7-4a3e-b0ad-b91f594bb..



This is a License Agreement between Maksym Sharma ("User") and Copyright Clearance Center, Inc. ("CCC") on behalf of the Rightsholder identified in the order details below. The license consists of the order details, the Marketplace Permissions General Terms and Conditions below, and any Rightsholder Terms and Conditions which are included below.

All payments must be made in full to CCC in accordance with the Marketplace Permissions General Terms and Conditions below.

Order Date	28-Jan-2024	Type of Use	Republish in a thesis/dissertation
Order License ID	1443044-1	Publisher Portion	SPIE Chapter/article
ISBN-13	9781510640306		

LICENSED CONTENT

Publication Title	Medical Imaging 2021 : Biomedical Applications in Molecular, Structural, and Functional Imaging	Rightsholder	SPIE
Article Title	Hyperpolarized gas magnetic resonance imaging texture analysis and machine learning to explain accelerated lung function decline in ex-smokers with and without COPD	Publication Type	e-Book
Date	01/01/2021	Start Page	11

REQUEST DETAILS

Portion Type	Chapter/article	Rights Requested	Main product
Page Range(s)	1-10	Distribution	Worldwide
Total Number of Pages	10	Translation	Original language of publication
Format (select all that apply)	Print, Electronic	Copies for the Disabled?	No
Who Will Republish the Content?	Academic institution	Minor Editing Privileges?	No
Duration of Use	Life of current and all future editions	Incidental Promotional Use?	No
Lifetime Unit Quantity	Up to 999	Currency	CAD

NEW WORK DETAILS

Title	Chest Computed Tomography and Magnetic Resonance Imaging Texture Measurements of Chronic Obstructive Pulmonary Disease	Institution Name	Western University
		Expected Presentation Date	2024-04-04

Instructor Name Maksym Sharma

ADDITIONAL DETAILS

The Requesting Person / Organization to Appear on the License Maksym Sharma

REQUESTED CONTENT DETAILS

Title, Description or Numeric Reference of the Portion(s)	Full Article	Title of the Article / Chapter the Portion Is From	Hyperpolarized gas magnetic resonance imaging texture analysis and machine learning to explain accelerated lung function decline in ex-smokers with and without COPD
Editor of Portion(s)	Sharma, Maksym; Westcott, Andrew R.; McCormack, David G.; Parraga, Grace	Author of Portion(s)	Sharma, Maksym; Westcott, Andrew R.; McCormack, David G.; Parraga, Grace
Volume / Edition	N/A	Publication Date of Portion	2021-03-18
Page or Page Range of Portion	11		

Appendix C – Don't Forget the Kids!: Novel Pulmonary MRI and AI of Neonatal Lung Disease
 – Editorial article was reproduced with the permission granted by the Radiological Society of North America (RSNA).

1/31/24, 12:48 PM

Manage Account



Special Requests > Special Request Details

Add To Cart
Decline Offer

Radiology : Artificial Intelligence

Article: Don't Forget the Kids!: Novel Pulmonary MRI and AI of Neonatal Lung Disease

GENERAL INFORMATION

Request ID	Request Date
600153885	28 Jan 2024
Request Status	Price
Accepted	0.00 CAD

ALL DETAILS

ISSN:	2638-6100
Type of Use:	Republish in a thesis/dissertation
Publisher:	Radiological Society of North America
Portion:	Chapter/article

LICENSED CONTENT

Publication Title	Radiology : Artificial Intelligence	Rightsholder	Radiological Society of North America
Article Title	Don't Forget the Kids!: Novel Pulmonary MRI and AI of Neonatal Lung Disease	Publication Type	e-journal
Date	01/01/2019	URL	http://rsna.org/ai
Language	English	Issue	6
Country	United States of America	Volume	5

REQUEST DETAILS

Page Range(s)	1-2	Distribution	Worldwide
Total Number of Pages	2	Translation	Original language of publication
Format (select all that apply)	Print, Electronic	Copies for the Disabled?	No
Who Will Republish the Content?	Academic institution	Minor Editing Privileges?	No
Duration of Use	Life of current and all future editions	Incidental Promotional Use?	No
Lifetime Unit Quantity	Up to 999	Currency	CAD
Rights Requested	Main product		

NEW WORK DETAILS

1/31/24, 12:48 PM

Manage Account

Title	Chest Computed Tomography and Magnetic Resonance Imaging Texture Measurements of Chronic Obstructive Pulmonary Disease	Institution Name	Western University
Instructor Name	Maksym Sharma	Expected Presentation Date	2024-04-04

ADDITIONAL DETAILS

The Requesting Person / Organization to Appear on the License Maksym Sharma

REQUESTED CONTENT DETAILS

Title, Description or Numeric Reference of the Portion(s)	Full Article	Title of the Article / Chapter the Portion Is From	Don't Forget the Kids!: Novel Pulmonary MRI and AI of Neonatal Lung Disease
Editor of Portion(s)	Parraga, Grace; Sharma, Maksym	Author of Portion(s)	Parraga, Grace; Sharma, Maksym
Volume / Edition	5	Publication Date of Portion	2023-11-01
Page or Page Range of Portion	1-2		

COMMENTS

 [Add Comment / Attachment](#)

28 Jan 2024 12:37:36 PM, by Maksym Sharma
This article will only be reproduced in my thesis.

 [Add To Cart](#)  [Decline Offer](#)

Figure 1-4. Permission to reproduce.

4/16/24, 2:07 PM

RightsLink Printable License

ELSEVIER LICENSE TERMS AND CONDITIONS

Apr 16, 2024

This Agreement between Western University -- Maksym Sharma ("You") and Elsevier ("Elsevier") consists of your license details and the terms and conditions provided by Elsevier and Copyright Clearance Center.

License Number	5770901148459
License date	Apr 16, 2024
Licensed Content Publisher	Elsevier
Licensed Content Publication	The Lancet
Licensed Content Title	Pathophysiology of airflow limitation in chronic obstructive pulmonary disease
Licensed Content Author	James C Hogg
Licensed Content Date	21–27 August 2004
Licensed Content Volume	364
Licensed Content Issue	9435
Licensed Content Pages	13
Start Page	709
End Page	721
Type of Use	reuse in a thesis/dissertation

Portion	figures/tables/illustrations
Number of figures/tables/illustrations	1
Format	both print and electronic
Are you the author of this Elsevier article?	No
Will you be translating?	No
Title of new work	Chest Computed Tomography and Magnetic Resonance Imaging Texture Measurements in Chronic Obstructive Pulmonary Disease
Institution name	Western University
Expected presentation date	Apr 2024
Order reference number	003
Portions	Figure 4. Parts A) and D).
Requestor Location	
Publisher Tax ID	GB 494 6272 12
Total	0.00 CAD
Terms and Conditions	

INTRODUCTION

1. The publisher for this copyrighted material is Elsevier. By clicking "accept" in connection with completing this licensing transaction, you agree that the following terms and conditions apply to this transaction (along with the Billing and Payment terms and conditions established by Copyright Clearance Center, Inc. ("CCC"), at the time that you opened your RightsLink account and that are available at any time at <https://myaccount.copyright.com>).

GENERAL TERMS

2. Elsevier hereby grants you permission to reproduce the aforementioned material subject to the terms and conditions indicated.

3. Acknowledgement: If any part of the material to be used (for example, figures) has appeared in our publication with credit or acknowledgement to another source, permission must also be sought from that source. If such permission is not obtained then that material may not be included in your publication/copies. Suitable acknowledgement to the source must be made, either as a footnote or in a reference list at the end of your publication, as follows:

"Reprinted from Publication title, Vol /edition number, Author(s), Title of article / title of chapter, Pages No., Copyright (Year), with permission from Elsevier [OR APPLICABLE SOCIETY COPYRIGHT OWNER]." Also Lancet special credit - "Reprinted from The Lancet, Vol. number, Author(s), Title of article, Pages No., Copyright (Year), with permission from Elsevier."

4. Reproduction of this material is confined to the purpose and/or media for which permission is hereby given. The material may not be reproduced or used in any other way, including use in combination with an artificial intelligence tool (including to train an algorithm, test, process, analyse, generate output and/or develop any form of artificial intelligence tool), or to create any derivative work and/or service (including resulting from the use of artificial intelligence tools).

5. Altering/Modifying Material: Not Permitted. However figures and illustrations may be altered/adapted minimally to serve your work. Any other abbreviations, additions, deletions and/or any other alterations shall be made only with prior written authorization of Elsevier Ltd. (Please contact Elsevier's permissions helpdesk [here](#)). No modifications can be made to any Lancet figures/tables and they must be reproduced in full.

6. If the permission fee for the requested use of our material is waived in this instance, please be advised that your future requests for Elsevier materials may attract a fee.

7. Reservation of Rights: Publisher reserves all rights not specifically granted in the combination of (i) the license details provided by you and accepted in the course of this licensing transaction, (ii) these terms and conditions and (iii) CCC's Billing and Payment terms and conditions.

8. License Contingent Upon Payment: While you may exercise the rights licensed immediately upon issuance of the license at the end of the licensing process for the transaction, provided that you have disclosed complete and accurate details of your proposed use, no license is finally effective unless and until full payment is received from you (either by publisher or by CCC) as provided in CCC's Billing and Payment terms and conditions. If full payment is not received on a timely basis, then any license preliminarily granted shall be deemed automatically revoked and shall be void as if never granted. Further, in the event that you breach any of these terms and conditions or any of CCC's Billing and Payment terms and conditions, the license is automatically revoked and shall be void as if never granted. Use of materials as described in a revoked license, as well as any use of the materials beyond the scope of an unrevoked license, may constitute

copyright infringement and publisher reserves the right to take any and all action to protect its copyright in the materials.

9. Warranties: Publisher makes no representations or warranties with respect to the licensed material.

10. Indemnity: You hereby indemnify and agree to hold harmless publisher and CCC, and their respective officers, directors, employees and agents, from and against any and all claims arising out of your use of the licensed material other than as specifically authorized pursuant to this license.

11. No Transfer of License: This license is personal to you and may not be sublicensed, assigned, or transferred by you to any other person without publisher's written permission.

12. No Amendment Except in Writing: This license may not be amended except in a writing signed by both parties (or, in the case of publisher, by CCC on publisher's behalf).

13. Objection to Contrary Terms: Publisher hereby objects to any terms contained in any purchase order, acknowledgment, check endorsement or other writing prepared by you, which terms are inconsistent with these terms and conditions or CCC's Billing and Payment terms and conditions. These terms and conditions, together with CCC's Billing and Payment terms and conditions (which are incorporated herein), comprise the entire agreement between you and publisher (and CCC) concerning this licensing transaction. In the event of any conflict between your obligations established by these terms and conditions and those established by CCC's Billing and Payment terms and conditions, these terms and conditions shall control.

14. Revocation: Elsevier or Copyright Clearance Center may deny the permissions described in this License at their sole discretion, for any reason or no reason, with a full refund payable to you. Notice of such denial will be made using the contact information provided by you. Failure to receive such notice will not alter or invalidate the denial. In no event will Elsevier or Copyright Clearance Center be responsible or liable for any costs, expenses or damage incurred by you as a result of a denial of your permission request, other than a refund of the amount(s) paid by you to Elsevier and/or Copyright Clearance Center for denied permissions.

LIMITED LICENSE

The following terms and conditions apply only to specific license types:

15. **Translation:** This permission is granted for non-exclusive world **English** rights only unless your license was granted for translation rights. If you licensed translation rights you may only translate this content into the languages you requested. A professional translator must perform all translations and reproduce the content word for word preserving the integrity of the article.

16. **Posting licensed content on any Website:** The following terms and conditions apply as follows: Licensing material from an Elsevier journal: All content posted to the web site must maintain the copyright information line on the bottom of each image; A hyper-text must be included to the Homepage of the journal from which you are licensing at <http://www.sciencedirect.com/science/journal/xxxxx> or the Elsevier homepage for books at <http://www.elsevier.com>; Central Storage: This license does not include permission for a scanned version of the material to be stored in a central repository such as that provided by Heron/XanEdu.

Licensing material from an Elsevier book: A hyper-text link must be included to the Elsevier homepage at <http://www.elsevier.com>. All content posted to the web site must maintain the copyright information line on the bottom of each image.

Posting licensed content on Electronic reserve: In addition to the above the following clauses are applicable: The web site must be password-protected and made available only to bona fide students registered on a relevant course. This permission is granted for 1 year only. You may obtain a new license for future website posting.

17. **For journal authors:** the following clauses are applicable in addition to the above:

Preprints:

A preprint is an author's own write-up of research results and analysis, it has not been peer-reviewed, nor has it had any other value added to it by a publisher (such as formatting, copyright, technical enhancement etc.).

Authors can share their preprints anywhere at any time. Preprints should not be added to or enhanced in any way in order to appear more like, or to substitute for, the final versions of articles however authors can update their preprints on arXiv or RePEc with their Accepted Author Manuscript (see below).

If accepted for publication, we encourage authors to link from the preprint to their formal publication via its DOI. Millions of researchers have access to the formal publications on ScienceDirect, and so links will help users to find, access, cite and use the best available version. Please note that Cell Press, The Lancet and some society-owned have different preprint policies. Information on these policies is available on the journal homepage.

Accepted Author Manuscripts: An accepted author manuscript is the manuscript of an article that has been accepted for publication and which typically includes author-incorporated changes suggested during submission, peer review and editor-author communications.

Authors can share their accepted author manuscript:

- immediately
 - via their non-commercial person homepage or blog
 - by updating a preprint in arXiv or RePEc with the accepted manuscript
 - via their research institute or institutional repository for internal institutional uses or as part of an invitation-only research collaboration work-group
 - directly by providing copies to their students or to research collaborators for their personal use
 - for private scholarly sharing as part of an invitation-only work group on commercial sites with which Elsevier has an agreement
- After the embargo period
 - via non-commercial hosting platforms such as their institutional repository
 - via commercial sites with which Elsevier has an agreement

In all cases accepted manuscripts should:

- link to the formal publication via its DOI
- bear a CC-BY-NC-ND license - this is easy to do
- if aggregated with other manuscripts, for example in a repository or other site, be shared in alignment with our hosting policy not be added to or enhanced in any way to appear more like, or to substitute for, the published journal article.

Published journal article (JPA): A published journal article (PJA) is the definitive final record of published research that appears or will appear in the journal and embodies all value-adding publishing activities including peer review co-ordination, copy-editing, formatting, (if relevant) pagination and online enrichment.

Policies for sharing publishing journal articles differ for subscription and gold open access articles:

Subscription Articles: If you are an author, please share a link to your article rather than the full-text. Millions of researchers have access to the formal publications on ScienceDirect, and so links will help your users to find, access, cite, and use the best available version.

Theses and dissertations which contain embedded PJAs as part of the formal submission can be posted publicly by the awarding institution with DOI links back to the formal publications on ScienceDirect.

If you are affiliated with a library that subscribes to ScienceDirect you have additional private sharing rights for others' research accessed under that agreement. This includes use for classroom teaching and internal training at the institution (including use in course packs and courseware programs), and inclusion of the article for grant funding purposes.

Gold Open Access Articles: May be shared according to the author-selected end-user license and should contain a [CrossMark logo](#), the end user license, and a DOI link to the formal publication on ScienceDirect.

Please refer to Elsevier's [posting policy](#) for further information.

18. **For book authors** the following clauses are applicable in addition to the above: Authors are permitted to place a brief summary of their work online only. You are not allowed to download and post the published electronic version of your chapter, nor may you scan the printed edition to create an electronic version. **Posting to a repository:** Authors are permitted to post a summary of their chapter only in their institution's repository.

19. **Thesis/Dissertation:** If your license is for use in a thesis/dissertation your thesis may be submitted to your institution in either print or electronic form. Should your thesis be published commercially, please reapply for permission. These requirements include permission for the Library and Archives of Canada to supply single copies, on demand, of the complete thesis and include permission for Proquest/UMI to supply single copies, on demand, of the complete thesis. Should your thesis be published commercially, please reapply for permission. Theses and dissertations which contain embedded PJAs as part of the formal submission can be posted publicly by the awarding institution with DOI links back to the formal publications on ScienceDirect.

Elsevier Open Access Terms and Conditions

You can publish open access with Elsevier in hundreds of open access journals or in nearly 2000 established subscription journals that support open access publishing. Permitted third party re-use of these open access articles is defined by the author's choice of Creative Commons user license. See our [open access license policy](#) for more information.

Terms & Conditions applicable to all Open Access articles published with Elsevier:

Any reuse of the article must not represent the author as endorsing the adaptation of the article nor should the article be modified in such a way as to damage the author's honour or reputation. If any changes have been made, such changes must be clearly indicated.

The author(s) must be appropriately credited and we ask that you include the end user license and a DOI link to the formal publication on ScienceDirect.

If any part of the material to be used (for example, figures) has appeared in our publication with credit or acknowledgement to another source it is the responsibility of the user to ensure their reuse complies with the terms and conditions determined by the rights holder.

Additional Terms & Conditions applicable to each Creative Commons user license:

CC BY: The CC-BY license allows users to copy, to create extracts, abstracts and new works from the Article, to alter and revise the Article and to make commercial use of the Article (including reuse and/or resale of the Article by commercial entities), provided the user gives appropriate credit (with a link to the formal publication through the relevant DOI), provides a link to the license, indicates if changes were made and the licensor is not represented as endorsing the use made of the work. The full details of the license are available at <http://creativecommons.org/licenses/by/4.0>.

CC BY NC SA: The CC BY-NC-SA license allows users to copy, to create extracts, abstracts and new works from the Article, to alter and revise the Article, provided this is not done for commercial purposes, and that the user gives appropriate credit (with a link to the formal publication through the relevant DOI), provides a link to the license, indicates if changes were made and the licensor is not represented as endorsing the use made of the work. Further, any new works must be made available on the same conditions. The full details of the license are available at <http://creativecommons.org/licenses/by-nc-sa/4.0>.

CC BY NC ND: The CC BY-NC-ND license allows users to copy and distribute the Article, provided this is not done for commercial purposes and further does not permit distribution of the Article if it is changed or edited in any way, and provided the user gives appropriate credit (with a link to the formal publication through the relevant DOI), provides a link to the license, and that the licensor is not represented as endorsing the use made of the work. The full details of the license are available at <http://creativecommons.org/licenses/by-nc-nd/4.0>. Any commercial reuse of Open Access articles published with a CC BY NC SA or CC BY NC ND license requires permission from Elsevier and will be subject to a fee.

Commercial reuse includes:

- Associating advertising with the full text of the Article
- Charging fees for document delivery or access
- Article aggregation
- Systematic distribution via e-mail lists or share buttons

Posting or linking by commercial companies for use by customers of those companies.

20. Other Conditions:

v1.10

Questions? customercare@copyright.com.

JOHN WILEY AND SONS LICENSE
TERMS AND CONDITIONS

Jan 28, 2024

This Agreement between Western University -- Maksym Sharma ("You") and John Wiley and Sons ("John Wiley and Sons") consists of your license details and the terms and conditions provided by John Wiley and Sons and Copyright Clearance Center.

License Number 5717821071801

License date Jan 28, 2024

Licensed Content Publisher John Wiley and Sons

Licensed Content Publication Magnetic Resonance in Medicine

Licensed Content Title Hyperpolarized 3He diffusion MRI and histology in pulmonary emphysema

Licensed Content Author James C. Hogg, Mark S. Conradi, Peter T. Macklem, et al

Licensed Content Date Oct 20, 2006

Licensed Content Volume 56

Licensed Content Issue 6

Licensed Content Pages 8

Type of use	Dissertation/Thesis
Requestor type	University/Academic
Format	Print and electronic
Portion	Figure/table
Number of figures/tables	1
Will you be translating?	No
Title of new work	Chest Computed Tomography and Magnetic Resonance Imaging Texture Measurements in Chronic Obstructive Pulmonary Disease
Institution name	Western University
Expected presentation date	Apr 2024
Order reference number	2
Portions	Figure 2. parts a) and b)
Requestor Location	
Publisher Tax ID	EU826007151
Total	0.00 CAD

TERMS AND CONDITIONS

This copyrighted material is owned by or exclusively licensed to John Wiley & Sons, Inc. or one of its group companies (each a "Wiley Company") or handled on behalf of a society with which a Wiley Company has exclusive publishing rights in relation to a particular work (collectively "WILEY"). By clicking "accept" in connection with completing this licensing transaction, you agree that the following terms and conditions apply to this transaction (along with the billing and payment terms and conditions established by the Copyright Clearance Center Inc., ("CCC's Billing and Payment terms and conditions"), at the time that you opened your RightsLink account (these are available at any time at <http://myaccount.copyright.com>).

Terms and Conditions

- The materials you have requested permission to reproduce or reuse (the "Wiley Materials") are protected by copyright.
- You are hereby granted a personal, non-exclusive, non-sub licensable (on a stand-alone basis), non-transferable, worldwide, limited license to reproduce the Wiley Materials for the purpose specified in the licensing process. This license, **and any CONTENT (PDF or image file) purchased as part of your order**, is for a one-time use only and limited to any maximum distribution number specified in the license. The first instance of republication or reuse granted by this license must be completed within two years of the date of the grant of this license (although copies prepared before the end date may be distributed thereafter). The Wiley Materials shall not be used in any other manner or for any other purpose, beyond what is granted in the license. Permission is granted subject to an appropriate acknowledgement given to the author, title of the material/book/journal and the publisher. You shall also duplicate the copyright notice that appears in the Wiley publication in your use of the Wiley Material. Permission is also granted on the understanding that nowhere in the text is a previously published source acknowledged for all or part of this Wiley Material. Any third party content is expressly excluded from this permission.
- With respect to the Wiley Materials, all rights are reserved. Except as expressly granted by the terms of the license, no part of the Wiley Materials may be copied, modified, adapted (except for minor reformatting required by the new Publication), translated, reproduced, transferred or distributed, in any form or by any means, and no derivative works may be made based on the Wiley Materials without the prior permission of the respective copyright owner. **For STM Signatory Publishers clearing permission under the terms of the [STM Permissions Guidelines](#) only, the terms of the license are extended to include subsequent editions and for editions in other languages, provided such editions are for the work as a whole in situ and does not involve the separate exploitation of the permitted figures or extracts**, You may not alter, remove or suppress in any manner any copyright, trademark or other notices displayed by the Wiley Materials. You may not license, rent, sell, loan, lease, pledge, offer as security, transfer or assign the Wiley Materials on a stand-alone basis, or any of the rights granted to you hereunder to any other

person.

- The Wiley Materials and all of the intellectual property rights therein shall at all times remain the exclusive property of John Wiley & Sons Inc, the Wiley Companies, or their respective licensors, and your interest therein is only that of having possession of and the right to reproduce the Wiley Materials pursuant to Section 2 herein during the continuance of this Agreement. You agree that you own no right, title or interest in or to the Wiley Materials or any of the intellectual property rights therein. You shall have no rights hereunder other than the license as provided for above in Section 2. No right, license or interest to any trademark, trade name, service mark or other branding ("Marks") of WILEY or its licensors is granted hereunder, and you agree that you shall not assert any such right, license or interest with respect thereto
- NEITHER WILEY NOR ITS LICENSORS MAKES ANY WARRANTY OR REPRESENTATION OF ANY KIND TO YOU OR ANY THIRD PARTY, EXPRESS, IMPLIED OR STATUTORY, WITH RESPECT TO THE MATERIALS OR THE ACCURACY OF ANY INFORMATION CONTAINED IN THE MATERIALS, INCLUDING, WITHOUT LIMITATION, ANY IMPLIED WARRANTY OF MERCHANTABILITY, ACCURACY, SATISFACTORY QUALITY, FITNESS FOR A PARTICULAR PURPOSE, USABILITY, INTEGRATION OR NON-INFRINGEMENT AND ALL SUCH WARRANTIES ARE HEREBY EXCLUDED BY WILEY AND ITS LICENSORS AND WAIVED BY YOU.
- WILEY shall have the right to terminate this Agreement immediately upon breach of this Agreement by you.
- You shall indemnify, defend and hold harmless WILEY, its Licensors and their respective directors, officers, agents and employees, from and against any actual or threatened claims, demands, causes of action or proceedings arising from any breach of this Agreement by you.
- IN NO EVENT SHALL WILEY OR ITS LICENSORS BE LIABLE TO YOU OR ANY OTHER PARTY OR ANY OTHER PERSON OR ENTITY FOR ANY SPECIAL, CONSEQUENTIAL, INCIDENTAL, INDIRECT, EXEMPLARY OR PUNITIVE DAMAGES, HOWEVER CAUSED, ARISING OUT OF OR IN CONNECTION WITH THE DOWNLOADING, PROVISIONING, VIEWING OR USE OF THE MATERIALS REGARDLESS OF THE FORM OF ACTION, WHETHER FOR BREACH OF CONTRACT, BREACH OF WARRANTY, TORT, NEGLIGENCE, INFRINGEMENT OR OTHERWISE (INCLUDING, WITHOUT LIMITATION, DAMAGES BASED ON LOSS OF PROFITS, DATA, FILES, USE, BUSINESS OPPORTUNITY OR CLAIMS OF THIRD PARTIES), AND WHETHER OR NOT THE PARTY HAS BEEN ADVISED OF THE POSSIBILITY OF SUCH DAMAGES. THIS LIMITATION SHALL APPLY NOTWITHSTANDING ANY FAILURE OF ESSENTIAL PURPOSE OF ANY LIMITED REMEDY PROVIDED HEREIN.
- Should any provision of this Agreement be held by a court of competent jurisdiction to be illegal, invalid, or unenforceable, that provision shall be deemed amended to achieve as nearly as possible the same economic effect as the original provision, and the legality, validity and enforceability of the remaining provisions of this Agreement shall not be affected or impaired thereby.

- The failure of either party to enforce any term or condition of this Agreement shall not constitute a waiver of either party's right to enforce each and every term and condition of this Agreement. No breach under this agreement shall be deemed waived or excused by either party unless such waiver or consent is in writing signed by the party granting such waiver or consent. The waiver by or consent of a party to a breach of any provision of this Agreement shall not operate or be construed as a waiver of or consent to any other or subsequent breach by such other party.
- This Agreement may not be assigned (including by operation of law or otherwise) by you without WILEY's prior written consent.
- Any fee required for this permission shall be non-refundable after thirty (30) days from receipt by the CCC.
- These terms and conditions together with CCC's Billing and Payment terms and conditions (which are incorporated herein) form the entire agreement between you and WILEY concerning this licensing transaction and (in the absence of fraud) supersedes all prior agreements and representations of the parties, oral or written. This Agreement may not be amended except in writing signed by both parties. This Agreement shall be binding upon and inure to the benefit of the parties' successors, legal representatives, and authorized assigns.
- In the event of any conflict between your obligations established by these terms and conditions and those established by CCC's Billing and Payment terms and conditions, these terms and conditions shall prevail.
- WILEY expressly reserves all rights not specifically granted in the combination of (i) the license details provided by you and accepted in the course of this licensing transaction, (ii) these terms and conditions and (iii) CCC's Billing and Payment terms and conditions.
- This Agreement will be void if the Type of Use, Format, Circulation, or Requestor Type was misrepresented during the licensing process.
- This Agreement shall be governed by and construed in accordance with the laws of the State of New York, USA, without regards to such state's conflict of law rules. Any legal action, suit or proceeding arising out of or relating to these Terms and Conditions or the breach thereof shall be instituted in a court of competent jurisdiction in New York County in the State of New York in the United States of America and each party hereby consents and submits to the personal jurisdiction of such court, waives any objection to venue in such court and consents to service of process by registered or certified mail, return receipt requested, at the last known address of such party.

WILEY OPEN ACCESS TERMS AND CONDITIONS

Wiley Publishes Open Access Articles in fully Open Access Journals and in Subscription journals offering Online Open. Although most of the fully Open Access journals publish open access articles under the terms of the Creative Commons Attribution (CC BY) License only, the subscription journals and a few of the Open Access Journals offer a choice of Creative Commons Licenses. The license type is clearly identified on the article.

The Creative Commons Attribution License

The [Creative Commons Attribution License \(CC-BY\)](#) allows users to copy, distribute and transmit an article, adapt the article and make commercial use of the article. The CC-BY license permits commercial and non-

Creative Commons Attribution Non-Commercial License

The [Creative Commons Attribution Non-Commercial \(CC-BY-NC\)License](#) permits use, distribution and reproduction in any medium, provided the original work is properly cited and is not used for commercial purposes.(see below)

Creative Commons Attribution-Non-Commercial-NoDerivs License

The [Creative Commons Attribution Non-Commercial-NoDerivs License](#) (CC-BY-NC-ND) permits use, distribution and reproduction in any medium, provided the original work is properly cited, is not used for commercial purposes and no modifications or adaptations are made. (see below)

Use by commercial "for-profit" organizations

Use of Wiley Open Access articles for commercial, promotional, or marketing purposes requires further explicit permission from Wiley and will be subject to a fee.

Further details can be found on Wiley Online Library
<http://olabout.wiley.com/WileyCDA/Section/id-410895.html>

Other Terms and Conditions:

v1.10 Last updated September 2015

Questions? customer@copyright.com.

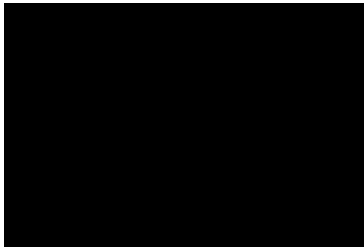
Figure 1-5. Permission to reproduce.

ELSEVIER LICENSE
TERMS AND CONDITIONS

Apr 16, 2024

This Agreement between Western University -- Maksym Sharma ("You") and Elsevier ("Elsevier") consists of your license details and the terms and conditions provided by Elsevier and Copyright Clearance Center.

License Number	5770860817297
License date	Apr 16, 2024
Licensed Content Publisher	Elsevier
Licensed Content Publication	The American Journal of Medicine
Licensed Content Title	Pulmonary Emphysema Subtypes on Computed Tomography: The MESA COPD Study
Licensed Content Author	Benjamin M. Smith,John H.M. Austin,John D. Newell,Belinda M. D'Souza,Anna Rozenshtein,Eric A. Hoffman,Firas Ahmed,R. Graham Barr
Licensed Content Date	Jan 1, 2014
Licensed Content Volume	127
Licensed Content Issue	1
Licensed Content Pages	17
Start Page	94.e7
End Page	94.e23
Type of Use	reuse in a thesis/dissertation

Portion	figures/tables/illustrations
Number of figures/tables/illustrations	1
Format	both print and electronic
Are you the author of this Elsevier article?	No
Will you be translating?	No
Title of new work	Chest Computed Tomography and Magnetic Resonance Imaging Texture Measurements in Chronic Obstructive Pulmonary Disease
Institution name	Western University
Expected presentation date	Apr 2024
Order reference number	002
Portions	Figure 1.
Requestor Location	
Publisher Tax ID	GB 494 6272 12
Total	0.00 CAD
Terms and Conditions	

INTRODUCTION

1. The publisher for this copyrighted material is Elsevier. By clicking "accept" in connection with completing this licensing transaction, you agree that the following terms and conditions apply to this transaction (along with the Billing and Payment terms and conditions established by Copyright Clearance Center, Inc. ("CCC"), at the time that you opened your RightsLink account and that are available at any time at <https://myaccount.copyright.com>).

GENERAL TERMS

2. Elsevier hereby grants you permission to reproduce the aforementioned material subject to the terms and conditions indicated.

3. Acknowledgement: If any part of the material to be used (for example, figures) has appeared in our publication with credit or acknowledgement to another source, permission must also be sought from that source. If such permission is not obtained then that material may not be included in your publication/copies. Suitable acknowledgement to the source must be made, either as a footnote or in a reference list at the end of your publication, as follows:

"Reprinted from Publication title, Vol /edition number, Author(s), Title of article / title of chapter, Pages No., Copyright (Year), with permission from Elsevier [OR APPLICABLE SOCIETY COPYRIGHT OWNER]." Also Lancet special credit - "Reprinted from The Lancet, Vol. number, Author(s), Title of article, Pages No., Copyright (Year), with permission from Elsevier."

4. Reproduction of this material is confined to the purpose and/or media for which permission is hereby given. The material may not be reproduced or used in any other way, including use in combination with an artificial intelligence tool (including to train an algorithm, test, process, analyse, generate output and/or develop any form of artificial intelligence tool), or to create any derivative work and/or service (including resulting from the use of artificial intelligence tools).

5. Altering/Modifying Material: Not Permitted. However figures and illustrations may be altered/adapted minimally to serve your work. Any other abbreviations, additions, deletions and/or any other alterations shall be made only with prior written authorization of Elsevier Ltd. (Please contact Elsevier's permissions helpdesk [here](#)). No modifications can be made to any Lancet figures/tables and they must be reproduced in full.

6. If the permission fee for the requested use of our material is waived in this instance, please be advised that your future requests for Elsevier materials may attract a fee.

7. Reservation of Rights: Publisher reserves all rights not specifically granted in the combination of (i) the license details provided by you and accepted in the course of this licensing transaction, (ii) these terms and conditions and (iii) CCC's Billing and Payment terms and conditions.

8. License Contingent Upon Payment: While you may exercise the rights licensed immediately upon issuance of the license at the end of the licensing process for the transaction, provided that you have disclosed complete and accurate details of your proposed use, no license is finally effective unless and until full payment is received from you (either by publisher or by CCC) as provided in CCC's Billing and Payment terms and conditions. If full payment is not received on a timely basis, then any license preliminarily granted shall be deemed automatically revoked and shall be void as if never granted. Further, in the event that you breach any of these terms and conditions or any of CCC's Billing and Payment terms and conditions, the license is automatically revoked and shall be void as if never granted. Use of materials as described in a revoked license, as well as any use of the materials beyond the scope of an unrevoked license, may constitute

copyright infringement and publisher reserves the right to take any and all action to protect its copyright in the materials.

9. Warranties: Publisher makes no representations or warranties with respect to the licensed material.

10. Indemnity: You hereby indemnify and agree to hold harmless publisher and CCC, and their respective officers, directors, employees and agents, from and against any and all claims arising out of your use of the licensed material other than as specifically authorized pursuant to this license.

11. No Transfer of License: This license is personal to you and may not be sublicensed, assigned, or transferred by you to any other person without publisher's written permission.

12. No Amendment Except in Writing: This license may not be amended except in a writing signed by both parties (or, in the case of publisher, by CCC on publisher's behalf).

13. Objection to Contrary Terms: Publisher hereby objects to any terms contained in any purchase order, acknowledgment, check endorsement or other writing prepared by you, which terms are inconsistent with these terms and conditions or CCC's Billing and Payment terms and conditions. These terms and conditions, together with CCC's Billing and Payment terms and conditions (which are incorporated herein), comprise the entire agreement between you and publisher (and CCC) concerning this licensing transaction. In the event of any conflict between your obligations established by these terms and conditions and those established by CCC's Billing and Payment terms and conditions, these terms and conditions shall control.

14. Revocation: Elsevier or Copyright Clearance Center may deny the permissions described in this License at their sole discretion, for any reason or no reason, with a full refund payable to you. Notice of such denial will be made using the contact information provided by you. Failure to receive such notice will not alter or invalidate the denial. In no event will Elsevier or Copyright Clearance Center be responsible or liable for any costs, expenses or damage incurred by you as a result of a denial of your permission request, other than a refund of the amount(s) paid by you to Elsevier and/or Copyright Clearance Center for denied permissions.

LIMITED LICENSE

The following terms and conditions apply only to specific license types:

15. **Translation:** This permission is granted for non-exclusive world **English** rights only unless your license was granted for translation rights. If you licensed translation rights you may only translate this content into the languages you requested. A professional translator must perform all translations and reproduce the content word for word preserving the integrity of the article.

16. **Posting licensed content on any Website:** The following terms and conditions apply as follows: Licensing material from an Elsevier journal: All content posted to the web site must maintain the copyright information line on the bottom of each image; A hyper-text must be included to the Homepage of the journal from which you are licensing at <http://www.sciencedirect.com/science/journal/xxxxx> or the Elsevier homepage for books at <http://www.elsevier.com>; Central Storage: This license does not include permission for a scanned version of the material to be stored in a central repository such as that provided by Heron/XanEdu.

Licensing material from an Elsevier book: A hyper-text link must be included to the Elsevier homepage at <http://www.elsevier.com>. All content posted to the web site must maintain the copyright information line on the bottom of each image.

Posting licensed content on Electronic reserve: In addition to the above the following clauses are applicable: The web site must be password-protected and made available only to bona fide students registered on a relevant course. This permission is granted for 1 year only. You may obtain a new license for future website posting.

17. **For journal authors:** the following clauses are applicable in addition to the above:

Preprints:

A preprint is an author's own write-up of research results and analysis, it has not been peer-reviewed, nor has it had any other value added to it by a publisher (such as formatting, copyright, technical enhancement etc.).

Authors can share their preprints anywhere at any time. Preprints should not be added to or enhanced in any way in order to appear more like, or to substitute for, the final versions of articles however authors can update their preprints on arXiv or RePEc with their Accepted Author Manuscript (see below).

If accepted for publication, we encourage authors to link from the preprint to their formal publication via its DOI. Millions of researchers have access to the formal publications on ScienceDirect, and so links will help users to find, access, cite and use the best available version. Please note that Cell Press, The Lancet and some society-owned have different preprint policies. Information on these policies is available on the journal homepage.

Accepted Author Manuscripts: An accepted author manuscript is the manuscript of an article that has been accepted for publication and which typically includes author-incorporated changes suggested during submission, peer review and editor-author communications.

Authors can share their accepted author manuscript:

- immediately
 - via their non-commercial person homepage or blog
 - by updating a preprint in arXiv or RePEc with the accepted manuscript
 - via their research institute or institutional repository for internal institutional uses or as part of an invitation-only research collaboration work-group
 - directly by providing copies to their students or to research collaborators for their personal use
 - for private scholarly sharing as part of an invitation-only work group on commercial sites with which Elsevier has an agreement
- After the embargo period
 - via non-commercial hosting platforms such as their institutional repository
 - via commercial sites with which Elsevier has an agreement

In all cases accepted manuscripts should:

- link to the formal publication via its DOI
- bear a CC-BY-NC-ND license - this is easy to do
- if aggregated with other manuscripts, for example in a repository or other site, be shared in alignment with our hosting policy not be added to or enhanced in any way to appear more like, or to substitute for, the published journal article.

Published journal article (JPA): A published journal article (PJA) is the definitive final record of published research that appears or will appear in the journal and embodies all value-adding publishing activities including peer review co-ordination, copy-editing, formatting, (if relevant) pagination and online enrichment.

Policies for sharing publishing journal articles differ for subscription and gold open access articles:

Subscription Articles: If you are an author, please share a link to your article rather than the full-text. Millions of researchers have access to the formal publications on ScienceDirect, and so links will help your users to find, access, cite, and use the best available version.

Theses and dissertations which contain embedded PJAs as part of the formal submission can be posted publicly by the awarding institution with DOI links back to the formal publications on ScienceDirect.

If you are affiliated with a library that subscribes to ScienceDirect you have additional private sharing rights for others' research accessed under that agreement. This includes use for classroom teaching and internal training at the institution (including use in course packs and courseware programs), and inclusion of the article for grant funding purposes.

Gold Open Access Articles: May be shared according to the author-selected end-user license and should contain a [CrossMark logo](#), the end user license, and a DOI link to the formal publication on ScienceDirect.

Please refer to Elsevier's [posting policy](#) for further information.

18. **For book authors** the following clauses are applicable in addition to the above: Authors are permitted to place a brief summary of their work online only. You are not allowed to download and post the published electronic version of your chapter, nor may you scan the printed edition to create an electronic version. **Posting to a repository:** Authors are permitted to post a summary of their chapter only in their institution's repository.

19. **Thesis/Dissertation:** If your license is for use in a thesis/dissertation your thesis may be submitted to your institution in either print or electronic form. Should your thesis be published commercially, please reapply for permission. These requirements include permission for the Library and Archives of Canada to supply single copies, on demand, of the complete thesis and include permission for Proquest/UMI to supply single copies, on demand, of the complete thesis. Should your thesis be published commercially, please reapply for permission. Theses and dissertations which contain embedded PJAs as part of the formal submission can be posted publicly by the awarding institution with DOI links back to the formal publications on ScienceDirect.

Elsevier Open Access Terms and Conditions

You can publish open access with Elsevier in hundreds of open access journals or in nearly 2000 established subscription journals that support open access publishing. Permitted third party re-use of these open access articles is defined by the author's choice of Creative Commons user license. See our [open access license policy](#) for more information.

Terms & Conditions applicable to all Open Access articles published with Elsevier:

Any reuse of the article must not represent the author as endorsing the adaptation of the article nor should the article be modified in such a way as to damage the author's honour or reputation. If any changes have been made, such changes must be clearly indicated.

The author(s) must be appropriately credited and we ask that you include the end user license and a DOI link to the formal publication on ScienceDirect.

If any part of the material to be used (for example, figures) has appeared in our publication with credit or acknowledgement to another source it is the responsibility of the user to ensure their reuse complies with the terms and conditions determined by the rights holder.

Additional Terms & Conditions applicable to each Creative Commons user license:

CC BY: The CC-BY license allows users to copy, to create extracts, abstracts and new works from the Article, to alter and revise the Article and to make commercial use of the Article (including reuse and/or resale of the Article by commercial entities), provided the user gives appropriate credit (with a link to the formal publication through the relevant DOI), provides a link to the license, indicates if changes were made and the licensor is not represented as endorsing the use made of the work. The full details of the license are available at <http://creativecommons.org/licenses/by/4.0>.

CC BY NC SA: The CC BY-NC-SA license allows users to copy, to create extracts, abstracts and new works from the Article, to alter and revise the Article, provided this is not done for commercial purposes, and that the user gives appropriate credit (with a link to the formal publication through the relevant DOI), provides a link to the license, indicates if changes were made and the licensor is not represented as endorsing the use made of the work. Further, any new works must be made available on the same conditions. The full details of the license are available at <http://creativecommons.org/licenses/by-nc-sa/4.0>.

CC BY NC ND: The CC BY-NC-ND license allows users to copy and distribute the Article, provided this is not done for commercial purposes and further does not permit distribution of the Article if it is changed or edited in any way, and provided the user gives appropriate credit (with a link to the formal publication through the relevant DOI), provides a link to the license, and that the licensor is not represented as endorsing the use made of the work. The full details of the license are available at <http://creativecommons.org/licenses/by-nc-nd/4.0>. Any commercial reuse of Open Access articles published with a CC BY NC SA or CC BY NC ND license requires permission from Elsevier and will be subject to a fee.

Commercial reuse includes:

- Associating advertising with the full text of the Article
- Charging fees for document delivery or access
- Article aggregation
- Systematic distribution via e-mail lists or share buttons

Posting or linking by commercial companies for use by customers of those companies.

20. Other Conditions:

v1.10

Questions? customercare@copyright.com.

Figure 1-8. Permission to reproduce.

BMJ PUBLISHING GROUP LTD. LICENSE
TERMS AND CONDITIONS

Jan 28, 2024

This Agreement between Western University -- Maksym Sharma ("You") and BMJ Publishing Group Ltd. ("BMJ Publishing Group Ltd.") consists of your license details and the terms and conditions provided by BMJ Publishing Group Ltd. and Copyright Clearance Center.

License Number	5717830001865
License date	Jan 28, 2024
Licensed Content Publisher	BMJ Publishing Group Ltd.
Licensed Content Publication	The BMJ
Licensed Content Title	The natural history of chronic airflow obstruction.
Licensed Content Author	C Fletcher, R Peto
Licensed Content Date	Jun 25, 1977
Licensed Content Volume	1
Type of Use	Dissertation/Thesis
Requestor type	Individual
Format	Print and electronic
Portion	Figure/table/extract

Number of figure/table/extracts 1

Description of figure/table/extracts Figure 1.

Will you be translating? No

Circulation/distribution 1000

Order reference number 3

Title of new work Chest Computed Tomography and Magnetic Resonance Imaging Texture Measurements in Chronic Obstructive Pulmonary Disease

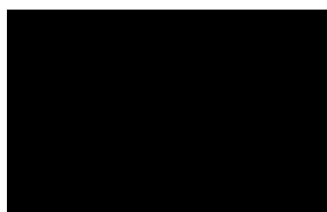
Institution name Western University

Expected presentation date Apr 2024

Order reference number 3

Portions Figure 1.

Requestor Location



Attn: Western University

Publisher Tax ID GB674738491

Total 0.00 CAD

Terms and Conditions

BMJ Terms and Conditions for Permissions

When you submit your order you are subject to the terms and conditions set out below. You will also have agreed to the Copyright Clearance Center's ("CCC") terms and conditions regarding billing and payment <https://s100.copyright.com/App/PaymentTermsAndConditions.jsp>. CCC are acting as BMJ Publishing Group Limited's ("BMJs") agent.

Subject to the terms set out herein, BMJ hereby grants to you (the Licensee) a non-exclusive, non-transferable licence to re-use material as detailed in your request for this/those purpose(s) only and in accordance with the following conditions:

- 1) **Scope of Licence:** Use of the Licensed Material(s) is restricted to the ways specified by you during the order process and any additional use(s) outside of those specified in that request, require a further grant of permission.
- 2) **Acknowledgement:** In all cases, due acknowledgement to the original publication with permission from BMJ should be stated adjacent to the reproduced Licensed Material. The format of such acknowledgement should read as follows:
"Reproduced from [publication title, author(s), volume number, page numbers, copyright notice year] with permission from BMJ Publishing Group Ltd."
- 3) **Third Party Material:** BMJ acknowledges to the best of its knowledge, it has the rights to licence your reuse of the Licensed Material, subject always to the caveat that images/diagrams, tables and other illustrative material included within, which have a separate copyright notice, are presumed as excluded from the licence. Therefore, you should ensure that the Licensed Material you are requesting is original to BMJ and does not carry the copyright of another entity (as credited in the published version). If the credit line on any part of the material you have requested in any way indicates that it was reprinted or adapted by BMJ with permission from another source, then you should seek permission from that source directly to re-use the Licensed Material, as this is outside of the licence granted herein.
- 4) **Altering/Modifying Material:** The text of any material for which a licence is granted may not be altered in any way without the prior express permission of BMJ. If adaptation of the material has been approved via bmj.permissions@bmj.com you must include the disclaimer: "Adapted by permission from BMJ Publishing Group Limited. [publication title, author, volume number, page numbers, copyright notice year]"
- 5) **Reservation of Rights:** BMJ reserves all rights not specifically granted in the combination of (i) the licence details provided by you and accepted in the course of this licensing transaction, (ii) these terms and conditions and (iii) CCC's Billing and Payment Terms and Conditions.
- 6) **Timing of Use:** First use of the Licensed Material must take place within 12 months of the grant of permission.
- 7) **Creation of Contract and Termination:** Once you have submitted an order via RightsLink and this is received by CCC, and subject to you completing accurate details of your proposed use, this is when a binding contract is in effect and our acceptance occurs. As you are ordering rights from a periodical, to the fullest extent permitted by law, you will have no right to cancel the contract from this point other than for BMJ's material breach or fraudulent misrepresentation or as otherwise permitted under a statutory right. Payment must be made in accordance with CCC's Billing and Payment Terms and conditions. In the event that you breach any material condition of these terms and condition or any of CCC's Billing and Payment Terms and Conditions, the license is automatically terminated upon written notice from BMJ or CCC or as otherwise provided

Materials beyond the scope of an unrevoked licence, may constitute intellectual property rights infringement and BMJ reserves the right to take any and all action to protect its intellectual property rights in the Licensed Materials.

8) **Warranties:** BMJ makes no express or implied representations or warranties with respect to the Licensed Material and to the fullest extent permitted by law this is provided on an "as is" basis. For the avoidance of doubt BMJ does not warrant that the Licensed Material is accurate or fit for any particular purpose.

9) **Limitation of Liability:** To the fullest extent permitted by law, BMJ disclaims all liability for any indirect, consequential or incidental damages (including without limitation, damages for loss of profits, information or interruption) arising out of the use or inability to use the Licensed Material or the inability to obtain additional rights to use the Licensed Material. To the fullest extent permitted by law, the maximum aggregate liability of BMJ for any claims, costs, proceedings and demands for direct losses caused by BMJ's breaches of its obligations herein shall be limited to twice the amount paid by you to CCC for the licence granted herein.

10) **Indemnity:** You hereby indemnify and hold harmless BMJ and their respective officers, directors, employees and agents, from and against any and all claims, costs, proceeding or demands arising out of your unauthorised use of the Licensed Material.

11) **No Transfer of License:** This licence is personal to you, and may not be assigned or transferred by you without prior written consent from BMJ or its authorised agent(s). BMJ may assign or transfer any of its rights and obligations under this Agreement, upon written notice to you.

12) **No Amendment Except in Writing:** This licence may not be amended except in a writing signed by both parties (or, in the case of BMJ, by CCC on BMJ's behalf).

13) **Objection to Contrary terms:** BMJ hereby objects to any terms contained in any purchase order, acknowledgment, check endorsement or other writing prepared by you, which terms are inconsistent with these terms and conditions or CCC's Billing and Payment Terms and Conditions. These terms and conditions, together with CCC's Billing and Payment Terms and Conditions (which to the extent they are consistent are incorporated herein), comprise the entire agreement between you and BMJ (and CCC) and the Licensee concerning this licensing transaction. In the event of any conflict between your obligations established by these terms and conditions and those established by CCC's Billing and Payment Terms and Conditions, these terms and conditions shall control.

14) **Revocation:** BMJ or CCC may, within 30 days of issuance of this licence, deny the permissions described in this licence at their sole discretion, for any reason or no reason, with a full refund payable to you should you have not been able to exercise your rights in full. Notice of such denial will be made using the contact information provided by you. Failure to receive such notice from BMJ or CCC will not, to the fullest extent permitted by law alter or invalidate the denial. For the fullest extent permitted by law in no event will BMJ or CCC be responsible or liable for any costs, expenses or damage incurred by you as a result of a denial of your permission request, other than a refund of the amount(s) paid by you to BMJ and/or CCC for denied permissions.

15) **Restrictions to the license:**

15.1) **Promotion:** BMJ will not give permission to reproduce in full or in part any Licensed Material for use in the promotion of the following:

- a) non-medical products that are harmful or potentially harmful to health
- b) medical products that do not have a product license granted by the Medicines and Healthcare products Regulatory Agency (MHRA) or its international equivalents.

members of the medical profession and must conform to the marketing authorization contained in the product license.

16) **Translation:** This permission is granted for non-exclusive world English language rights only unless explicitly stated in your licence. If translation rights are granted, a professional translator should be employed and it must be a true reproduction, accurately conveying the original meaning and of the same quality.

17) **STM Permissions Guidelines:** For content reuse in journals that qualify for permission under the STM Permissions Guidelines (which may be updated from time to time) the terms and conditions of the Guidelines supersede those in this licence.

<https://www.stm-assoc.org/intellectual-property/permissions/permissions-guidelines/>

18) **General:** Neither party shall be liable for failure, default or delay in performing its obligations under this Licence, caused by a Force Majeure event which shall include any act of God, war, or threatened war, act or threatened act of terrorism, riot, strike, lockout, individual action, fire, flood, drought, tempest or other event beyond the reasonable control of either party.

18.1) In the event that any provision of this Agreement is held to be invalid, the remainder of the provisions shall continue in full force and effect.

18.2) There shall be no right whatsoever for any third party to enforce the terms and conditions of this Agreement. The Parties hereby expressly wish to exclude the operation of the Contracts (Rights of Third Parties) Act 1999 and any other legislation which has this effect and is binding on this agreement.

18.3) To the fullest extent permitted by law, this Licence will be governed by the laws of England and shall be governed and construed in accordance with the laws of England. Any action arising out of or relating to this agreement shall be brought in courts situated in England save where it is necessary for BMJ for enforcement to bring proceedings to bring an action in an alternative jurisdiction.

V1.1

Appendix E – Health Science Research Ethics Board Approval Notices



**Western
Research**

Research Ethics

Western University Health Science Research Ethics Board
HSREB Amendment Approval Notice

Principal Investigator: Dr. Grace Parraga

Department & Institution: Schulich School of Medicine and Dentistry\Imaging,Robarts Research Institute

Review Type: Full Board

HSREB File Number: 6014

Study Title: Longitudinal Study of Helium-3 Magnetic Resonance Imaging of COPD (REB #15930)

Sponsor: UWO Internal Research Fund

HSREB Amendment Approval Date: June 07, 2017

HSREB Expiry Date: February 10, 2018

Documents Approved and/or Received for Information:

Document Name	Comments	Version Date
Revised Western University Protocol		2017/05/02
Letter of Information & Consent		2017/05/02

The Western University Health Science Research Ethics Board (HSREB) has reviewed and approved the amendment to the above named study, as of the HSREB Initial Approval Date noted above.

HSREB approval for this study remains valid until the HSREB Expiry Date noted above, conditional to timely submission and acceptance of HSREB Continuing Ethics Review.

The Western University HSREB operates in compliance with the Tri-Council Policy Statement Ethical Conduct for Research Involving Humans (TCPS2), the International Conference on Harmonization of Technical Requirements for Registration of Pharmaceuticals for Human Use Guideline for Good Clinical Practice Practices (ICH E6 R1), the Ontario Personal Health Information Protection Act (PHIPA, 2004), Part 4 of the Natural Health Product Regulations, Health Canada Medical Device Regulations and Part C, Division 5, of the Food and Drug Regulations of Health Canada.

Members of the HSREB who are named as Investigators in research studies do not participate in discussions related to, nor vote on such studies when they are presented to the REB.

The HSREB is registered with the U.S. Department of Health & Human Services under the IRB registration number IRB 00000940.

EO: Erika Basile ___ Grace Kelly ___ Katelyn Harris ___ Nicola Morphet ___ Karen Gopaul Patricia Sargeant ___

Western University, Research, Support Services Bldg., Rm. 5150
London, ON, Canada N6G 1G9 t. 519.661.3036 f. 519.850.2466 www.uwo.ca/research/ethics



Date: 15 January 2019

To: Dr. Grace Parraga

Project ID: 6014

Study Title: Longitudinal Study of Helium-3 Magnetic Resonance Imaging of COPD

Application Type: Continuing Ethics Review (CER) Form

Review Type: Delegated

REB Meeting Date: 29/Jan/2019

Date Approval Issued: 15/Jan/2019

REB Approval Expiry Date: 10/Feb/2020

Dear Dr. Grace Parraga,

The Western University Research Ethics Board has reviewed the application. This study, including all currently approved documents, has been re-approved until the expiry date noted above.

REB members involved in the research project do not participate in the review, discussion or decision.

Western University REB operates in compliance with, and is constituted in accordance with, the requirements of the TriCouncil Policy Statement: Ethical Conduct for Research Involving Humans (TCPS 2); the International Conference on Harmonisation Good Clinical Practice Consolidated Guideline (ICH GCP); Part C, Division 5 of the Food and Drug Regulations; Part 4 of the Natural Health Products Regulations; Part 3 of the Medical Devices Regulations and the provisions of the Ontario Personal Health Information Protection Act (PHIPA 2004) and its applicable regulations. The REB is registered with the U.S. Department of Health & Human Services under the IRB registration number IRB 00000940.

Please do not hesitate to contact us if you have any questions.

Sincerely,

Daniel Wyzynski, Research Ethics Coordinator, on behalf of Dr. Joseph Gilbert, HSREB Chair

Note: This correspondence includes an electronic signature (validation and approval via an online system that is compliant with all regulations).



Western Research

Date: 17 January 2020

To: Dr. Grace Parraga

Project ID: 6014

Study Title: Longitudinal Study of Helium-3 Magnetic Resonance Imaging of COPD

Application Type: Continuing Ethics Review (CER) Form

Review Type: Delegated

REB Meeting Date: 28/Jan/2020

Date Approval Issued: 17/Jan/2020

REB Approval Expiry Date: 10/Feb/2021

Dear Dr. Grace Parraga,

The Western University Research Ethics Board has reviewed the application. This study, including all currently approved documents, has been re-approved until the expiry date noted above.

REB members involved in the research project do not participate in the review, discussion or decision.

Western University REB operates in compliance with, and is constituted in accordance with, the requirements of the TriCouncil Policy Statement: Ethical Conduct for Research Involving Humans (TCPS 2); the International Conference on Harmonisation Good Clinical Practice Consolidated Guideline (ICH GCP); Part C, Division 5 of the Food and Drug Regulations; Part 4 of the Natural Health Products Regulations; Part 3 of the Medical Devices Regulations and the provisions of the Ontario Personal Health Information Protection Act (PHIPA 2004) and its applicable regulations. The REB is registered with the U.S. Department of Health & Human Services under the IRB registration number IRB 00000940.

Please do not hesitate to contact us if you have any questions.

Sincerely,

Daniel Wyzynski, Research Ethics Coordinator, on behalf of Dr. Joseph Gilbert, HSREB Chair

Note: This correspondence includes an electronic signature (validation and approval via an online system that is compliant with all regulations).



Date: 26 January 2021

To: Dr. Grace Parraga

Project ID: 6014

Study Title: Longitudinal Study of Helium-3 Magnetic Resonance Imaging of COPD

Application Type: Continuing Ethics Review (CER) Form

Review Type: Delegated

REB Meeting Date: 09/Feb/2021

Date Approval Issued: 26/Jan/2021

REB Approval Expiry Date: 10 Feb/2022

Dear Dr. Grace Parraga,

The Western University Research Ethics Board has reviewed the application. This study, including all currently approved documents, has been re-approved until the expiry date noted above.

REB members involved in the research project do not participate in the review, discussion or decision.

Western University REB operates in compliance with, and is constituted in accordance with, the requirements of the Tri-Council Policy Statement: Ethical Conduct for Research Involving Humans (TCPS 2); the International Conference on Harmonisation Good Clinical Practice Consolidated Guideline (ICH GCP); Part C, Division 5 of the Food and Drug Regulations; Part 4 of the Natural Health Products Regulations; Part 3 of the Medical Devices Regulations and the provisions of the Ontario Personal Health Information Protection Act (PHIPA 2004) and its applicable regulations. The REB is registered with the U.S. Department of Health & Human Services under the IRB registration number IRB 00000940.

Please do not hesitate to contact us if you have any questions.

Sincerely,

The Office of Human Research Ethics

Note: This correspondence includes an electronic signature (validation and approval via an online system that is compliant with all regulations).



Date: 25 January 2022

To: Dr. Grace Parraga

Project ID: 6014

Study Title: Longitudinal Study of Helium-3 Magnetic Resonance Imaging of COPD

Application Type: Continuing Ethics Review (CER) Form

Review Type: Delegated

Date Approval Issued: 25/Jan/2022

REB Approval Expiry Date: 10/Feb/2023

Dear Dr. Grace Parraga,

The Western University Research Ethics Board has reviewed the application. This study, including all currently approved documents, has been re-approved until the expiry date noted above.

REB members involved in the research project do not participate in the review, discussion or decision.

Western University REB operates in compliance with, and is constituted in accordance with, the requirements of the Tri-Council Policy Statement: Ethical Conduct for Research Involving Humans (TCPS 2); the International Conference on Harmonisation Good Clinical Practice Consolidated Guideline (ICH GCP); Part C, Division 5 of the Food and Drug Regulations; Part 4 of the Natural Health Products Regulations; Part 3 of the Medical Devices Regulations and the provisions of the Ontario Personal Health Information Protection Act (PHIPA 2004) and its applicable regulations. The REB is registered with the U.S. Department of Health & Human Services under the IRB registration number IRB 00000940.

Please do not hesitate to contact us if you have any questions.

Sincerely,

The Office of Human Research Ethics

Note: This correspondence includes an electronic signature (validation and approval via an online system that is compliant with all regulations).



Date: 13 January 2023

To: Dr. Grace Parraga

Project ID: 6014

Review Reference: 2023-6014-74913

Study Title: Longitudinal Study of Helium-3 Magnetic Resonance Imaging of COPD

Application Type: Continuing Ethics Review (CER) Form

Review Type: Delegated

REB Meeting Date: 24/Jan/2023

Date Approval Issued: 13/Jan/2023 16:19

REB Approval Expiry Date: 10/Feb/2024

Dear Dr. Grace Parraga,

The Western University Research Ethics Board has reviewed the application. This study, including all currently approved documents, has been re-approved until the expiry date noted above.

REB members involved in the research project do not participate in the review, discussion or decision.

Western University REB operates in compliance with, and is constituted in accordance with, the requirements of the Tri-Council Policy Statement: Ethical Conduct for Research Involving Humans (TCPS 2); the International Conference on Harmonisation Good Clinical Practice Consolidated Guideline (ICH GCP); Part C, Division 5 of the Food and Drug Regulations; Part 4 of the Natural Health Products Regulations; Part 3 of the Medical Devices Regulations and the provisions of the Ontario Personal Health Information Protection Act (PHIPA 2004) and its applicable regulations. The REB is registered with the U.S. Department of Health & Human Services under the IRB registration number IRB 00000940.

Please do not hesitate to contact us if you have any questions.

Electronically signed by:

Karen Gopaul, Ethics Officer on behalf of Dr. P. Jones, HSREB Chair 13/Jan/2023 16:19

Reason: I am approving this document

Note: This correspondence includes an electronic signature (validation and approval via an online system that is compliant with all regulations).



Western Research

Date: 26 January 2024

To: Dr. Grace Parraga

Project ID: 6014

Review Reference: 2024-6014-87969

Study Title: Longitudinal Study of Helium-3 Magnetic Resonance Imaging of COPD

Application Type: Continuing Ethics Review (CER) Form

Review Type: Delegated

Date Approval Issued: 26/Jan/2024 20:45

REB Approval Expiry Date: 10/Feb/2025

Dear Dr. Grace Parraga,

The Western University Research Ethics Board has reviewed the application. This study, including all currently approved documents, has been re-approved until the expiry date noted above.

REB members involved in the research project do not participate in the review, discussion or decision.

Western University REB operates in compliance with, and is constituted in accordance with, the requirements of the Tri-Council Policy Statement: Ethical Conduct for Research Involving Humans (TCPS 2); the International Conference on Harmonisation Good Clinical Practice Consolidated Guideline (ICH GCP); Part C, Division 5 of the Food and Drug Regulations; Part 4 of the Natural Health Products Regulations; Part 3 of the Medical Devices Regulations and the provisions of the Ontario Personal Health Information Protection Act (PHIPA 2004) and its applicable regulations. The REB is registered with the U.S. Department of Health & Human Services under the IRB registration number IRB 00000940.

Please do not hesitate to contact us if you have any questions.

Electronically signed by:

Mr. Joshua Hatherley, Ethics Coordinator on behalf of Dr. N. Poonai, HSREB Chair 26/Jan/2024 20:45

Reason: I am approving this document

Note: This correspondence includes an electronic signature (validation and approval via an online system that is compliant with all regulations).

Appendix F – Curriculum Vitae
Curriculum Vitae – Maksym Sharma BSc (Hons)

PhD Candidate, Department of Medical Biophysics

Supervisor: Dr. Grace Parraga

EDUCATION

- 2019-2024** Ph.D. Candidate (CAMPEP stream) – Department of Medical Biophysics
Robarts Research Institute (*Supervisor* – Dr. Grace Parraga)
The University of Western Ontario, London, Canada
- 2015-2019** Honours B.Sc. – Biomedical Physics Specialist program
Additional Double Minor in Chemistry and Biology
University of Toronto, Toronto, Canada
- 2011-2015** High School Diploma – Science stream
Embassy of India School (Kendriya Vidyalaya Moscow)
Moscow, Russia

EMPLOYMENT AND RESEARCH POSITIONS

- 2023-Present** **University of Western Ontario, Robarts Research Institute**
Graduate Student Assistant, Advanced Pulmonary Imaging (API) Lab
- 2021-Present** **University of Western Ontario, Department of Medical Biophysics**
Graduate Teaching Assistant, Course instructor – Dr. John McGuire
Course: BIOPHYS 3501 – Biophysics of Transport Systems (Fall Semester)
- 2019-Present** **University of Western Ontario, Department of Medical Biophysics**
Graduate Fellowship, Supervised by – Dr. Grace Parraga
- 2019-2019** **Credit Valley Hospital, Trillium Health Partners**
Medical Physics Department, Supervised by – Dr. Xia Wu
Project titled – A tool to decode DICOM files for display and co-registering of patient respiratory wave with 4DCT images
- 2018-2019** **University of Toronto, Department of Chemical & Physical Sciences**
Undergraduate Research Student, Supervised by – Dr. Virginijus Barzda
Project titled – Classification of Hand-written digits using an artificial neural network (ANN)
- 2018-2019** **University of Toronto, Department of Chemical & Physical Sciences**
Undergraduate Research Student, Supervised by – Dr. Claudiu Gradinaru
Project titled – Studying the Action of Different Phosphorylation Kinases on the Intrinsically Disordered Sic1 Protein
- 2018-2019** **University of Toronto, Office of Student Engagement**
Research Assistant, Supervised by – Laura Walkling
- 2018-2019** **TutorBright Company**
Private Tutor, STEM field subjects for students in grades 7-12

HONOURS, AWARDS, AND RECOGNITIONS

Total	Value	International	National	Provincial	Institutional
17	> \$118,280	6	3	3	5

2023	<p>Natural Sciences and Engineering Research Council of Canada (NSERC) Post-graduate Scholarship – Doctoral (PGSD3) <i>Awarded to high-calibre scholars who are engaged in a doctoral program in the natural sciences or engineering (\$63,000 CAD across 3-years)</i> National \$21,000 CAD</p> <p>University of Western Ontario, Department of Medical Biophysics - WGRS <i>Western Graduate Research Scholarship (WGRS) - Awarded to full time graduate students for stipend support who had maintained an average of 80% or more</i> Institutional \$5,000 CAD</p> <p>Canadian Institutes of Health Research – Institute of Circulatory and Respiratory Health (CIHR-ICRH) Spring Travel Award <i>Awarded to trainees as travel funds in support of knowledge mobilization activities aligned with the CIHR-ICRH vision, mandate, and strategic directions</i> National \$1,500 CAD</p>
2022	<p>University of Western Ontario, Department of Medical Biophysics – WGRS <i>Western Graduate Research Scholarship (WGRS) - Awarded to full time graduate students for stipend support who had maintained an average of 80% or more</i> Institutional \$5,000 CAD</p> <p>London Imaging Discovery Day (LIDD) Conference - Honourable Mention <i>Awarded to the oral presenter in recognition of the distinction of their talk</i> Provincial</p> <p>Ontario Graduate Scholarship (OGS) - Doctoral <i>Awarded to high-calibre scholars who are engaged in all disciplines of graduate study programs</i> Provincial \$15,000 CAD - <u>Declined</u></p> <p>Natural Sciences and Engineering Research Council of Canada (NSERC) Post-graduate Scholarship – Doctoral (PGSD3) <i>Awarded to high-calibre scholars who are engaged in a doctoral program in the natural sciences or engineering (\$63,000 CAD across 3-years)</i> National \$21,000 CAD</p> <p>International Society for Magnetic Resonance in Medicine (ISMRM) – Educational Stipend</p>

Awarded ISMRM trainee members who submitted an outstanding abstract to the ISMRM & SMRT Annual Meeting & Exhibition
International
\$655 USD

2021

University of Western Ontario, Department of Medical Biophysics - WGRS

Western Graduate Research Scholarship (WGRS) - Awarded to full time graduate students for stipend support who had maintained an average of 80% or more
Institutional
\$5,000 CAD

American Thoracic Society (ATS) – Abstract Scholarship, Respiratory Structure and Function (RSF)

Awarded to an ATS member who submitted an outstanding abstract to the ATS Annual Scientific Meeting
International
\$325 USD

International Society for Magnetic Resonance in Medicine (ISMRM) – Trainee Educational Stipend

Awarded ISMRM trainee members who submitted an outstanding abstract to the ISMRM & SMRT Annual Meeting & Exhibition
International
\$250 USD

International Society of Photo-Optical Instrumentation Engineers (SPIE) – Robert F. Wagner (RFW) All-Conference Student Paper Award

Awarded to top-ranking student manuscript submissions across all sessions of the conference - Finalist with submission Paper No: 11600-11
International

International Society of Photo-Optical Instrumentation Engineers (SPIE) – Biomedical Applications in Molecular, Structural, and Functional Imaging (11600) Session Award

Secured 1st Place in session #11600 for abstract submission and presentation
International

2020

University of Western Ontario, Department of Medical Biophysics – WGRS

Western Graduate Research Scholarship (WGRS) - Awarded to full time graduate students for stipend support who had maintained an average of 80% or more
Institutional
\$5,000 CAD

American Thoracic Society (ATS) – Abstract Scholarship, Respiratory Structure and Function (RSF)

Awarded to an ATS member who submitted an outstanding abstract to the ATS Annual Scientific Meeting
International
\$50 USD

2019

University of Western Ontario, Department of Medical Biophysics – WGRS

Western Graduate Research Scholarship (WGRS) - Awarded to full time graduate students for stipend support who had maintained an average of 80% or more Institutional
\$5,000 CAD

Cancer Care Ontario (CCO), Harold E. Johns Studentship Award
Once-in-a-lifetime studentship position, awarded based on academic and research accolades and held at the Carlo Fidani Regional Cancer Centre
Provincial
\$12,500 CAD

PUBLICATIONS AND PRESENTATIONS

A Peer-Reviewed Journal Manuscripts

Published/In-press – (7 total; 4 first-author)

1. **M Sharma**, M Kirby, DG McCormack and G Parraga. Machine Learning and CT Texture Features in Ex-smokers with no CT Evidence of Emphysema and Mildly Abnormal Diffusing Capacity. *Academic Radiology Journal*. 2023. (Accepted Manuscript ID: ARAD-D-23-02040R1).
2. G Parraga and **M Sharma**. Don't forget the kids! Novel pulmonary MRI and AI of neonatal lung disease. *Radiology: Artificial Intelligence*. 2023. <https://doi.org/10.1148/ryai.230400>
3. JM Wild, FV Gleeson, S Svenningsen, JT Grist, LC Saunders, GJ Collier, **M Sharma**, S Tchnerer, A Mozaffaripour, AM Matheson and G Parraga. Review of Hyperpolarized Pulmonary Functional ¹²⁹Xe MR for Long-COVID. *Journal of Magnetic Resonance Imaging*, 2023. <https://doi.org/10.1002/jmri.28940>
4. **M Sharma**, PV Wyszkievicz, AM Matheson, DG McCormack and G Parraga. Chest MRI and CT Predictors of 10-Year All-cause Mortality in COPD. *Journal of Chronic Obstructive Pulmonary Disease*, 11 September 2023. <https://doi.org/10.1080/15412555.2023.2259224>
5. PV Wyszkievicz, **M Sharma**, V Desaigoudar, IA Cunningham, DG McCormack, M Abdelrazek, M Kirby and G Parraga. Reduced Total Airway Count and Airway Wall Tapering after Three-Years in Ex-Smokers. *Journal of Chronic Obstructive Pulmonary Disease*. (3 July 2023). <https://doi.org/10.1080/15412555.2023.2222831>
6. **M Sharma**, PV Wyszkievicz, V Desaigoudar, F Guo, DPI Capaldi and G Parraga. Quantification of pulmonary functional MRI: state-of-the-art and emerging image processing methods and measurements. *Physics in Medicine & Biology* 2022. <https://doi.org/10.1088/1361-6560/ac9510>
7. **M Sharma**, AR Westcott, DG McCormack and G Parraga. Hyperpolarized gas magnetic resonance imaging texture analysis and machine learning to explain accelerated lung function decline in ex-smokers with and without COPD. *Proc. SPIE 11600, Medical Imaging 2021: Biomedical Applications in Molecular, Structural, and Functional Imaging*, 116000E (14 February 2021). <https://doi.org/10.1117/12.2580451>

Submitted – (5 total, 1 first-author)

8. JJ Hofmann, VC Poulos, J Zhou, **M Sharma**, G Parraga and MJ McIntosh. Review of Quantitative and Functional Lung Imaging Evidence of Vaping-related Lung Injury. *Submitted to Frontiers in Medicine* (Manuscript ID: 1285361)

9. VC Poulos, S Kassirian, MJ McIntosh, **M Sharma**, HK Kooner, G Parraga and MA Mitchell. Oscillometry, Lung Clearance Index and ^{129}Xe MRI Detect Small Airways Dysfunction in Sarcoidosis. *Submitted to Thorax Journal 2023* (Manuscript ID: thorax-2023-221198)
10. HK Kooner, **M Sharma**, MJ McIntosh, I Dhaliwal, JM Nicholson, M Kirby, S Svenningsen, and G Parraga. Long-COVID: ^{129}Xe MRI Ventilation Textures and Longitudinal Quality-of-Life Improvements. *Submitted to Radiology* (Manuscript ID: RAD-23-2762).
11. **M Sharma**, A Fenster, DG McCormack and G Parraga. Machine-learning and Texture Analysis of Hyperpolarized gas MRI Predicts Accelerated Disease Progression Across 3-years in COPD. *Submitted to Journal of Medical Imaging*. (Manuscript ID: JMI 24004G)
12. A Mozaffaripour, S Tchner, **M Sharma**, HK Kooner, MJ McIntosh, M Sherwood, N Paul, JM Nicholson, I Dhaliwal, S Jeimy, C Licskai, CA Mackenzie, M Kuprowski, A Bhalla, C Yamashita and G Parraga. ^{129}Xe Ventilation MRI and Asthma Control After Six-Weeks ICS/LABA/LAMA in Poorly-Controlled Asthma. 2024. *Submitted to CHEST*. (Manuscript ID: CHEST-D-24-00014)

In-preparation – (2 total)

13. A Mozaffaripour, **M Sharma**, S Tchner, HK Kooner, I Dhaliwal, C Yamashita and G Parraga. ^{129}Xe MRI Texture Analysis and Machine-learning Predicts Improvements in Asthma after 6-weeks of Therapy. *Journal of Magnetic Resonance in Medicine*.
14. J Zhou, **M Sharma**, MJ McIntosh, A Price, JM Nicholson and G Parraga. Hyperpolarized ^{129}Xe MRI Following Three-months of Elexacaftor/Tezacaftor/Ivacaftor in Cystic Fibrosis. *Thorax*.

ABSTRACTS AND PRESENTATIONS

B Peer-Reviewed Conference Abstracts

Total	Oral / Poster	International	National	Provincial	Institutional
36	24 / 12	16	3	9	8

Published – (36 total; 17 first-author; 9 submitted)

1. **M Sharma**, PV Wyszkiwicz, MJ McIntosh, HK Kooner, AM Matheson, DG McCormack and G Parraga. *MRI and CT Measurements Uniquely Explain All-cause Mortality in Ex-smokers with and without COPD*. Roberts Research Retreat. London, ON. June 28, 2023. (Institutional)
2. PV Wyszkiwicz, **M Sharma**, HK Kooner, DG McCormack, M Kirby and G Parraga. *Terminal Airspace Enlargement Measured Using Pulmonary Functional MRI Predicts CT Airway Loss in COPD*. Annual International Society of Magnetic Resonance in Medicine Scientific Meeting 2023, Toronto, Canada. June 3-8, 2023. (International)
3. MJ McIntosh, **M Sharma**, HK Kooner, H Serajeddini, A Bhalla, C Yamashita, and G Parraga. *Hyperpolarized ^{129}Xe MRI ventilation textures predict short and long-term response to Anti-IL-5Ra Biologic Therapy in Eosinophilic Asthma*. Annual International Society of Magnetic Resonance in Medicine Scientific Meeting 2023, Toronto, Canada. June 3-8, 2023. (International)
4. HK Kooner, **M Sharma**, MJ McIntosh, I Dhaliwal, JM Nicholson, and G Parraga. *^{129}Xe MRI Ventilation Predicts Longitudinal Quality-of-Life Improvement in Post-Acute COVID-19 Syndrome*. Annual International Society of Magnetic Resonance in Medicine Scientific Meeting 2023, Toronto, Canada. June 3-8, 2023. (International)

5. **M Sharma**, PV Wyszkievicz, MJ McIntosh, HK Kooner, AM Matheson, DG McCormack and G Parraga. *MRI and CT Measurements Uniquely Explain All-cause Mortality in Ex-smokers with and without COPD*. American Thoracic Society Annual Scientific Meeting. Washington, DC. May 19-24, 2023. (International)
6. PV Wyszkievicz, **M Sharma**, V Desaigoudar, DG McCormack, M Kirby and G Parraga. *Progressive Airway Wall Thinning and Loss of Total Airway Count after Three-Years in COPD*. American Thoracic Society Annual Scientific Meeting. Washington, DC. May 19-24, 2023. (International)
7. MJ McIntosh, **M Sharma**, HK Kooner, H Serajeddini, A Bhalla, C Yamashita, and G Parraga. *Hyperpolarized ^{129}Xe MRI ventilation textures predict short and long-term response to Anti-IL-5Ra Biologic Therapy in Eosinophilic Asthma*. Imaging Network of Ontario Annual Symposium, London Ontario. March 23-24, 2023. (Provincial)
8. **M Sharma**, PV Wyszkievicz, MJ McIntosh, HK Kooner, AM Matheson, DG McCormack and G Parraga. *CT and MRI Measurements Uniquely Explain All-cause Mortality in Ex-smokers*. Imaging Network of Ontario Annual Symposium, London Ontario. March 23-24, 2023. (Provincial)
9. PV Wyszkievicz, **M Sharma**, V Desaigoudar, DG McCormack, M Kirby and G Parraga. *Progressive Airway Wall Thinning and Loss of Total Airway Count after Three-Years in COPD*. Imaging Network Ontario Annual Symposium. London, ON. March 23-24, 2023. (Provincial)
10. V Desaigoudar, PV Wyszkievicz, AM Matheson, **M Sharma**, MJ McIntosh, HK Kooner, DG McCormack and G Parraga. *Pulmonary Small Vessel Worsening in Ex-smokers with COPD*. Imaging Network of Ontario Annual Symposium, London Ontario. March 23-24, 2023. (Provincial)
11. V Desaigoudar, PV Wyszkievicz, AM Matheson, **M Sharma**, MJ McIntosh, HK Kooner, DG McCormack and G Parraga. *CT Pulmonary Vascular, Airway, Pulmonary Artery and Aorta Measurements in Ex-Smokers with and without COPD*. Canadian Undergraduate Medical Physics Conference. August 25 2022. Virtual. (National)
12. **M Sharma**, MJ McIntosh, HK Kooner, DG McCormack and G Parraga. *Machine-Learning and Texture Analysis of Hyperpolarized ^3He MRI Ventilation Predicts Quality-of-life Worsening in Ex-smokers with and without COPD*. 68th annual Canadian Organization of Medical Physicists (COMP) scientific meeting, June 22-25 2022, Quebec City, QC, Canada. (National)
13. **M Sharma**, MJ McIntosh, HK Kooner, AM Matheson, PV Wyszkievicz, DG McCormack, and G Parraga. *Texture Analysis and Machine Learning of Hyperpolarized ^3He MRI Ventilation Predicts Quality-of-life Worsening in Ex-smokers with and without COPD*. Robarts Research Retreat. London ON, Canada. June 16 2022. (Institutional)
14. PV Wyszkievicz, **M Sharma**, DG McCormack, IA Cunningham, and G Parraga. *CT Pulmonary Airways in Chronic Obstructive Pulmonary Disease: Longitudinal Worsening in the TINCan Cohort Study*. Robarts Research Retreat. London ON, Canada. June 16 2022. (Institutional)
15. HK Kooner, MJ McIntosh, AM Matheson, **M Sharma**, PV Wyszkievicz, I Dhaliwal, M Abdelrazek, M Nicholson, and G Parraga. *^{129}Xe MRI Ventilation Defects in People with Post-Acute COVID-19 Syndrome*. Robarts Research Retreat. London ON, Canada. June 16 2022. (Institutional)
16. **M Sharma**, MJ McIntosh, HK Kooner, AM Matheson, PV Wyszkievicz, DG McCormack, and G Parraga. *Texture Analysis and Machine Learning of Hyperpolarized ^3He MRI Ventilation Predicts Quality-of-life Worsening in Ex-smokers with and without COPD*. London Imaging Discovery Day. London ON, Canada. June 9 2022. (Provincial)

17. HK Kooner, MJ McIntosh, AM Matheson, **M Sharma**, PV Wyszkievicz, I Dhaliwal, M Nicholson, M Abdelrazek, and G Parraga. *¹²⁹Xe MRI Ventilation Defects in People with Post-Acute COVID-19 Syndrome*. London Imaging Discovery Day. London ON, Canada. June 9 2022. (Provincial)
18. PV Wyszkievicz, **M Sharma**, DG McCormack, IA Cunningham, and G Parraga. *CT Pulmonary Airways in Chronic Obstructive Pulmonary Disease: Longitudinal Worsening in the TINCan Cohort Study*. London Imaging Discovery Day. London ON, Canada. June 9 2022. (Provincial)
19. **M Sharma**, HK Kooner, MJ McIntosh, DG McCormack and G Parraga. *Quality-of-life Worsening Predicted Using Baseline Hyperpolarized ³He MRI Ventilation Texture Features and Machine-Learning*. Joint annual International Society of Magnetic Resonance in Medicine-European Society for Magnetic Resonance in Medicine and Biology (ISMRM-ESMRMB) Scientific Meeting 2022, London, England, UK May 7-12 2022. (International)
20. MJ McIntosh, **M Sharma**, AM Matheson, HK Kooner, RL Eddy, C Licksai, DG McCormack, M Nicholson, C Yamashita and G Parraga. *Respiratory System Resistance Explained using Hyperpolarized ¹²⁹Xe MRI Texture Features and Machine Learning*. Joint annual International Society of Magnetic Resonance in Medicine-European Society for Magnetic Resonance in Medicine and Biology (ISMRM-ESMRMB) Scientific Meeting 2022, London, England, UK May 7-12, 2022. (International)
21. HK Kooner, MJ McIntosh, **M Sharma**, GV Singh, N Nasir, E Blake, I Dhaliwal, M Nicholson, M Kirby and G Parraga. *Post-Acute COVID-19 Syndrome: Longitudinal ¹²⁹Xe MRI Ventilation Heterogeneity Measurements*. Joint annual International Society of Magnetic Resonance in Medicine-European Society for Magnetic Resonance in Medicine and Biology (ISMRM-ESMRMB) Scientific Meeting 2022, London, England, UK May 7-12, 2022. (International)
22. MJ McIntosh, AM Matheson, **M Sharma**, HK Kooner, RL Eddy, DG McCormack, C Yamashita and G Parraga. *Pulmonary 1H MRI Lobar Classification using Convolutional Neural Networks*. 67th annual Canadian Organization of Medical Physicist scientific meeting, June 22-25, 2021, Virtual. (National)
23. **M Sharma**, AM Matheson, DG McCormack, DA Palma and G Parraga. *Hyperpolarized ³He MRI ADC and Ventilation Features Predict Rapidly Worsening Emphysema Using Machine-learning*. 29th annual International Society of Magnetic Resonance in Medicine scientific meeting, May 15-20, 2021, Virtual. (International)
24. HK Kooner, MJ McIntosh, **M Sharma**, AM Matheson, Y Rajapaksa, I Dhaliwal, M Nicholson and G Parraga. *Hyperpolarized ¹²⁹Xe MRI Ventilation Texture Features to Characterize Long-haul COVID-19 Survivors*. 29th annual International Society for Magnetic Resonance in Medicine scientific meeting, May 15-20, 2021, Virtual. (International)
25. **M Sharma**, MJ McIntosh, AM Matheson, HK Kooner, DG McCormack, DA Palma and G Parraga. *6MWD worsening in COPD predicted using CT and MRI Texture Features and Machine Learning*. 117th annual American Thoracic Society scientific meeting, May 14-19, 2021, Virtual. (International)
26. **M Sharma**, MJ McIntosh, AM Matheson, HK Kooner, DG McCormack, DA Palma and G Parraga. *Six Minute Walk Distance worsening in COPD predicted using CT and MRI Texture Features and Machine Learning*. Annual Robarts Research Retreat, June 17, 2021, Virtual. (Institutional)
27. HK Kooner, MJ McIntosh, **M Sharma**, AM Matheson, Y Rajapaksa, I Dhaliwal, M Nicholson and G Parraga. *Hyperpolarized ¹²⁹Xe MRI Ventilation Texture Features to Characterize Long-haul COVID-19 Survivors*. Annual Robarts Research Retreat, June 17, 2021, Virtual. (Institutional)

28. MJ McIntosh, AM Matheson, **M Sharma**, HK Kooner, RL Eddy, DG McCormack, C Yamashita and G Parraga. *Pulmonary 1H MRI Lobar Classification using Convolutional Neural Networks*. Annual Roberts Research Retreat, June 17, 2021, Virtual. (Institutional)
29. **M Sharma**, AR Westcott, A Fenster, DG McCormack and G Parraga. *Hyperpolarized Gas Magnetic Resonance Imaging Texture Analysis and Machine Learning Explains Accelerated Lung Function Decline in Ex-smokers with COPD*. Annual Society for Photo-optical Instrumentation Engineers scientific meeting, February 15-19, 2021, Virtual. (International)
30. **M Sharma**, AR Westcott, JL MacNeil, DG McCormack and G Parraga. *Machine Learning and Texture Analysis of Thoracic X-ray Computed Tomography to Reveal Subclinical Emphysema*. The American Association of Physicists in Medicine – Canadian Organization of Medical Physicists Joint meeting, July 12-16, 2020, Virtual. (International)
31. **M Sharma**, AR Westcott, JL MacNeil, DG McCormack and G Parraga. *Machine Learning with Texture Analysis Reveals Subclinical Emphysema in Thoracic X-ray Computed Tomography*. Annual Roberts Research Retreat, June 19, 2020, Virtual. (Institutional)
32. **M Sharma**, AR Westcott, JL MacNeil, B Hou, DG McCormack and G Parraga. *Hidden Computed Tomography Texture Features in Ex-smokers with Abnormal Spirometry? Playing Hide and Seek Using Machine Learning*. 116th annual American Thoracic Society scientific meeting May 15-20, 2020, Virtual. (International)
33. JL MacNeil, B Hou, **M Sharma**, DG McCormack and G Parraga. *Ex-smokers with Abnormal Diffusing Capacity and Normal CT: Multi-parametric Response Map Phenotypes*. 116th annual American Thoracic Society scientific meeting, May 15-20, 2020, Virtual. (International)
34. **M Sharma**, AR Westcott, JL MacNeil, DG McCormack and G Parraga. *Extracting Computed Tomography Texture Features That Explain Abnormal Pulmonary Diffusion Using Machine Learning*. 9th annual London Health Research Day scientific meeting, May 5, 2020, London ON. (Provincial, Cancelled due to COVID19)
35. **M Sharma**, AR Westcott, A Fenster, DG McCormack and G Parraga. *Can Hyperpolarized Gas MRI and Machine Learning Predict Longitudinal Changes in Airflow Limitation in Ex-smokers?* 28th annual International Society of Magnetic Resonance in Medicine scientific meeting, April 18-23, 2020, Virtual. (International)
36. **M Sharma**, AR Westcott, JL MacNeil, DG McCormack and G Parraga. *Identifying Functional Information Determinants in Thoracic Computed Tomography Images Using Machine Learning*. 18th annual Imaging Network of Ontario scientific meeting, March 26-27, 2020, Virtual. (Provincial)

Submitted – (9 total; 3 first-author; 9 international)

1. **M Sharma**, HK Kooner, S Tchnerer, A Mozaffaripour, N Paul, C Yamashita, and G Parraga. *Rapid 6-week Response to ICS/LABA/LAMA which persists in Mild-moderate Asthma*. American Thoracic Society Annual Scientific Meeting. San Diego, CA, USA. May 17-24, 2024. (International)
2. S Tchnerer, A Mozaffaripour, HK Kooner, **M Sharma**, Y Aseffa, N Paul, C Yamashita, and G Parraga. *CT Mucus Score predicts Response to ICS/LABA/LAMA in Moderate Asthma*. American Thoracic Society Annual Scientific Meeting. San Diego, CA, USA. May 17-24, 2024. (International)
3. A Mozaffaripour, S Tchnerer, **M Sharma**, HK Kooner, MJ McIntosh, N Paul, C Yamashita and G Parraga. *¹²⁹Xe MRI and oscillometry evidence of small airways response after 6-weeks ICS/LABA/LAMA in Moderate Asthma*. American Thoracic Society Annual Scientific Meeting. San Diego, CA, USA. May 17-24, 2024. (International)

4. HK Kooner, S Tchner, H Serajeddini, A Mozaffaripour, **M Sharma**, Y Aseffa, N Paul, C Yamashita, and G Parraga. *What is CT Mucus Burden in Mild-moderate versus Severe Asthma?* American Thoracic Society Annual Scientific Meeting. San Diego, CA, USA. May 17-24, 2024. (International)
5. **M Sharma**, HK Kooner, S Tchner, A Mozaffaripour, N Paul, C Yamashita, and G Parraga. *¹²⁹Xe MR evidence of Abnormal Gas-exchange in Mild-moderate and Severe Asthma.* American Thoracic Society Annual Scientific Meeting. San Diego, CA, USA. May 17-24, 2024. (International)
6. HK Kooner, A Mozaffaripour, S Tchner, **M Sharma**, MJ McIntosh, N Paul, C Yamashita, and G Parraga. *Are there Pulmonary Vascular Differences Across Asthma Severity?* American Thoracic Society Annual Scientific Meeting. San Diego, CA, USA. May 17-24, 2024. (International)
7. HK Kooner, **M Sharma**, A Mozaffaripour, S Tchner, C Yamashita, and G Parraga. *¹²⁹Xe MRS Biomarkers Predict 6-week Response to ICS/LAMA/LABA in Moderate Asthma.* International Society for Magnetic Resonance in Medicine Annual Meeting & Exhibition. Singapore. May 4-9, 2024. (International)
8. **M Sharma**, HK Kooner, A Mozaffaripour, S Tchner, C Yamashita, and G Parraga. *¹²⁹Xe MR Spectroscopy Reveals Abnormal Gas-exchange in Moderate and Severe Asthma.* Annual International Society of Magnetic Resonance in Medicine Scientific Meeting 2024. Singapore. May 04-09, 2024. (International)
9. A Mozaffaripour, S Tchner, **M Sharma**, HK Kooner, MJ McIntosh, C Yamashita, and G Parraga. *¹²⁹Xe MRI Ventilation Texture Features and Machine Learning to Predict Response to ICS/LABA/LAMA in Moderate Asthma.* International Society for Magnetic Resonance in Medicine Annual Meeting & Exhibition. Singapore. May 4-9, 2024. (International)

C Proffered Oral Presentations

Published – (24 total; 11 first-author) *presenter

1. PV Wyszkievicz, * **M Sharma**, V Desai, DG McCormack, M Kirby and G Parraga. *Progressive Airway Wall Thinning and Loss of Total Airway Count after Three-Years in COPD.* American Thoracic Society Annual Scientific Meeting. Washington, DC. May 19-24, 2023.
2. **M Sharma**,* PV Wyszkievicz, MJ McIntosh, HK Kooner, AM Matheson, DG McCormack and G Parraga. *MRI and CT Measurements Uniquely Explain All-cause Mortality in Ex-smokers with and without COPD.* American Thoracic Society Annual Scientific Meeting. Washington, DC. May 19-24, 2023.
3. MJ McIntosh,* **M Sharma**, HK Kooner, H Serajeddini, A Bhalla, C Yamashita, and G Parraga. *Hyperpolarized ¹²⁹Xe MRI ventilation textures predict short and long-term response to Anti-IL-5Ra Biologic Therapy in Eosinophilic Asthma.* Imaging Network of Ontario Annual Symposium, London Ontario. March 23-24, 2023.
4. PV Wyszkievicz,* **M Sharma**, V Desai, DG McCormack, M Kirby and G Parraga. *Progressive Airway Wall Thinning and Loss of Total Airway Count after Three-Years in COPD.* Imaging Network Ontario Annual Symposium. London, ON. March 23-24, 2023.
5. V Desai,* PV Wyszkievicz, AM Matheson, **M Sharma**, MJ McIntosh, HK Kooner, DG McCormack and G Parraga. *CT Pulmonary Vascular, Airway, Pulmonary Artery and Aorta Measurements in Ex-Smokers with and without COPD.* Canadian Undergraduate Medical Physics Conference. August 25 2022. Virtual.

6. **M Sharma,*** MJ McIntosh, HK Kooner, DG McCormack and G Parraga. *Machine-Learning and Texture Analysis of Hyperpolarized ^3He MRI Ventilation Predicts Quality-of-life Worsening in Ex-smokers with and without COPD.* 68th annual Canadian Organization of Medical Physicists (COMP) scientific meeting, June 22-25 2022, Quebec City, QC, Canada.
7. **M Sharma,*** MJ McIntosh, HK Kooner, AM Matheson, PV Wyszkievicz, DG McCormack, and G Parraga. *Texture Analysis and Machine Learning of Hyperpolarized ^3He MRI Ventilation Predicts Quality-of-life Worsening in Ex-smokers with and without COPD.* London Imaging Discovery Day. London ON, Canada. June 9 2022.
8. **M Sharma,*** HK Kooner, MJ McIntosh, DG McCormack and G Parraga. *Quality-of-life Worsening Predicted Using Baseline Hyperpolarized ^3He MRI Ventilation Texture Features and Machine-Learning.* Joint annual International Society of Magnetic Resonance in Medicine-European Society for Magnetic Resonance in Medicine and Biology (ISMRM-ESMRMB) Scientific Meeting 2022, London, England, UK May 7-12 2022.
9. MJ McIntosh,* **M Sharma,** AM Matheson, HK Kooner, RL Eddy, C Licksai, DG McCormack, M Nicholson, C Yamashita and G Parraga. *Respiratory System Resistance Explained using Hyperpolarized ^{129}Xe MRI Texture Features and Machine Learning.* Joint annual International Society of Magnetic Resonance in Medicine-European Society for Magnetic Resonance in Medicine and Biology (ISMRM-ESMRMB) Scientific Meeting 2022, London, England, UK May 7-12, 2022.
10. HK Kooner,* MJ McIntosh, **M Sharma,** GV Singh, N Nasir, E Blake, I Dhaliwal, M Nicholson, M Kirby and G Parraga. *Post-Acute COVID-19 Syndrome: Longitudinal ^{129}Xe MRI Ventilation Heterogeneity Measurements.* Joint annual International Society of Magnetic Resonance in Medicine-European Society for Magnetic Resonance in Medicine and Biology (ISMRM-ESMRMB) Scientific Meeting 2022, London, England, UK May 7-12, 2022.
11. HK Kooner,* MJ McIntosh, AM Matheson, **M Sharma,** PV Wyszkievicz, I Dhaliwal, M Abdelrazek, M Nicholson, and G Parraga. *^{129}Xe MRI Ventilation Defects in People with Post-Acute COVID-19 Syndrome.* Robarts Research Retreat. London ON, Canada. June 16 2022.
12. **M Sharma,*** MJ McIntosh, HK Kooner, AM Matheson, PV Wyszkievicz, DG McCormack, and G Parraga. *Texture Analysis and Machine Learning of Hyperpolarized ^3He MRI Ventilation Predicts Quality-of-life Worsening in Ex-smokers with and without COPD.* London Imaging Discovery Day. London ON, Canada. June 9 2022.
13. HK Kooner,* MJ McIntosh, AM Matheson, **M Sharma,** PV Wyszkievicz, I Dhaliwal, M Nicholson, M Abdelrazek, and G Parraga. *^{129}Xe MRI Ventilation Defects in People with Post-Acute COVID-19 Syndrome.* London Imaging Discovery Day. London ON, Canada. June 9 2022.
14. PV Wyszkievicz,* **M Sharma,** DG McCormack, IA Cunningham, and G Parraga. *CT Pulmonary Airways in Chronic Obstructive Pulmonary Disease: Longitudinal Worsening in the TINCan Cohort Study.* London Imaging Discovery Day. London ON, Canada. June 9 2022.
15. **M Sharma,*** AR Westcott, A Fenster, DG McCormack and G Parraga. *Hyperpolarized Gas Magnetic Resonance Imaging Texture Analysis and Machine Learning Explains Accelerated Lung Function Decline in Ex-smokers with COPD.* Annual Society for Photo-optical Instrumentation Engineers scientific meeting, February 15-19 2021, Virtual.
16. HK Kooner,* MJ McIntosh, **M Sharma,** AM Matheson, Y Rajapaksa, I Dhaliwal, M Nicholson and G Parraga. *Hyperpolarized ^{129}Xe MRI Ventilation Texture Features to Characterize Long-haul COVID-19 Survivors.* 29th annual International Society for Magnetic Resonance in Medicine scientific meeting. May 15-20 2021, Virtual.

17. **M Sharma**,* MJ McIntosh, AM Matheson, HK Kooner, DG McCormack, DA Palma and G Parraga. *6MWD worsening in COPD predicted using CT and MRI Texture Features and Machine Learning*. 117th annual American Thoracic Society scientific meeting, May 14-19 2021, Virtual.
18. MJ McIntosh,* AM Matheson, **M Sharma**, HK Kooner, RL Eddy, DG McCormack, C Yamashita and G Parraga. *Pulmonary 1H MRI Lobar Classification using Convolutional Neural Networks*. 67th annual Canadian Organization of Medical Physicist scientific meeting, June 22-25 2021, Virtual.
19. **M Sharma**,* MJ McIntosh, AM Matheson, HK Kooner, DG McCormack, DA Palma and G Parraga. *Six Minute Walk Distance worsening in COPD predicted using CT and MRI Texture Features and Machine Learning*. Annual Robarts Research Retreat, June 17 2021, Virtual.
20. MJ McIntosh,* AM Matheson, **M Sharma**, HK Kooner, RL Eddy, DG McCormack, C Yamashita and G Parraga. *Pulmonary 1H MRI Lobar Classification using Convolutional Neural Networks*. Annual Robarts Research Retreat, June 17 2021, Virtual.
21. **M Sharma**,* AR Westcott, JL MacNeil, DG McCormack and G Parraga. *Machine Learning and Texture Analysis of Thoracic X-ray Computed Tomography to Reveal Subclinical Emphysema*. The American Association of Physicists in Medicine – Canadian Organization of Medical Physicists Joint meeting, July 12-16 2020, Virtual.
22. **M Sharma**,* AR Westcott, JL MacNeil, DG McCormack and G Parraga. *Machine Learning with Texture Analysis Reveals Subclinical Emphysema in Thoracic X-ray Computed Tomography*. Annual Robarts Research Retreat, June 19th 2020, Virtual.
23. JL MacNeil,* B Hou, **M Sharma**, DG McCormack and G Parraga. *Ex-smokers with Abnormal Diffusing Capacity and Normal CT: Multi-parametric Response Map Phenotypes*. 116th annual American Thoracic Society scientific meeting, May 15-20 2020, Virtual.
24. **M Sharma**,* AR Westcott, JL MacNeil, DG McCormack and G Parraga. *Identifying Functional Information Determinants in Thoracic Computed Tomography Images Using Machine Learning*. 18th annual Imaging Network of Ontario scientific meeting, March 26-27 2020, Virtual.

D Proffered Poster Presentations

Published – (12 total; 6 first-author) *presenter

1. **M Sharma**,* PV Wyszkievicz, MJ McIntosh, HK Kooner, AM Matheson, DG McCormack and G Parraga. *MRI and CT Measurements Uniquely Explain All-cause Mortality in Ex-smokers with and without COPD*. Robarts Research Retreat. London, ON. June 28, 2023.
2. HK Kooner,* **M Sharma**, MJ McIntosh, I Dhaliwal, JM Nicholson, and G Parraga. *¹²⁹Xe MRI Ventilation Predicts Longitudinal Quality-of-Life Improvement in Post-Acute COVID-19 Syndrome*. Annual International Society of Magnetic Resonance in Medicine Scientific Meeting 2023, Toronto, Canada. June 3-8, 2023.
3. MJ McIntosh,* **M Sharma**, HK Kooner, H Serajeddini, A Bhalla, C Yamashita, and G Parraga. *Hyperpolarized ¹²⁹Xe MRI ventilation textures predict short and long-term response to Anti-IL-5Ra Biologic Therapy in Eosinophilic Asthma*. Annual International Society of Magnetic Resonance in Medicine Scientific Meeting 2023, Toronto, Canada. June 3-8, 2023.
4. PV Wyszkievicz,* **M Sharma**, HK Kooner, DG McCormack, M Kirby and G Parraga. *Terminal Airspace Enlargement Measured Using Pulmonary Functional MRI Predicts CT Airway Loss in COPD*. Annual International Society of Magnetic Resonance in Medicine Scientific Meeting 2023, Toronto, Canada. June 3-8, 2023.

5. **M Sharma,*** PV Wyszkievicz, MJ McIntosh, HK Kooner, AM Matheson, DG McCormack and G Parraga. *CT and MRI Measurements Uniquely Explain All-cause Mortality in Ex-smokers*. Imaging Network of Ontario Annual Symposium, London Ontario. March 23-24, 2023.
6. V Desai goudar,* PV Wyszkievicz, AM Matheson, **M Sharma**, MJ McIntosh, HK Kooner, DG McCormack and G Parraga. *Pulmonary Small Vessel Worsening in Ex-smokers with COPD*. Imaging Network of Ontario Annual Symposium, London Ontario. March 23-24, 2023.
7. **M Sharma,*** MJ McIntosh, HK Kooner, AM Matheson, PV Wyszkievicz, DG McCormack, and G Parraga. *Texture Analysis and Machine Learning of Hyperpolarized ³He MRI Ventilation Predicts Quality-of-life Worsening in Ex-smokers with and without COPD*. Robarts Research Retreat. London ON, Canada. June 16 2022.
8. PV Wyszkievicz,* **M Sharma**, DG McCormack, IA Cunningham, and G Parraga. *CT Pulmonary Airways in Chronic Obstructive Pulmonary Disease: Longitudinal Worsening in the TINCan Cohort Study*. Robarts Research Retreat. London ON, Canada. June 16 2022.
9. **M Sharma,*** AM Matheson, DG McCormack, DA Palma and G Parraga. *Hyperpolarized 3He MRI ADC and Ventilation Features Predict Rapidly Worsening Emphysema Using Machine-learning*. 29th annual International Society of Magnetic Resonance in Medicine scientific meeting, May 15-20 2021, Virtual.
10. HK Kooner,* MJ McIntosh, **M Sharma**, AM Matheson, Y Rajapaksa, I Dhaliwal, M Nicholson and G Parraga. *Hyperpolarized ¹²⁹Xe MRI Ventilation Texture Features to Characterize Long-haul COVID-19 Survivors*. Annual Robarts Research Retreat, June 17 2021, Virtual.
11. **M Sharma,*** AR Westcott, JL MacNeil, B Hou, DG McCormack and G Parraga. *Hidden Computed Tomography Texture Features in Ex-smokers with Abnormal Spirometry? Playing Hide and Seek Using Machine Learning*. 116th annual American Thoracic Society scientific meeting May 15-20 2020, Virtual.
12. **M Sharma,*** AR Westcott, A Fenster, DG McCormack and G Parraga. *Can Hyperpolarized Gas MRI and Machine Learning Predict Longitudinal Changes in Airflow Limitation in Ex-smokers? 28th annual International Society of Magnetic Resonance in Medicine scientific meeting, April 18-23 2020, Virtual.*

INVITED TALKS

1. HK Kooner,* **M Sharma**, MJ McIntosh, I Dhaliwal, JM Nicholson, and G Parraga. *¹²⁹Xe MRI Ventilation Predicts Longitudinal Quality-of-Life Improvement in Post-Acute COVID-19 Syndrome*. Hyperpolarized Study Group Business Meeting, Toronto, Canada. June 7, 2023.

SUPERVISORY AND MENTORSHIP ACTIVITIES

09/2023- Present	Graduate Student Mentor Graduate Student: Yibeltal Aseffa MSc Candidate Project: "Automated CT Mucus Scoring Using a Convolutional Neural Network"
09/2023- Present	Graduate Student Mentor Graduate Student: Ali Muzaffaripour MSc Candidate Project: " ¹²⁹ Xe MRI Texture Features 6-weeks post-therapy in Asthma Patients"
09/2023- Present	Graduate Student Mentor Graduate Student: Sam Tchnerer MSc Candidate Project: " ¹²⁹ Xe MRI Ventilation Defects and CT Measurements in Asthma Patients"

- 09/2022-Present** **Graduate Student Mentor**
Graduate Student: Alexander Biancaniello MSc Candidate
Project: "Dissolved-phase ¹²⁹Xe MRI and Spectroscopy Measurements in COPD"
- 09/2022-04/2023** **Graduate Student Mentor**
Undergraduate Thesis Student: Vedanth Desaigoudar BSc Candidate
Project: "CT vascular, airway, pulmonary artery-to-aorta measures in ex-smokers"
- 09/2021-04/2023** **Graduate Student Mentor**
Graduate Student: Paulina V. Wyszkievicz MSc Candidate
Project: "CT Airway Measurements in ex-smokers with and without COPD"
- 05/2021-04/2022** **Graduate Student Mentor**
Undergraduate Student: Vedanth Desaigoudar BSc Candidate
Project: "Quantitative Hyperpolarized Gas MR Imaging Biomarkers"
- 09/2020-Present** **Graduate Student Mentor**
Graduate Student: Harkiran K Kooner PhD Candidate
Project: "MRI Ventilation Texture and Quality-of-life Improvements in COVID-19"
- 09/2020-04/2021** **Graduate Student Mentor**
Undergraduate Student: Yasal Rajapaksa BSc Candidate
Project: "Pulmonary Imaging Biomarkers of Post-Acute COVID-19 Syndrome"

COMMUNITY SERVICE AND VOLUNTEER ACTIVITIES

- 2019-Present** **Co-President**
Deep Learning Club, Western University
Organize member meetings and design presentations/demonstrations
- 2019-Present** **Member**
CAMPEP Student Club, Western University
Journal club, discuss new topics in medical physics, practice exam questions
- 2022-2023** **Member**, Graduate Student Association (GSA), Western University
GSA Roles – Social media coordinator, Volunteer opportunities coordinator, and Academic events coordinator. Plan and organize events for graduate students in the department of medical biophysics
- 2022-2023** **Mentor**, Academic Mentorship Program (AMP), Western University
Mentee – Amandeep Bains, PhD
Monthly activities and meetings with Dr. Bains during his CAMPEP MSc.
- 2022-2022** **Judge**
Thames Valley Science & Engineering Fair, Western University
Judging science projects for a 2-day science fair for regional high-schools
- 2017-2019** **Volunteer**
Credit Valley Hospital, Trillium Health Partners, Mississauga
Volunteered over two hundred hours at Neonatal and Paediatric Intensive Care Units – RMHC Family Rooms
- 2017-2019** **Volunteer**
Physics Club, The University of Toronto, Mississauga
Aided in teaching PHY136/137 course content in Facilitated Study Groups (FSG)

LANGUAGES

Fluent reading, writing and speaking in – English, Ukrainian, Russian and Hindi.

PROFESSIONAL TRAINING AND CERTIFICATES

2020-2021 **Anatomy, Radiology, and Contouring (ARC) Bootcamp for Radiation Oncology and Medical Physics Residents**
London Health Sciences Center, London, Ontario, Canada

PROFESSIONAL SOCIETIES

2021-Present European Respiratory Society (ERS)
2020-Present International Society for Optics and Photonics (SPIE)
2019-Present The Canadian Organization of Medical Physicists (COMP)
2019-Present American Association of Physicists in Medicine (AAPM)
2019-Present Canadian Thoracic Society (CTS)
2019-Present American Thoracic Society (ATS)
2019-Present The International Society for Magnetic Resonance in Medicine (ISMRM)